ornl

OAK RIDGE NATIONAL LABORATORY

MARTIN MARIETTA

NUREG/CR-3459
ORNL/TM-8889

Experiment Data Report for Multirod Burst Test (MRBT) Bundle B-5

R. H. Chapman
J. L. Crowley
A. W. Longest

Prepared for the U.S. Nuclear Regulatory Commission
Office of Nuclear Regulatory Research
Under Interagency Agreements DOE 40-551-75 and 40-552-75

OPERATED BY
MARTIN MARIETTA ENERGY SYSTEMS, INC.
FOR THE UNITED STATES
DEPARTMENT OF ENERGY

Printed in the United States of America. Available from
National Technical Information Service
U.S. Department of Commerce
5285 Port Royal Road, Springfield, Virginia 22161

Available from
GPO Sales Program
Division of Technical Information and Document Control
U.S. Nuclear Regulatory Commission
Washington, D.C. 20555

NUREG/CR-3459
ORNL/TM-8889
Dist. Category R2, R3

Engineering Technology Division

EXPERIMENT DATA REPORT FOR MULTIROD BURST TEST (MRBT) BUNDLE B-5

R. H. Chapman J. L. Crowley
A. W. Longest

Manuscript Completed — July 3, 1984
Date Published — August 1984

Prepared for the
U.S. Nuclear Regulatory Commission
Office of Nuclear Regulatory Research
Under Interagency Agreements DOE 40-551-75 and 40-552-75

NRC Fin No. B0120

Prepared by the
OAK RIDGE NATIONAL LABORATORY
Oak Ridge, Tennessee 37831
operated by
MARTIN MARIETTA ENERGY SYSTEMS, INC.
for the
U.S. DEPARTMENT OF ENERGY
under Contract No. DE-AC05-84OR21400

CONTENTS

LIST OF FIGURES

LIST OF TABLES

FOREWORD

Examination, analysis, and interpretation of a bundle test take place over a long period of time, and our practice has been to report progress and results as they become available. Dissemination of the information in this manner results in its being disjointed and scattered throughout several publications. This presents some problems to the users in that one is never sure if the information at hand is the most recent. Our intention has been to alleviate some of these problems by (1) publication of a data report on each bundle test and (2) publication of analytic and interpretative reports when sufficient information has been developed.

Consistent with this intention, the objective of this data report is to provide a reference source of information and results obtained during the B-5 test and from pretest and posttest examination of the test array. We believe the data presented herein, consisting of plots, tabulations, photographs, and some important observations, are necessary for analysis and interpretation of the test. A decision was made that the data should be presented with a minimum of interpretation and that analysis or "second-generation" data, such as comparative temperature vs time plots, should be excluded.

This report is derived from research performed by the (now completed) Multirod Burst Test (MRBT) Program at Oak Ridge National Laboratory (ORNL). This program was sponsored by the Division of Accident Evaluation of the Nuclear Regulatory Commission, and the results were published routinely in a series of progress reports, topical reports and papers, quick-look test reports, and test data reports.

Progress reports published by the MRBT Program include:

NUREG Report No.	ORNL Report No.	Period covered
	ORNL/TM-4729	July—September 1974
	ORNL/TM-4805	October—December 1974
	ORNL/TM-4914	January—March 1975
	ORNL/TM-5021	April—June 1975
	ORNL/TM-5154	July—September 1975
	ORNL/NUREG/TM-10	October—December 1975
	ORNL/NUREG/TM-36	January—March 1976
	ORNL/NUREG/TM-74	April—June 1976
	ORNL/NUREG/TM-77	July—September 1976
	ORNL/NUREG/TM-95	October—December 1976
	ORNL/NUREG/TM-108	January—March 1977
	ORNL/NUREG/TM-135	April—June 1977
NUREG/CR-0103	ORNL/NUREG/TM-200	July—December 1977
NUREG/CR-0225	ORNL/NUREG/TM-217	January—March 1978
NUREG/CR-0398	ORNL/NUREG/TM-243	April—June 1978
NUREG/CR-0655	ORNL/NUREG/TM-297	July—December 1978
NUREG/CR-0817	ORNL/NUREG/TM-323	January—March 1979
NUREG/CR-1023	ORNL/NUREG/TM-351	April—June 1979
NUREG/CR-1450	ORNL/NUREG/TM-392	July—December 1979
NUREG/CR-1883	ORNL/NUREG/TM-426	January—June 1980

NUREG/CR-1919	ORNL/NUREG/TM-436	July—December 1980
NUREG/CR-2366, Vol. 1	ORNL/TM-8058	January—June 1981
NUREG/CR-2366, Vol. 2	ORNL/TM-8'9'	July—December 1981
NUREG/CR-2911	ORNL/TM-8485	January—June 1982

Topical reports and papers pertaining to research and development carried out by this program are:

1. R. H. Chapman (comp.), *Characterization of Zircaloy-4 Tubing Procured for Fuel Cladding Research Programs*, ORNL/NUREG/TM-29 (July 1976).

2. W. E. Baucum and R. E. Dial, *An Apparatus for Spot Welding Sheathed Thermocouples to the Inside of Small-Diameter Tubes at Precise Locations*, ORNL/NUREG/TM-33 (August 1976).

3. W. A. Simpson, Jr., et al., *Infrared Inspection and Characterization of Fuel-Pin Simulators*, ORNL/NUREG/TM-55 (November 1976).

4. R. H. Chapman et al., *Effect of Creep Time and Heating Rate on Deformation of Zircaloy-4 Tubes Tested in Steam with Internal Heaters*, NUREG/CR-0343 (ORNL/NUREG/TM-245) (October 1978).

5. J. F. Mincey, *Steady-State Axial Pressure Losses Along the Exterior of Deformed Fuel Cladding: Multirod Burst Test (MRBT) Bundles B-1 and B-2*, NUREG/CR-101' (ORNL/NUREG/TM-350) (January 1980).

6. R. W. McCulloch, P. T. Jacobs, and D. L. Clark, *Development of a Fabrication Procedure for the MRBT Fuel Simulator Based on the Use of Cold-Pressed Boron Nitride Preforms*, NUREG/CR-1111 (ORNL/NUREG/TM-362) (March 1980).

7. R. H. Chapman, J. V. Cathcart, and D. O. Hobson, "Status of Zircaloy Deformation and Oxidat' ı Research at Oak Ridge National Laboratory," in *Proceedings of Spec lists Meeting on the Behavior of Water Reactor Fuel Elements under Accident Conditions, Spatind, Norway, September 13–16, 1976*, CSNI Report No. 13 (1977).

8. R. H. Chapman et al., "Zircaloy Claddin Deformation in a Steam Environment with Transient Heating," pp. 43–8 in *Zirconium in the Nuclear Industry (Fourth Conference)*, ASTM STP 681, American Society for Testing and Materials, 1979.

9. R. L. Anderson, K. R. Carr, and T. G. Kollie, *Thermometry in the Multirod Burst Test Program*, NUREG/CR-2470 (ORNL/TM-8024) (March 1982).

10. A. W. Longest, J. L. Crowley, and R. H. Chapman, *Variations in Zircaloy-4 Cladding Deformation in Replicate LOCA Simulation Tests*, NUREG/CR-2810 (ORNL/TM-8413) (September 1982).

11. A. W. Longest, R. H. Chapman, and J. L. Crowley, "Boundary Effects on Zircaloy-4 Cladding Deformation in LOCA Simulation Tests," *Trans. Am. Nucl. Soc.* 41, 383 (1982).

12. R. H. Chapman, J. L. Crowley, and A. W. Longest, "Effect of Bundle Size on Cladding Deformation in LOCA Simulation Tests," in *Zirconium in the Nuclear Industry: Sixth International Symposium, ASTM STP 824*, ed. D. G. Franklin, R. B. Adamson, and B. Cox, American Society for Testing and Materials (in publication).

The following bundle test quick-look and data reports have been issued by this program:

1. R. H. Chapman (comp.), *Quick-look Report on MRBT No. 1 4 × 4 Bundle Burst Test*, Internal Report ORNL/MRBT-2 (September 1977).

2. R. H. Chapman (comp.), *Quick-look Report on MRBT No. 2 4 × 4 Bundle Burst Test*, Internal Report ORNL/MRBT-3 (November 1977).

3. R. H. Chapman, *Quick-look Report on MRBT No. 3 4 × 4 Bundle Burst Test*, Internal Report ORNL/MRBT-4 (August 1978).

4. R. H. Chapman, *Quick-look Report on MRB B-4 (6 × 6) Bundle Test*, Internal Report ORNL/MRBT-6 (February 1981).

5. R. H. Chapman et al., *Quick-look Report on MRBT B-5 (8 × 8) Bundle Test*, Internal Report ORNL/MRBT-5 (July 1980).

6. R. H. Chapman et al., *Quick-look Report on MRBT B-6 (8 × 8) Bundle Test*, Internal Report ORNL/MRBT-7 (January 1982).

7. R. H. Chapman et al., *Bundle B-1 Test Data*, ORNL/NUREG/TM-322 (June 1979).

8. R. H. Chapman et al., *Bundle B-2 Test Data*, ORNL/NUREG/TM-337 (August 1979).

9. R. H. Chapman et al., *Bundle B-3 Test Data*, ORNL/NUREG/TM-360 (January 1980).

10. A. W. Longest et al., *Experiment Data Report for Multirod Burst Test (MRBT) Bundle B-4*, NUREG/CR-2968 (ORNL/TM-8509) (December 1982).

11. R. H. Chapman et al., *Experiment Data Report for Multirod Burst Test (MRBT) Bundle B-6*, NUREG/CR-3460 (ORNL/TM-8890) (in publication).

12. R. T. Bailey, *Steady-State Pressure Losses for Multirod Burst Test (MRBT) Bundle B-5*, NUREG/CR-2597 (ORNL/Sub/80-40441/1) (April 1982).

EXPERIMENT DATA REPORT FOR MULTIROD BURST TEST (MRBT) BUNDLE B-5

R. H. Chapman J. L. Crowley
A. W. Longest

ABSTRACT

A reference source of MRBT bundle B-5 test data is presented with interpretation limited to that necessary to understand pertinent features of the test. Primary objectives of this 8 × 8 multirod burst test were to investigate the effects of array size and rod-to-rod interactions on cladding deformation in the high-alpha-Zircaloy temperature range under simulated light-water reactor loss-of-coolant accident (LOCA) conditions. B-5 test conditions, nominally the same as used in an earlier 4 × 4 (B-3) test, simulated the adiabatic heatup (reheat) phase of an LOCA and were conducive to large deformation. The fuel pin simulators were electrically heated (average linear power generation of 3.0 kW/m) and were slightly cooled with a very low flow (Re ~ 140) of low-pressure superheated steam. The cladding temperature increased from the initial temperature (335°C) to the burst temperature at a rate of 9.8°C/s. The simulators burst in a very narrow temperature range, with an average of 768°C. Cladding burst strain ranged from 32% to 95%, with an average of 61%. Volumetric expansion over the heated length of the cladding ranged from 35% to 79%, with an average of 52%. Although the average burst strain for the interior simulators was only slightly greater than that for the exterior simulators, the average volumetric expansion was significantly greater. The maximum coolant channel flow area reduction was 69% for the entire 8 × 8 array, 83% if based on the interior 6 × 6 array, and 91% if based on the central 4 × 4 array. The results clearly show deformation was greater in the bundle interior and suggest rod-to-rod mechanical interactions caused axial propagation of the deformation.

Keywords: Zircaloy, nuclear fuel cladding, tubes, bundle burst tests, loss-of-coolant accident, deformation, flow blockage, boundary conditions, rod-to-rod interactions, fuel pin simulators.

---

1. INTRODUCTION

This report presents, in considerable detail, the experimental data for the B-5 test (the first of two 8 × 8 multirod burst tests) conducted by the Multirod Burst Test (MRBT) Program at Oak Ridge National Laboratory (ORNL). This work (now completed) was sponsored by the Division of Accident Evaluation of the Nuclear Regulatory Commission (NRC) and was designed to investigate Zircaloy cladding deformation behavior under simulated loss-of-coolant accident (LOCA) conditions. Although preliminary versions of the data have been published in a quick-look report[1] and in periodic progress reports,[2-5] the data are collected in final form in this report to provide a reference source document for the B-5 test results. Interpretation of the data is limited to that necessary to understand pertinent features of the test. Because of this, this report should be used in conjunction with other published results and interpretations.[2-8] (The Foreword lists all publications issued by this program.)

The primary objectives of the B-5 test, which was conducted May 30, 1980, were to investigate the effects of array size and rod-to-rod interactions on cladding deformation with a low heating rate in the high-alpha-Zircaloy temperature range. To realize the objectives, test conditions nominally the same as used in an earlier 4 × 4 (B-3) test[9] were selected. These parameters (i.e., high-alpha-Zircaloy temperature range and a low heating rate) and other features of the MRBT mode of testing were known to be conducive to large deformation and, thus, favorable to rod-to-rod interactions. In addition, these conditions are representative of predictions from LOCA licensing calculations for a range of postulated light-water reactor (LWR) accidents.

Because test conditions used in this program simulate the adiabatic heatup (reheat) phase of an LOCA and are generally considered to be conservative, the B-5 test results are believed to provide an upper-limit estimate of the deformation that can be anticipated in most accidents with cladding failures in the high-alpha-Zircaloy temperature range. Similarly, the results of the B-6 test[5,10] (the second 8 × 8 array tested by this program) are believed to be a reasonable upper limit of the deformation that can be expected for failures in the alpha-plus-beta temperature range. Based on the burst strains characteristic of these two temperature ranges (i.e., 50% to 100% for the high-alpha and 25% to 50% for the alpha-plus-beta temperature range), the B-5 and B-6 deformation results taken together bracket the variation in the upper limit of expected deformation over a wide temperature range of interest.

Following the format of the other reports[9-13] in this series, a brief description of the test design and an overview of test operations are given first. These are followed, in turn, by a section giving a summary of the test results and a section giving detailed test results, including photographic documentation of the bundle before and after testing and of the 59 cross sections on which the deformation measurements were made. Because the transient test data and the posttest deformation data are voluminous, much of the data is presented (in computer-generated graphical and tabular formats) on microfiche in the pocket attached to the inside back cover. Similar to the B-6 report,[10] a final section is devoted to interpretation and important observations; however, the interpretation is limited to that we believe necessary to understand and explain the test results.

2. TEST DESCRIPTION

2.1 Assembly

Figure 1 shows a simplified drawing of the B-5 test assembly installed in the test vessel. An *unheated* (electrically) shroud surrounded the test array as indicated in Sect. A-A of the figure. The shroud was constructed of thin (0.13-mm-thick) stainless steel, with a highly reflective gold-plated surface to minimize thermal capacity and radiative thermal losses. The stainless steel sheet was backed by a layer of insulating material to reduce heat losses, and the insulating material was backed by a strong structure to withstand radial forces during the test transient. The thin shroud was spaced 1.75 mm (i.e., one-half of a coolant channel distance) from the outer rod surfaces. This permitted some deformation of these simulators before contact with the shroud but prevented gross outward movement of the simulators.

The test array and shroud assembly were separately suspended from the test vessel cover flange to allow free and independent axial movement. Four Inconel-718 grids, typical of the type used in commercial pressurized-water reactor 15 × 15 fuel bundles, provided proper spacing (14.43-mm center-to-center) of the fuel pin simulators (10.92-mm diam) in a square array. Because grid tie-rods were not used, the grids were held in position only by grid-spring forces acting on the individual simulators and were free to move axially to compensate for growth or shrinkage of the bundle during the test.

Design features of the fuel pin simulators are illustrated in Fig. 2 and as-built data are listed in Table 1. The fuel simulators (internal heaters) were anchored to the cladding tubes by the lower seal glands. Differential movement (thermal expansion, growth, and/or shrinkage of the cladding) between the fuel simulator and cladding tube was accommodated by a flexible section in the upper electrical lead. Different simulator lengths were required to accommodate the dimensions of the upper seal gland (Figs. 1 and 2), but ceramic inserts were used in both types to adjust the free volume to the same nominal value. The average free volume of the B-5 simulators was 50.1 cm^3, with a standard deviation of 1.0 cm^3.

Although the simulator gas volume was reasonably typical, the distribution of the volume was not typical of a full-length fuel rod. Of the total initial volume (at room temperature), about 13% was in the heated portion of the annulus between the fuel simulator and the inside diameter of the Zircaloy tube, 10% was in the unheated portion of the annulus, 33% was in the pressure transducer and connecting tube, and 44% was distributed in the end regions (mostly at the upper end) of the fuel pin simulator.

The fuel simulators (internal heaters) were produced in the ORNL Fuel Rod Simulator Technology Development Laboratory, using fabrication procedures[14] developed specifically for the needs of this program. A thin plasma-sprayed ZrO_2 protective coating was applied to the outside surface (over the heated length) of the simulators. The axial heat generation profile of each of the coated simulators was characterized (before assembly within the Zircaloy tube) under transient heating conditions, using a high-temperature infrared (IR) scanning technique.[15] The highest-quality simulators, as judged by heat generation uniformity, were selected for the array interior positions.

The Zircaloy-4 tubes (10.92-mm OD by 0.635-mm wall thickness) came from the master lot of well-characterized[16-18] tubing purchased for use in several NRC-sponsored cladding research programs. Tube serial numbers, given in Table 1, can be used to relate the individual tubes to their fabrication history.[16] The tubes were lightly oxidized in superheated steam for 30 min at 480°C on both internal and external surfaces prior to fabrication of the fuel pin simulators to better simulate the conditions of fuel cladding after a period of reactor operation. Metallographic examination of typical specimens oxidized under these conditions showed the oxide film to be very uniform and thin (1 to 2 μm); this should not have materially affected the metallurgical conditions of the tubes.

Each fuel pin simulator was instrumented with a fast-response, strain-gage-type pressure transducer and four Inconel-sheathed (0.71-mm-OD) type K (Chromel-Alumel) thermocouples with ungrounded junctions. The thermocouples were spot-welded to the inside surface of the Zircaloy-4 tubes, using a device developed specifically for this purpose,[19] at the positions shown in Fig. 3. The figure also gives thermocouple identifications for use in subsequent figures and discussions (the nomenclature TE 10-4 identifies thermocouple 4 in simulator 10). Axial locations of the thermocouples are shown more clearly in Fig. 4. As evident from the figure, 32 internal thermocouples (average of one for every two simulators) were installed at each of the 7 instrumented elevations of primary interest, with 16 thermocouples at the lowest instrumented elevation and 8 thermocouples at each of the 2 grid elevations. The orientations of the thermocouples (Fig. 3) at any given elevation were selected (within the limitations imposed by a number of design constraints) to provide supplementary temperature information of potential benefit for plotting radial temperature profiles and for detecting rod-to-rod thermal interactions.

Four 0.25-mm-diam bare-wire type S (Pt vs Pt-10% Rh) thermocouples were spot-welded to the outside surface of each of four simulators (Nos. 5, 28, 39, and 44) in an attempt to obtain azimuthal temperature gradient information (Fig. 3). These thermocouples were equally spaced around the tubes at the 48-cm elevation. An internal thermocouple was also located at this elevation in each of these simulators.

Sixteen 0.076-mm-diam bare-wire type S thermocouples were spot-welded directly to the outside surface of the thin shroud surrounding the test array. Four thermocouples were attached to each side of the shroud at different positions (Fig. 3) to obtain information on both the axial and circumferential temperature distributions. The shroud thermocouple identifications are also given in the figure for use in subsequent temperature plots.

As noted in Fig. 3, four of the simulator internal thermocouples (TE 23-1, TE 24-2, TE 30-4, and TE 53-1) became detached and one (TE 52-2) developed a grounded junction during fabrication of the simulators. One of the internal thermocouples (TE 46-1) became inoperative after the array was installed in the test vessel. Three of the fragile bare-wire exterior thermocouples on simulator 39 (TE 39-5, TE 39-7, and TE 39-8) and three of the shroud thermocouples (TE 91-3, TE 91-4, and TE 93-1) were broken during subsequent assembly of the test array and could not be replaced. Two of the type S thermocouples (TE 44-7 and TE 93-4) malfunctioned before the test, and one (TE 91-1) malfunctioned during the transient. Although it is not apparent from the data, the detached interior thermocouples might have indicated temperatures slightly higher than those they would have indicated if they had remained attached to the Zircaloy tubes. For this reason they were not considered reliable indicators of the burst temperature.

Eight thermocouples (TE 14-3, TE 18-4, TE 21-1, TE 27-4, TE 36-1, TE 38-2, TE 47-2, and TE 51-1) at the 38-cm elevation on interior simulators were averaged electronically (in real time) to represent the bundle average temperature. This average, identified as TAV-10, was recorded and displayed to provide on-line information as the test progressed.

Three thermocouples (TE-320 through TE-322) were located in the tube matrix at the 107-cm elevation (centerline elevation of the steam inlet nozzle; see Fig. 1) to obtain inlet steam temperature measurements across the bundle. Five thermocouples (TE-323 through TE-327) were located in the tube matrix at the bottom of the heated zone (0-cm elevation) to obtain outlet steam temperature measurements at the centers of the bundle and quadrants of the bundle at this elevation. Figure 5 shows the identifications and locations of these sensors. These were 0.71-mm-diam, stainless-steel-sheathed, type K thermocouples with insulated junctions.

A detailed description of the temperature measurement systems and a comprehensive analysis of the errors and uncertainties associated with the measurements have been reported previously.[20]

Millivolt signals from the pressure transducers, thermocouples, and electrical power measuring instruments were recorded on magnetic tape by a computer-controlled data acquisition system (CCDAS) for subsequent analysis. Calibration corrections, preprogrammed into the computer system, were automatically applied to the millivolt signals before printout of the data.

Each fuel pin simulator was electrically connected in parallel at the upper end through separately fused electrical circuits to a common dc constant-voltage power supply and was attached to a current collector at the lower end of the array as indicated in Fig. 1. Because the electrical characteristics were nearly the same for all the simulators (average value for the resistance data given in Table 1 of 1.98 Ω with a standard deviation of 0.02 Ω), it was not necessary to provide for redistribution of the current to improve uniformity of the power generation in the bundle.

2.2 Operations

Heatup of the vessel containing the test assembly was initiated early in the afternoon of the day before the test; the temperature was ~200°C at the end of the work shift. Power adjustments to the vessel heaters were made to maintain the temperature near this value during the next 12 h to avoid temperature cycling the test assembly. Early on the day of the test, power to the vessel heaters was increased, and superheated steam was admitted to the vessel in the approach to the initial test temperature. Throughout this phase of operation, electrical power was not applied to the simulators; periodic leak checks indicated the simulator seals were performing very well (i.e., <10-kPa helium pressure loss per min at 7600 kPa and ~330°C).

After thermal equilibration (~336°C) of the test assembly was attained, the simulators were pressurized to ~7700 kPa, and a short powered run (~9.0-s transient) was conducted to ascertain that the data acquisition system and all the instrumentation were functioning properly and that the performance of the test components was as expected. Examination and evaluation of the limited quick-look data from this short transient (during which the temperature of the simulators increased to ~390°C) indicated that slight adjustments were needed to achieve the desired heating rate.

During the high-temperature hold time (~6 h) between the pretest power-bump and the burst test transient, the lower gasket seal (Fig. 2) on simulator 62 developed a gross leak. The magnitude of the leak was such that its effect could not be counteracted by inflow of helium. Because of the location of this simulator in the test array (Fig. 3), we reasoned that the influence of its lack of deformation on the remainder of the simulators would be small, and it was decided to continue the test with the simulator unpressurized. However, the simulator was heated so that the proper temperature boundary conditions would be preserved.

Following the power adjustments and restabilization of the bundle temperature at ~335°C, all the fuel pin simulators except No. 62 (with the leaking seal) were pressurized simultaneously to ~11,620 kPa (differential above the external pressure) and individually isolated from the supply header to provide a constant helium inventory in each one during the transient. The header was vented, and the leak rate of each of the simulators was checked over a 2-min period, with the pressure loss being $\lesssim$10 kPa/min. With these initial conditions established, the test transient was initiated by applying dc voltage to the simulators. The applied voltage was maintained constant throughout the powered portion of the transient and resulted in an average linear power generation of 3.0 kW/m in the simulators.

During the powered portion of the transient, superheated steam entered the test array through a single inlet nozzle located at the 107-cm elevation on the north side of the bundle (Fig. 1) and flowed downward through the test assembly at the same mass flux used in the B-3 (4 × 4) reference test — ~288 g/s·m^2. Inlet steam conditions of ~355°C and 290 kPa (absolute) resulted in a Reynolds number of 140. These inlet conditions remained essentially constant until disrupted by helium escaping from the ruptured tubes and by the opening of valves to admit posttest cooling steam. When power to the bundle was terminated, the steam flow was increased to an estimated minimum of 2000 g/s·m^2 to effect rapid cooldown of the bundle.

Termination of the powered portion of the test could be initiated by any of four actions: (1) CCDAS action resulting from a signal that 60 of the 63 pressurized simulators had burst, (2) CCDAS action resulting from a signal that 150 simulator thermocouples had exceeded the high-temperature limit (50°C above the anticipated burst temperature) on each of three successive data scans, (3) a timer that limited the transient to 60 s, and (4) operator override. The choice to program criterion (1) to terminate power to the bundle after 60 tube bursts (with the expectation that all 63 pressurized tubes would burst) was made to minimize the temperature overshoot at the end of the test. Also, criterion (2), the high-temperature limit, was established close to the expected burst temperature for the same reason. The test was terminated by criterion (1), and all 63 pressurized tubes burst.

ORNL–DWG 79–6684 ETD

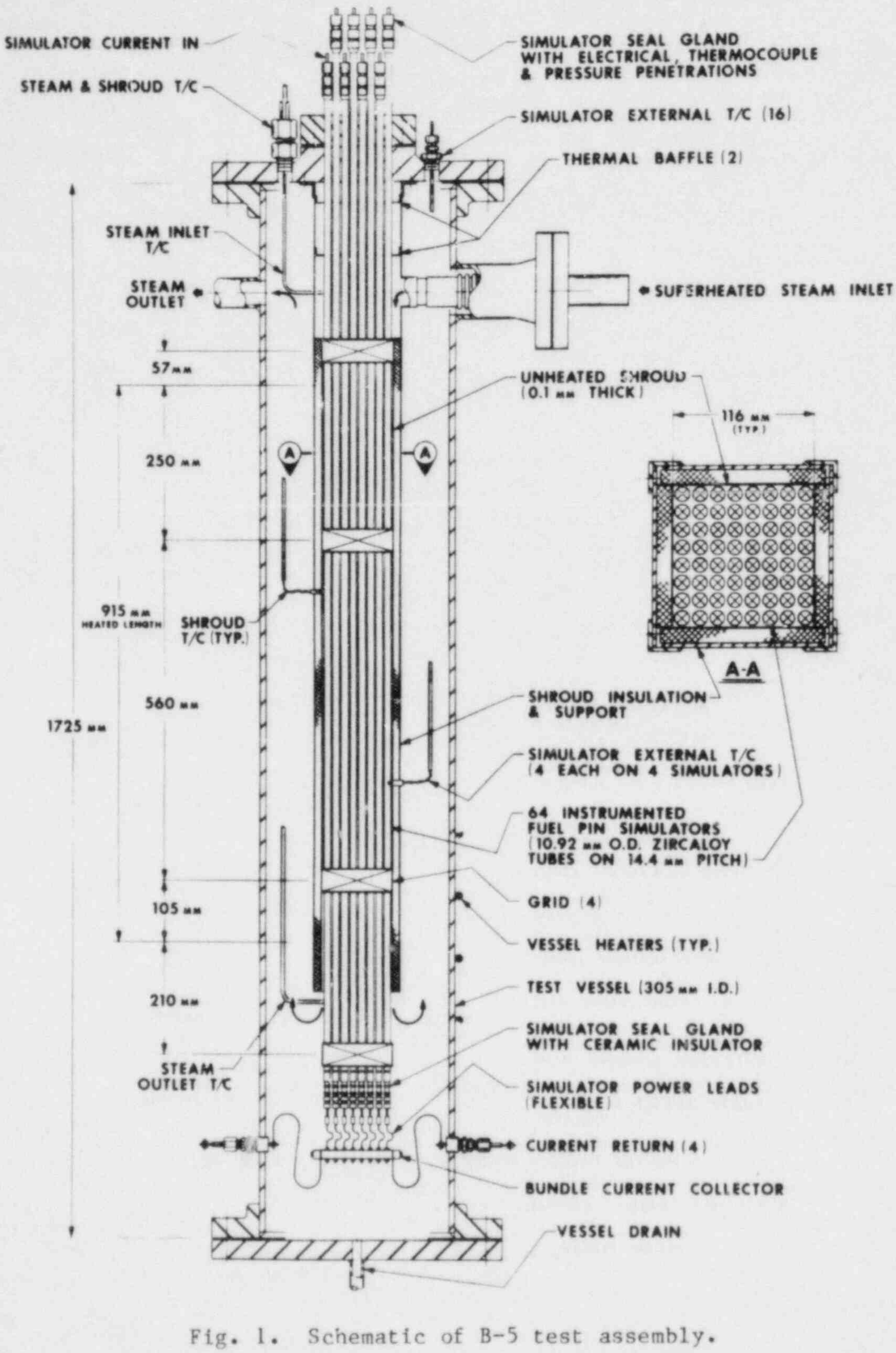

Fig. 1. Schematic of B-5 test assembly.

ORNL-DWG 77-8293

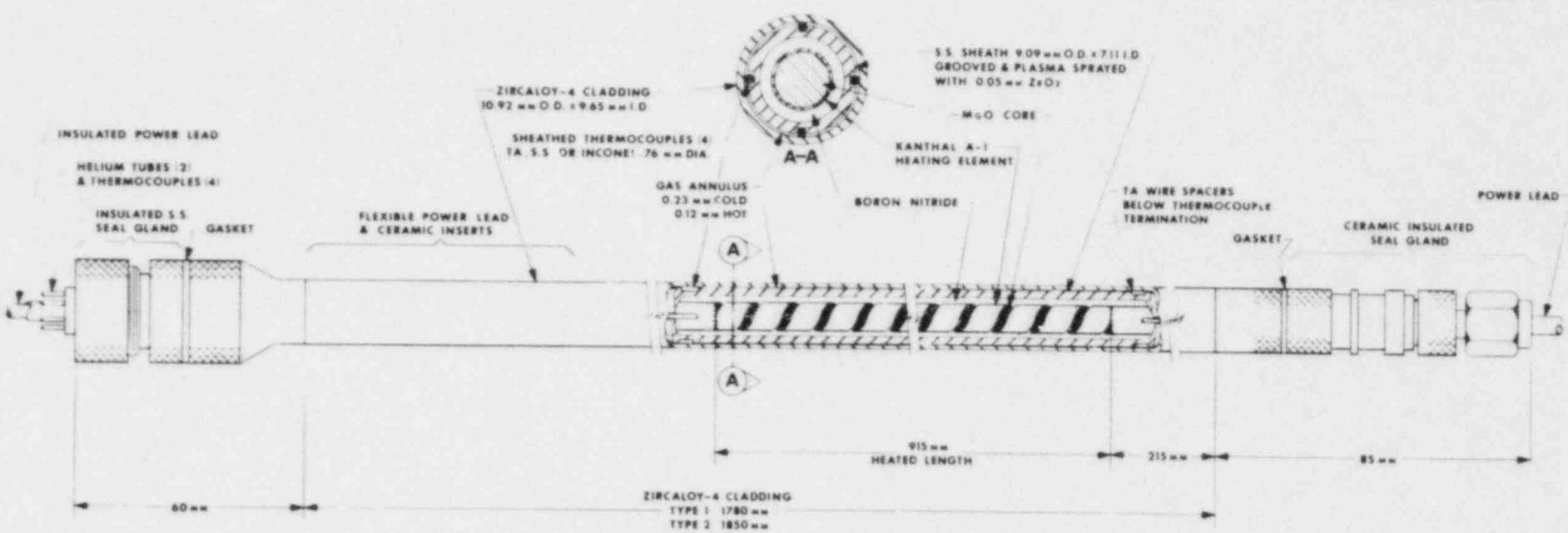

Fig. 2. Typical fuel pin simulator.

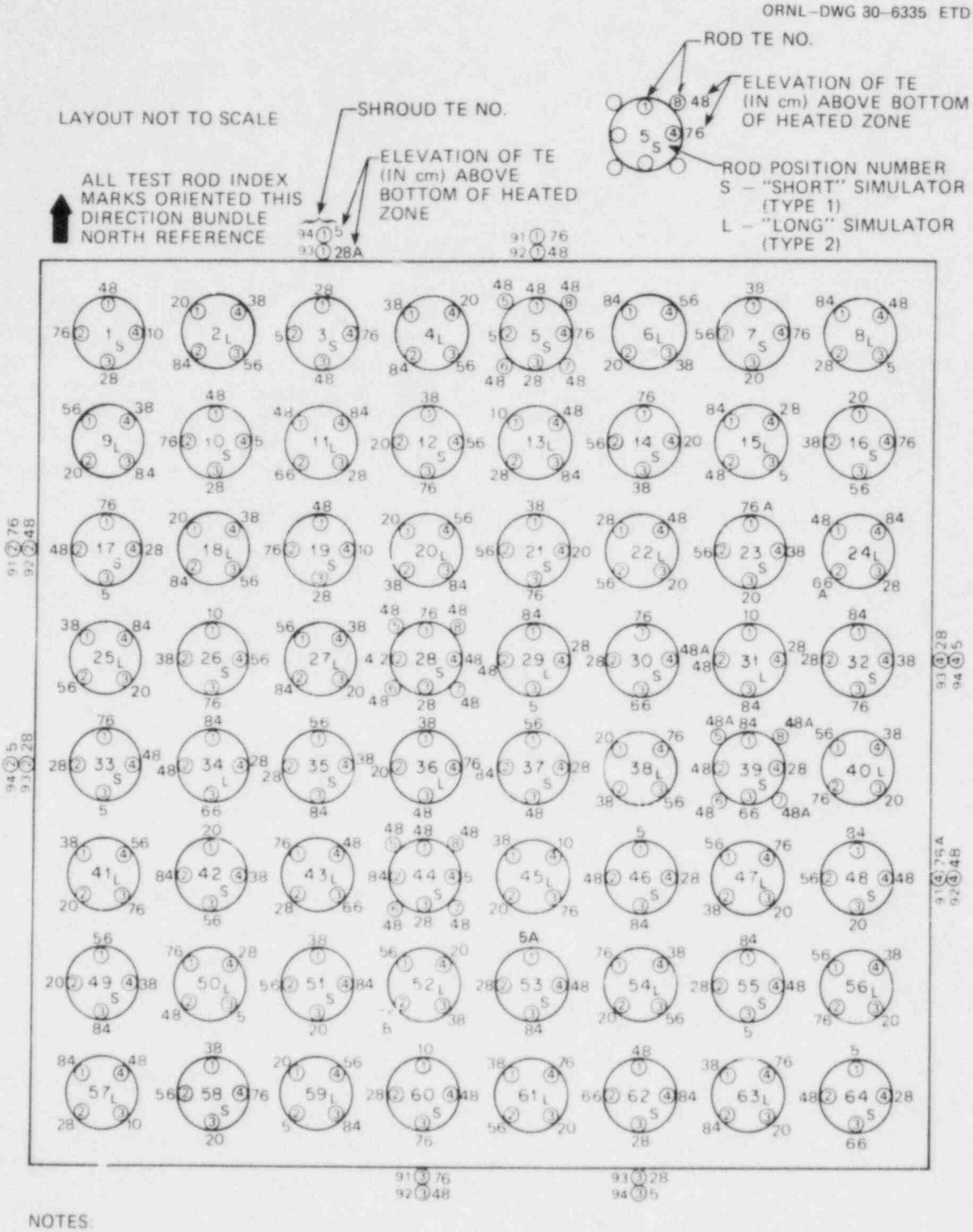

NOTES:

A. BECAME DETACHED DURING ASSEMBLY.
B. JUNCTION BECAME GROUNDED AFTER ASSEMBLY.

Fig. 3. Thermocouple identifications and as-built locations in B-5 test (plan view).

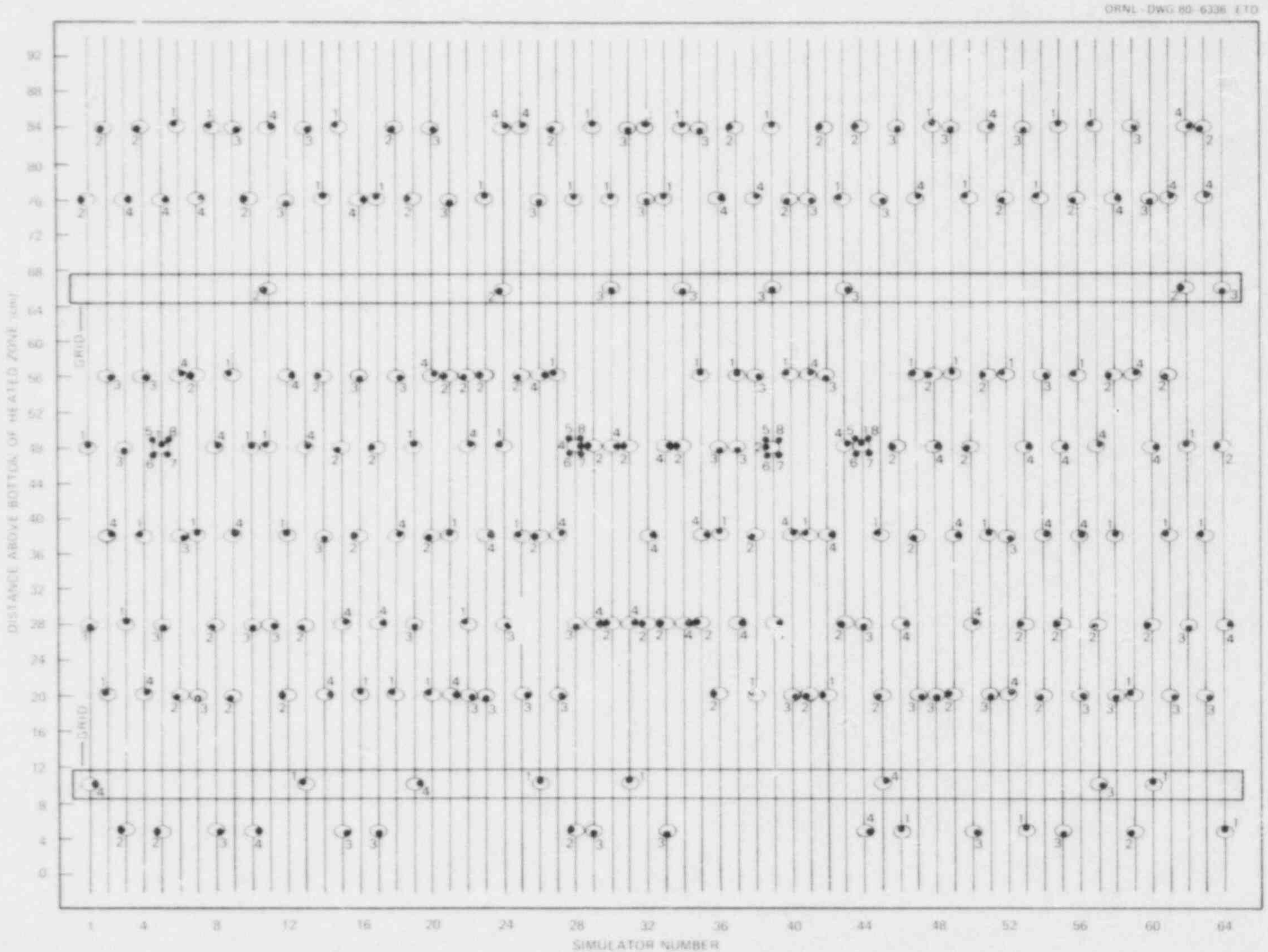

Fig. 4. As-built axial locations of simulator thermocouples in B-5 test (elevation view).

ORNL–DWG 80–6337 ETD

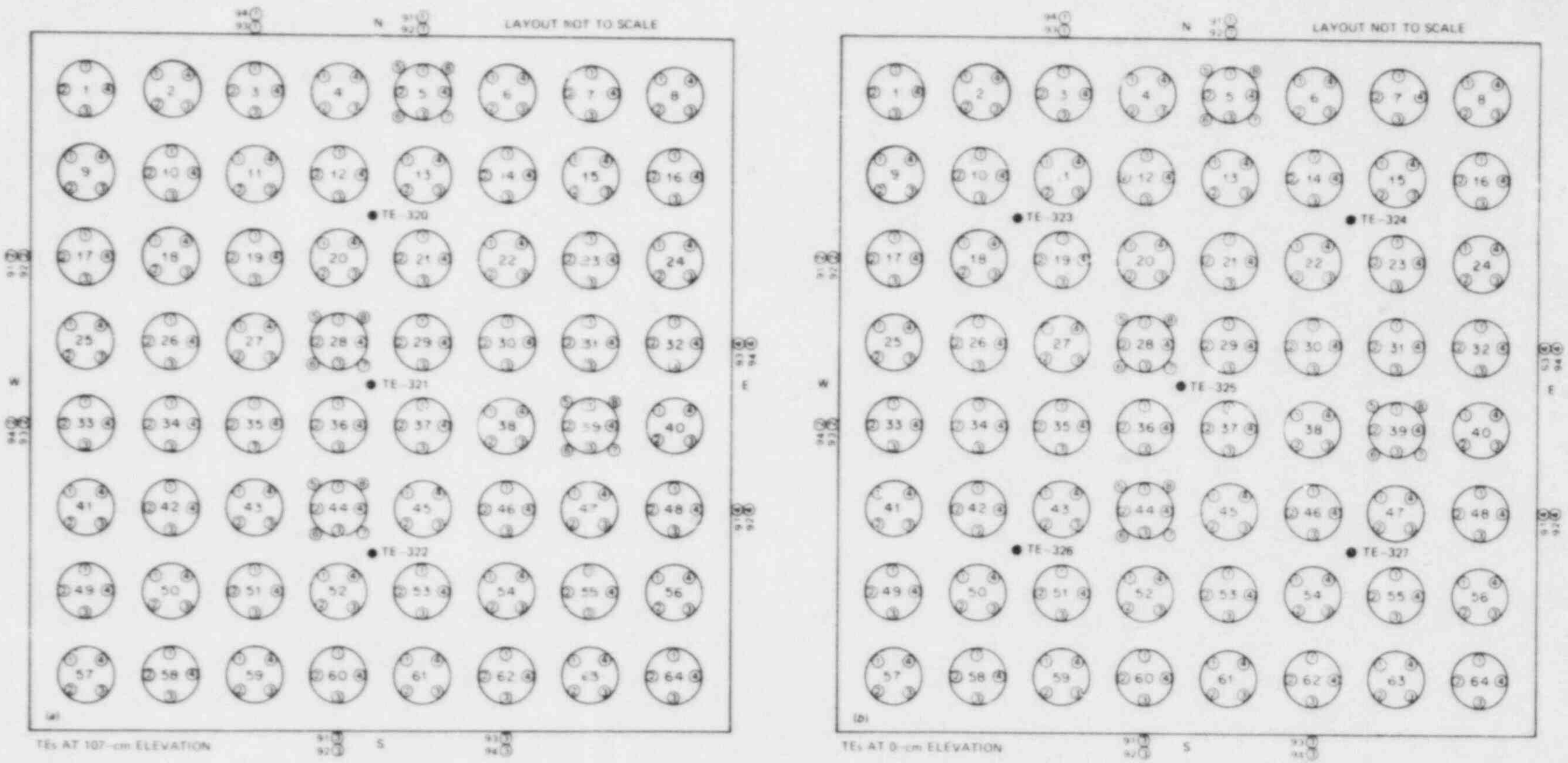

Fig. 5. Locations and identifications of thermocouples for measuring steam (*a*) inlet and (*b*) outlet temperatures in B-5 test.

Table 1. As-built data for B-5 fuel pin simulators

Bundle position No.	Zircaloy tube serial No.	Internal fuel simulator[a] Serial No.	Internal fuel simulator[a] Element resistance (Ω)	Fuel pin simulator gas volume[b] (cm^3)	Bundle position No.	Zircaloy tube serial No.	Internal fuel simulator[a] Serial No.	Internal fuel simulator[a] Element resistance (Ω)	Fuel pin simulator gas volume[b] (cm^3)
1	0738	MNL-012	2.00	48.4	33	0760	MNL-070	1.96	48.2
2	0101	MNL-053	1.97	50.0	34	0130	MNL-065	1.98	52.1
3	0739	MNL-078	2.01	48.3	35	0761	MNL-058	1.98	50.2
4	0102	MNL-052	1.97	49.8	36	0131	MNL-039	1.98	51.6
5	0166	MNL-026	1.96	49.2	37	0789	MNL-017	1.98	49.5
6	0103	MNL-015	1.99	49.4	38	0132	MNL-071	1.97	51.0
7	0741	MNL-024	1.96	50.3	39	0806	MNL-068	1.98	48.4
8	0104	MNL-080	1.98	51.3	40	0155	MNL-031	1.96	49.7
9	0115	MNL-025	1.98	49.1	41	0134	MNL-016	1.98	50.3
10	0742	MNL-014	1.97	50.3	42	0764	MNL-060	1.98	50.2
11	0116	MNL-020	1.97	51.3	43	0135	MNL-036	1.96	51.3
12	0791	MNL-029	1.95	49.7	44	0773	MNL-077	1.97	51.1
13	0117	MNL-073	2.00	51.8	45	0136	MNL-022	1.97	50.6
14	0747	MNL-050	1.97	50.6	46	0774	MNL-008	1.97	50.1
15	0118	MNL-083	2.03	51.0	47	0137	MNL-064	1.95	49.3
16	0748	MNL-004	1.96	49.9	48	0803	MNL-081	2.00	48.4
[illegible]	0749	MNL-088	2.01	47.9	49	0776	MNL-063	1.98	48.2
18	0157	MNL-037	1.95	50.7	50	0141	MNL-055	2.00	51.0
19	0750	MNL-092	2.00	50.3	51	0777	MNL-019	2.00	49.9
20	0153	MNL-027	1.98	49.8	52	0142	MNL-048	1.96	51.5
21	0751	MNL-034	1.95	50.1	53	0778	MNL-021	2.01	50.1
22	0124	MNL-041	1.99	50.9	54	0158	MNL-038	1.98	49.6
23	0752	MNL-018	1.97	49.5	55	0779	MNL-084	2.02	50.1
24	0125	MNL-079	2.00	50.1	56	0156	MNL-054	1.96	49.8
25	0126	MNL-062	1.97	50.7	57	0154	MNL-013	1.97	49.7
26	0753	MNL-086	2.01	50.2	58	0792	MNL-049	1.96	50.6
27	0127	MNL-082	1.96	52.0	59	0146	MNL-093	2.02	51.6
28	0754	MNL-061	1.97	50.6	60	0793	MNL-007	1.97	48.7
29	0128	MNL-047	1.96	49.4	61	0147	MNL-030	1.96	49.9
30	0755	MNL-028	1.98	49.0	62	0787	MNL-076	1.99	48.9
31	0129	MNL-057	1.95	51.3	63	0148	MNL-051	2.00	50.4
32	0756	MNL-040	1.99	49.7	64	0790	MNL-044	1.95	50.1

[a] All 64 fuel simulators were fabricated in the ORNL Fuel Pin Simulator Development Laboratory.

[b] Fuel pin simulator volume was measured at room temperature before installation into bundle. The volume measured included a pressure transducer and connecting tube identical to the facility hookup for each simulator.

3. SUMMARY OF TEST RESULTS

Initial conditions of the test, obtained by averaging each data channel over the time interval (~10 s) from the start of scanning to the power-on time, are summarized in Table 2. The simulators were pressurized simultaneously from a common manifold and then individually isolated from the manifold for the test. After isolation the average simulator pressure was 11,622 kPa differential above the external steam pressure. The initial cladding average temperature was 335°C; however, the temperature distribution in the bundle was skewed a few degrees both radially and axially as will be discussed later. The average temperature indicated by the ten operative shroud thermocouples was 339°C. Superheated steam entered the bundle at an indicated average temperature of 355°C and a pressure of 290 kPa (absolute) and flowed downward through the bundle at a constant mass flow rate of 288 $g/s \cdot m^2$; the indicated average steam outlet temperature prior to initiation of the transient was 339°C. Based on the inlet steam conditions and flow rate, the Reynolds number at the top of the heated zone (91.5-cm elevation) was 140 throughout the powered portion of the transient.

Figure 6 shows the power parameters and the bundle average temperature represented by TAV-10 (i.e., the average of ten thermocouples attached to the inside surface of the cladding at the 38-cm elevation on interior simulators) during the transient. Constant voltage was applied to the bundle for 48.45 s; power generation (3.0 kW/m) and the temperature rate of increase were nearly constant during this time as indicated in the figure. From 5 to 43 s after power-on (i.e. ~1 s before the first tube burst), the bundle average heating rate was 9.8°C/s. The average temperature, as indicated by TAV-10, reached a maximum of ~804°C about 8 s after power was terminated.

The time at which maximum pressure occurred in each simulator is a measure of the onset of significant deformation (i.e., the time when the rate of pressure increase caused by thermodynamic heating equals the rate of pressure decrease caused by increasing volume) and is given in Table 3 with the corresponding cladding temperature and pressure conditions. The bundle average maximum differential pressure was 12,157 kPa and occurred at an average time of 31.1 s after power-on. The observation that the maximum pressures and the times at which they occurred were approximately the same in all the simulators is indicative of uniform heating and the absence of seal leaks.

Times (after power-on), temperatures, and differential pressures measured at the burst time of each tube are given in Table 4. The first tube (No. 21) burst 44.00 s after power-on, and the last one (No. 1) burst 5.60 s later (i.e., 1.15 s after termination of the applied voltage). Figure 7 shows the tube burst times plotted in three groups to indicate radial positions in the bundle. A histogram (in 0.5-s intervals) of the burst times is given in Fig. 8. Because heat losses from the outer ring of simulators were greater (resulting in slightly lower heating rates for these simulators and slightly longer times for them to reach the burst temperature), the exterior simulators generally burst later than the interior simulators. The corner simulators, with the greatest heat losses, were among the last tubes to burst. The average burst time for the entire bundle was 46.29 s.

Our practice has been to select the burst temperature as the maximum measured temperature at the time of failure, without regard to the location of the measurement with respect to the burst. This definition rests on the premise that the temperature at the point of failure is at least as high as the maximum measured temperature but does not preclude the possibility of its being higher. As will be discussed in Sect. 5, this definition presented difficulties and inconsistent results in relation to the observed deformation patterns caused by rod-to-rod interactions. The quick-look burst temperature data[2] were based on the above definition but were subsequently revised[3,5] to take into account new information as it became available from posttest examination. All the information was reevaluated, and a measured temperature was selected[5] as the burst temperature. This temperature was not necessarily the maximum measured at the time of failure but was consistent with it, the measurement locations, and the deformation profiles. These data, given in the summary of test results (Table 5), differ only slightly from the maximum measured values (Table 4) at the time of failure and represent the best-estimate burst temperatures in the absence of more definitive analysis of the data. Based on these data, the bundle average burst temperature was 768°C.

The bundle average burst pressure (Table 5) was 8806 kPa; however, a significant variation was observed in the burst pressures for a rather narrow burst temperature range. The data are plotted in Fig. 9, using greatly expanded scales and different symbols to differentiate the data for the three radial zones of the bundle. Burst pressures for the interior simulators were generally much lower than those for simulators nearer the outer boundary. Although the burst temperatures were less, as indicated in the figure, the data for the outer ring of simulators were in reasonable agreement with the prediction from a correlation[5] based on our single-rod *heated* shroud tests. This correlation predicts higher burst temperatures than one we published[21] earlier (and used by Powers and Meyer[22] in their LOCA analysis models) for our single-rod *unheated* shroud tests. The lack of better agreement is understandable; we used fewer thermocouples in bundle simulators than in single-rod test simulators (i.e., 4 vs 12) to measure temperatures, and thus a greater statistical probability existed for underestimating burst temperatures in bundle tests. The interior simulators did not show the expected trend of increasing burst temperature with decreasing burst pressure for reasons that will be discussed later.

The initial-to-burst pressure ratio is a qualitative measure of the volumetric expansion and has been shown[3] to be a useful parameter for modeling average deformation in the absence of measured geometrical data. This parameter is given in Table 5 and is plotted in Fig. 10 for the three radial zones of the test array. As evident from the figure, greater volumetric expansion is indicated for the interior zones.

The test array was cast in an epoxy matrix and sectioned at a number of axial nodes 10 to 20 mm apart. Enlarged photographs of the sections were digitized and processed (by the procedures described in Sect. 4.3.4) to obtain geometric parameters describing the deformation of each tube at each axial node. The strain profiles were used to calculate the volumetric expansion of the cladding heated length (based on the outside perimeter of the tubes) by assuming circular cross sections at each node. This parameter is tabulated in Table 5 and is plotted in Fig. 11 in a format similar to the previous figure. The average and the sample standard deviation limits of the data are also indicated in the figure; the bundle average volumetric increase was 52.4%. The average strain in each tube was also calculated, by assuming that the volumetric expansion was uniformly distributed over the heated length, and is given in Table 5. The data show clearly that the interior simulators deformed more than the exterior ones.

The volumetric increase of the heated length obtained from the deformation profiles was assumed equal to the increase in total gas volume and used to calculate the fuel pin simulator volumetric increase (Table 5) appropriate for analysis with the measured temperature and pressure data. However, as discussed in Sect. 2.1, the major fraction of the gas volume was distributed in regions in which the temperature during the test ranged from room temperature to the initial temperature, with only a small fraction of the gas in the heated zone.

Tube burst strains are plotted in Fig. 12 for each of the three radial zones; the average and the sample standard deviation limits are also indicated for each zone. The bundle average burst strain was 61%. As evident, the average burst strain was approximately the same in each of the three zones, indicating that burst strain was not a strong function of position. This was an unexpected observation because azimuthal temperature gradients were presumably greater in the outer ring of simulators (as a result of heat losses to the relatively cold shroud surrounding the array) than in the interior simulators. An explanation for this observation will be given in Sect. 5.

The measured tube areas were summed at each axial node and combined to obtain the flow area restriction data shown in Fig. 13 as a function of array size. The maximum loss in flow area occurred at the 26.4-cm elevation and amounted to 69.2% for the entire 8 × 8 array, 82.5% for the inner 6 × 6 array, and 90.7% for the central 4 × 4 array. These data confirm the previous observation that the interior simulators deformed more than the exterior ones.

Prior to destructive examination, flow tests were conducted on the deformed B-5 array and on an 8 × 8 reference array (identified as B-5R) that was geometrically identical to the undeformed B-5 array. The two series of tests were performed in the same flow shroud with 49°C water at five flow rates to characterize the flow resistance over a Reynolds number range of $1.7 \times 10^4 \leqslant Re \leqslant 1.7 \times 10^5$. Because deformation of the outer ring of simulators in the B-5 array was constrained by a close-fitting unheated shroud and there were no tube burst flare-outs to accommodate, it was possible to design a close-fitting flow shroud (square cross section with 12.23-cm dimensions on each side) to minimize bypass flow. With the undeformed reference bundle in the shroud, the equivalent hydraulic diameter of the combined wall and corner subchannels was the same as that of an interior subchannel. Twelve pressure taps, arranged as illustrated in Fig. 14, were located at each of 40 axial positions to define the axial and local pressure loss distributions.

The flow tests provided experimental pressure loss data that can be correlated with deformation resistance characteristics and used for validation of deformed bundle pressure loss calculational models. Because the flow tests have been described in detail in a test data report[23] (the data also reside in the NRC Thermal Hydraulic Data Bank maintained at the

Idaho National Engineering Laboratory), only a summary of the results is included here. Figure 15 compares the bundle-averaged pressure loss profiles of the B-5 and the B-5R reference bundle at a Reynolds number of ~1×10^5. (Bundle-averaged data is defined as the data obtained by averaging all 12 pressure tap measurements at 1 axial position, as opposed to side-averaged data or individual pressure tap data.) The bundle-averaged overall pressure losses (axial Δp for the heated zone) for the B-5 and B-5R reference bundles are plotted as a function of Reynolds number (in the undeformed region) in Fig. 16. At a Reynolds number of ~1×10^5, the overall axial pressure loss difference between the two bundles was ~98 kPa. Thus, bundle deformation caused permanent pressure losses equal to ~360% (98/27 × 100) of the total loss of the undeformed reference bundle in the same flow shroud test configuration.

Figure 17 compares the B-5 pressure loss profile with the flow area restriction data (from Fig. 13) for the entire 8 × 8 array. Excellent correlation between the salient features of the two curves is evident. The figure also shows that a parameter (the number of burst openings per unit length of bundle) related qualitatively to the axial distribution of the deformation is also a reasonable qualitative indicator of the flow restriction. Note that the data presented in the figures (and in the data report[23]) are specific for the B-5 bundle in a particular flow shroud. As discussed above, the interior simulators deformed more than the exterior ones and, hence, the flow resistance would be greater in the bundle interior. This is not apparent from the figure, because it reflects the resistance of the entire 8 × 8 array. Although not performed, detailed subchannel analysis of the combined deformation and flow data sets, as was done by Mincey[24] for the MRBT B-1 and B-2 tests, would be required to show this effect.

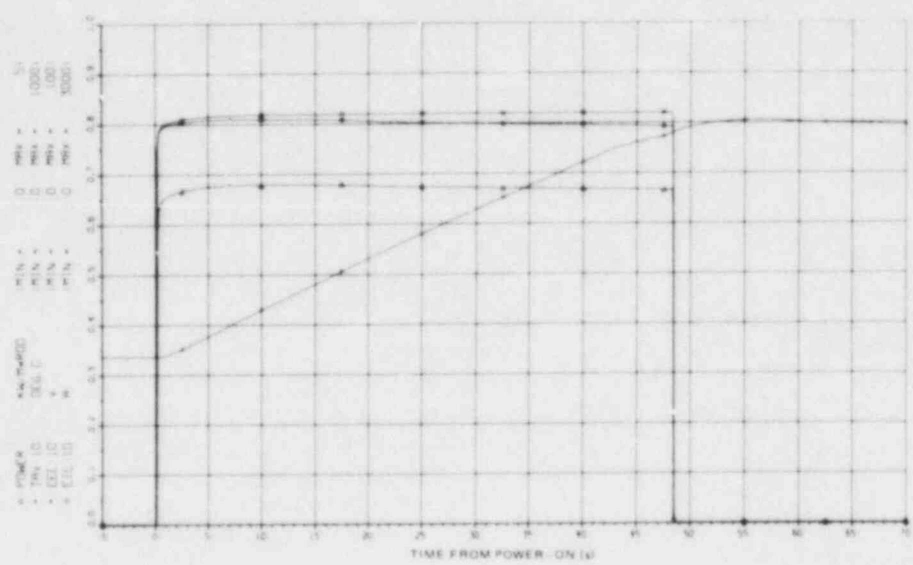

Fig. 6. B-5 power parameters and bundle average temperature.

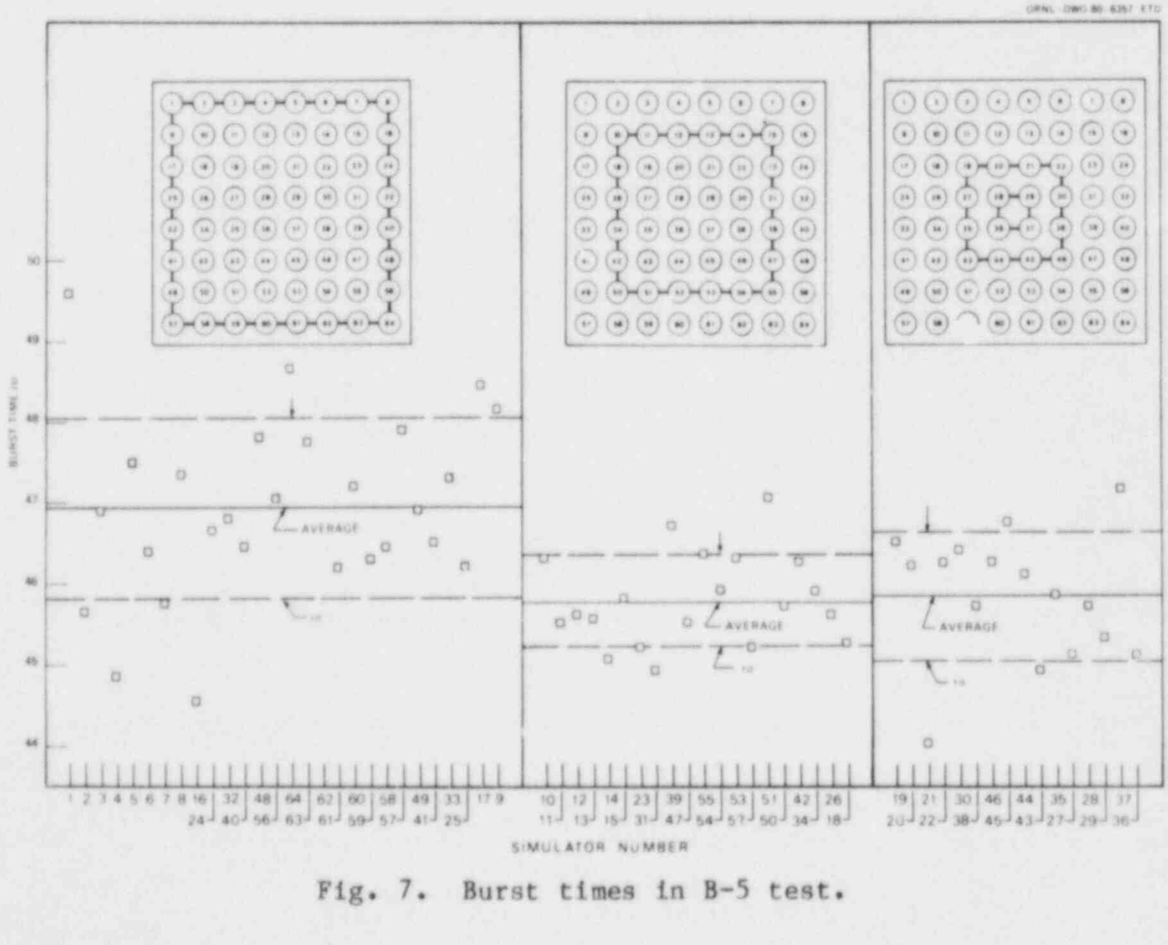

Fig. 7. Burst times in B-5 test.

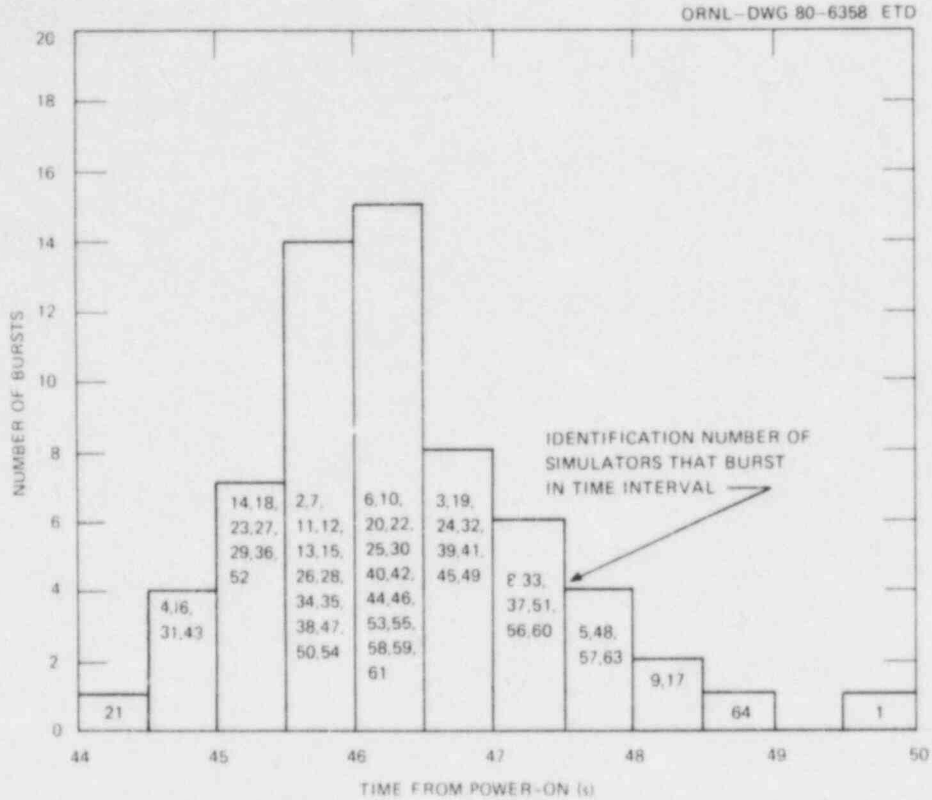

Fig. 8. Burst frequency in B-5 test.

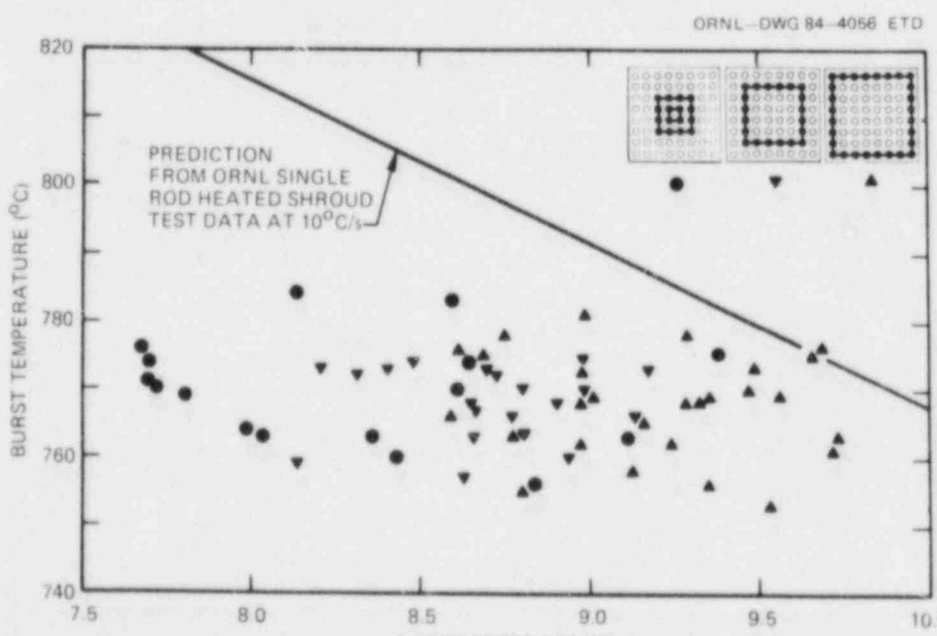

Fig. 9. Comparison of B-5 burst data with prediction from single-rod heated shroud test data.

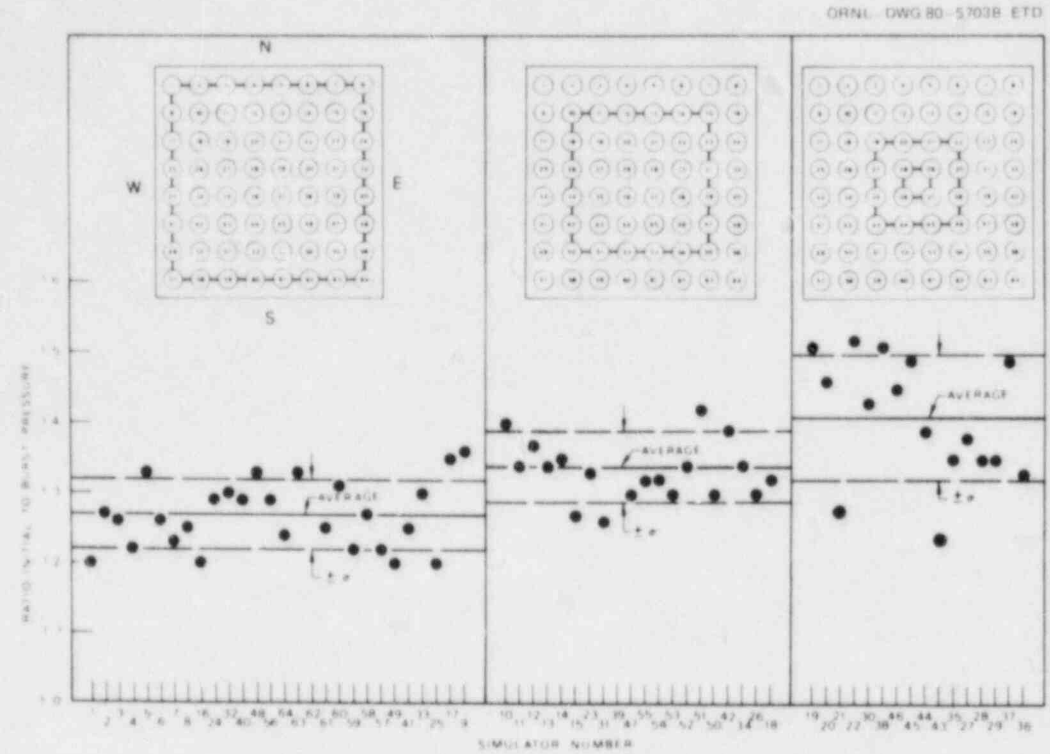

Fig. 10. Initial-to-burst pressure ratios in B-5 test.

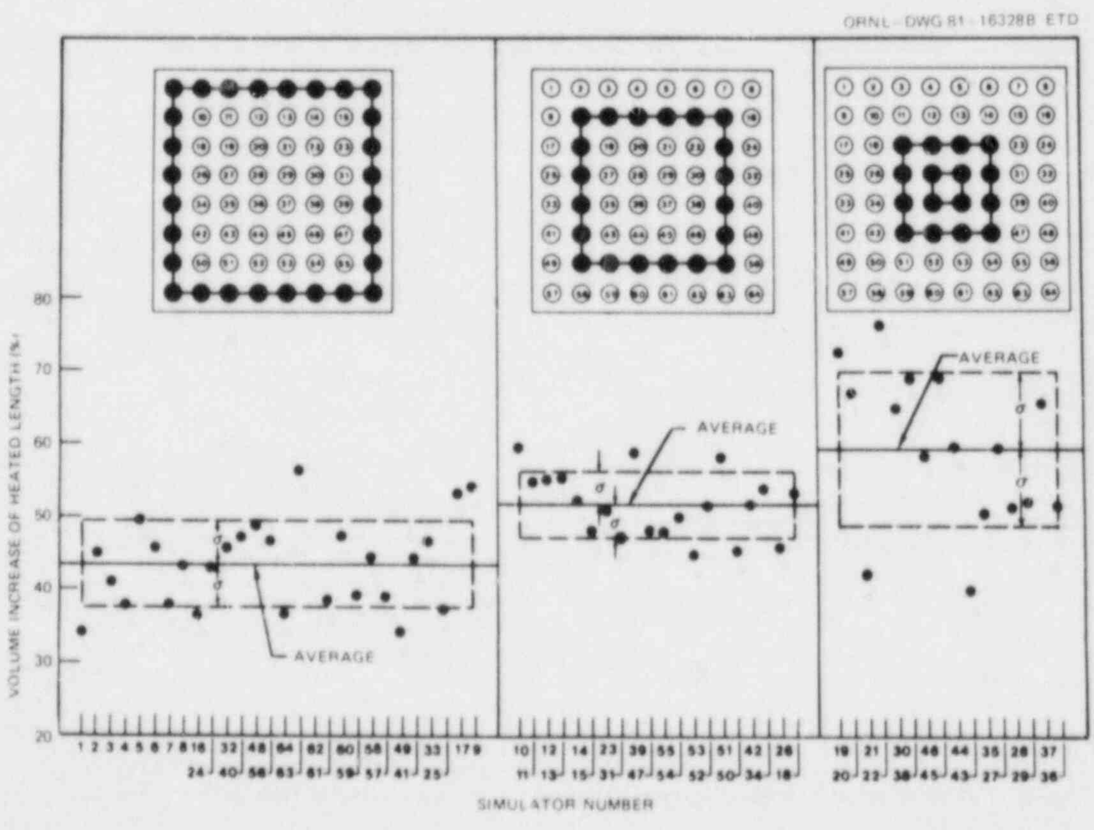

Fig. 11. Volume increase of B-5 tubes.

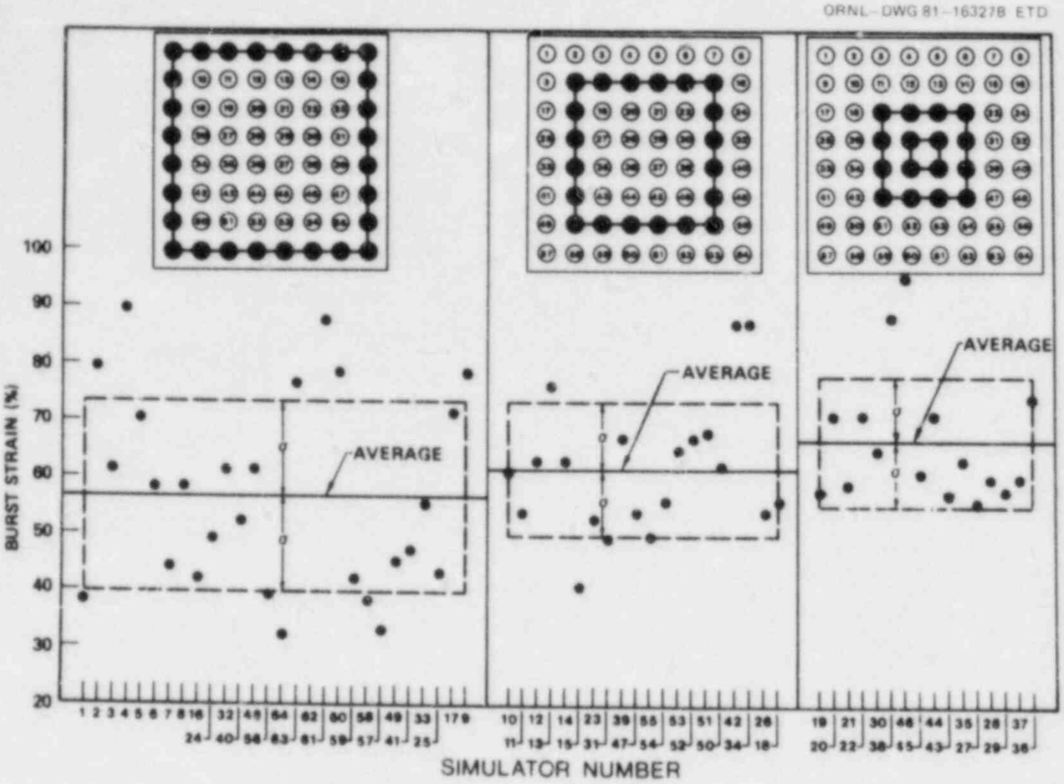

Fig. 12. Burst strain of B-5 tubes.

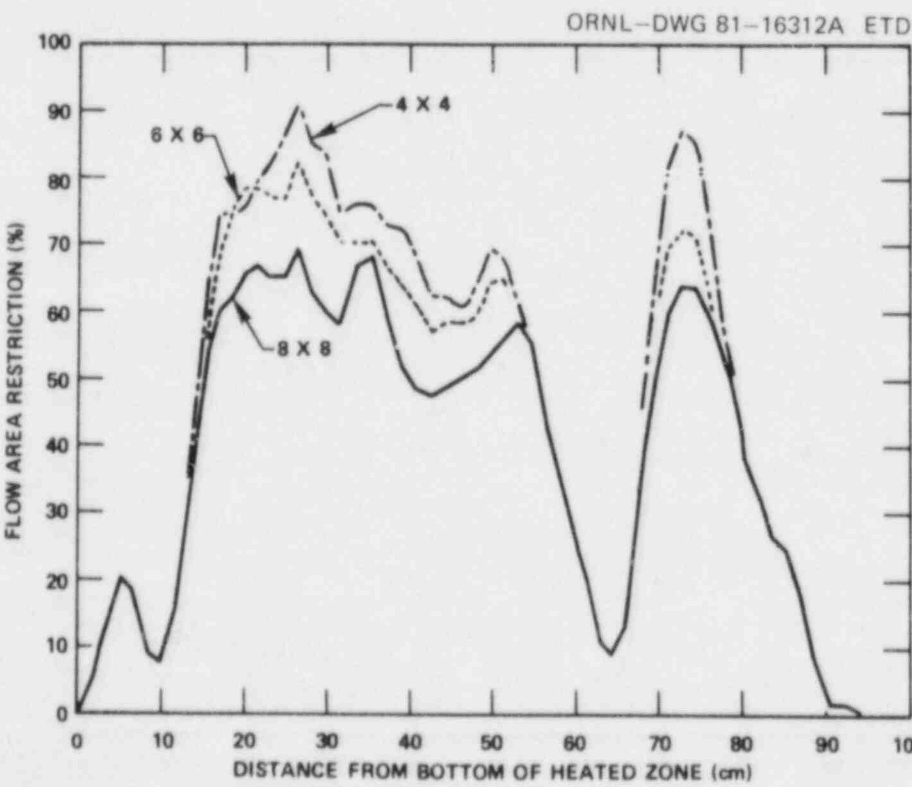

Fig. 13. Flow area restriction of B-5 central 4 × 4 array, inner 6 × 6 array, and entire 8 × 8 array.

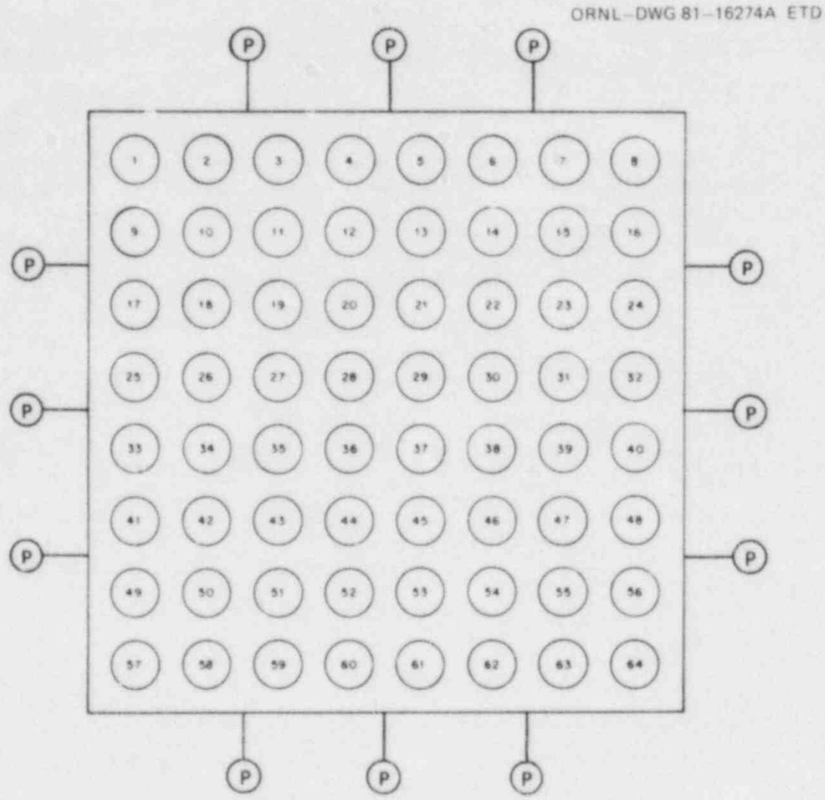

Fig. 14. Pressure tap arrangement used for B-5 flow tests.

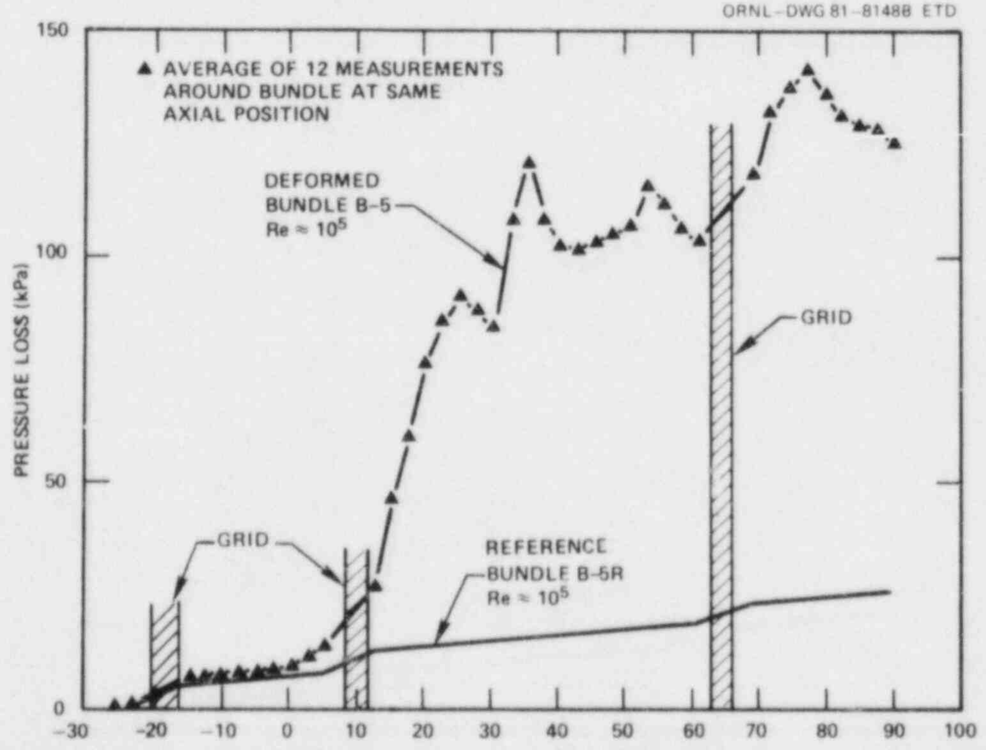

Fig. 15. Comparison of B-5 and B-5R reference bundle pressure loss profiles.

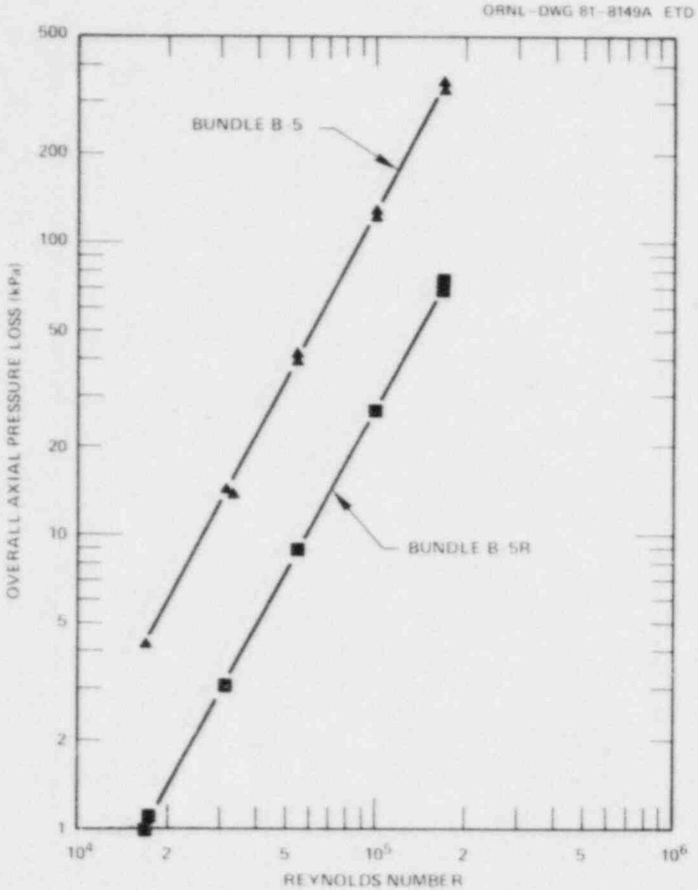

Fig. 16. Bundle-averaged overall axial pressure losses of B-5 and B-5R reference bundles.

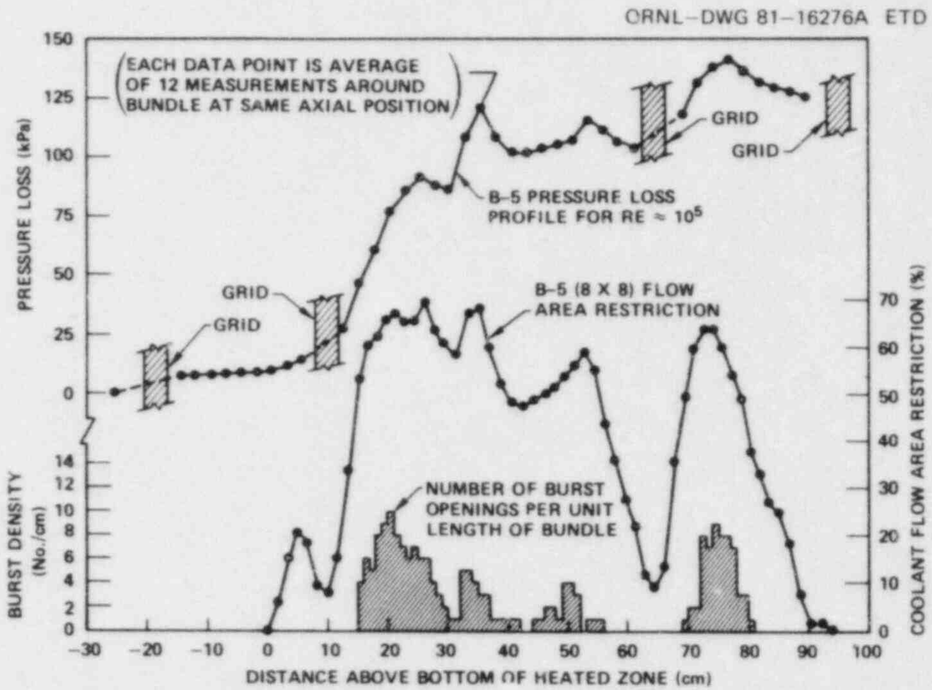

Fig. 17. Comparison of B-5 pressure loss profile with flow area restriction.

Table 2. Summary of B-5 initial conditions

ROD NO.	DIFFERENTIAL PRESSURE (KPA)	TEMPERATURES (DEG C) TE-1	TE-2	TE-3	TE-4	AVG	ROD NO.	DIFFERENTIAL PRESSURE (KPA)	TEMPERATURES (DEG C) TE-1	TE-2	TE-3	TE-4	AVG
1	11650	340	345	336	337	340	33	11649	333	332	333	333	333
2	11646	337	348	343	338	342	34	11614	330	334	333	333	332
3	11619	338	337	341	347	341	35	11624	334	333	334	333	334
4	11643	340	349	344	337	343	36	11739	333	332	334	338	334
5	11662	342	337	337	349	341	37	11633	335	340	334	334	336
6	11634	349	338	340	344	343	38	11638	333	334	336	336	335
7	11644	339	344	337	347	342	39	11633	331	334	334	333	333
8	11648	347	337	338	341	341	40	11617	336	334	333	334	334
9	11638	342	337	341	338	339	41	11687	333	333	331	334	333
10	11637	340	342	337	336	339	42	11650	332	327	332	333	331
11	11593	341	344	338	346	342	43	11632	332	332	332	333	332
12	11606	340	338	347	343	342	44	11644	333	336	333	332	334
13	11641	338	339	350	343	342	45	11632	333	332	335	333	333
14	11651	346	344	341	339	342	46	11623	235[a]	334	333	332	333
15	11634	345	342	338	338	341	47	11627	333	333	332	330	332
16	11626	337	338	343	345	341	48	11631	329	333	331	333	332
17	11633	340	339	337	337	338	49	11620	332	331	328	331	331
18	11646	334	335	337	335	335	50	11586	325	329	330	329	328
19	11629	337	340	335	334	336	51	11557	329	329	328	325	328
20	11656	335	336	344	339	339	52	11584	330	330	331	329	330
21	11637	337	340	343	335	339	53	11573	330	329	330	330	330
22	11640	336	340	335	339	337	54	11597	330	331	332	331	331
23	11621	340	339	335	337	338	55	11584	327	331	331	332	330
24	11608	337	340	335	339	338	56	11573	333	331	331	331	331
25	11630	334	335	334	333	334	57	11579	329	331	332	331	331
26	11644	334	334	334	335	334	58	11590	331	331	331	331	331
27	11635	336	338	334	335	336	59	11560	332	332	330	332	331
28	11585	341	333	335	336	336	60	11565	331	332	334	331	332
29	11648	343	337	333	335	337	61	11560	331	333	331	332	332
30	11622	339	335	338	337	337	62	-20[b]	332	332	331	331	331
31	11606	333	336	335	335	335	63	11583	331	330	331	332	331
32	11628	335	334	337	334	335	64	11578	332	336	333	331	333

[a] TE 46-1 was inoperative and is excluded from average.

[b] Simulator was heated but unpressurized.

Table 3. Summary of B-5 conditions at times of maximum pressures

ROD NO.	CONDITIONS AT TIME OF MAXIMUM PRESSURES: DIFFERENTIAL PRESSURE (KPA)	TEMPERATURES (DEG C)					TIME[a] (SEC)
		TE-1	TE-2	TE-3	TE-4	AVG	
1	12197	630	644	639	616	632	32.30
2	12206	632	639	635	630	634	31.10
3	12191	625	618	622	624	622	30.10
4	12166	617	623	623	608	618	29.20
5	12185	603	601	605	614	[illegible]	28.40
6	12349	657	648	656	654	[illegible]	33.30
7	12163	641	644	641	65[illegible]	645	31.75
8	12202	587	583	579	58[illegible]	583	25.55
9	12114	574	565	574	573	571	24.60
10	12174	653	653	653	646	651	32.60
11	12110	633	617	632	636	630	30.35
12	12165	538	534	541	540	538	19.95
13	12162	625	637	644	643	6[illegible]	31.50
14	12169	646	640	642	639	642	30.70
15	12133	652	647	640	[illegible]	647	32.60
16	12181	637	641	644	644	641	31.05
17	12137	644	635	634	[illegible]	637	31.80
18	12185	645	646	649	[illegible]49	647	31.80
19	12158	626	[illegible]	631	[illegible]	625	30.35
20	12127	[illegible]	637	64[illegible]	64[illegible]	640	31.60
21	12169	623	622	628	[illegible]	623	29.30
22	12168	627	630	624	628	627	29.85
23	121[illegible]7	629	627	625	628	[illegible]	29.90
24	12143	641	625	641	641	637	32.25
25	12160	644	645	640	635	641	32.95
26	12183	629	644	644	642	640	32.00
27	12172	652	645	640	647	646	31.65
28	12127	647	[illegible]	641	632	[illegible]	31.35
29	12168	645	644	635	642	641	31.50
30	12117	630	625	612	627	623	30.10
31	[illegible]	608	622	619	619	617	29.30
32	[illegible]	634	638	629	636	634	31.80
33	12162	636	637	636	640	637	32.10
34	12135	633	641	612	644	633	31.65
35	12163	647	647	641	646	645	32.30
36	12267	630	627	625	627	627	30.35
37	12119	639	639	640	640	640	31.80
38	12166	623	621	621	626	623	29.65
39	12191	637	639	627	640	636	32.00
40	12155	649	649	647	647	648	32.55
41	12207	636	635	639	646	639	32.45
42	12183	641	632	642	641	639	31.80
43	12169	643	643	629	642	639	31.95
44	12166	634	643	647	636	640	31.65
45	12135	625	627	627	612	623	30.20
46	12181	233[b]	634	629	636	633	31.45
47	12140	629	627	627	628	628	30.35
48	12179	630	636	632	632	632	31.80
49	12168	641	638	635	647	640	33.15
50	12119	613	622	618	620	618	30.50
51	12089	633	63[illegible]	636	629	632	31.85
52	12125	640	624	639	636	637	31.60
53	12093	63[illegible]	636	634	639	635	32.30
54	12148	[illegible]	638	637	640	639	32.05
55	12135	634	637	632	637	635	32.60
56	12108	64[illegible]	638	630	630	635	31.90
57	12119	632	634	614	630	[illegible]	31.95
58	12152	645	642	641	642	643	32.65
59	12102	632	622	632	637	631	31.80
60	12164	[illegible]21	638	634	629	630	31.80
61	12111	645	640	645	641	643	32.70
62	[illegible]18[c]	772[c]	739[c]	[illegible]60[c]	749[c]	755[c]	53.85[c]
63	12138	645	640	639	647	643	32.75
64	12121	634	634	598	642	627	32.60

[a] Time after power-on.

[b] TE 46-1 was inoperative and is excluded from average.

[c] Simulator was heated but unpressurized; data correspond to conditions after all tubes had burst.

Table 4. Summary of B-5 conditions measured at times of bursts

ROD NO.	DIFFERENTIAL PRESSURE (KPA)	TE-1	TE-2	TE-3	TE-4	AVG	BURST TIME[a] (SEC)	ROD NO.	DIFFERENTIAL PRESSURE (KPA)	TE-1	TE-2	TE-3	TE-4	AVG	BURST TIME[a] (SEC)
	APPROXIMATE BURST CONDITIONS	TEMPERATURES (DEG C)							APPROXIMATE BURST CONDITIONS	TEMPERATURES (DEG C)					
1	9687	708	670	776	747	725	49.60	33	8972	772	674	719	761	732	47.30
2	9159	756	742	770	719	747	45.65	34	8695	752	752	739	773	754	45.90
3	9241	728	740	755	749	743	46.90	35	8644	768	774	746	779	767	45.85
4	9561	769	751	762	753	759	44.85	36	8834	754	768	755	754	758	45.10
5	8750	732	730	758	778	750	47.50	37	7697	774	760	770	765	767	47.20
6	9290	768	762	778	725	758	46.40	38	7715	767	770	769	777	771	45.70
7	9485	746	751	756	766	755	45.75	39	8206	765	759	750	773	762	46.70
8	9327	739	768	730	693	733	47.35	40	8977	782	771	750	767	768	46.45
9	8588	733	666	787	709	724	48.15	41	9360	748	720	748	769	746	46.50
10	8310	756	759	772	738	756	46.30	42	8405	773	759	769	761	766	46.25
11	8650	762	747	764	768	760	45.50	43	9386	768	775	745	753	761	44.90
12	8478	772	780	77[illegible]	765	773	45.60	44	8353	751	708	763	738	740	46.10
13	8659	760	758	767	757	760	45.55	45	7800	769	765	769	765	767	46.75
14	8657	763	777	773	762	769	45.05	46	8036	261[b]	762	761	762	762	46.25
15	9129	766	761	744	765	759	45.80	47	8975	777	734	762	773	762	45.50
16	9657	763	768	775	765	768	44.55	48	8776	748	762	763	684	739	47.80
17	8615	776	748	726	786	759	48.45	49	9722	742	744	730	761	744	46.90
18	8802	765	774	770	768	769	45.25	50	8900	739	768	740	754	750	45.70
19	7693	763	763	774	742	760	46.50	51	8134	771	760	756	756	761	47.05
20	7984	761	764	759	760	761	46.20	52	8629	754	741	756	765	754	45.20
21	9110	745	752	763	766	757	44.00	53	8936	732	769	741	760	750	46.30
22	7670	774	780	764	762	770	46.25	54	8770	771	751	765	761	762	45.90
23	8724	772	771	756	767	766	45.20	55	8784	745	763	741	752	750	46.35
24	9007	771	755	759	751	759	46.65	56	8983	781	779	745	745	763	47.05
25	9732	763	754	756	737	752	46.20	57	9528	749	720	752	745	742	47.90
26	8978	758	770	751	758	759	45.60	58	9123	757	745	658	748	727	46.45
27	8432	768	751	756	756	758	45.10	59	9471	755	731	745	770	750	46.30
28	8595	783	754	777	752	767	45.70	60	8801	748	755	709	743	739	47.20
29	8606	770	764	743	768	761	45.30	61	9287	768	742	752	746	752	46.20
30	8133	784	769	753	765	768	46.40	62	[c]		* ROD DID NOT BURST *				
31	9174	751	773	766	769	765	44.90	63	8684	775	739	678	753	736	47.75
32	8972	752	768	739	753	753	46.80	64	9348	743	728	703	703	719	48.65

[a] Time from power-on.

[b] TE 46-1 was inoperative and is excluded from average.

[c] Simulator heated but unpressurized.

Table 5. Summary of B-5 test results

Rod	Burst conditions			Tube heated length[a]		Fuel pin simulator[b]	
	Pressure (kPa)	Temperature (°C)	Strain[a] (%)	Volume increase[c] (%)	Average strain[d] (%)	Volume increase[e] (ratio)	Pressure decrease[f] (ratio)
1	9685	776	38	34.6	16	1.618	1.203
2	9160	765	79	48.4	22	1.836	1.272
3	9240	762	62	41.5	19	1.743	1.257
4	9560	769	89	47.7	19	1.740	1.218
5	8750	778	70	50.3	23	1.883	1.333
6	9290	778	58	45.8	21	1.817	1.252
7	9485	773	45	39.6	18	1.681	1.22[illegible]
8	9325	768	51	42.6	19	1.716	1.249
9	8590	766	78	56.1	25	1.988	1.355
10	9310	772	59	61.4	27	2.055	1.400
11	9650	768	54	56.9	25	1.959	1.340
12	8480	774	63	57.2	25	1.994	1.369
13	[illegible]	767	76	59.8	26	1.99[illegible]	1.344
14	8655	763	65	57.7	26	1.986	1.345
15	9130	766	43	48.7	22	1.825	1.274
16	9655	775	42	36.4	17	1.629	1.204
17	8615	776	71	54.3	24	1.980	1.350
18	8800	770	56	55.9	25	1.953	1.323
19	7695	774	58	74.5	32	2.279	1.512
20	7985	764	71	68.5	30	2.188	1.460
21	9110	763	59	45.7	21	1.788	1.277
22	7670	776	68	78.8	34	2.337	1.518
23	8725	772	52	52.6	24	1.917	1.332
24	9005	769	49	48.5	22	1.837	1.289
25	9730	763	43	38.1	18	1.650	1.195
26	8980	770	54	49.0	22	1.842	1.297
27	8430	760	56	62.9	28	2.045	1.380
28	8595	783	60	54.3	24	1.926	1.348
29	8605	770	58	58.6	26	2.025	1.353
30	8135	784	65	63.9	28	2.126	1.429
31	9175	773	47	48.4	22	1.815	1.265
32	8970	768	61	46.6	2[illegible]	1.810	1.296

Rod	Burst conditions			Tube heated length[a]		Fuel pin simulator[b]	
	Pressure (kPa)	Temperature (°C)	Strain[a] (%)	Volume increase[c] (%)	Average strain[d] (%)	Volume increase[e] (ratio)	Pressure decrease[f] (ratio)
33	8970	762	55	47.6	21	1.853	1.298
34	8695	773	87	56.2	25	1.932	1.336
35	8645	774	63	55.2	25	1.950	1.345
36	8835	756	66	55.8	25	1.935	1.329
37	7695	771	60	66.7	29	2.165	1.511
38	7715	770	88	74.6	32	2.264	1.508
39	8205	773	66	59.9	26	2.069	1.418
40	8975	773	52	48.5	22	1.843	1.294
41	9360	769	47	45.4	21	1.780	1.24[illegible]
42	8405	773	87	59.8	26	2.029	1.386
43	9385	775	57	43.7	20	1.736	1.239
44	8355	763	71	60.9	27	2.029	1.394
45	7800	769	64	71.3	31	2.217	1.491
46	8035	763	95	65.9	29	2.136	1.446
47	8975	774	54	50.6	23	1.887	1.295
48	8775	763	64	49.[illegible]	22	1.880	1.325
49	9720	761	45	34.8	16	1.623	1.195
50	8900	768	62	51.3	23	1.869	1.302
51	8135	759	76	59.9	26	2.036	1.421
52	8630	75[illegible]	67	55.4	25	1.930	1.342
53	8935	760	63	46.3	21	1.793	1.295
54	8770	766	56	52.7	24	1.917	1.322
55	8785	763	50	48.7	22	1.840	1.319
56	8985	781	39	47.9	22	1.830	1.288
57	9530	753	33	39.4	18	1.684	1.215
58	9125	757	39	44.7	20	1.762	1.270
59	9470	770	42	40.4	18	1.675	1.221
60	8800	755	78	48.6	22	1.862	1.314
61	9285	768	87	43.7	20	1.756	1.245
62	[g]	[g]	[g]	[g]	[g]	[g]	[g]
63	8685	775	76	54.6	24	1.936	1.334
64	9350	756	32	37.3	17	1.643	1.239

[a] Measurements based on tube outside perimeter.

[b] Includes fuel pin simulator, pressure transducer, and connecting tube.

[c] From deformation profiles assuming circular cross sections.

[d] Assumes volume increased is uniformly distributed over heated length.

[e] Ratio of final to initial volume (see note *b*).

[f] Ratio of initial pressure to burst pressure.

[g] Simulator heated but unpressurized.

4. DETAILED TEST RESULTS

The previous section summarized the important test results; this section presents, in a number of subsections, detailed results of the B-5 test. The purpose of this presentation is to provide a fairly complete reference source of uninterpreted data that can be used for analysis and evaluation by those interested.

4.1 Thermometry Difficulties and Corrections

The thermometry data obtained during the test were generally of high quality; however, a few problems were encountered, particularly with the small-diameter, bare-wire type S thermocouples that were attached to the shroud and to the outside surface of four of the simulators. Some of these problems were such that posttest corrections could be made to improve the quality of data from those thermocouples that were affected.

Because of their small diameter, the type S thermocouples were very fragile and difficult to install. The wires were broken on six of them (TE 39-5, TE 39-7, TE 39-8, TE 91-3, TE 91-4, and TE 93-1) during assembly of the test array and could not be replaced. In addition, the wires of three of the type S thermocouples were incorrectly connected to form reversed junctions inside the test array at the point where the small wires were joined to larger diameter sheathed thermocouple extension wires. Because the characteristics of the type S wires are very nearly the same, these wiring errors were not discovered during fabrication and were not detectable during isothermal pretest checkout operations. The errors became apparent after the test while checking and analyzing the isothermal and transient temperature data for qualification purposes. Because the temperature of the reversed junctions would have to be accurately known during the transient to compensate for the errors, it was not possible to make posttest corrections to the data. Three of the type S thermocouples (TE 5-5, TE 44-7, and TE 93-4) were erratic throughout the transient, and one (TE 91-1) became erratic after about 25 s of the transient. As a result of these difficulties, data recorded for the above discussed thermocouples were disqualified and are considered invalid.

Another difficulty encountered with the type S thermocouples could be, and was, corrected posttest to improve the quality of the data from these thermocouples. This was associated with an apparent error of ~20°C between the type S and type K thermocouple readings that was first noticed during the isothermal pretest checkout operations. The cause was attributed at the time to calibration differences and to different millivolt-to-temperature conversion routines programmed into the CCDAS. Because the offset was also present during the thermal transient, several checks were performed after the test to locate and quantify the type S thermocouple temperature errors. The thermocouple material was recalibrated, a check of the CCDAS zero-offset was made, and tests were performed on several of the thermocouples (though not in a bundle or a fuel pin simulator) connected to the CCDAS using different modes of grounding.

All errors measured by these checks were small compared with the 20°C error. Although not proven by these checks, we concluded that complex grounding paths most likely caused the observed 20°C zero-offset within the CCDAS measurement circuits.

Based on the above conclusion, a zero-offset correction of −0.202 mV was applied posttest to all the type S thermocouple voltages. This value was derived from the average indicated temperature difference between the external (type S) and internal (type K) thermocouples located at the same elevation during the pretest isothermal phase of the test.

Aside from one thermocouple (TE 46-1) that was inoperative throughout the transient, the type K thermocouples that were used to measure cladding inside surface temperature performed quite well. The only difficulty encountered was the occurrence of electrical noise spikes on about 30% of the thermocouple response signals as typified by the example depicted in Fig. 18.

The noise spikes were caused by interference from the electrically heated furnaces that were used for thermocouple cold junction compensation. The magnitude and polarity of the spikes depended on the particular signal multiplexer and the thermocouple reference furnace used for each signal; the sequence and time of occurrence of the spikes depended on the data sampling order of the sensors in the CCDAS scan list.

Because erroneous temperatures would be used in computer analysis of the data if the temperature were sampled at the time of a noise spike, the spikes were removed from the data from the time of power-on to the time of burst for each simulator thermocouple exhibiting such behavior. However, if a spike were superimposed on another event that caused a rapid change in the indicated temperature, the spike was not removed. Figure 19 shows the data of the previous figure without the noise spikes.

The software used to convert the as-recorded millivolt data tapes to engineering units was modified to correct the type S thermocouple zero-offset and to remove the type K thermocouple noise spikes, and a new engineering units tape was generated and used to produce the data plots and tabulations presented in this report.

4.2 Transient Results

4.2.1 Bundle behavior

Information contained in this section was obtained during the course of the test transient. The data were recorded by the CCDAS in the continuous scan mode (i.e., each sensor was sampled every 0.025 s) over a period of ~10 min, starting ~10 s before power-on. Pressure and temperature data were obtained for each simulator from fast-response pressure transducers and sheathed thermocouples spot-welded to the inside cladding surface at various positions (Figs. 3 and 4). The temperature of the thin, (electrically) unheated shroud was measured by small-diameter, bare-wire thermocouples (located as indicated in Fig. 3) spot-welded to the outside surface of the shroud. Steam temperature measurements were made with sheathed thermocouples at the locations shown in Fig. 5. Also, the electrical power parameters were measured and recorded by the CCDAS.

Superheated steam entered the test array through a single inlet nozzle located at the 107-cm elevation on the north side of the bundle (Fig. 1) at an average temperature of 355°C and a pressure of 290 kPa (absolute) and flowed downward through the array at a constant mass flux of 288 $g/s \cdot m^2$. With these conditions the nominal Reynolds number at the top of the heated zone (91.5-cm elevation) was 140. These inlet conditions remained essentially constant until disrupted by escaping helium from the bursting tubes. When power to the bundle was terminated, the steam mass flux was increased to an estimated minimum of 2000 $g/s \cdot m^2$ for rapid cooldown. Inlet and outlet steam temperatures measured 0.5 s before power-on and 1.0 s before the first tube burst are indicated in Figs. 20 and 21, respectively.

With the single inlet nozzle and the very low steam flow, it was not possible to obtain a uniform steam temperature distribution across the top of the bundle, as shown by Figs. 20(*a*) and 21(*a*). The inlet steam was cooled (giving up heat to the simulators) as it traversed the array from the inlet (north) side to the opposite (south) side, creating a 20° to 25°C gradient in the steam. The major portion of the heat gained by the simulators from the steam was conducted upward to the top of the vessel (Fig. 1), where it was dissipated to the closure flange and the external surrounding. A portion of the heat gained by the simulators on the north side of the bundle was conducted downward and contributed to a small gradient in the axial temperature distribution. The measured initial steam temperature distribution at the bottom of the heated zone was fairly uniform (within ~2°C) as shown by Fig. 20(*b*). Attempts were made during the hold time between the pretest power-bump (for checking performance and data acquisition instrumentation) and the burst test transient to correct the radial temperature distribution. These attempts were largely unsuccessful, primarily because of the low steam flow and the relatively cold top closure flange, and the test was conducted under these conditions. As will be discussed later, they had a significant influence on the deformation.

Figures 22–31 present cladding temperatures measured at the instrumented elevations 0.5 s before power-on and 1.0 s before the first tube burst. The data are presented in a format intended as a schematic layout of the thermocouple locations. If the thermocouple junction is at the elevation for which the particular map applies, the thermocouple number circle is filled in to denote the azimuthal position of the measurement, and the temperature measurement is given. The row average temperatures are printed on the left; the column average temperatures, at the top of the layout. The cross section average temperature is also included in the format.

The overall radial temperature distribution may be visualized somewhat more easily using the temperature map depicted in Fig. 32. The temperature given for each simulator is the average of the thermocouple measurements for that simulator without regard to elevation. The effect of the aforementioned nonuniform inlet steam temperature distribution on the bundle average radial temperature distribution is evident in the figure.

The temperature maps provide considerable insight and greatly facilitate visualization, interpretation, and evaluation of local and overall temperature distributions. They were used to obtain the axial temperature profiles plotted in Fig. 33; the average at each instrumented elevation, the range of the data, and the number of thermocouples on which the average is based are also noted in the plot. Based on the average temperature at each elevation, the initial axial temperature distribution was very uniform (335 ± 2°C), although the north-to-south gradient is evident in the range shown for temperature measurements at each elevation. Except for grid and end effects, the average axial distribution measured 1.0 s before the first tube burst was also reasonably uniform; however, the temperature variation, as indicated by the data range-width at each elevation, was greater than initially present. The small temperature depression (~7°C) at the 48-cm elevation was caused by the presence of simulator external thermocouples in this region and will be discussed in a later section.

The bundle radial temperature distributions shown in Fig. 32 suggest the north-to-south temperature gradient was on the order of 10°C. This is somewhat misleading because the gradient varied at each instrumented elevation. For example, Fig. 22(*a*) shows the initial gradient at the 84-cm elevation was ~20°C, with an average temperature of 337°C for the section, while Fig. 31(*a*) shows the gradient was only ~5°C at the 5-cm elevation, with a section average temperature of 334°C. Although the overall average axial gradient was only ~3°C, simulators on the north side of the array had initial axial gradients of ~11°C, while those on the south side had negative gradients of ~3°C. Although the radial and axial gradients decreased during the transient, as indicated by the temperatures measured at each of the instrumented elevations 1.0 s before the first tube burst, they influenced the deformation distribution significantly.

Differential pressures measured 0.5 s before power-on and 1.0 s before the first tube burst are presented in a similar format in Fig. 34. Because the simulators were pressurized simultaneously from a common header and then individually isolated, the uniformity in initial pressure indicates the absence of seal leaks. The data in Fig. 34(*b*) are consistent with Fig. 32(*b*) and indicate that the interior simulators were slightly hotter and had deformed slightly more at this time than the exterior ones and that the simulators on the north half of the array had deformed more than those on the south half.

A number of data plots are presented below to illustrate significant features of the test as it progressed and to provide an indication of the general conditions prevailing at the times of important events. A parameter, TAV-10, is plotted in a number of these figures to represent the bundle average temperature. This parameter is in reality the average of eight thermocouples (TE 14-3, TE 18-4, TE 21-1, TE 27-4, TE 36-1, TE 38-2, TE 47-2, and TE 51-1) at the 38-cm elevation (see Fig. 3 for relative positions) that were electronically averaged and recorded during the test to facilitate characterization and visualization of the bundle temperature as a function of time.

Figure 6, presented earlier, showed this parameter and the electrical power parameters as a function of time after power-on. Constant voltage (dc) was applied to the simulators for 48.45 s; this point is noted in the figure (and subsequent plots) for reference purposes by an arrow on the time axis. Because the temperature coefficient of resistivity of the heating element material (Kanthal A-1) is very low (<0.005%/°C above 700°C), the power generation varied very little from the average of 3.0 kW/m. As a result the cladding temperature increased at a nearly constant rate as indicated in the figure. The average heating rate from ~5 s after power-on to ~43 s after power-on (i.e., to 1.0 s before the first tube burst) was 9.8°C/s. Near the end of the transient, the heating rate decreased slightly because of increased heat losses at the higher temperatures; deformation feedback effects may have contributed also to the reduction of the heating rate. The average temperature, as indicated by TAV-10, reached a maximum of 804°C about 8 s after power-off and then slowly decreased.

Figure 35 depicts the applied voltage, the bundle characteristic temperature (TAV-10), and several pertinent pressures. In particular, the vessel gage pressure is shown by PE-301, and differential pressures are shown by PE-21 for simulator 21 (the first simulator to burst) and by PE-1 for simulator 1 (an outside corner simulator and the last simulator to burst). The interior simulators, in general, exhibited pressure traces similar to that for No. 21, while those for the exterior simulators were similar to that for No. 1; the rate of pressure decrease during deformation was much more rapid for the interior simulators. The vessel pressure remained constant until the first tube burst, at which time it increased because of the release of the hot, high-pressure gas from the ruptured simulators. The increased external pressure caused a small (<225-kPa) decrease in the differential pressure and retarded deformation of those simulators not yet burst and will be discussed in Sect. 5. About 3 s after power-off, the steam control valves opened to reduce the vessel pressure and to permit increased steam cooling; at this time the vessel pressure decreased rapidly to near atmospheric.

Figure 36 shows the vessel gage pressure (PE-301) and the inlet steam temperature measurements made at the top of the bundle (see Fig. 5 for thermocouple locations) during the transient. Steam temperature measurements made at the bottom of the bundle are depicted in Fig. 37. The thermocouples used for measuring both inlet and outlet steam temperature indicated unstable temperatures during the time the simulators were bursting. The perturbations in the inlet steam temperature measurements were caused by reversed flow patterns that were initiated by the sudden increase in vessel pressure. Because the steam control valves downstream of the test vessel could not pass the steam flow and the copious quantities of high-temperature gas released by the failing simulators without a pressure increase, some of the high-temperature gas was transported upward and caused the inlet steam thermocouples to indicate higher temperatures.

As indicated in Fig. 37, the steam temperature measurements at the bottom of the bundle diverged from an initial maximum difference of 2° to 72°C after 43 s of heating [compare Figs. 20(*b*) and 21(*b*)]. Although several possibilities for explaining the temperature divergence exist, the most likely one is related to the exact location of the thermocouple measuring junctions. Very large axial temperature gradients exist in the simulators at the end of the heated zone, and these gradients affect the local steam temperature. Therefore, small differences in the exact locations of the measuring junctions can affect the measured values significantly. While this effect would be readily apparent in the transient measurements, it would not be discernible in the initial (steady state) temperature measurements, because temperature gradients were almost nonexistent at this end of the bundle prior to power-on. The perturbations in the temperature measurements during the time the tubes were failing were caused by the high-temperature gas-steam mixture flowing past the sensors.

The tube bursts occurred over a 5.60-s time interval, starting at 44.00 s after power-on, as indicated in Fig. 7. Although the burst frequency distribution (Fig. 8) was similar to a Gaussian distribution, the exterior simulators, in general, burst later than the interior ones, with the corner simulators being among the last to burst. This would be expected because the boundary conditions caused the exterior simulators to have greater heat losses and slightly lower heating rates, and thus slightly longer times would be required to reach the burst temperature range.

4.2.2 Shroud behavior

The need for electrical isolation between the test array and the closely fitted shroud precluded Joule heating of the shroud. Although the shroud had a highly polished, gold-plated surface to reflect thermal radiation, the temperature of the shroud increased significantly during the test. Figure 38 compares measured shroud temperatures on each of the four sides at the 48-cm elevation (see Fig. 3 for thermocouple identifications and locations) with the characteristic bundle temperature (TAV-10). Differences of ~100°C were measured around the shroud during the time of deformation; these large differences were probably caused by variations in contact resistance between the outside of the thin shroud and the backup thermal insulating material (see Sect. A-A of Fig. 1) and by contact between the shroud and the simulators, which will be discussed later.

Temperature measurements made on the west side of the shroud are shown in Fig. 39. These data indicate the shroud axial temperature gradient was only ~20°C. Similar plots for the other shroud thermocouples are included in Appendix A. The average shroud temperature was ~200°C less than the bundle average temperature during the time deformation was occuring (i.e., 1.0 s before the first tube burst). About 45 s after power-on, the shroud thermocouples indicated significant and rapid temperature increases that were probably caused by the release of significant quantities of high-temperature gas from the rupturing tubes (the first tube burst 44.00 s after power-on). Although the major cause of the sudden increase can be attributed to heating by hot gas escaping from failed interior simulators, some of the increase can be attributed to contact between the deforming simulators and the shroud.

4.2.3 Fuel pin simulator behavior

Although the temperature distributions presented in Sect. 4.2.1 characterize the bundle as a whole, the individual simulators behaved differently from these smoothed (averaged) profiles. This would be expected, because the simulator temperature distributions would be strongly influenced by the heat generation characteristics of the individual simulators, by their locations within the array, and by contact with other simulators.

Each of the 64 simulators was instrumented with four thermocouples, spot-welded to the inside surface of the cladding at the locations shown in Fig. 3, and a pressure sensor to provide cladding temperature and pressure data during the test transient. Plots of these data provide considerable insight and qualitative information that supplement the tabulated data for analytical purposes. However, to include plots and data tabulations of convenient sizes for easy reading would add considerable bulk to this report. Instead, a typical example is displayed in Fig. 40 to illustrate the type of information that is included for each simulator in the computer-generated microfiche enclosures in the pocket on the inside back cover. The figure shows the pressure (differential above the external pressure in the test vessel) and temperature data for the first simulator (No. 21) to burst. A reference arrow is located on the abscissa to mark the time power was terminated. The time of burst is indicated by the sudden drop in pressure and frequently by a perturbation in the temperature traces. The figure shows that the temperature distribution was unusually uniform before the power was terminated; after this time the individual temperature traces (for different measurement elevations in the simulators) diverged as a result of the increased posttest cooling steam flow. Similar plots for all the simulators are presented in Appendix A.

Attempts were made to measure azimuthal temperature gradients at the 48-cm elevation of selected simulators (5, 28, 39, and 44) by spot-welding four small-diameter, bare-wire, type S thermocouples to the cladding outside surface of these four simulators at the orientations noted in Fig. 3; each of these simulators also had an internal thermocouple located at the same elevation to provide comparative temperature measurements. Because of difficulties encountered with the fragile external thermocouples (see Sect. 4.1), several of them did not function. However, those that functioned provided reliable temperature data. Typical data, for simulator 28, are plotted with greatly expanded scales in Fig. 41 for a 20-s interval of the transient, starting about the time of maximum pressure. The azimuthal temperature gradient in the simulator was <4°C for the first 38 s of the transient and then increased uniformly to about 17°C by the time the simulator burst. Figure 42, plotted with the same scale factors as the previous figure, shows that the internal temperature measurement was within (and near the lower bound of) the bandwidth of the external measurements. Similar plots for the other simulators instrumented with external thermocouples are given in Appendix A.

Qualitative information on burst time, temperature, pressure, and other measured parameters can be obtained from the data plots in Appendix A, but quantitative information is best obtained from the computer-generated summary tables presented in Appendix B for the conditions measured at the time each tube burst. An example, for simulator 21, is given in Table 6 to illustrate the format and type of information available in the appendix. The tables include (1) the times from power-on and power-off and the magnetic data tape record from which the tabulation was printed, (2) the simulator differential pressure, (3) the cladding temperatures measured by each of the four thermocouples and their average, and (4) the times from other tube bursts (relative to that for which the table pertains). Pertinent miscellaneous measurements include (1) cladding temperatures obtained from the functional type S thermocouples on the outside surface of four of the simulators (TE 5-6 through TE 5-8, TE 28-5 through TE 28-8, TE 39-6, and TE 44-8; see Fig. 3 for locations); (2) shroud temperatures (TE 91-2, TE 92-1 through TE 92-4, TE 93-2, TE 93-3, and TE 94-1 through TE 94-3; see Fig. 3 for locations); (3) inlet steam temperatures (TE-320 through TE-322; see Fig. 5 for locations); (4) outlet steam temperatures (TE-323 through TE-327; see Fig. 5 for locations); (5) vessel gage pressure (PE-301); (6) total current through bundle (EIE-10); (7) voltage drop across bundle (EEE-10); and (8) characteristic bundle average temperature (TAV-10; see Sect. 2.1 for definition).

Similar tables are also given in Appendix B at selected time intervals for 70 s of the transient; these can be used to approximate the transient of either the individual simulators or the bundle as a whole.

4.3 Pretest and Posttest Results

The information contained in this section was obtained from the pretest and posttest examinations of the test array. Some information, such as the simulator IR scans, resulted from quality assurance efforts made to characterize the test components. Other information, such as the bundle pretest and posttest photographs, was obtained for documentation of the test conditions. The results are presented in considerable detail, because we believe the data are extremely important to the interpretation of the test in terms of deformation behavior and distribution.

4.3.1 Bundle pretest photographic documentation

Selected photographs of the bundle assembly and of various details of the construction and monitoring instrumentation are included in this section. Some of these details are of general interest, while others are directly applicable to the interpretation of the test.

A view of the test array before installation of the shroud is shown in Fig. 43. The array was supported from the top flange and was free to move axially during the test. A close-fitting shroud was also supported from the top flange and was used to simulate the radial restraint in a nuclear fuel assembly without restricting axial movement of the simulators and grids. The shroud was constructed of thin stainless steel strips, having highly polished, gold-plated surfaces, backed by insulating material; construction details are illustrated in Fig. 44. The four shroud panels were assembled into a box around the test array as illustrated in Fig. 45. The completely assembled array is shown in Fig. 46.

Figure 47 shows a typical shroud thermocouple attachment. Each thermocouple was formed by making a ball junction (~0.25-mm diam) on the end of 0.076-mm-diam type S wires. The ball was then spot-welded to the back side of the thin shroud reflector strip. The mass of the thermocouple was kept small to minimize thermal shunting, that is, cooling of the reflector strip at the point of attachment by the thermocouple itself. The fragile 0.076-mm wires exited the shroud box through an insulator at the center of a plug, as shown in Fig. 48, and were then spliced to 0.25-mm-diam wires that exited the end of sheathed type S thermocouple extension material through a glass end seal to prevent ingress of moisture.

Typical installation details of the thermocouples that were used to measure azimuthal temperature gradients at the 48-cm elevation are shown in Fig. 49. The wires were isolated with high-purity (99%), oval-shaped (dimensions of 1.19 by 1.98 mm with two 0.5-mm holes) alumina pellets and exited the bundle on the east and west sides along the paths indicated in Fig. 50 (see Figs. 43—45 also). The insulated wires penetrated the shroud box and were spliced to type S thermocouple extension material, (the same as used for the shroud thermocouples) as shown in Fig. 51.

A view of the lower end of the bundle showing one of the outlet steam thermocouples is shown in Fig. 52. All the steam thermocouples were 0.71-mm-diam, stainless-steel-sheathed, type K with insulated junctions. The junction end was centered within the flow channel with a ceramic spacer.

4.3.2 Bundle posttest photographic documentation

After performing posttest instrumentation checks, the assembly was removed from the test vessel and partially disassembled for visual inspection and dimensional checks of the test array. Figure 53 shows the west face of the array at this stage of posttest examination. The meter scale is suspended (in this and subsequent photographs) with the zero point at the bottom end of the heated zone and can be used as a reference for the discussion throughout this report. The west face panel of the shroud box is also shown in its relative axial position; the polished reflector strip shows discoloration and distortion patterns that reflect the image of the test array.

Further disassembly was then accomplished to prepare the array for flow characterization tests and detailed photographic documentation of the salient deformation features. Although procedures and techniques found useful in removing the fuel simulators (internal heaters) from previously tested bundles were employed, these operations were not entirely successful. Because large ballooning permitted the thermocouples and/or the spacer wires to become entangled, most of the fuel simulators were difficult to remove, and 11 were impossible to remove with these ordinary means. Because these 11 simulators would have no effect on the subsequent flow characterization tests, it was decided to sacrifice these simulators and leave them in the array.

Figure 54 gives a perspective of the four faces of the array after removal of the lower end seals and the internal fuel simulators. As evident in the photographs, ballooning was extensive and was distributed in an undulating pattern along the length of the bundle. Frontal views of the north and east faces, depicting the region between the interior grids, are shown in Fig. 55, and frontal views of the south and west faces are shown in Fig. 56. Similar views of the upper end of the bundle are presented in Fig. 57.

Several deformation features are evident in the photographs. One of the more striking is the amount of axial shrinkage that occurred during the test. The meter scale in the photographs is positioned with its zero point at the average posttest location of the bottom of the bundle heated zone. A measure of the average shrinkage, which was caused by texture effects and is characteristic of Zircaloy deformation in the high-alpha temperature range, is given by the location (64 cm) of the No. 2 grid in the photographs. Based on the pretest elevation (66 cm) of the grid, the average shrinkage (Table 7) was 2.5%. Individual tube shrinkages (Table 8) varied from 1.6% to 2.9%, indicating relative movement (axially) between the tubes and the grids. [The grids were supported by friction forces (generated by the spring forces acting on the individual tubes), and the array was fixed in and suspended from the upper flange as indicated in Fig. 1.]

Another indication of the shrinkage is given by the posttest locations of the internal thermocouples, which can be identified in the photographs by small discolored areas where the thin oxide layer was removed from the Zircaloy tubes before the thermocouples were spot-welded to the inside surfaces. A typical example is shown on the burst of tube 16 (on the east face) in Fig. 57. Because of the axial shrinkage, the posttest locations of the thermocouples, as indicated by the meter scale in the photographs, appear at lower elevations than given by the pretest data of Fig. 3. These differences must be taken into account when analyzing the deformation at points where temperature measurements were made.

Extensive deformation and a number of tube bursts occurred between grids 2 and 3, Fig. 57. Pretest calculations had indicated that with the steam mass flux and other test parameters the same as in the B-3 reference test, deformation and tube bursts would be concentrated between grids 1 and 2. The initial north-to-south temperature gradient, resulting from the nonuniform inlet steam temperature distribution, was the major cause for this unexpected behavior, because it produced a small axial temperature gradient in the simulators on the north side. Although the north-to-south temperature gradient was only ~11°C (Fig. 22), its effect on deformation is clearly evident in Fig. 58.

Another significant deformation feature may be seen in the region where the simulator external thermocouple wires exited the bundle interior, about midway between grids 1 and 2 in Figs. 55 and 56. An enlarged photograph of the west face in this region of the bundle, taken before the remains of the wires were removed, is shown in Fig. 59. Although the section average temperature at the 48-cm (pretest) instrumented elevation was only 7° to 8°C lower than the averages at the two adjacent instrumented elevations (Figs. 25-27), there was noticeably less deformation in the region of the wires.

Clearly, the presence of the thermocouple wires and their alumina insulators (see Figs. 49 and 50 for installation details) influenced the temperature and, therefore, deformation. This was unanticipated and, because of its widespread distribution within the array, appears unrelated to thermocouple fin-cooling effects. The cladding temperature of the simulators with external thermocouples, as measured by the internal thermocouples [Fig. 26(*b*)] and confirmed by the external thermocouple measurements, was only ~3°C lower than the average for the section. However, because there were only four simulators with external thermocouples, these slightly cooler simulators would not account for the section average being 7° to 8°C cooler than the adjacent instrumented section averages. The degraded temperature condition also appears unrelated to flow pattern perturbations because of the very low steam flow (Re ~140 at the top of the heated zone). Most likely, the wires and alumina insulators acted as heat sinks during the transient and, as a result of thermal radiation and/or contact heat losses, cooled the affected simulators.

An enlarged view of some interesting deformation details on the south face of the bundle is shown in Fig. 60. The undulating pattern of deformation is evident, and some thermocouple locations are noted. The inverted dimple in the ballooned (burst zone) region of simulator 61 was apparently caused by contact with the closely fitted shroud after the tube burst. This tube burst earlier than the neighboring interior tubes; presumably deformation of the interior tubes forced simulator 61 against the shroud and caused the dimple to form.

The thin, highly polished reflector strips used in the shroud panels were preloaded axially with high-temperature springs (Fig. 44) to compensate for differential thermal expansion and to keep the strips taut during the test. The design was not entirely successful, because the strips wrinkled (bowed inward) and contacted the simulators as illustrated by the irregular discoloration and distortion patterns in Fig. 61; the locations of the grids (noted by transverse marks on the polished surfaces) and remnants of the thermocouples can be used for convenient reference points. Evidently the two-dimensional temperature gradients in the thin strips and/or restricted movement caused them to buckle and touch the simulators. Undoubtedly this influenced the distribution of the cladding deformation as will be discussed in a later section. The corner simulators, although they deformed almost as much as their neighbors, touched the strips infrequently. Shroud box corner restraints probably prevented the transverse buckling patterns from bowing inward and contacting the corner simulators.

4.3.3 Bundle cross section photographs

Following photographic and dimensional documentation and flow characterization of the test array, it was cast into an epoxy matrix and sectioned transversely at 10- to 20-mm intervals for measurement of the deformation in each tube. The sections were polished sufficiently to sharply define the tube wall boundaries and photographed. Although they facilitated measurement of the tube strains at the axial nodes, we believe careful study of the photographs provides considerable insight into the deformation behavior and temperature distributions during the deformation process. For these reasons, the section photographs are given in Figs. 62—121 for documentary purposes.

The photographs were taken looking down on the surface at the given elevation with the No. 1 simulator in the northwest corner. This corresponds to the layout of Fig. 3, which can be used as a convenient reference for tube identification in each section photograph. All the figures have white arrow points in the upper left corner. The distance along the edge of the epoxy matrix between the arrow points is proportional to the elevation of the section and can be used to calculate the height (above the bottom of the heated zone) of the actual plane of the photograph. A 1-in. scale (subdivided into 50 divisions of an inch) is included on the north edge of the matrix to facilitate calculation of the actual magnification factor of the photograph.

The array was sectioned at carefully selected axial nodes to reveal as much qualitative and quantitative information as feasible within a number of constraints. Primary consideration was given to the desire that every burst appear in a section to provide an accurate measurement of the burst strain. It was also desired to section the array in the plane of as many of the thermocouples as could be accommodated within the other constraints. As a consequence, Figs. 66, 75, 80, 85, 91, 96, 108, and 115 show the posttest planes of the majority of the thermocouple attachments. It should be noted that these appear at lower elevations than the pretest locations (Figs. 3 and 4) because of axial shrinkage that occurred during the test.

The remains of the thermocouples and internal heaters that could not be removed from the inside of the cladding tubes of 11 of the simulators can be seen in the section photographs. Not all appear in each photograph because they were not firmly held in the epoxy matrix and were removed before the photographs were taken. An undeformed tube (No. 62) appears in the third position from the right corner in the bottom row of each section and can be used for visual comparisons. (It also served as a convenient check of the data reduction techniques discussed in the following section.) This simulator developed a seal leak during pretest operations and was not pressurized; however, it was heated to preserve the proper temperature boundary conditions.

Figure 62 shows an undeformed section of the array taken well below the bottom of the heated zone. Sections through the lower grid are shown in Figs. 68–70 and the upper grid in Figs. 101–103; cross sections of the bands that tightly retained the outer ring of simulators within the grids appear in Figs. 69 and 102. Some flattening of the tubes at the spring-loaded contacts is evident in the figures. Strain in the tubes at the grid nodes ranged from 4% to 11%.

The figures show the effect of confinement, exerted by the closely fitted shroud, and rod-to-rod interactions on the deformation patterns. The shroud, in general, prevented outward movement of the simulators to accommodate deformation in the interior of the array. However, because it was unpressurized and did not deform, simulator 62 was displaced outward by deformation, and outward movement of the interior simulators as may be seen, for example, in Fig. 86. This behavior illustrates the effect of simulator movement caused by the lack of constraint boundary conditions in small bundle tests without deforming guard simulators. Extensive localized ballooning and distortion in the vicinity of the bursts are evident throughout the bundle. For example, compare the shapes and the strains of tubes 42 and 46 in Figs. 74 and 77. Although these sections are only 4.5 cm apart, they appear unrelated. The severe distortion occurred after the tubes burst and was caused by the action of neighboring tubes as they deformed and burst. In fact, the tube burst sequence can be deduced qualitatively from the distortion patterns.

As discussed earlier, thermocouple wires with alumina insulators passed through the bundle (see Figs. 49 and 50) to thermocouples attached to the outside surface of four of the simulators and affected the temperature and, as a result, the deformation distribution in the vicinity. The remains of the wires and insulators, trapped within the array, are evident in Figs. 90–93. The figures also show that the simulators in the vicinity of the wires (Fig. 50) deformed much less than those unaffected by the wires. The average temperature of this zone was only 7° to 8°C below that for the adjacent instrumented elevations (Fig. 33), but its effect on deformation can be seen by comparing Fig. 90 with Fig. 85. Deformation in the latter is significantly greater and more uniformly distributed in the bundle.

The effect of the north-to-south temperature gradient at the upper end of the heated zone, caused by the nonuniform temperature distribution of the inlet steam (Fig. 21), is evident in Fig. 112, for example. On the other hand, Fig. 72 for a section with approximately the same bundle average deformation but with a negligible radial temperature gradient shows the deformation to be uniformly distributed across the array.

Three of the tube bursts initiated at thermocouple spot-welds and resulted in pinhole failures. Two of these are shown in Figs. 91 (tube 53) and 96 (tube 59). The third pinhole failure, like the first two, was observed in tube 7 during examination with a borescope prior to encapsulation in the epoxy matrix but was removed by the saw cut when the bundle was sectioned. The necked down region of the tube wall at the edge of the pinhole is evident in Fig. 109 and more clearly in the enlarged photograph of the tube in Fig. 122. Sections made at other planes containing thermocouples or in the immediate vicinity of thermocouples (unequal axial contraction of the tubes caused the posttest locations to vary a few millimeters) are shown in Figs. 66, 75, 80, 85, 108, and 115. Although a number of bursts appear in the sections shown in these figures, burst midpoint orientations could be correlated with posttest thermocouple positions for only tubes 34 and 42. However, the burst strains and burst openings were unusually large for these failures. The thermocouple spot-welds may have acted as defects and initiated the failures, but they did not significantly affect the failure.

Localized ballooning with strains equal to or greater than that at the failure point was observed on several of the tubes. In some of these cases, the localized balloons had nonuniform wall thinning, indicating potential failure sites. For example, compare tube 45 in Figs. 81 and 110; other examples are easily identified on the deformation profiles presented in a later section.

The sections were carefully examined to define the tube burst locations given in Table 9. The axial locations were determined first by internal examination of the tubes with a borescope before encapsulation with epoxy and confirmed later from measurements of the sections; the midpoint elevations and burst lengths are considered reasonably accurate (to within 3 to 5 mm). The azimuthal orientations were determined from angle measurements made on the sections near the end of the burst opening and are probably accurate to within 5° to 10° of arc length. Burst midpoint elevations and orientations are shown schematically in Fig. 123.

The burst orientations of the tubes in the outer ring of 28 simulators provide evidence of significant azimuthal temperature gradients that were caused by nonuniform heat losses. With five exceptions, the bursts in the exterior tubes were directed inward, that is, toward the higher temperature portion of the tubes. The burst directions for the exceptions were directed toward adjacent tubes. (See tubes 7, 8, 16, 61, and 63 in Fig. 123.) Interestingly, the bursts in tubes 61 and 63 occurred at approximately the same elevation and were directed toward the undeformed (but heated) tube (62) between them. Burst directions of the tubes in the inner 6 × 6 array had a preferred orientation toward an open flow channel and, in general, toward the northeast corner of the array; only 8 of the 36 were directed toward adjacent tubes. The tendency for the burst directions to be toward the open flow areas was caused by rod-to-rod interactions, while the tendency for the bursts to be in the northeasterly direction was the result of the small temperature gradient across the bundle that was caused by the nonuniform temperature distribution of the inlet steam.

4.3.4 Deformation data reduction methodology and results

Enlarged (~3X) photographs of the sections were digitized to facilitate computer reduction of the photographic data to geometrical parameters describing strains, areas, volumes, centroids, and displacements. Fifty to ninety points, depending on tube shape and the degree of distortion, on both the outside and inside perimeters of each tube were digitized to provide x-y coordinates with respect to an arbitrary origin established at the same relative position on each section photograph. The digitized points were smoothed by forward fitting a quadratic curve to four consecutive points and then using the curve to generate ten points between each successive pair of digitized points. Thusly the series of curves (equal to the number of digitized points) was used to expand the number of digitized points by a factor of 10 for use in generating areas, centroids, and chord lengths.

Calculation of these geometrical parameters for distorted tube shapes at nonburst nodes presented no difficulties other than taking care that a sufficient number of points were digitized to mathematically describe the shapes accurately in those regions where the tube radius of curvature changed rapidly. However, the nodes containing tube bursts required special treatment because the software algorithms required closed perimeters. The endpoints of the burst lips were connected by straight line segments, drawn in such a way as to not enclose any of the adjacent tubes, to provide a continuous (but fictitious) perimeter for use in the fitting and integration algorithms. All the area enclosed by the fictitious perimeter was included as tube cross-sectional area at the burst node at this step in the data reduction process. At later steps, depending on the purpose, the area of a circular tube shape was derived from the perimeter and used to calculate other geometrical parameters of interest at both the burst and nonburst nodes. Because the same line segments were used for completing both the inside and outside perimeters, the segments also represented fictitious tube wall regions (of zero thickness) in calculating the area of the deformed tube. Of course, the length of the line segments was not included as part of the perimeter in the strain calculations.

The photographic data for each section were thus reduced to a table of geometric parameters that were used for verification of the digitized data and as a source file for further processing to obtain desired output parameters. Because these tables transform and summarize the section photographs into geometric parameters for analysis, they are included in Appendix C; an example is shown in Table 10 for illustrative purposes.

The table, for the section at the 17.0-cm elevation, gives for each tube the cross-sectional areas enclosed by the tube outside and inside perimeters and (by difference) the tube wall area, the lengths of the outside and inside perimeters, the x- and y-coordinates of the outside and inside tube area centroids referenced to the arbitrary origin established at the same relative position on each section photograph, and the strains (total circumferential elongation) based on the outside and inside perimeters.

One of the verification procedures made use of the digitized data and the computer graphics software to reconstruct the section image for comparison with the original photograph. An example of the application of this procedure to one of the more difficult sections to process (because of the odd shape of tube 42) is illustrated by Fig. 124, which shows the tube identification number, the strain based on outside tube perimeter, and the tube centroid and outline correctly located on the arbitrary coordinate grid. Comparison with Fig. 73 shows that the reconstructed image is an excellent reproduction of the section photograph.

Another and perhaps more important data verification procedure involved comparing the measured inside and outside perimeter strains to the theoretical expression relating the two (assuming constant tube wall area) as illustrated in Fig. 125. The corresponding inside and outside tube strain data of Table 10 are plotted on the graph as a single data point for each tube. Assuming constant tube wall area, the data points should lie on the theoretical curve. Because the inside and outside strain values were derived from separate measurements, if either is incorrect the data point will deviate significantly from the theoretical curve. As evident by the figure, the data are in excellent agreement with the curve and can be assumed to represent the true strains adequately.

After verification of the digitized data, the data tapes were reprocessed to generate a strain matrix (Table 11) of the strain in each tube at each axial node; the values in the table are given as percentage increase of original tube outside circumference. Burst strains, underlined in the table, were summarized earlier in Table 5 and displayed graphically in Fig. 12 as a function of tube radial position. As was evident in the section photographs (Figs. 62–121), the axial lengths of some of the bursts were such that they appeared in two or three of the section photographs and thus multiple values of the burst strain could result. We selected the value (underlined in the table) from the section nearest the burst midpoint as the most representative.

Examination of the tabulated strain values around the indicated burst strain will reveal an occasional value significantly greater than that selected as the burst strain, the most noticeable example being tube 19. The cause for this discrepancy is readily apparent from comparison of the tube burst in Figs. 86 and 87. The plane of the section in Fig. 87 is near the axial midpoint of the burst and is more or less normal to the tube wall. That is, the radius of curvature is parallel to the plane of the section, and the periphery is a correct measure of the circumferential elongation at this node. On the other hand, the plane of the section shown in Fig. 86 is at the end of the burst (barely evident in the photograph) and, because of the sharply changing and complex surface shape, is not parallel to the radius of curvature, particularly at the 8 o'clock position. The tube wall is cut at an angle and appears thicker in this region than it would be if the cut were normal to the wall. As a result of the plane of the cut not being parallel to the radius of curvature at all points on deformed surface, the measured periphery is greater than the true value that is required for calculating the strain. Interestingly, because it is normal to the flow channel, the projected area of the tube in the plane of the section is correct for calculating the reduction in coolant flow area. Similar examples, though not as prominent, are represented by tube 8 in Fig. 114, tube 14 in Fig. 108, tube 42 in Fig. 73, and tube 47 in Fig. 94.

The burst strain of some of the tubes in the outer ring of the array was unusually high (see Fig. 12), considering the boundary conditions. This was unanticipated because azimuthal temperature gradients in the exterior simulators were expected to localize the deformation and significantly reduce the burst strain in a given tube. The temperature gradients did localize deformation sufficiently to cause the burst orientations to be directed toward the bundle interior (Fig. 123) as expected. Contact between the shroud and the exterior simulators, as will be discussed in Sect. 5, reduced the gradients (locally) in some of the simulators and, as a result, they experienced very large deformation before failure.

The strain matrix (Table 11) was used to plot the axial profile of the deformation in each tube. These are presented in Appendix D; however, some examples are presented in Figs. 126—129 to elucidate certain features and to illustrate the type and format of the information available in the appendix. The posttest centerline positions of the two interior grids and the axial locations and lengths of the bursts are noted on the deformation profiles. The pretest IR characterization scan of the fuel simulator (internal heater), the approximate posttest axial positions of the thermocouples, and the direction of steam flow are also shown for reference purposes.

In general, the deformation profiles correlate reasonably well with the pretest IR characterization scans, as illustrated by Figs. 126 and 127. However, because Zircaloy deformation is extremely sensitive to temperature in the high-alpha-phase temperature range, deformation in certain regions was more sensitive to other temperature perturbations than to the minor variations in simulator heat generation. For example, intermittent contact between the shroud and the exterior simulators (see Fig. 61) modified the local temperature distributions and caused a cyclic pattern in their deformation profiles that was more or less independent of the IR scans, as typified by Fig. 128.

All the deformation profiles have certain characteristics, more or less independent of the characteristics of the individual fuel simulators. These include strains of 4% to 11% in the region of the grids and maximum strains of 7% to 17% in the region between the bottom of the heated zone and the lower grid. A much greater variation in maximum strain was observed in the region between the upper grid and the top of the heated zone (see Figs. 126 and 129). Strain in this region was strongly influenced by axial and radial temperature gradients and the cooling effect of the inlet steam. Because of localized contact with the shroud, deformation of the exterior simulators tended to be less uniform than that of the interior simulators in the region between the interior grids.

The bursts in three of the tubes initiated at thermocouple welds and resulted in pinholes, as noted in Fig. 123. The deformation plots in Appendix D suggest other bursts may have initiated at thermocouples; an example is shown in Fig. 127. In all but two cases (tubes 34 and 42), however, these can be eliminated from consideration by comparison of the burst orientations in Fig. 123 with the thermocouple locations in Fig. 3. Although the thermocouple spot-welds may have initiated the failures in these two cases, the deformation characteristics were not significantly affected because the burst strains and burst openings were unusually large.

Excessive ballooning over an extended length is a concern in LOCA analyses. For the tubes and spacing (1.32 pitch-to-diameter ratio) used in our tests, adjacent tubes will touch with 32% uniform expansion. As evident from the deformation profiles and Table 11, most of the tubes exceeded this value over considerable portions of the heated zone. Ordinarily, maximum ballooning occurs in the vicinity of the burst as illustrated by Fig. 126. Because of rod-to-rod interactions in this test, there were numerous cases in which comparable ballooning (typical examples are shown in Figs. 128 and 129), and in a few cases significantly greater ballooning (an example is shown in Fig. 127), was observed in regions remote from the burst zone.

Another important characterization of tube deformation is the volumetric expansion over the heated length. This parameter is closely related to flow resistance, because the volume increase takes into account deformation along the length of the tube. The volume increase was calculated for each of the tubes from the geometric data given in Appendix C. The calculation assumed that the tube cross section at each axial node was circular in shape and had a perimeter equal to the deformed tube outside perimeter; this is considered a reasonable approximation of the shape of the tube just before failure. The area of the tube was then calculated at each node and integrated over the tube heated length, using the trapezoidal rule, to obtain the volume occupied by the outside diameter. This value was expressed as a percentage increase over the original volume and was tabulated in Table 5 and displayed graphically in Fig. 11 as a function of tube radial position.

Individual tube overall deformation was also characterized by computing an average strain value from the volumetric expansion data. This calculation assumed the expansion was uniformly distributed over the tube heated length, that is, no account was taken of local variations caused by grid and end effects. The average strains thus calculated were also tabulated in Table 5.

The total expansion for all tubes at each axial node is also of interest because it determines the coolant channel flow area restriction. This parameter is normally expressed as an average value for an array cross section and was calculated on the basis of a rod-centered unit cell, using the equation

$$B = 100 \times \frac{\sum_{}^{n=N} (A_{d,n} - A_o)}{N\,(p^2 - A_o)} ,$$

where

B = percentage restriction in coolant channel flow area,
$A_{d,n}$ = outside area of deformed tube (mm^2),
A_o = outside area of original tube (mm^2),
p = tube-to-tube pitch in square array (mm),
N = number of tubes in square array.

With this definition, B is 0 for no deformation and 100% if all the tubes deform into a square whose sides are of length p (completely filling the open area). For the case of uniform ballooning such that the tubes just come into contact (i.e., 32% strain for the dimensions appropriate to this test), B is 61%.

In summing the deformed tube areas in the above equation for those nodes that contain bursts, one must decide how to treat the burst lips. As in the past, we used two treatments that appear to be reasonable upper and lower limits for the flow restriction. At the burst nodes, the upper-limit computation used the area enclosed by the fictitious tube outside perimeter (discussed earlier in this section) for $A_{d,n}$; the actual (measured) area was used for $A_{d,n}$ at the nonburst nodes. Tube areas obtained this way are tabulated as "OD Area" in the tables of Appendix C. For the lower limit, the software compared the area enclosed by the fictitious perimeter with that enclosed by a circular tube having the same (actual) perimeter of the burst tube and used the latter if smaller to describe the deformed tube area, $A_{d,n}$, at the burst nodes. Similarly, the software compared the actual (measured) area with that of a circular tube of the same perimeter and selected the smaller for $A_{d,n}$ at the nonburst nodes. This automatically selected the measured area, even for the severely distorted (nonburst) shapes, because the area enclosed by a circle is greater than that enclosed in any other closed region having the same perimeter as the circle. Results from processing the data in this manner are tabulated in Table 12. The right-hand column of the fourth page of the table is the sum of the 64 tube areas at any elevation.

The percentage flow area restriction was calculated at each axial node, using the above equation and appropriately defined values for the parameters, for the entire 8 × 8 array, the inner 6 × 6 array, and the central 4 × 4 array; the results are tabulated in Table 13. The cross-sectional area occupied by the grids (~200 mm^2) was not included in the calculation; including this area slightly increases the restriction at the grid nodes. The values listed under "maximum" correspond to the upper-limit computation discussed above and are based on outside tube areas given in Appendix C; those listed under "minimum" correspond to the lower-limit computation and are based on the data in Table 12. Because the measured tube areas were used for nonburst nodes in both calculations, the two values differ only at those nodes where tube bursts occurred. Even at these nodes, the differences are small because the burst openings were constrained by neighboring rods and the two definitions for $A_{d,n}$ gave results that were not greatly different.

The minimum flow area restriction data of Table 13 were depicted graphically in Fig. 13. It is noted that lower limit of coolant channel flow area restriction, as defined above, was also used by Powers and Meyer in NUREG-0630 (Ref. 22).

Restraint conditions of a full-size fuel bundle were simulated in the B-5 test by surrounding the 8 × 8 test array with a closely spaced shroud that limited outward movement of the simulators. The pretest spacing (1.75 mm) was such that contact would be made when the exterior simulators deformed 32%, provided the simulators were neither displaced nor bowed outward. Posttest examination showed that contact forces during deformation and/or thermal bowing caused permanent displacement of the simulators.

Simulator displacements were estimated at each axial node by a least-squares fitting routine that simultaneously minimized all the displacements. The manner in which this was accomplished can be visualized by imagining placement of a rigid grid (with pretest tube centroids at the center of each grid cell) on the section photograph and then translating and rotating the grid on the plane of the photograph until the average displacement between the pretest and posttest centroids of the 64 tubes is minimized. Using the centroids of the areas enclosed by tube outside perimeter from the geometric data source file (Appendix C) and the pretest tube pitch, the data were processed to provide the displacements in both tabular and graphical form. An example of the tabular output (for the section displayed in Fig. 124) is presented in Table 14; tables for all the sections are given in Appendix E. Although the computations were performed with reference to the arbitrary coordinate system that was established relative to the north side of the epoxy matrix when the section photographs were digitized, the results were translated to a new coordinate system that has its origin at the pretest centroid of simulator 1 (see Fig. 3). This facilitates interpretation and use of the displacement data. As evident from the pretest centroid coordinates in Table 14, the coordinate system used for digitizing the data was not perfectly aligned with the epoxy matrix; instead, it was rotated slightly clockwise.

As an example, the graphical output for the section displayed in Fig. 124 is shown, referenced to the digitizing coordinate system, in Fig. 130 to illustrate tube displacements relative to an imaginary grid that defines the pretest unit cells at this elevation. Similar plots are presented in Appendix F for all the axial nodes. In the figure, dots are used to denote the tube pretest centroids at the midpoints of the unit cells and crosses to denote the posttest centroids of the tube out-lines. The latter correspond to the shapes of the areas enclosed by the tube outside perimeters. Straight line segments, representing fictitious perimeters, are drawn in the burst regions of those tubes that have bursts at this elevation (see Fig. 73). The outside of the imaginary grid corresponds to the pretest dimensions and the position of the shroud.

The figure shows the permanent displacements of the tubes within the original unit cells and aids visualization of subchannel flow area restriction.

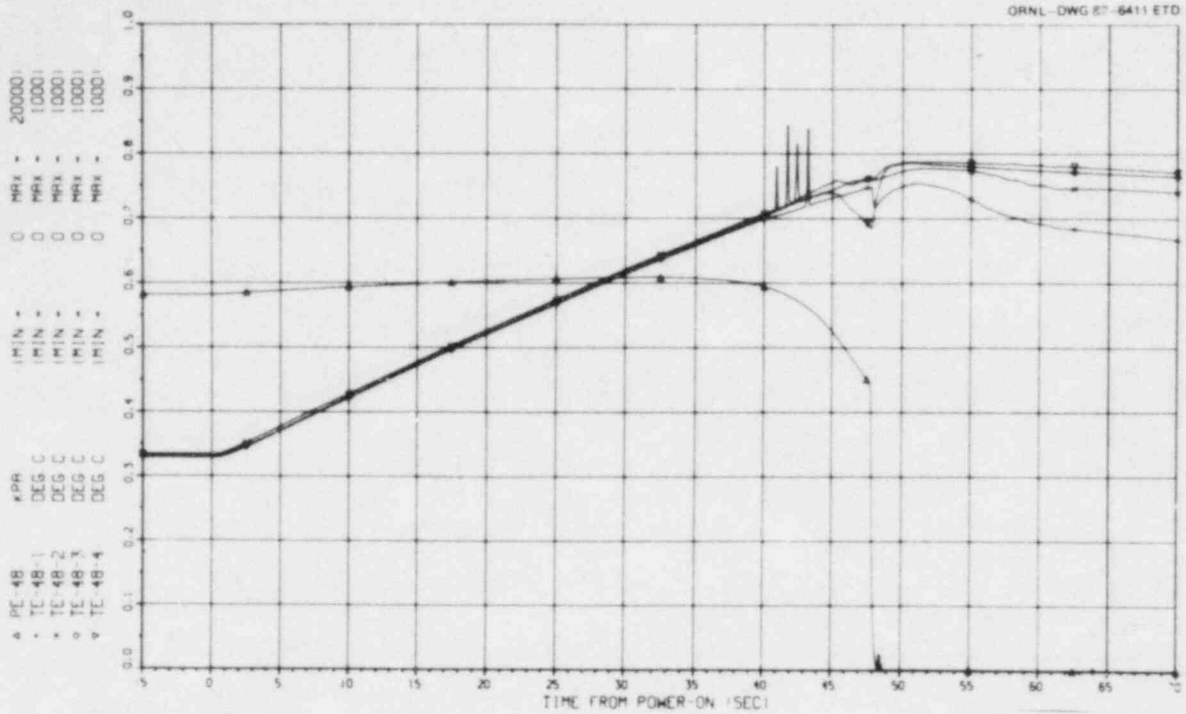

Fig. 18. Typical temperature (and pressure) data plot showing noise spikes caused by thermocouple reference box.

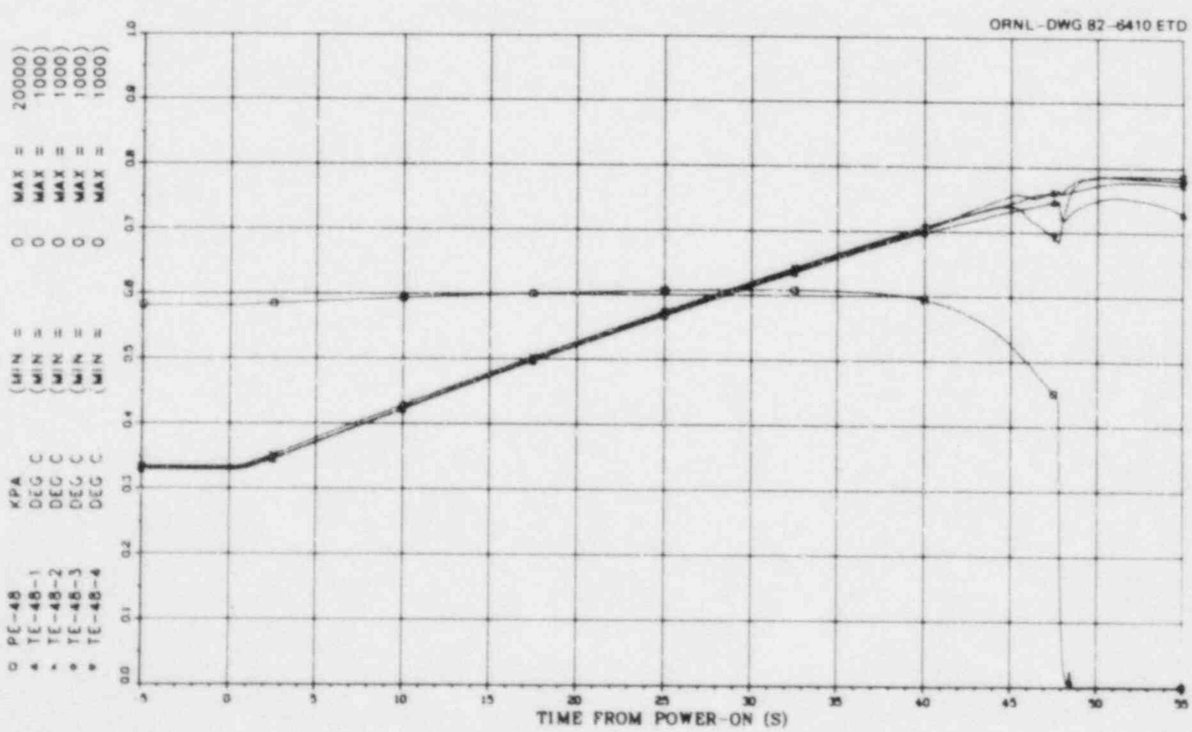

Fig. 19. Temperature (and pressure) data plot from previous figure after thermocouple noise spikes were removed.

ORNL–DWG 80–6338 ETD

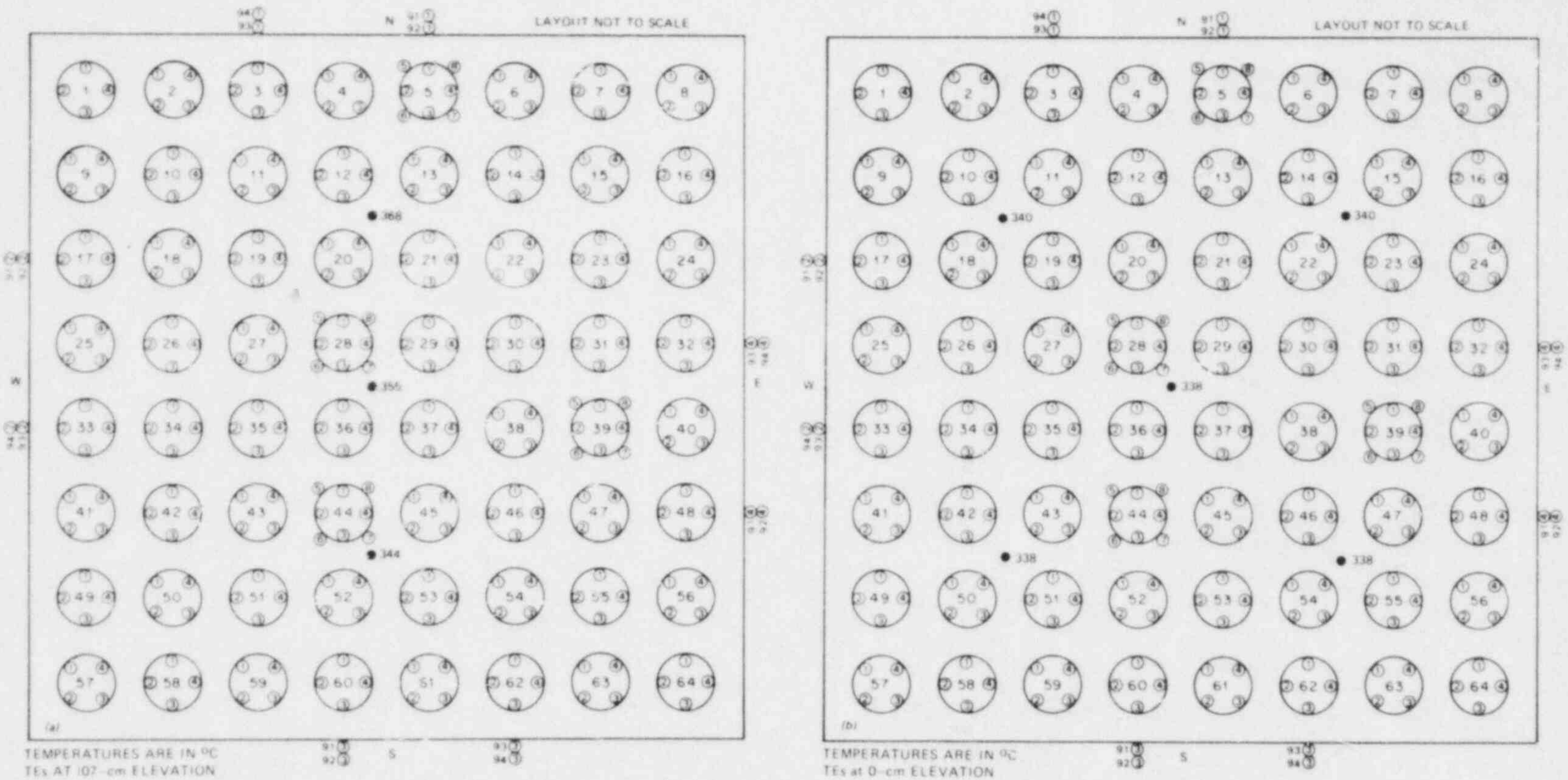

Fig. 20. Steam (*a*) inlet and (*b*) outlet temperatures measured 0.5 s before power-on.

ORNL–DWG 80–6339 ETD

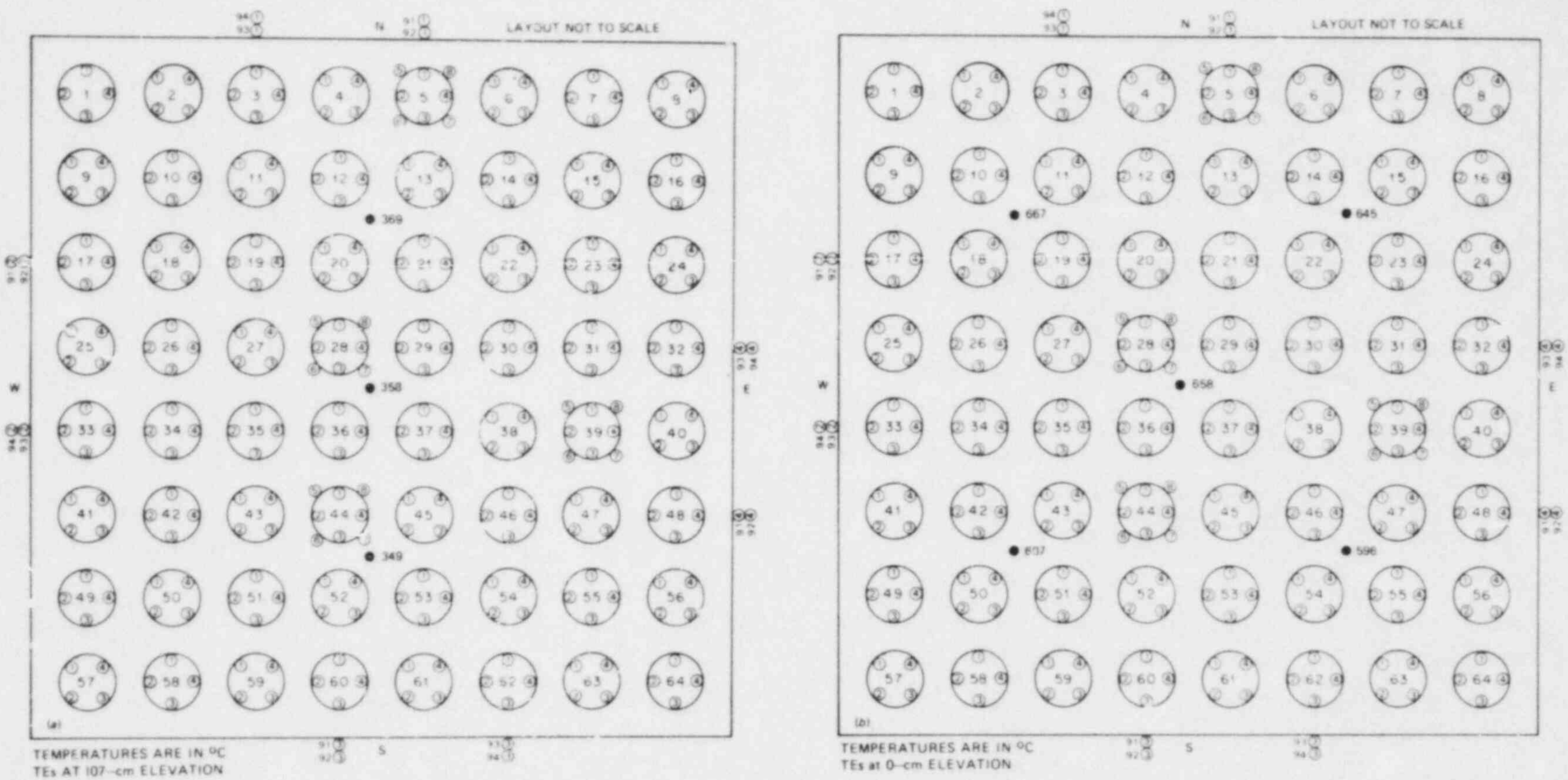

Fig. 21. Steam (*a*) inlet and (*b*) outlet temperatures measured 1.0 s before the first tube burst.

ORNL-DWG 80-6340 ETD

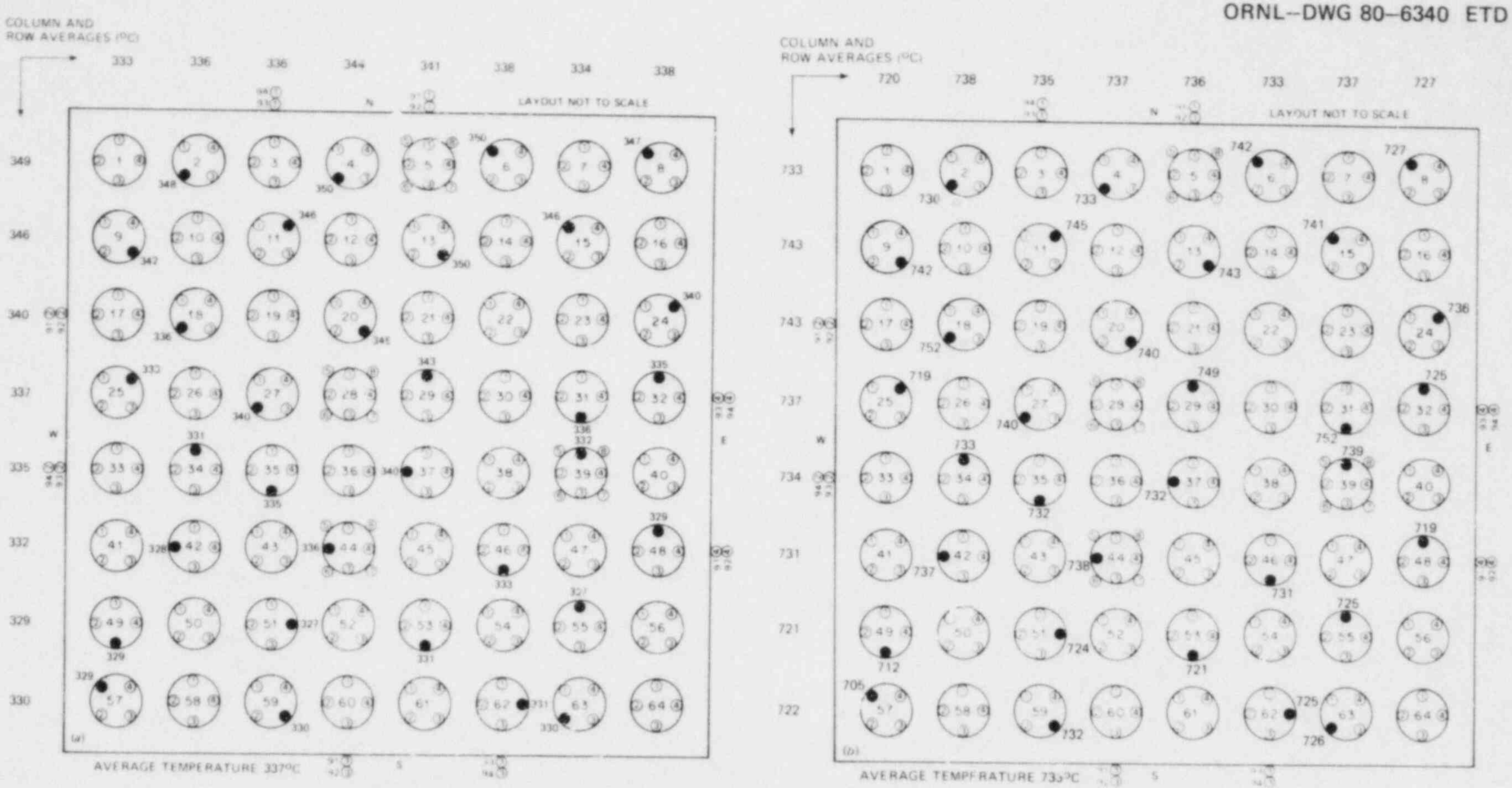

Fig. 22. Cladding temperatures measured at 84-cm elevation (*a*) 0.5 s before power-on and (*b*) 1.0 s before first tube burst.

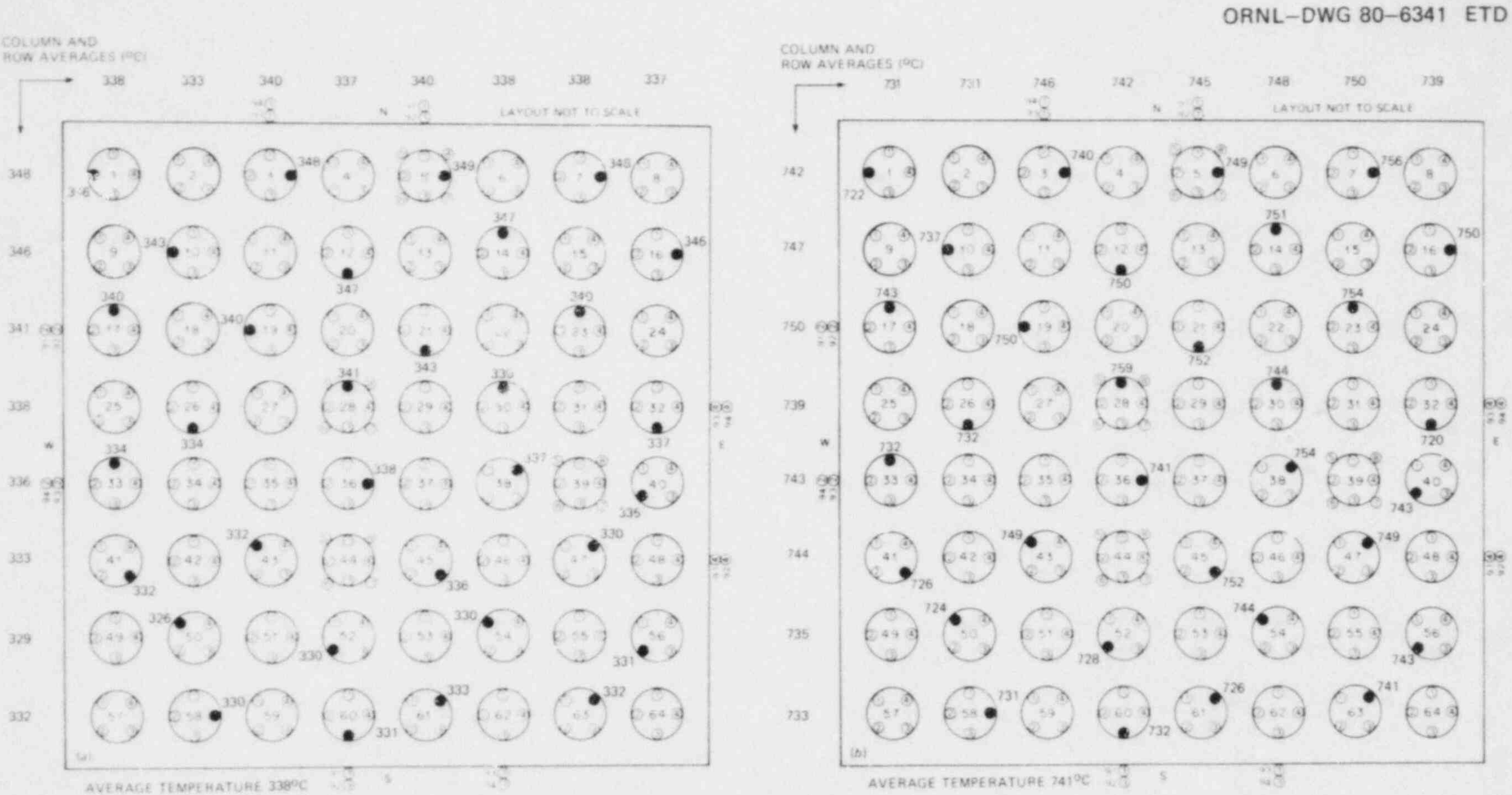

Fig. 23. Cladding temperatures measured at 76-cm elevation (*a*) 0.5 s before power-on and (*b*) 1.0 s before first tube burst.

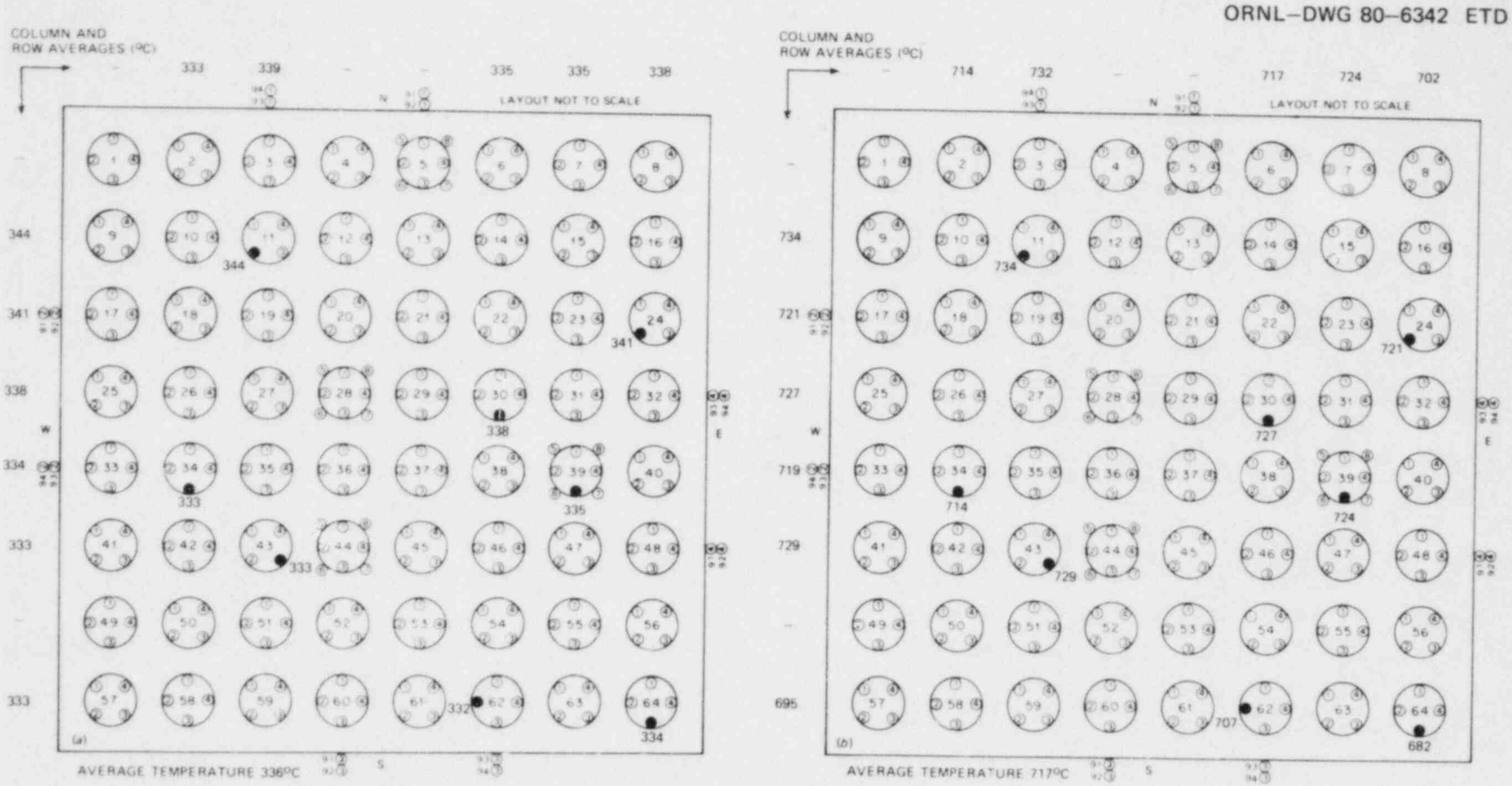

Fig. 24. Cladding temperatures measured at 66-cm (upper grid) elevation (*a*) 0.5 s before power-on and (*b*) 1.0 s before first tube burst.

ORNL-DWG 80-6343 ETD

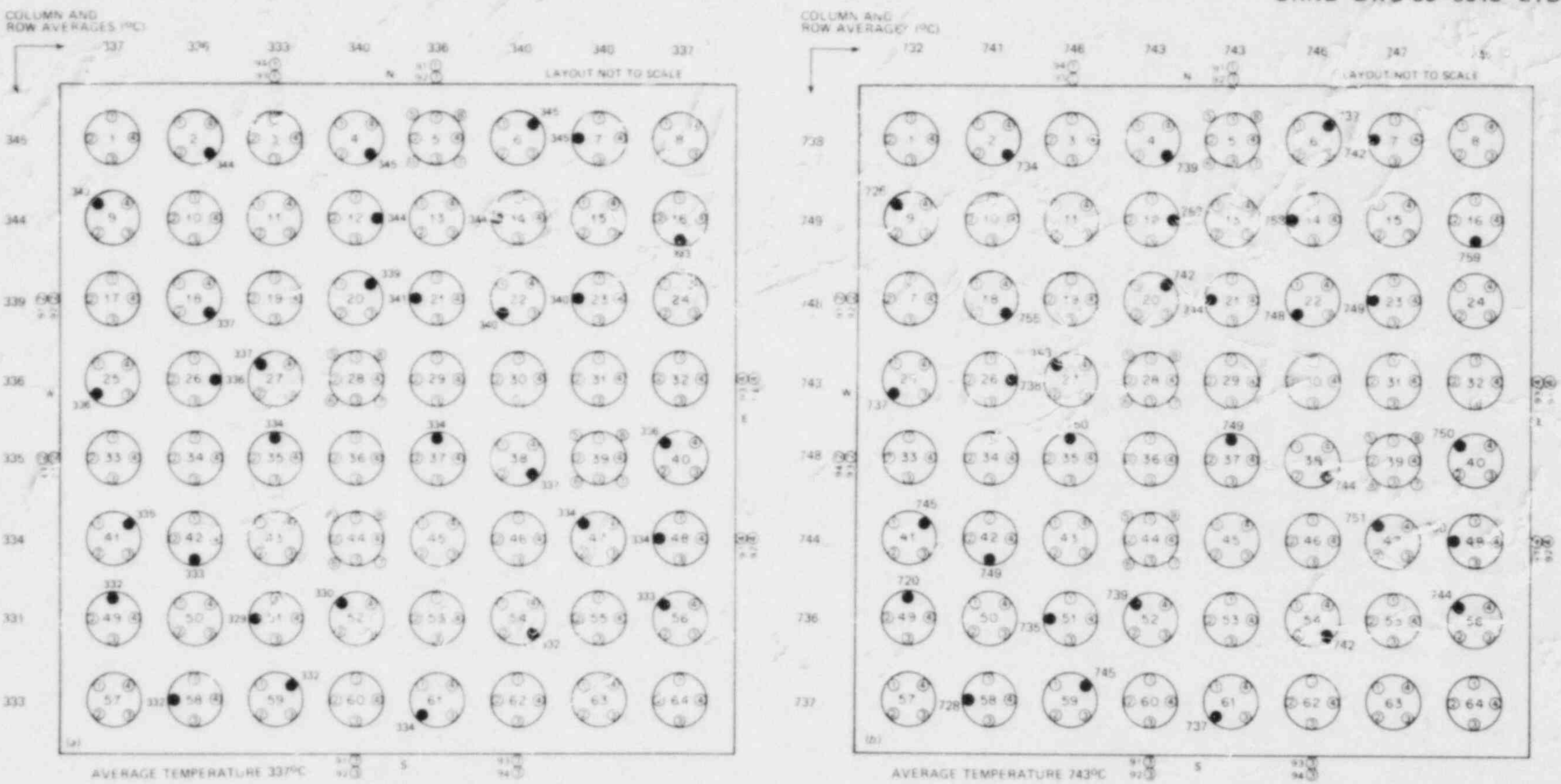

Fig. 25. Cladding temperatures measured at 56-cm elevation (*a*) 0.5 s before power-on and (*b*) 1.0 s before first tube burst.

ORNL–DWG 80–6344 ETD

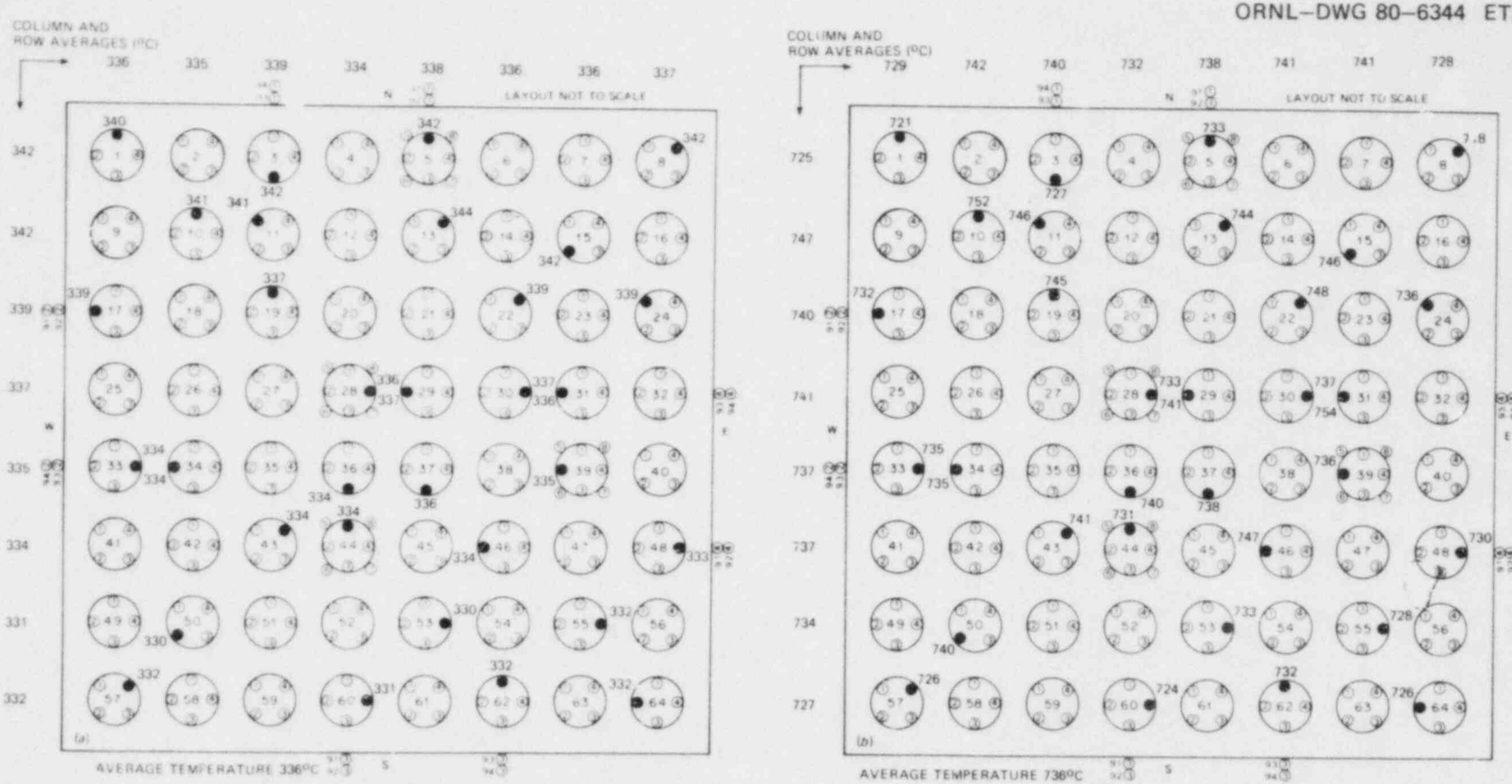

Fig. 26. Cladding temperatures measured at 48-cm elevation (*a*) 0.5 s before power-on and (*b*) 1.0 s before first tube burst.

ORNL–DWG 80–6345 ETD

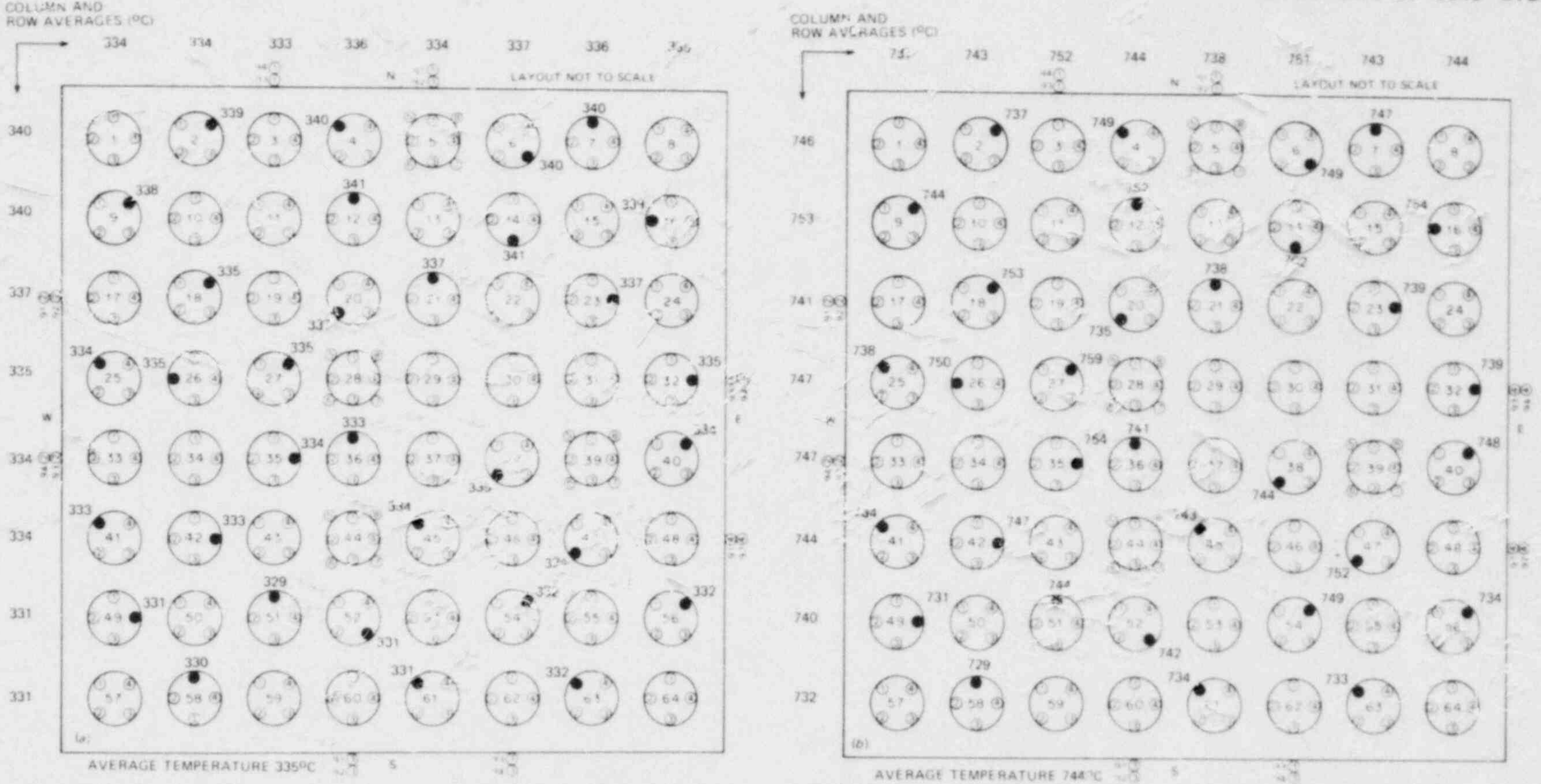

Fig. 27. Cladding temperatures measured at 38-cm elevation (*a*) 0.5 s before power-on and (*b*) 1.0 s before first tube burst.

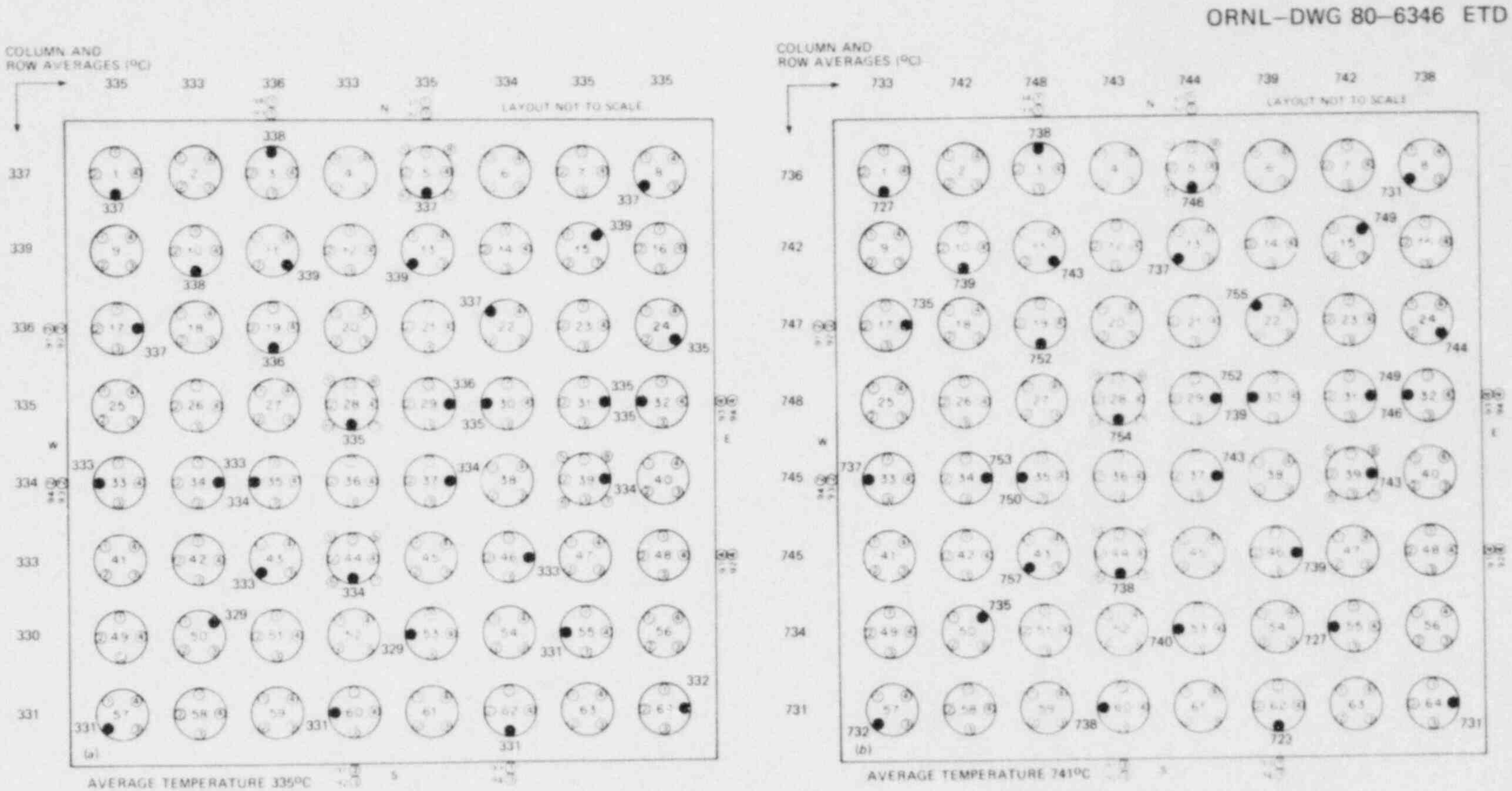

Fig. 28. Cladding temperatures measured at 28-cm elevation (*a*) 0.5 s before power-on and (*b*) 1.0 s before first tube burst.

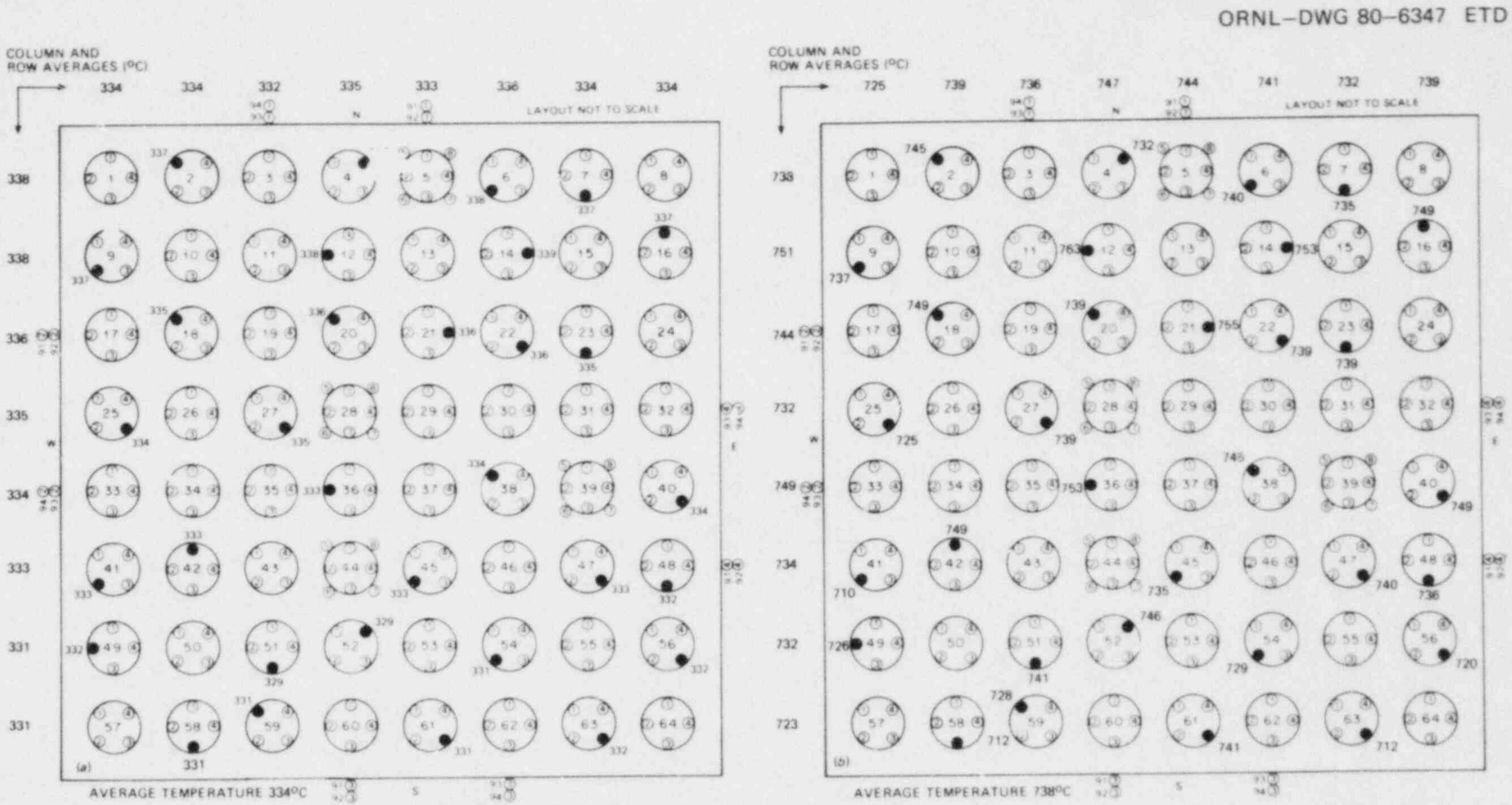

Fig. 29. Cladding temperatures measured at 20-cm elevation (*a*) 0.5 s before power-on and (*b*) 1.0 s before first tube burst.

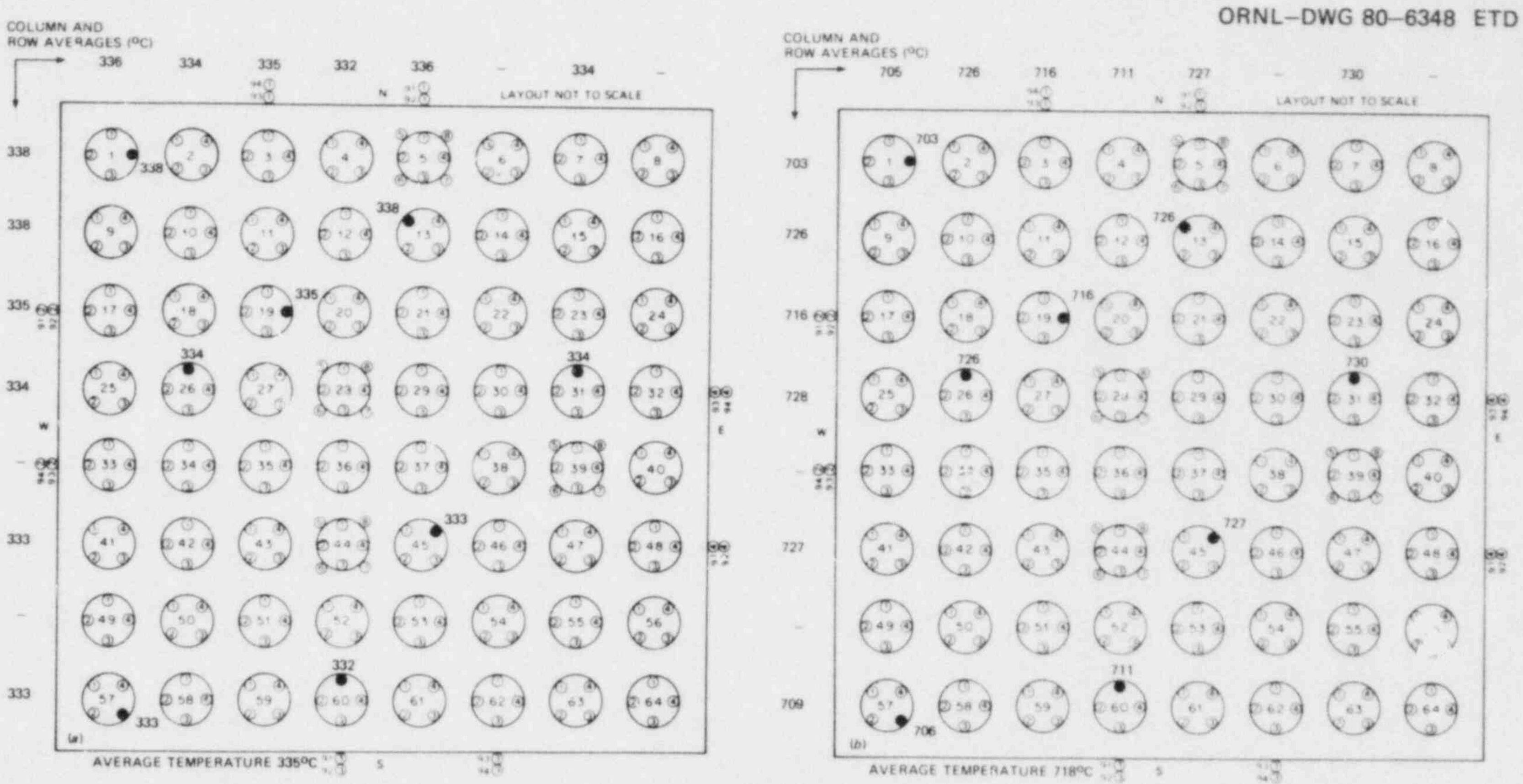

Fig. 30. Cladding temperatures measured at 10-cm (lower grid) elevation (*a*) 0.5 s before power-on and (*b*) 1.0 s before first tube burst.

ORNL–DWG 80–6349 ETD

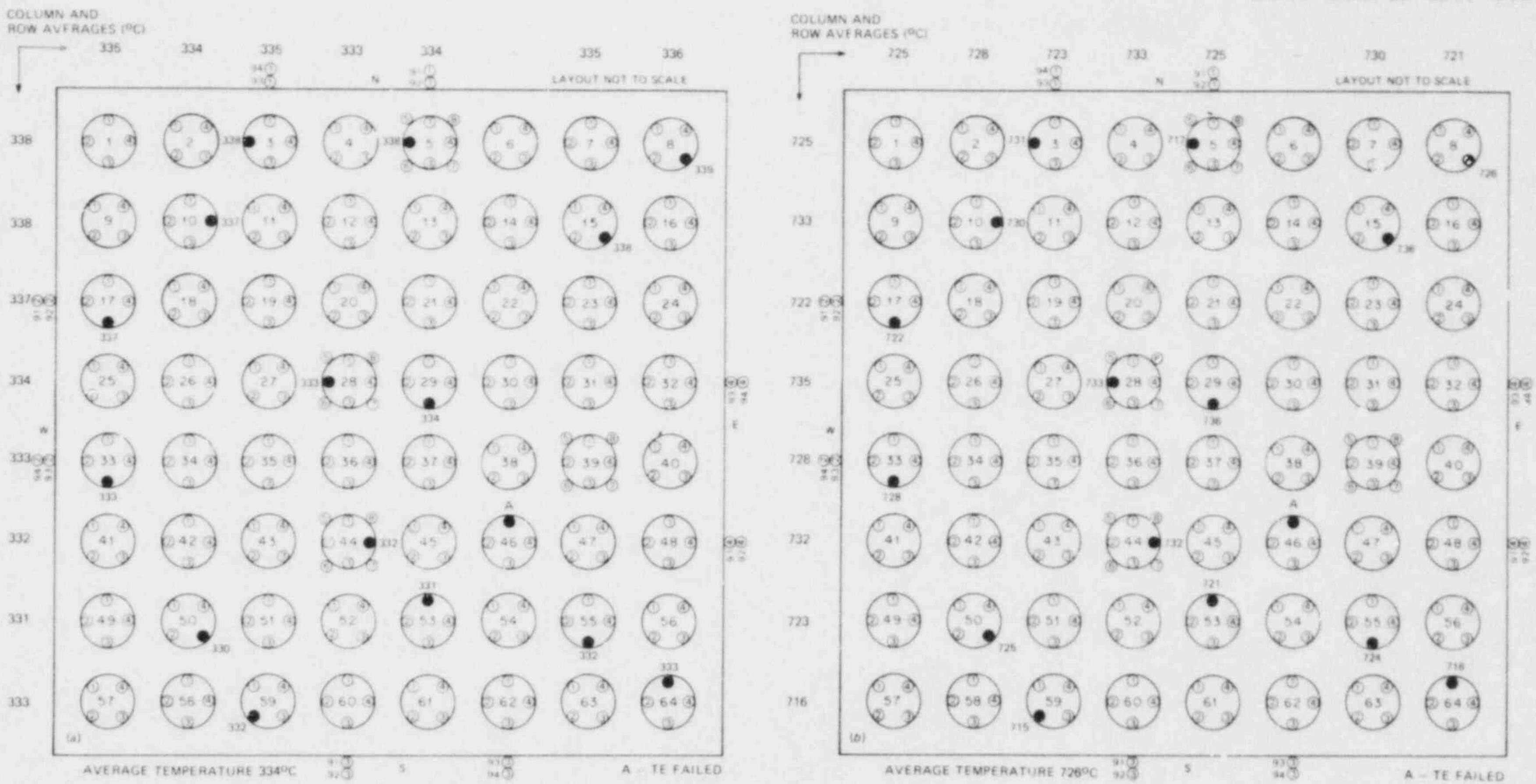

Fig. 31. Cladding temperatures measured at 5-cm elevation (*a*) 0.5 s before power-on and (*b*) 1.0 s before first tube burst.

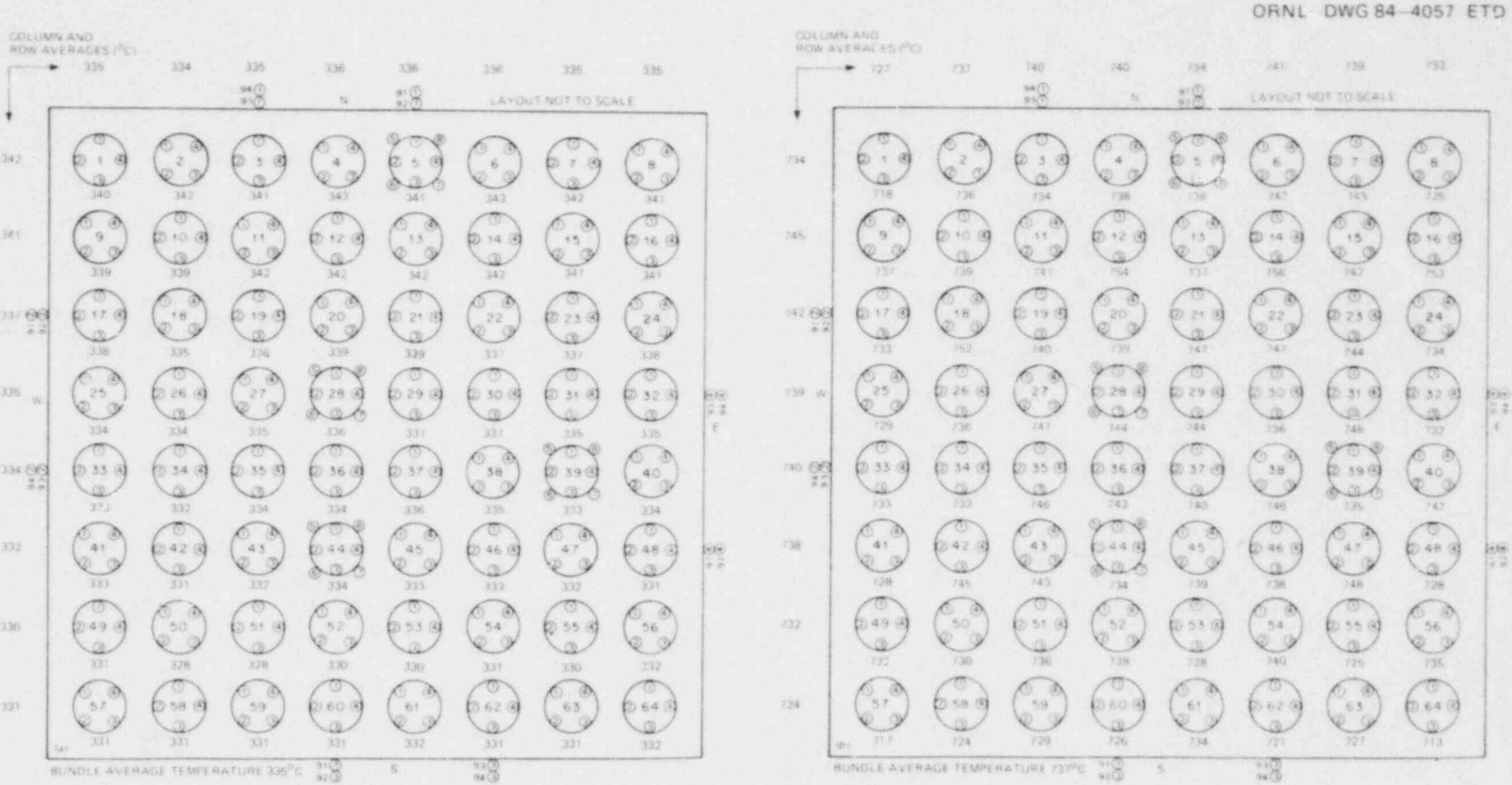

Fig. 32. Simulator-averaged cladding temperature measurements (*a*) 0.5 s before power-on and (*b*) 1.0 s before first tube burst.

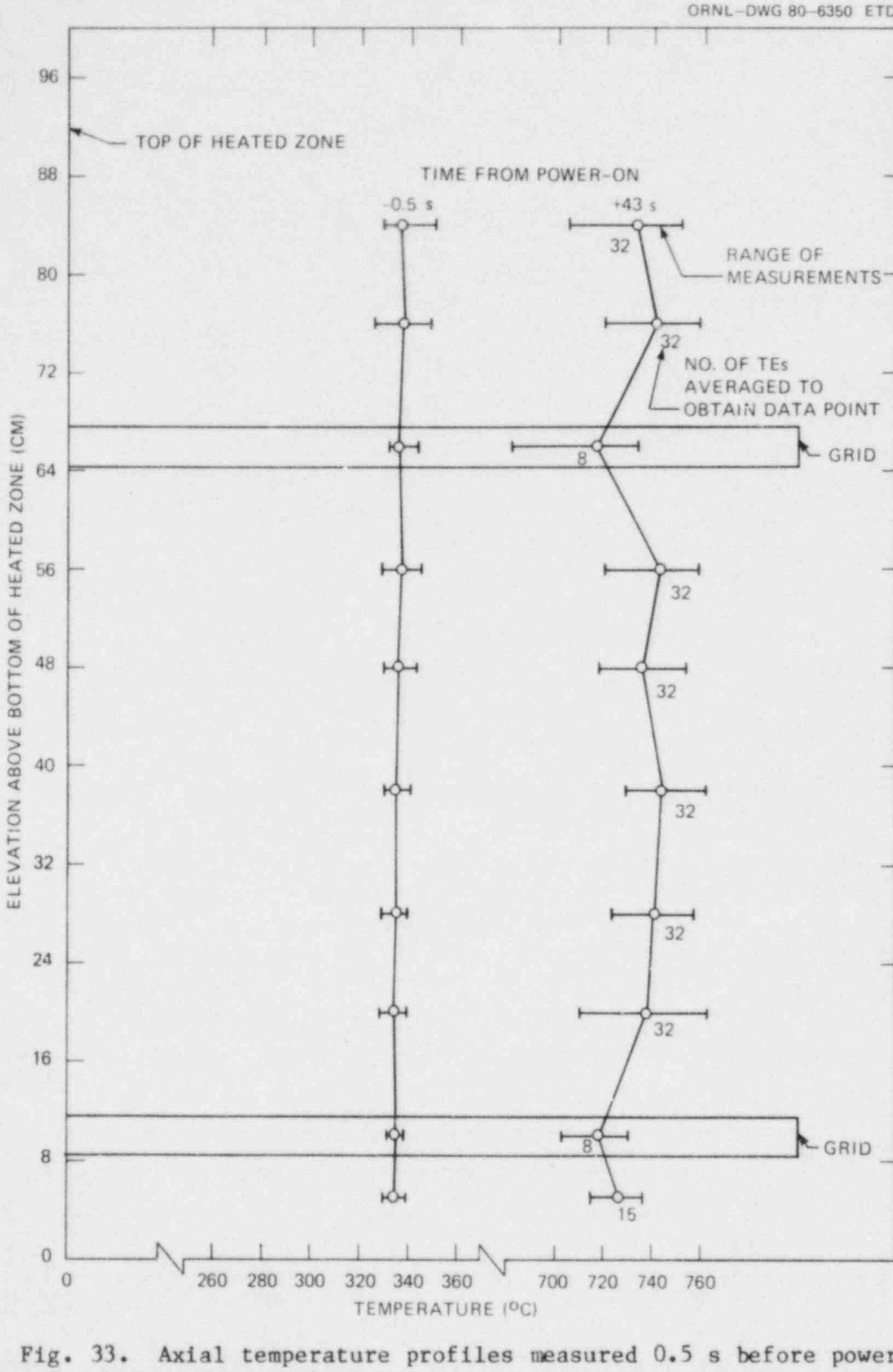

Fig. 33. Axial temperature profiles measured 0.5 s before power-on and 1.0 s before first tube burst.

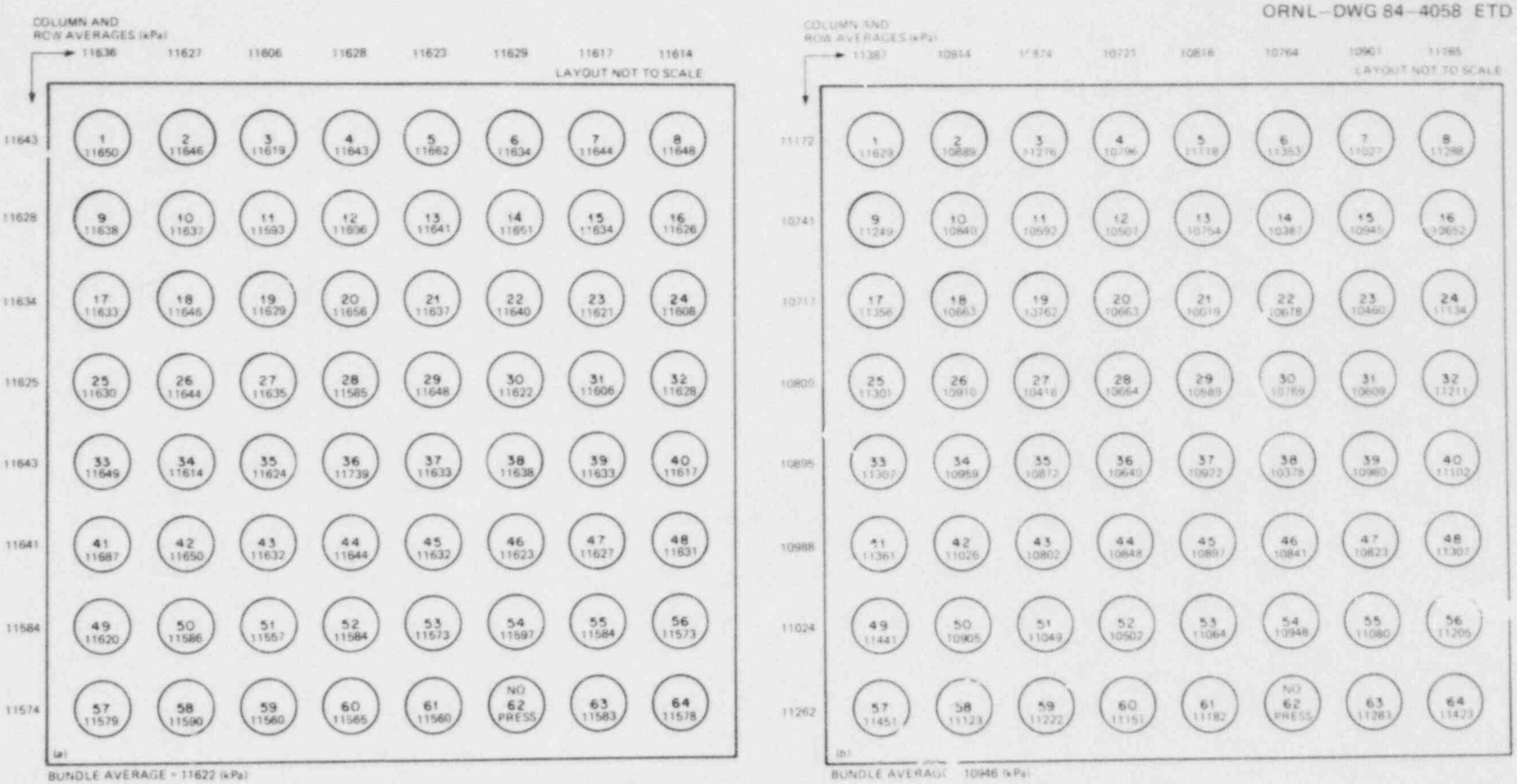

Fig. 34. Differential pressures measured (*a*) 0.5 s before power-on and (*b*) 1.0 s before first tube burst.

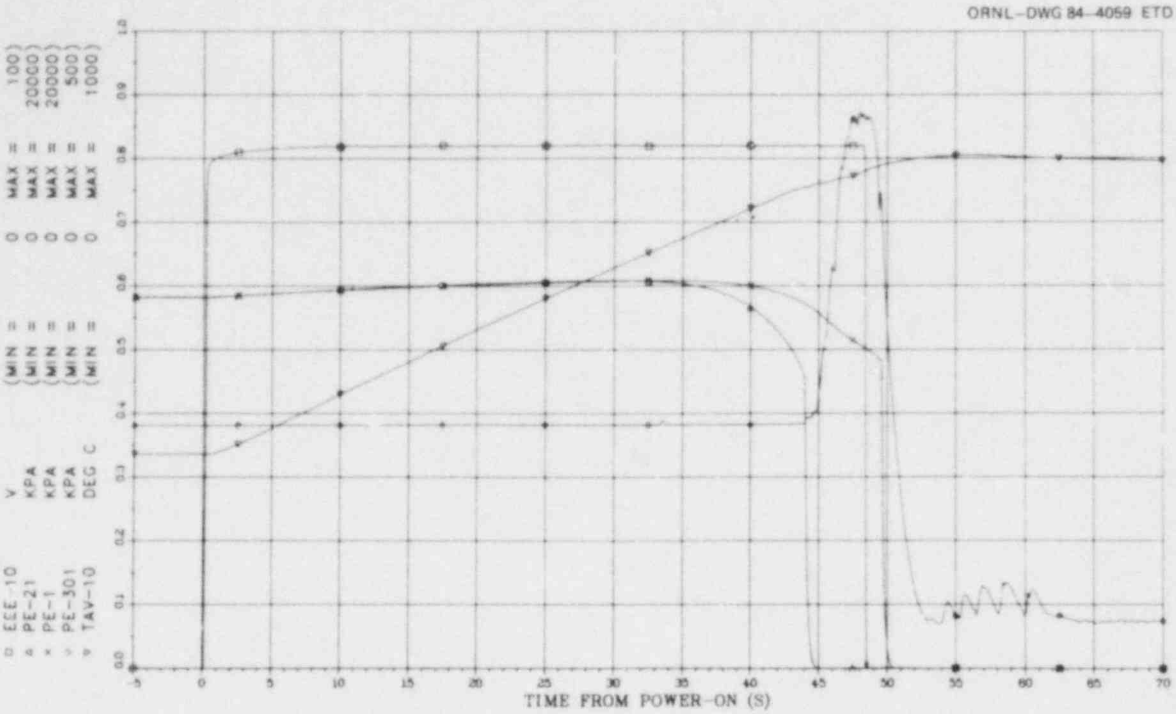

Fig. 35. Typical temperature and pressure behavior during test.

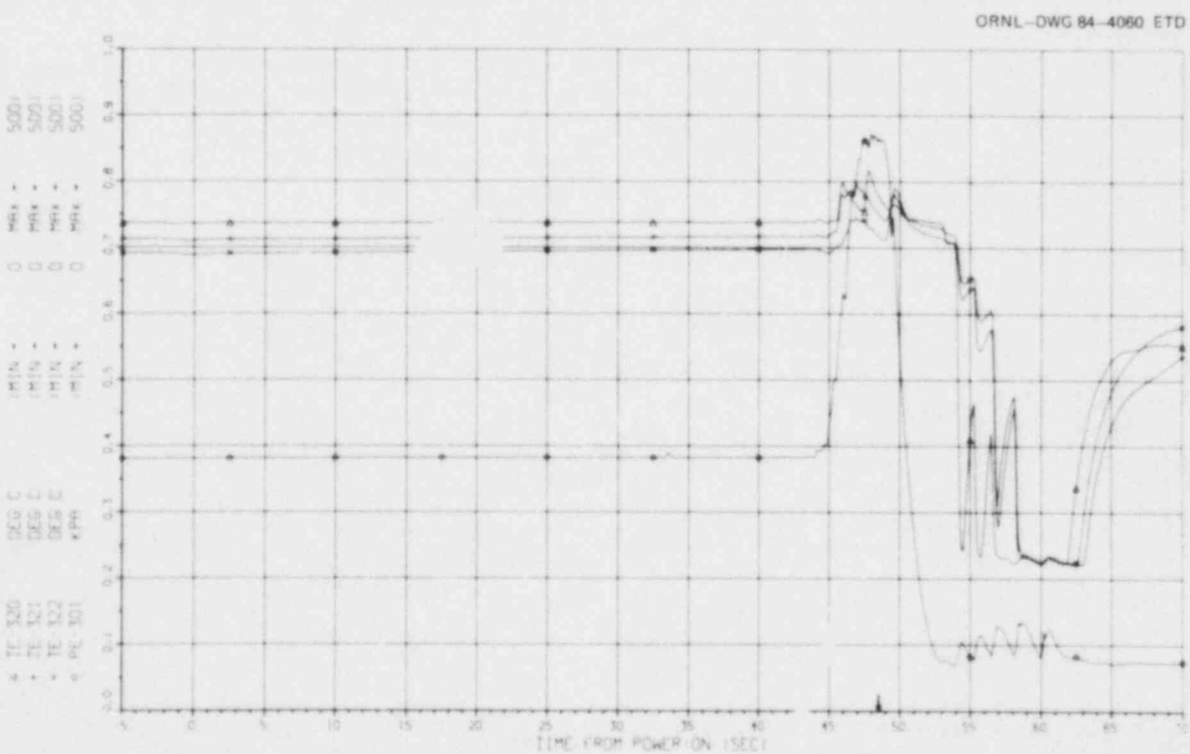

Fig. 36. Steam inlet temperature and vessel pressure during test.

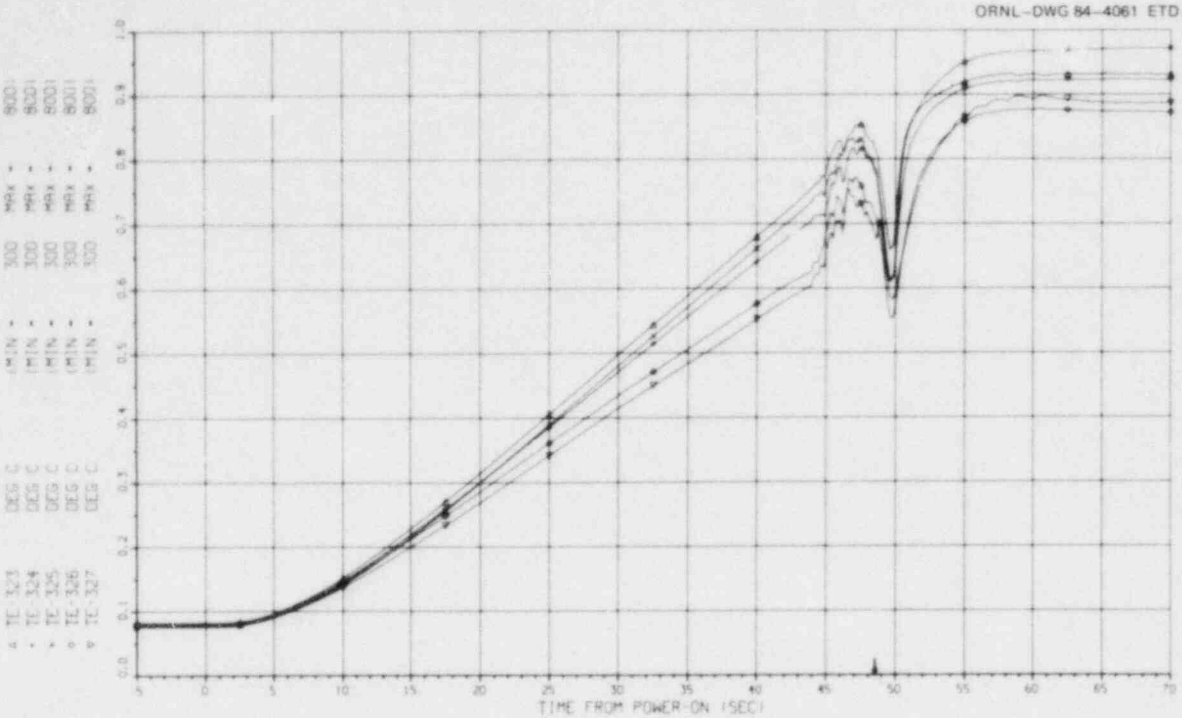

Fig. 37. Steam outlet temperature measured during test.

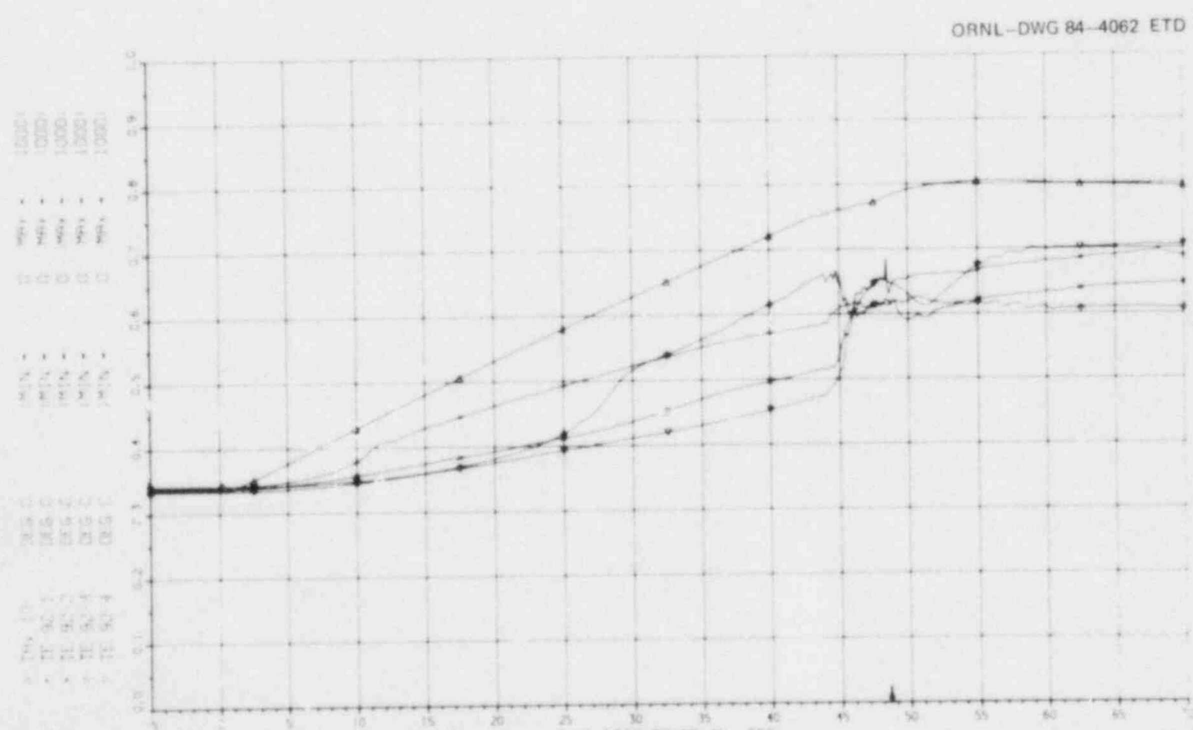

Fig. 38. Shroud temperature measurements at the 48-cm elevation.

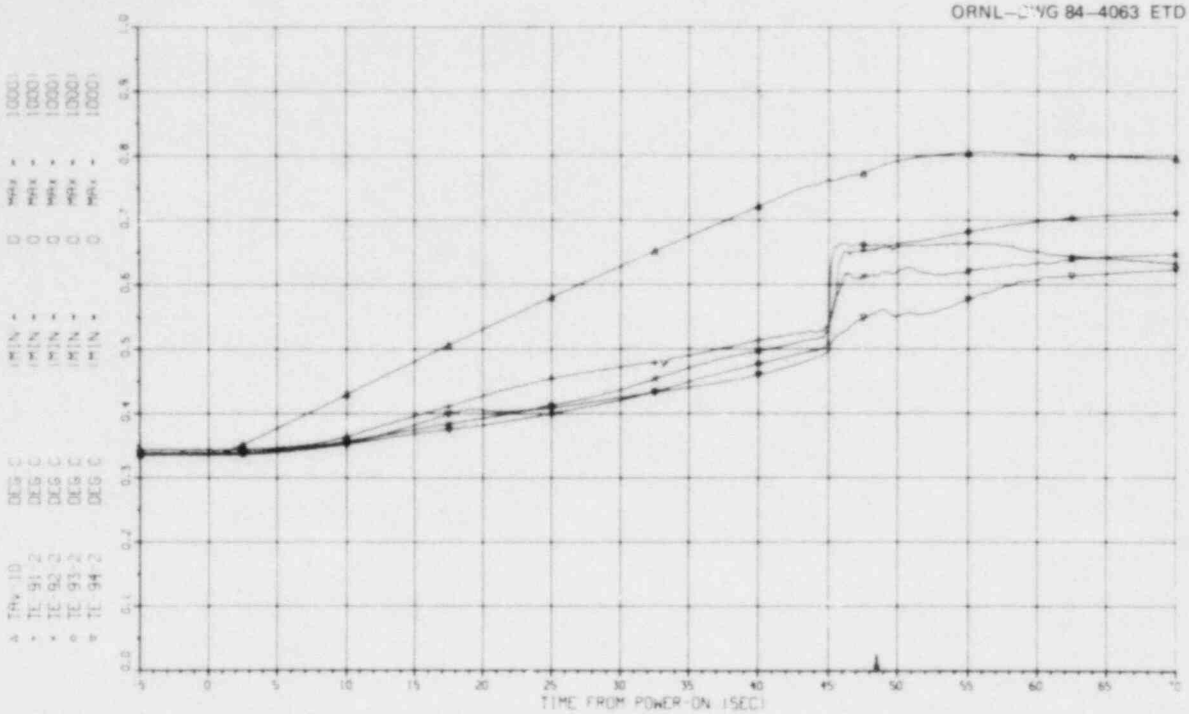

Fig. 39. Shroud temperature measurements on west side of bundle.

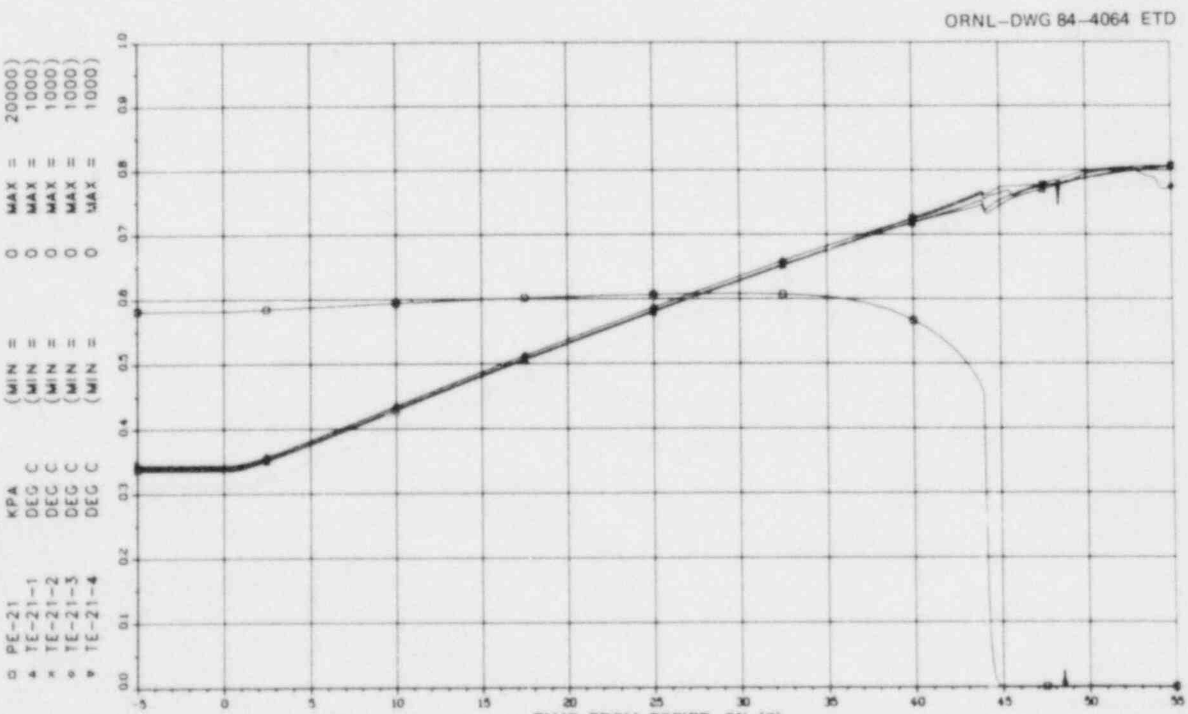

Fig. 40. Typical cladding pressure and temperat ıre behavior for an interior simulator.

ORNL-DWG 84-4065 ETD

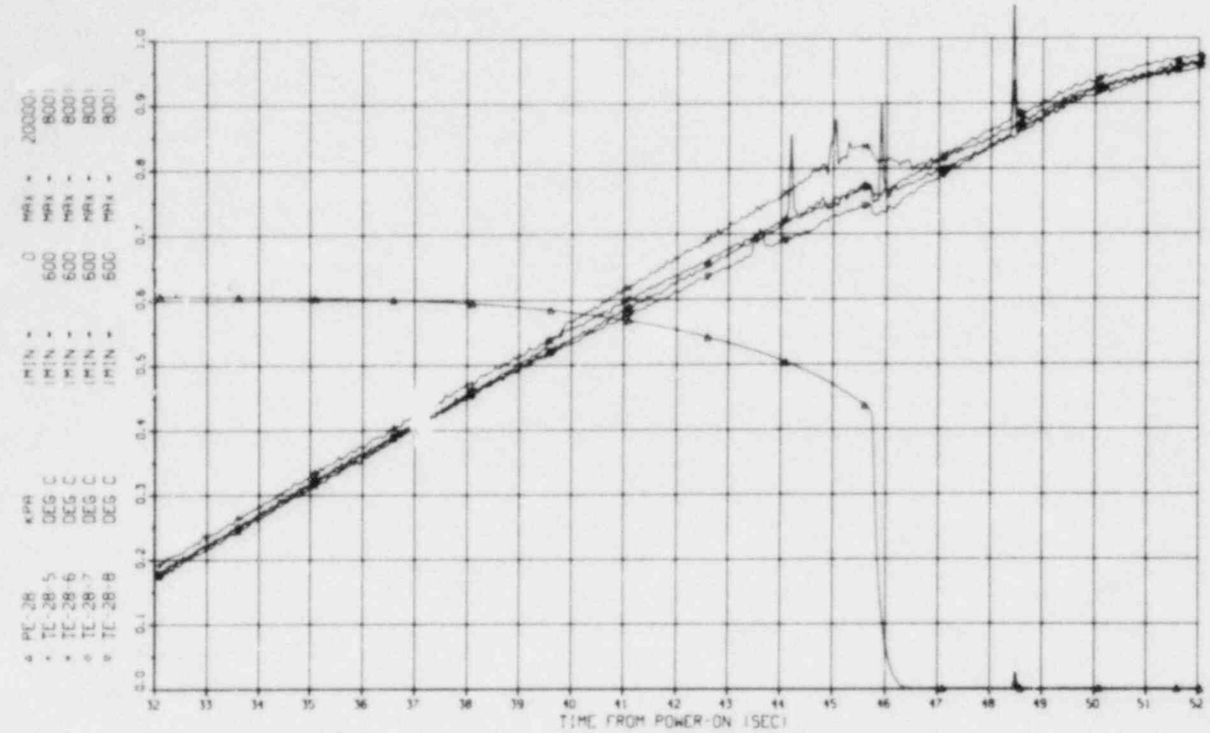

Fig. 41. Pressure and typical cladding temperature behavior at four azimuthal positions.

ORNL-DWG 84-4066 ETD

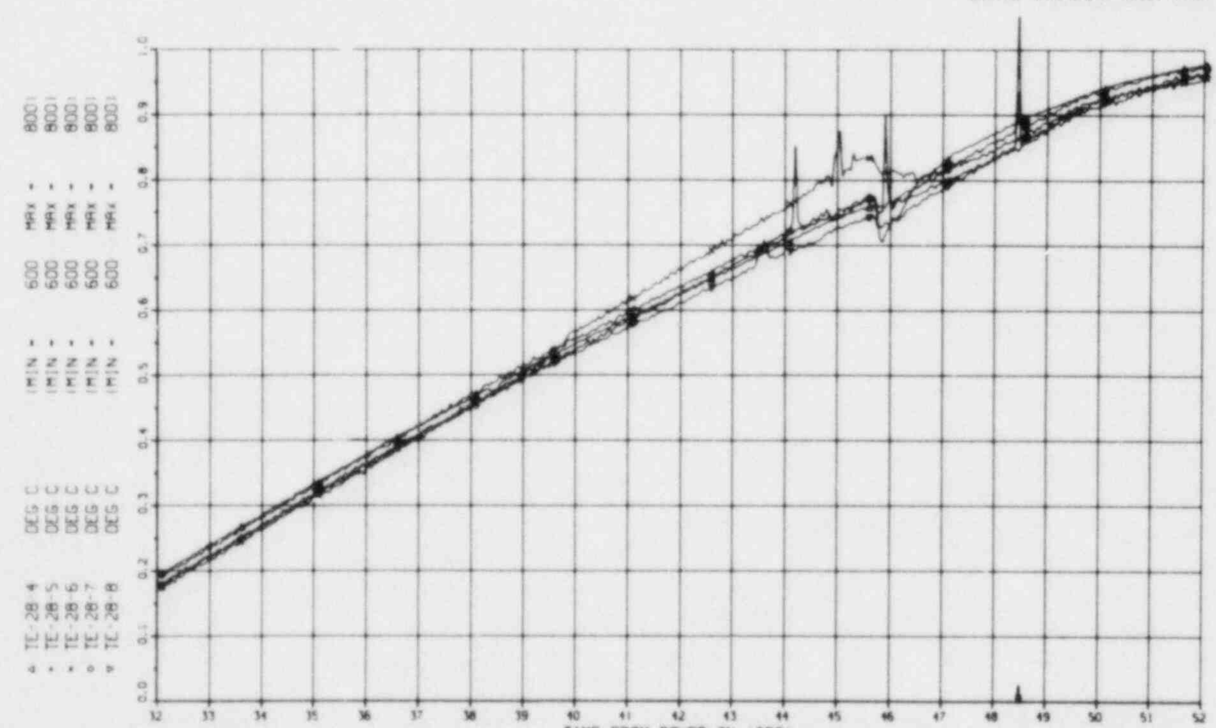

Fig. 42. Comparison of cladding internal temperature with external temperatures measured at four azimuthal positions.

ORNL–PHOTO 6499-80A

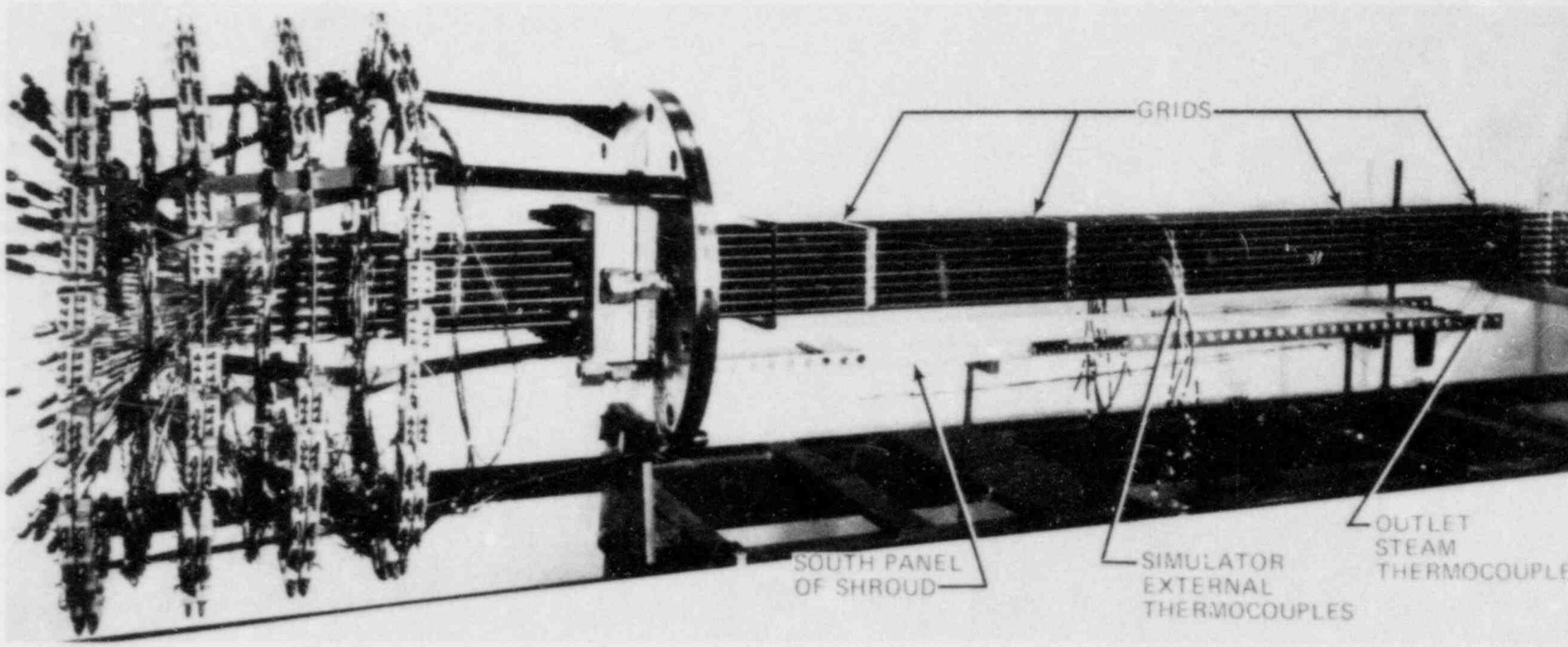

Fig. 43. Partially assembled B-5 test array.

ORNL–PHOTO 6459–80A

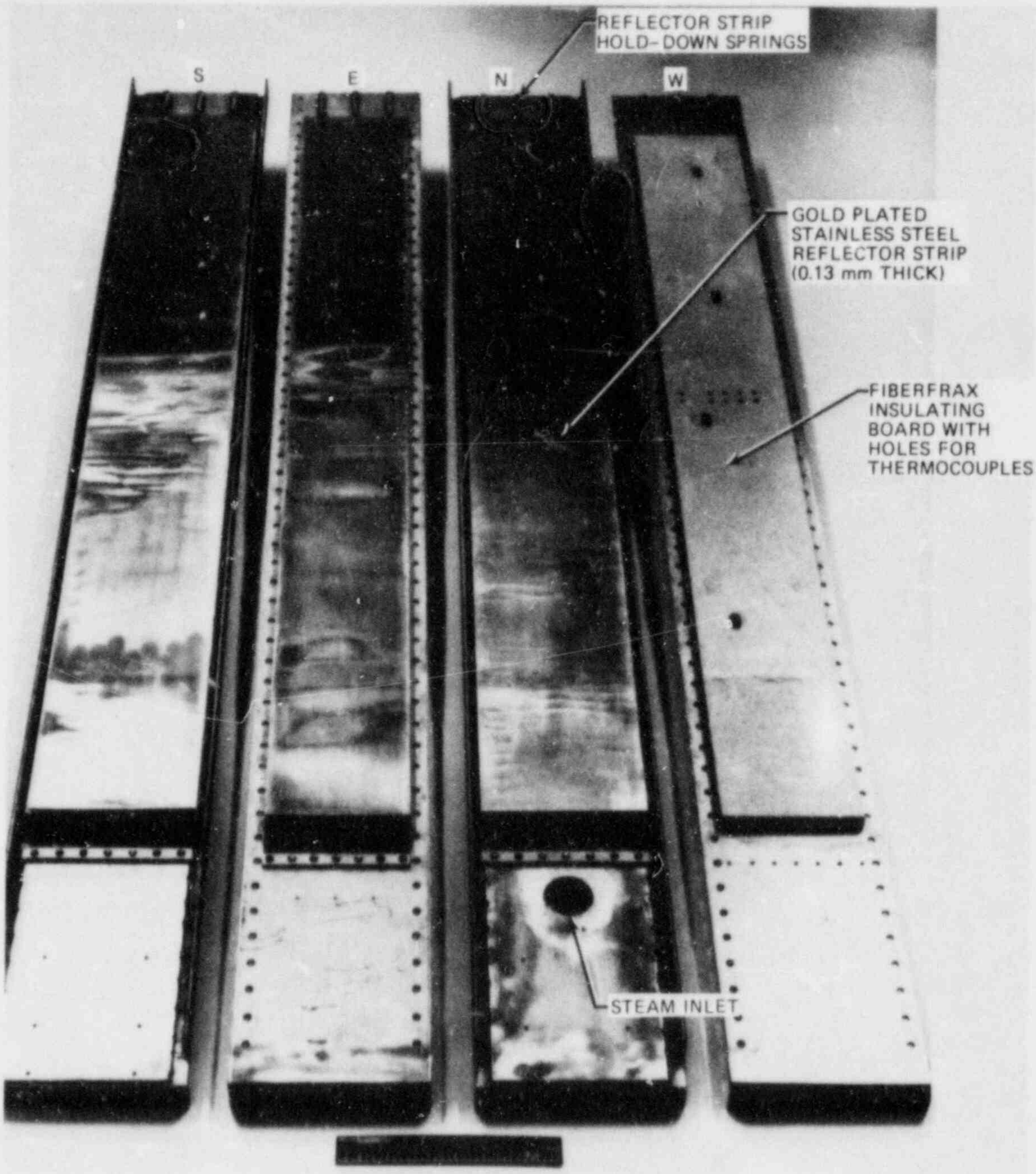

Fig. 44. Shroud panels with reflector strip removed from west panel to show insulating material.

ORNL–PHOTO 6523–80A

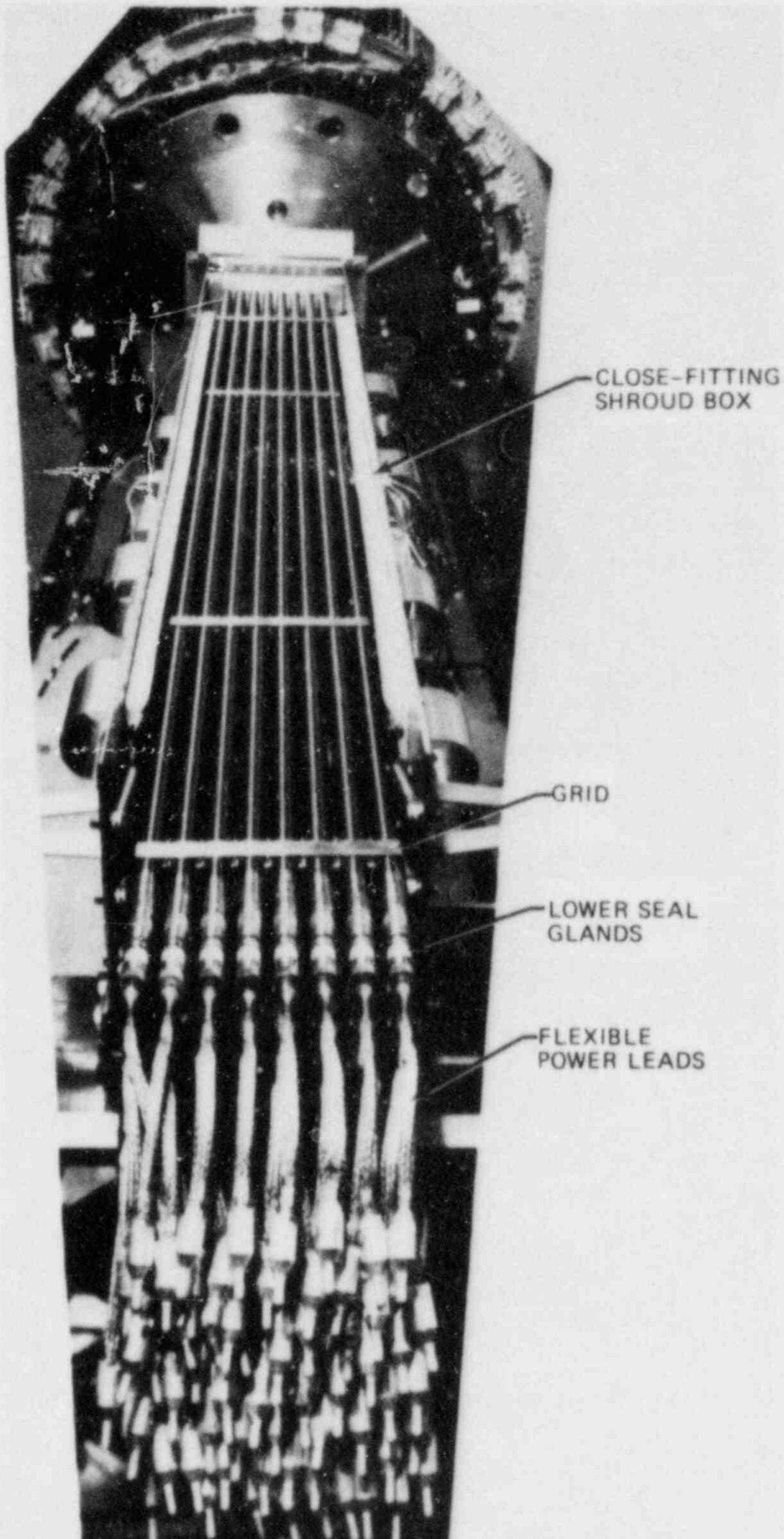

Fig. 45. Bundle before installation of north panel of shroud box.

ORNL–PHOTO 6589–80A

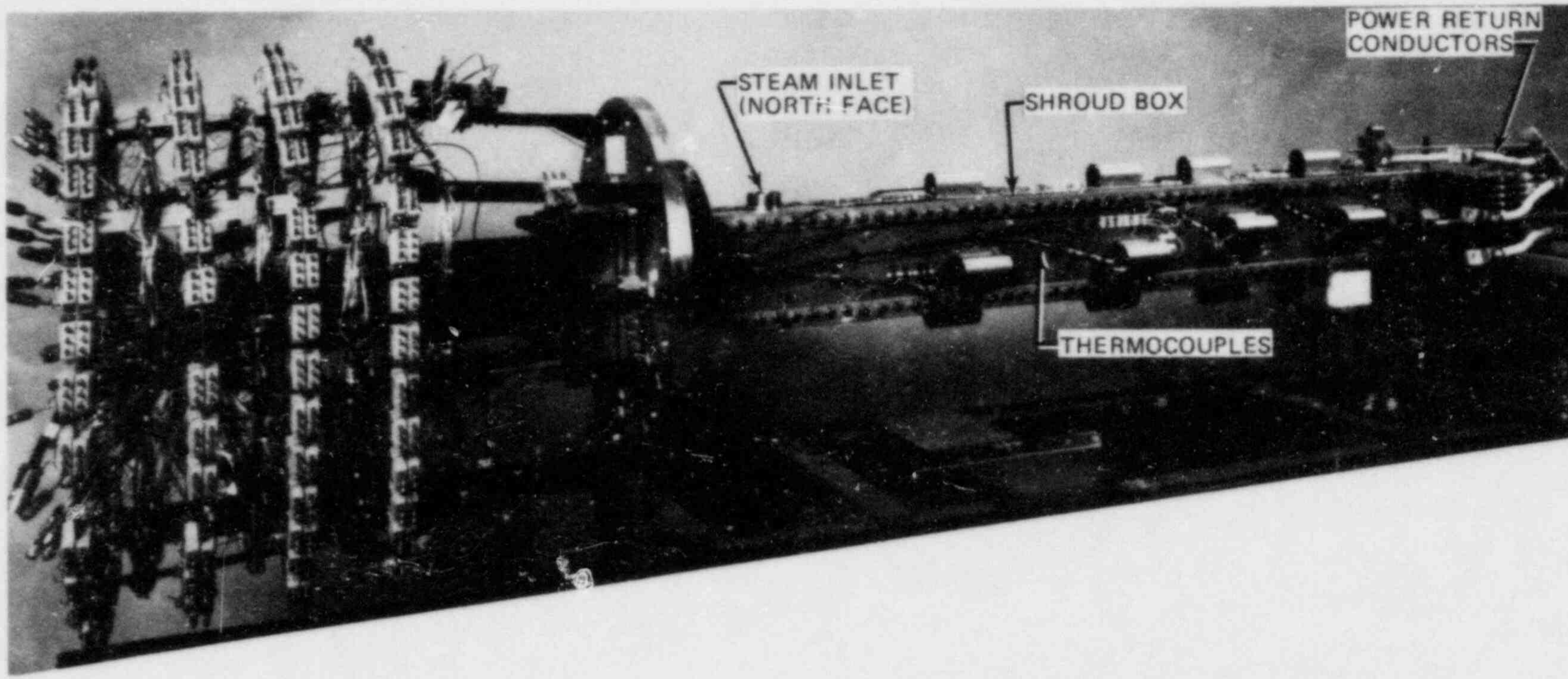

Fig. 46. Completely assembled B-5 test array.

ORNL–PHOTO 9496–80B

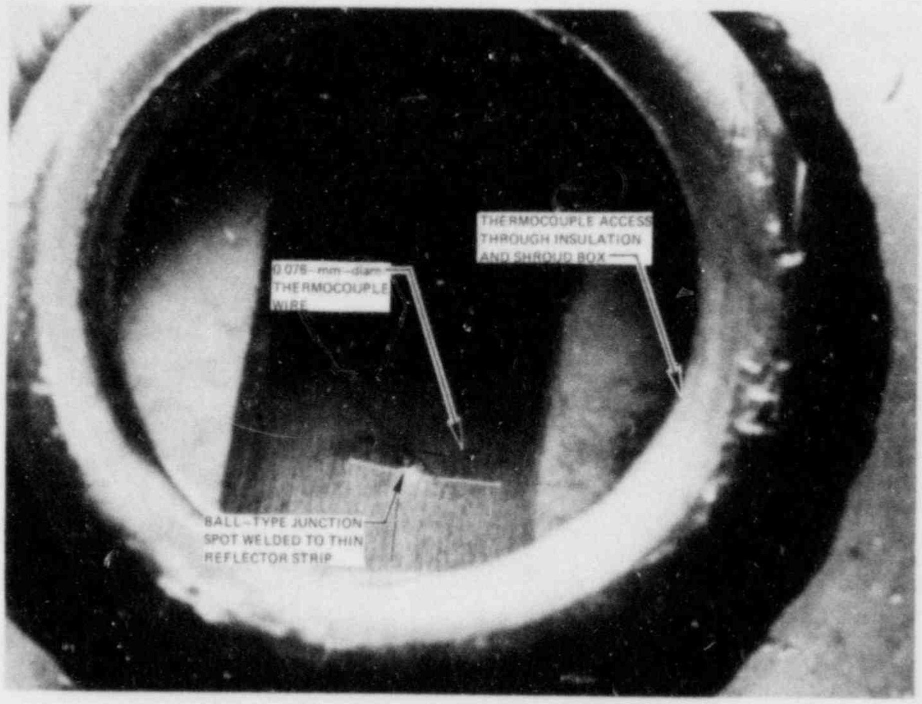

Fig. 47. Typical shroud thermocouple attachment.

ORNL–PHOTO 6570–80A

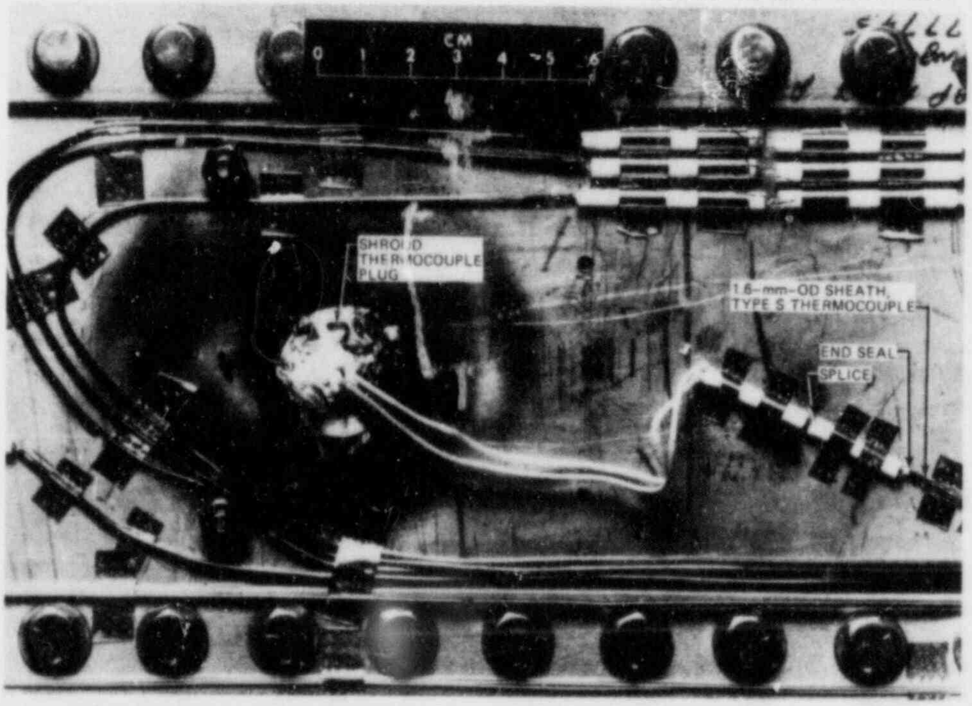

Fig. 48. Typical shroud thermocouple installation.

ORNL–PHOTO 6363–80R

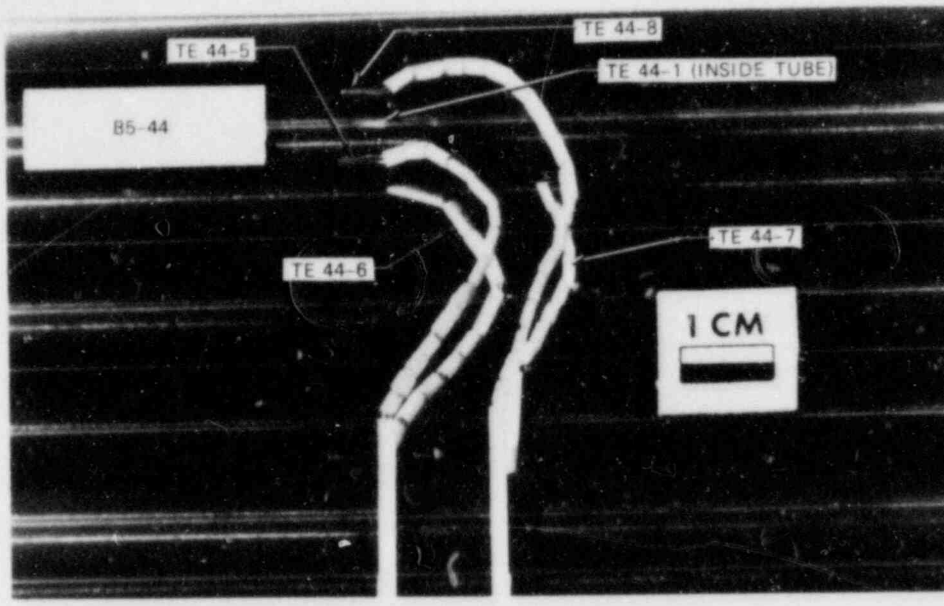

Fig. 49. Typical installation of thermocouples for measuring azimuthal temperature gradients.

ORNL–DWG 80–6366 ETD

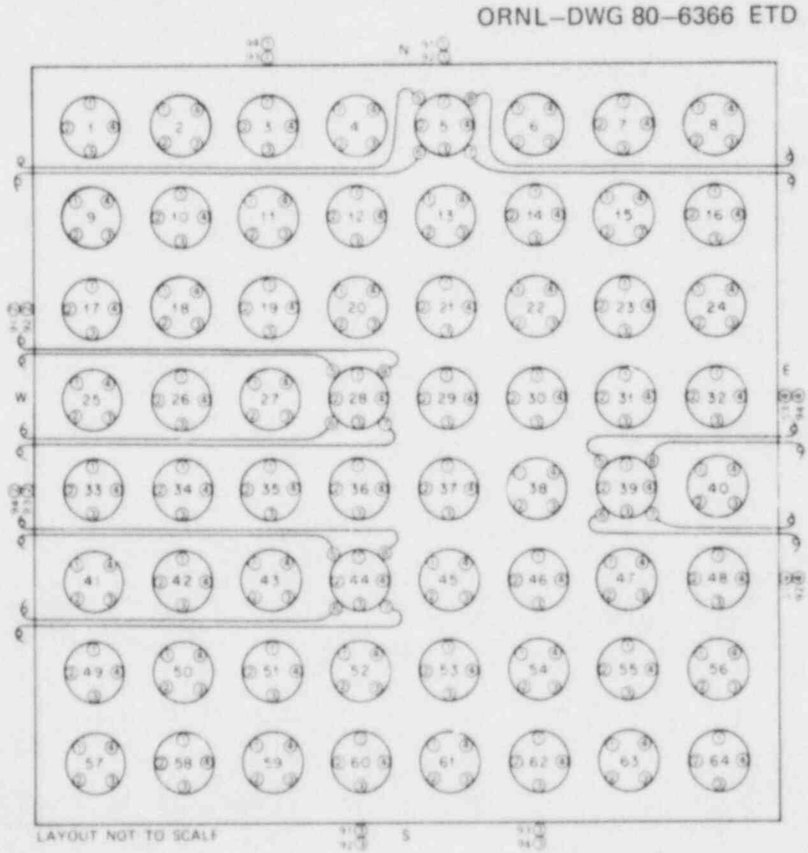

Fig. 50. Schematic diagram showing how external thermocouples (see Fig. 49) exited bundle.

ORNL–PHOTO 6571–80A

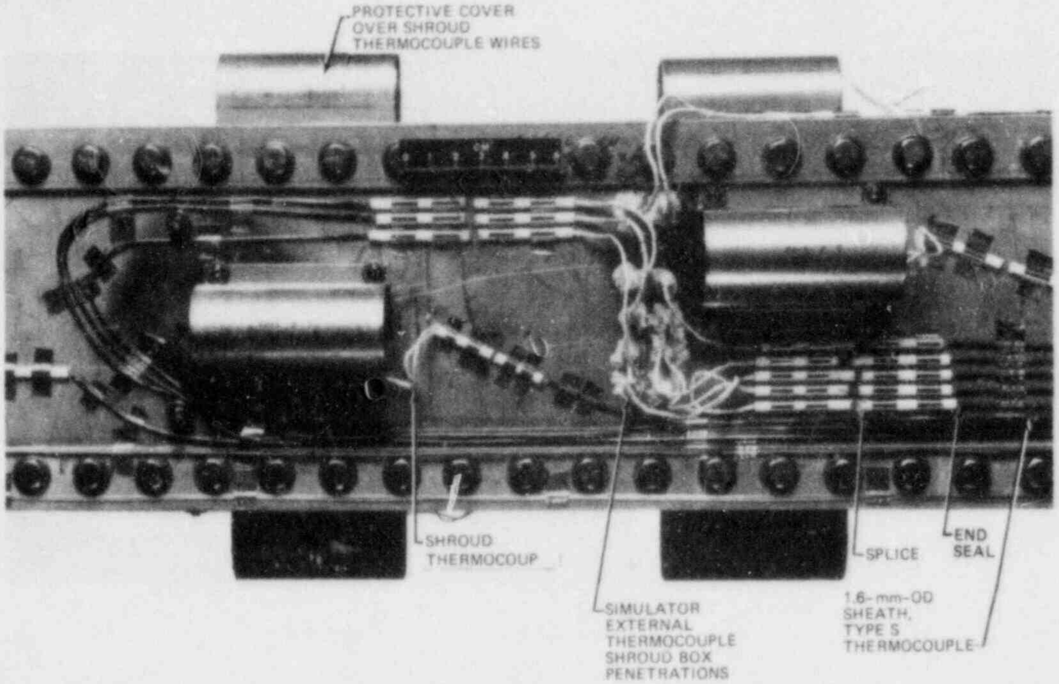

Fig. 51. Detail of thermocouple installation on outside of shroud.

ORNL–PHOTO 6488–80A

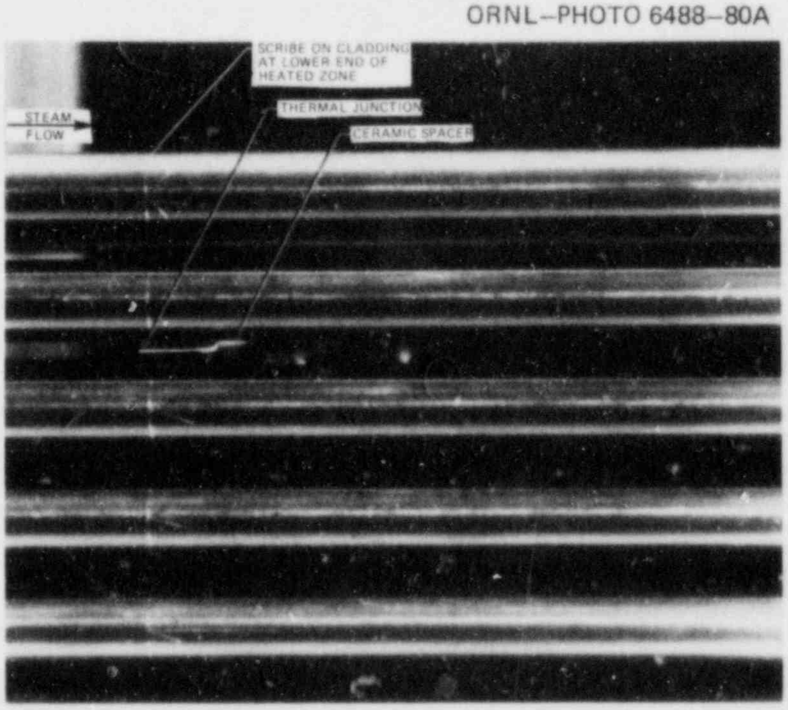

Fig. 52. Detail of outlet steam thermocouple installation.

ORNL–PHOTO 6767–80

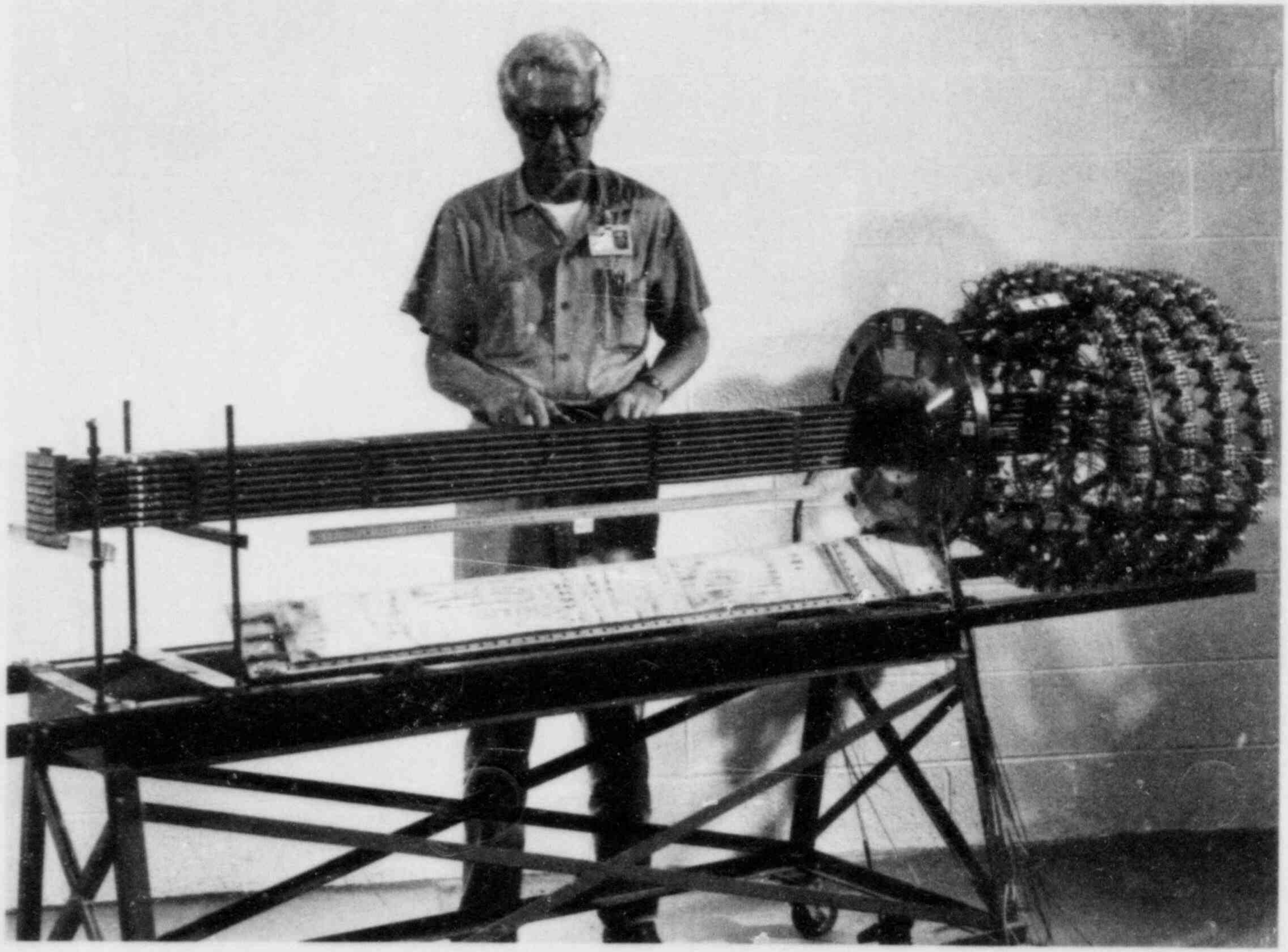

Fig. 53. Posttest view of west face of test array and shroud panel.

ORNL–PHOTO 5575–80A

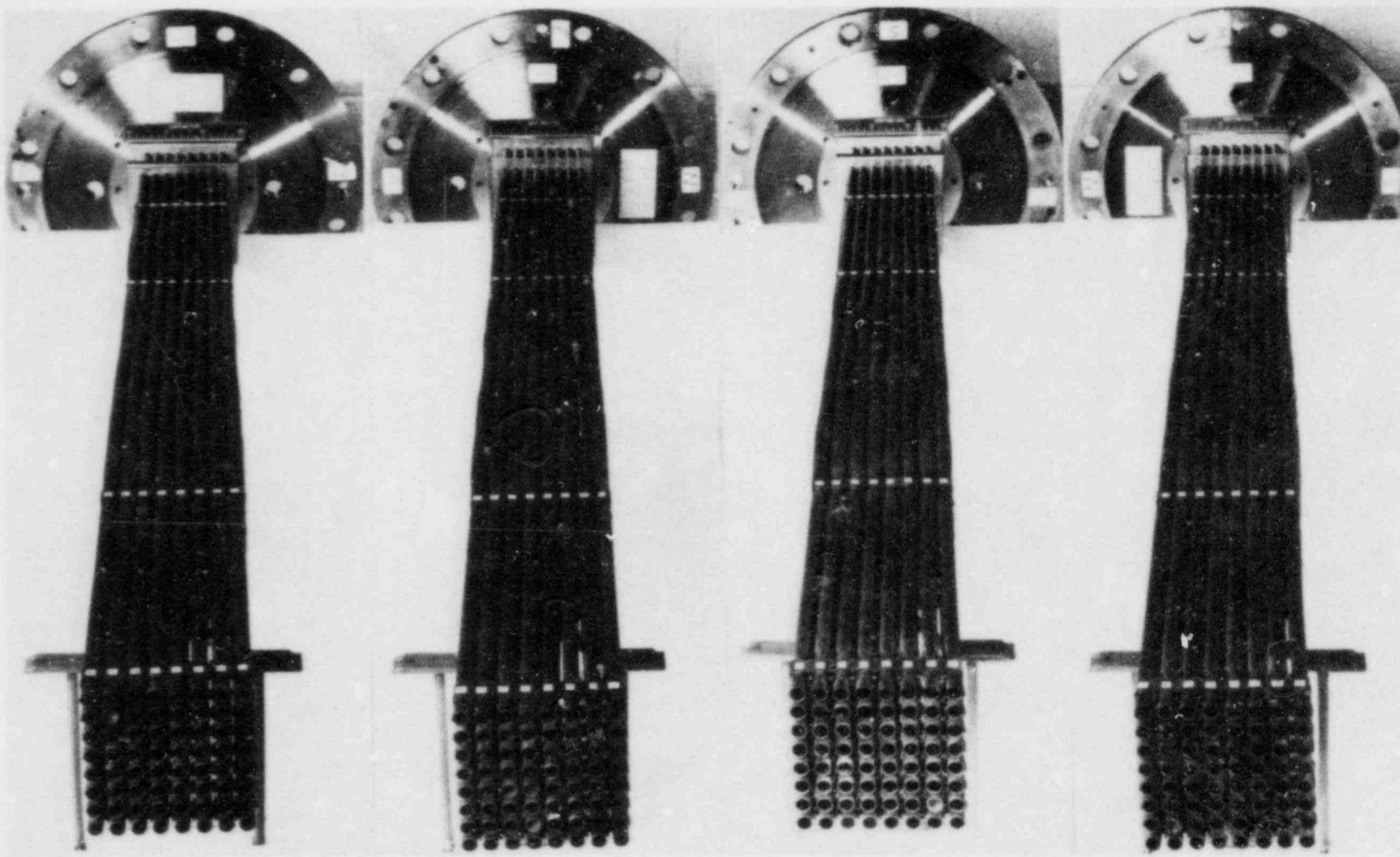

Fig. 54. Posttest views of four faces of test array.

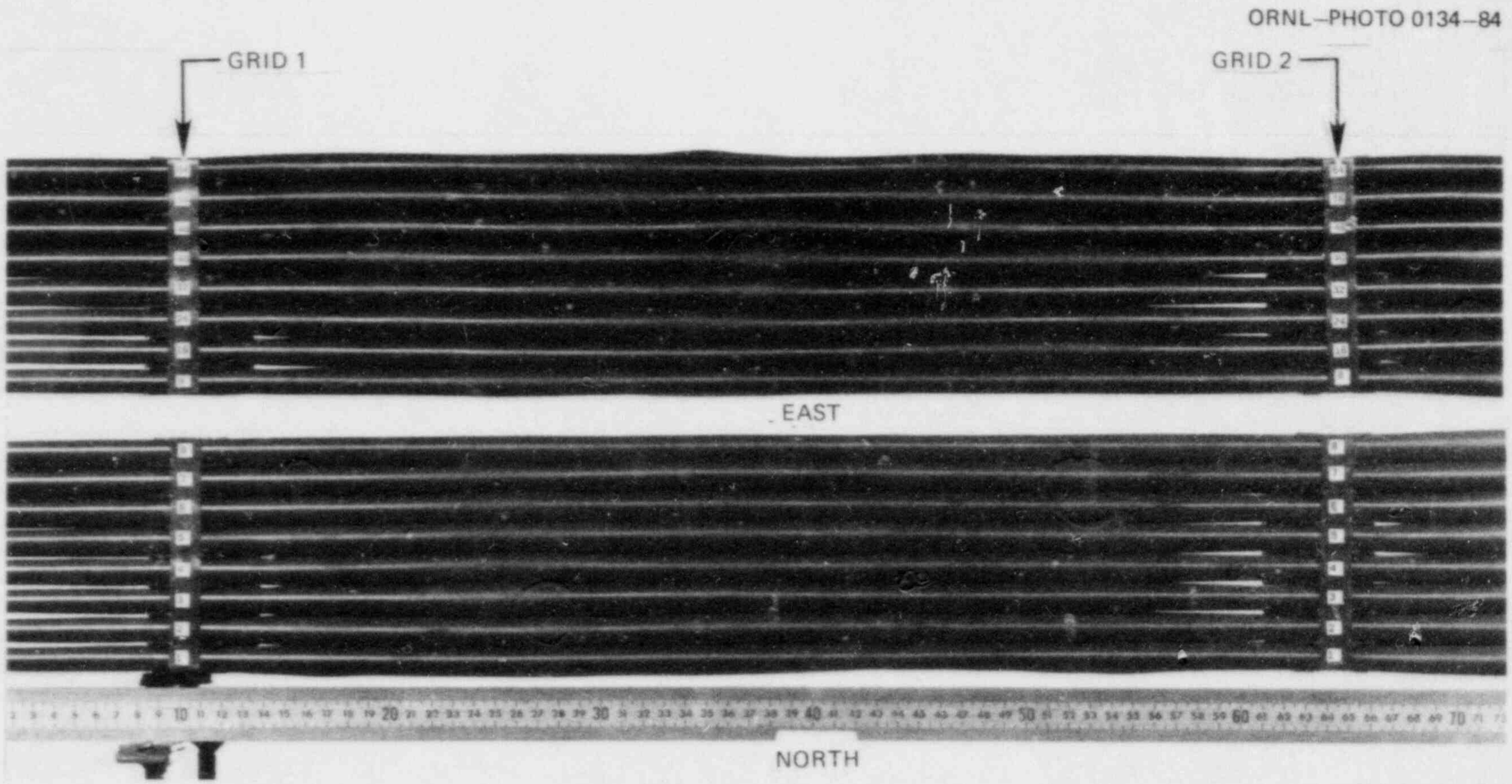

Fig. 55. North and east faces of bundle between interior grids.

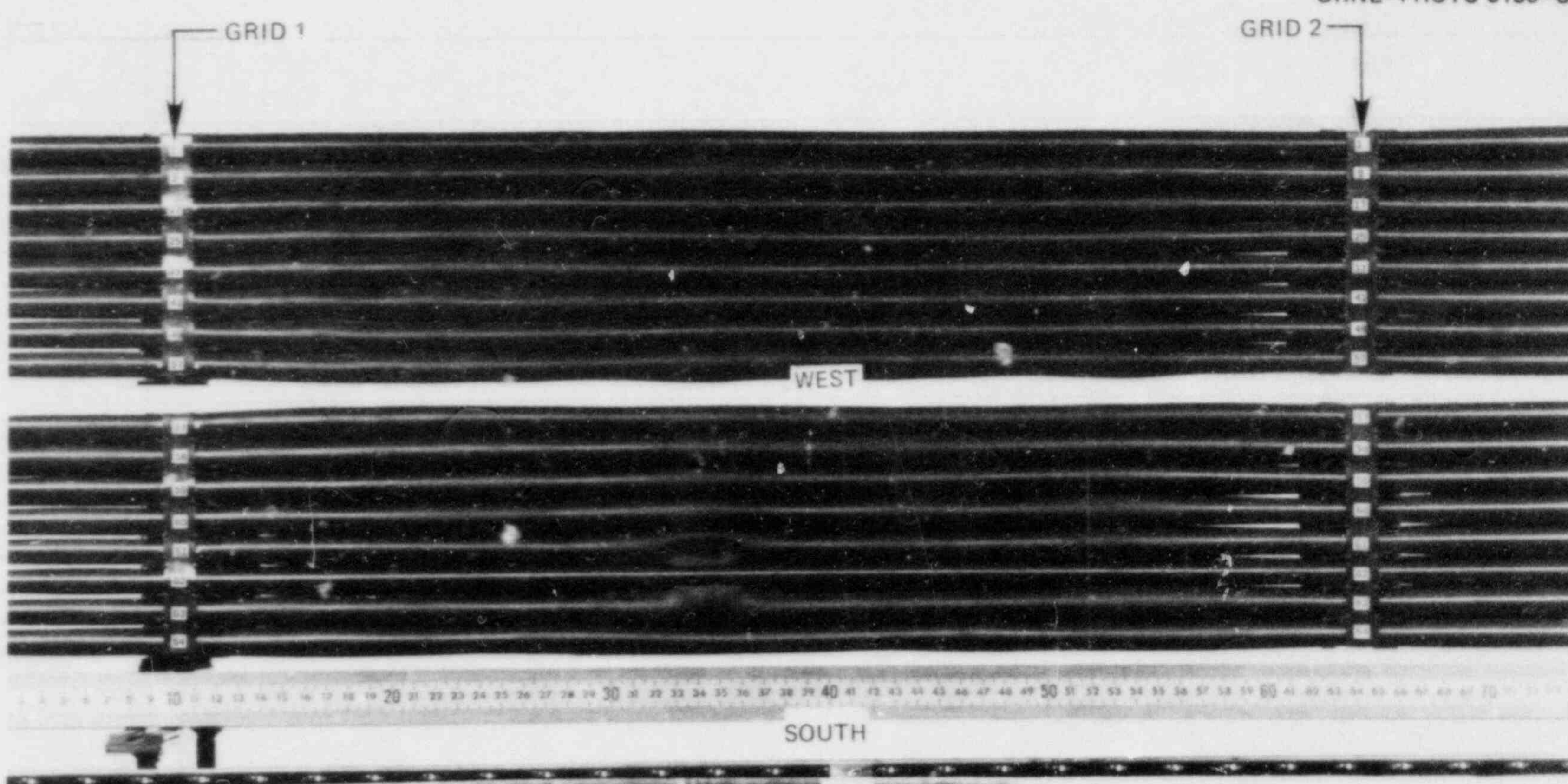

Fig. 56. South and west faces of bundle between interior grids.

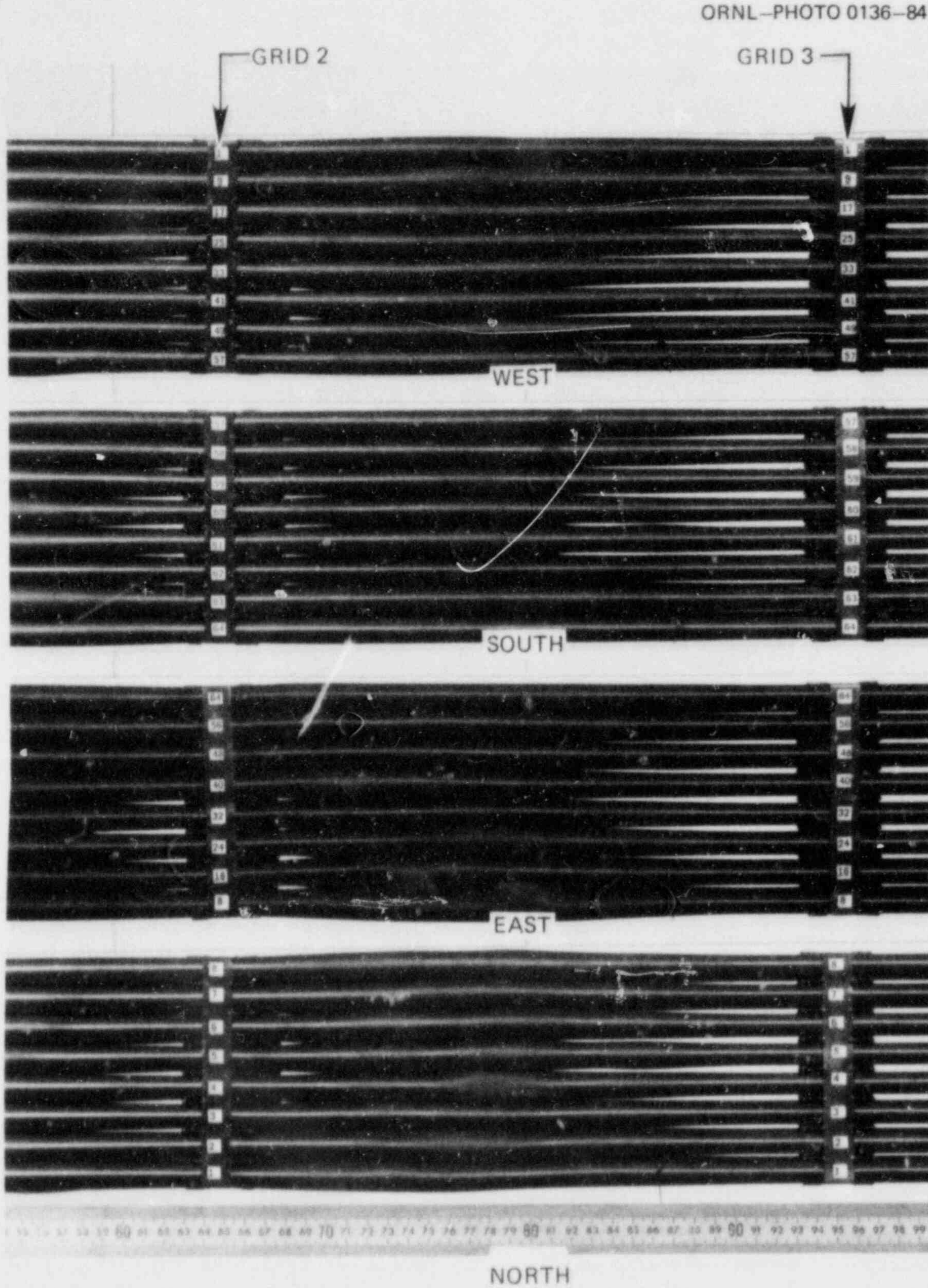

Fig. 57. Upper end of bundle heated zone.

ORNL–PHOTO 6756–80AR2

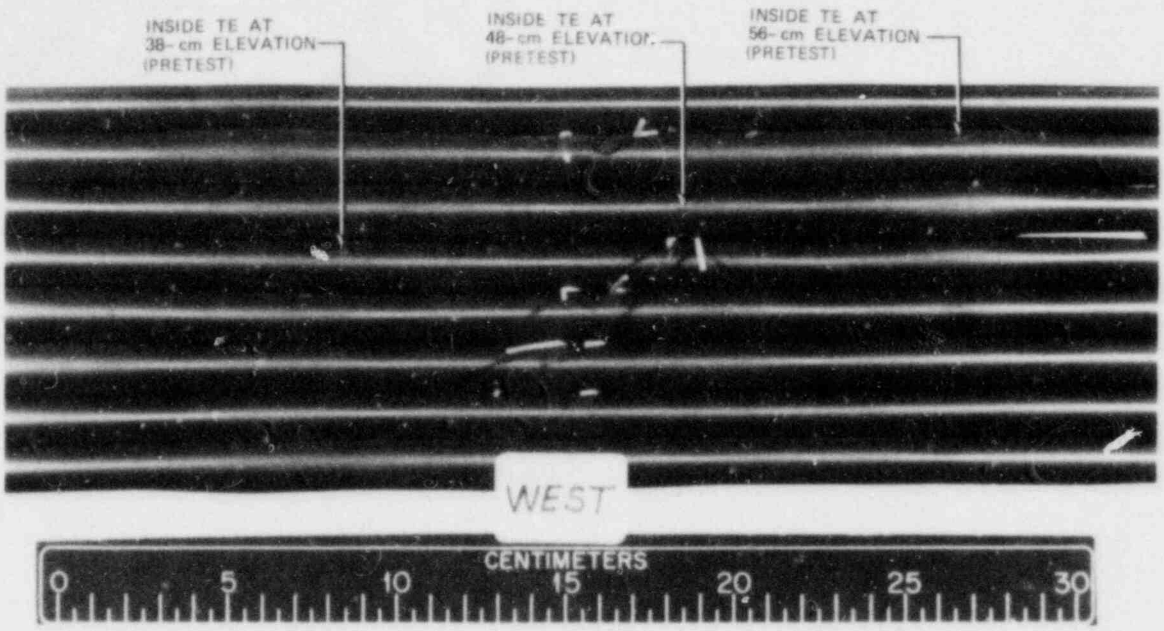

Fig. 58. Detail of deformation between upper grids of array showing effect of north-to-south temperature gradient.

ORNL–PHOTO 6757–80AR2

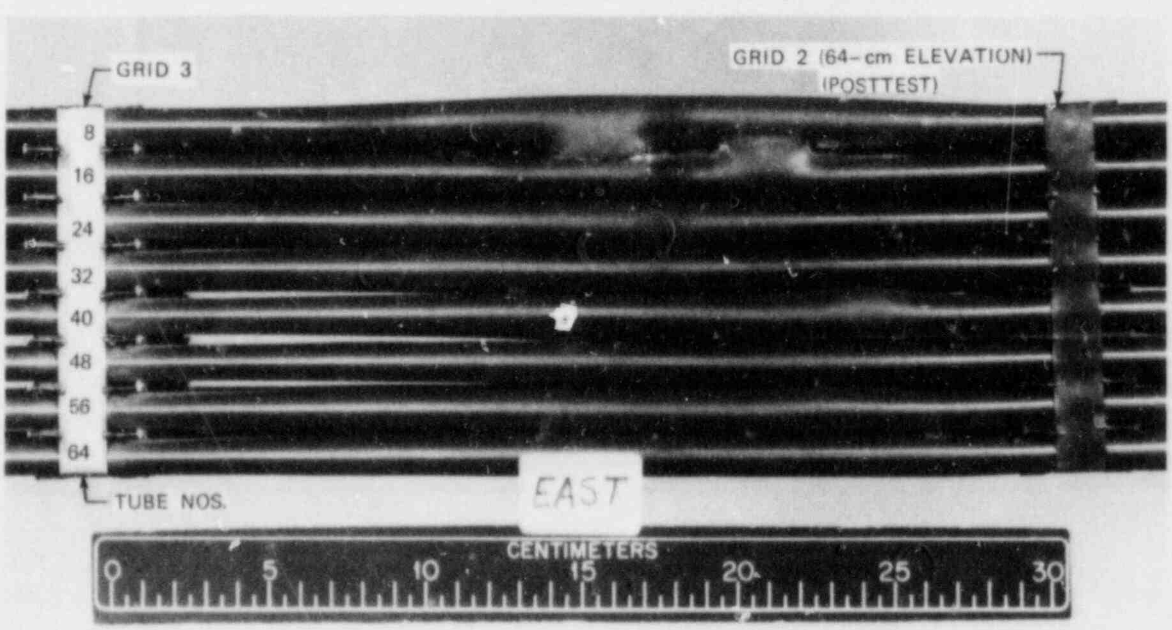

Fig. 59. Detail of deformation in region where external thermocouple wires exited west face of bundle.

ORNL–PHOTO 6755–80B

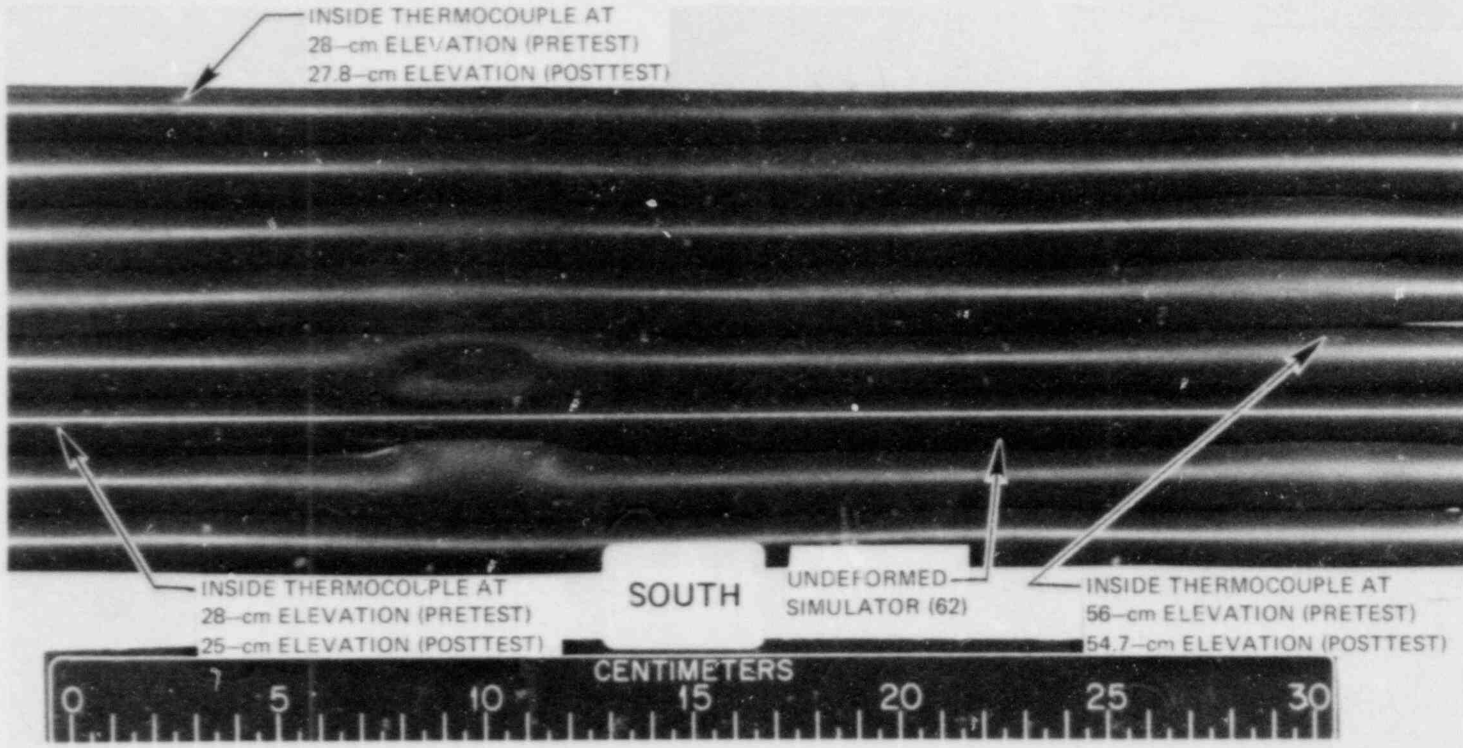

Fig. 60. Detail showing inverted dimple and undulating pattern of localized ballooning on south face of bundle.

ORNL–PHOTO 6771–80

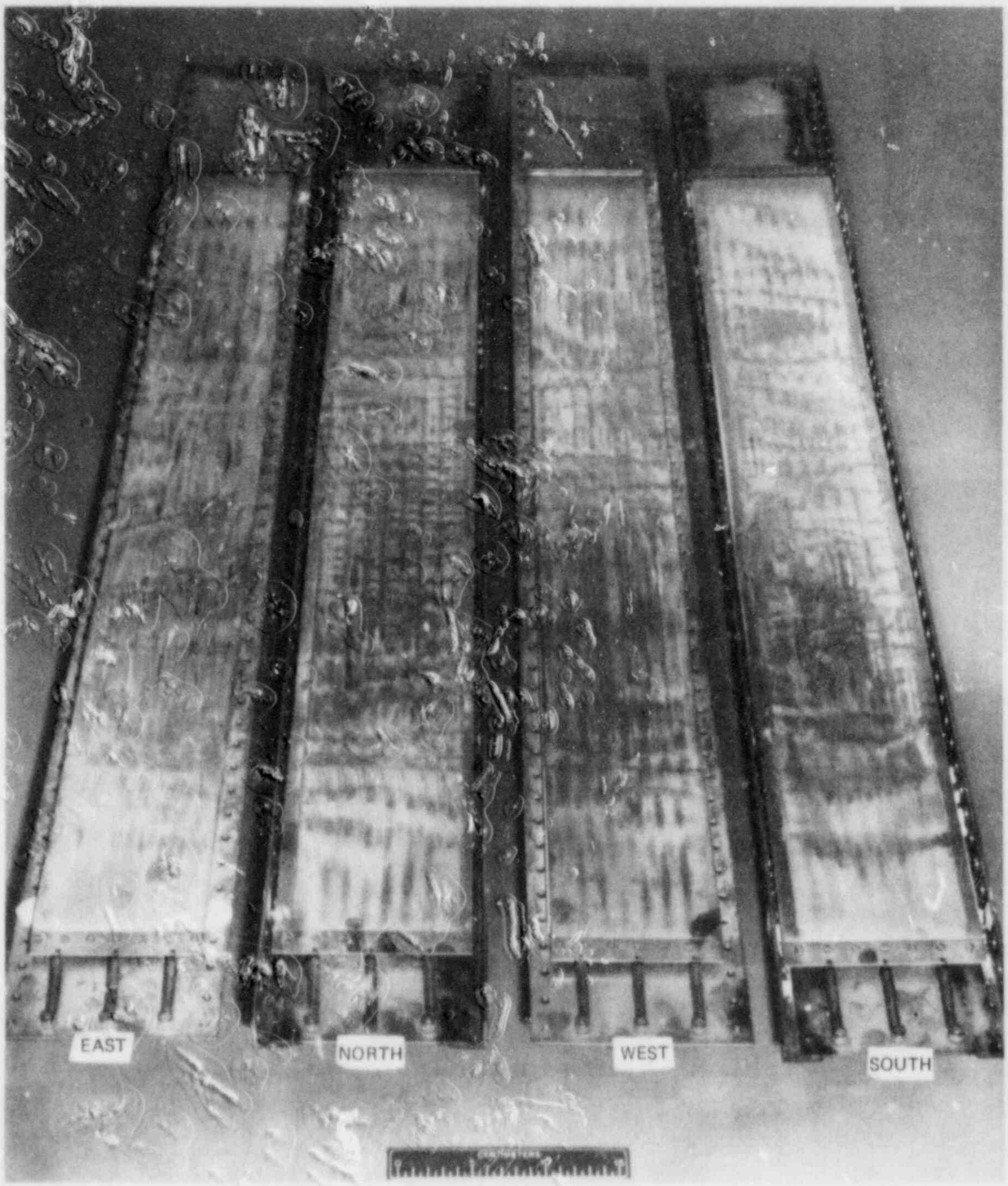

Fig. 61. Posttest views of shroud panels showing distortion and discoloration from contact with simulators.

M&C PHOTO Y-179370

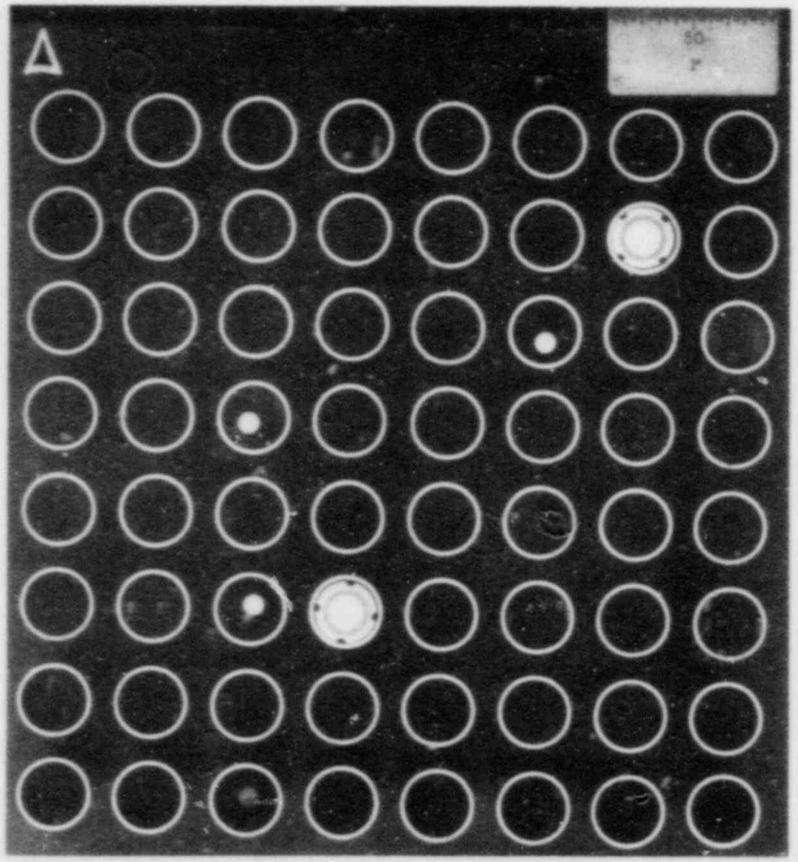

Fig. 62. Section in undeformed region at −6.5-cm elevation.

M&C PHOTO Y-179372

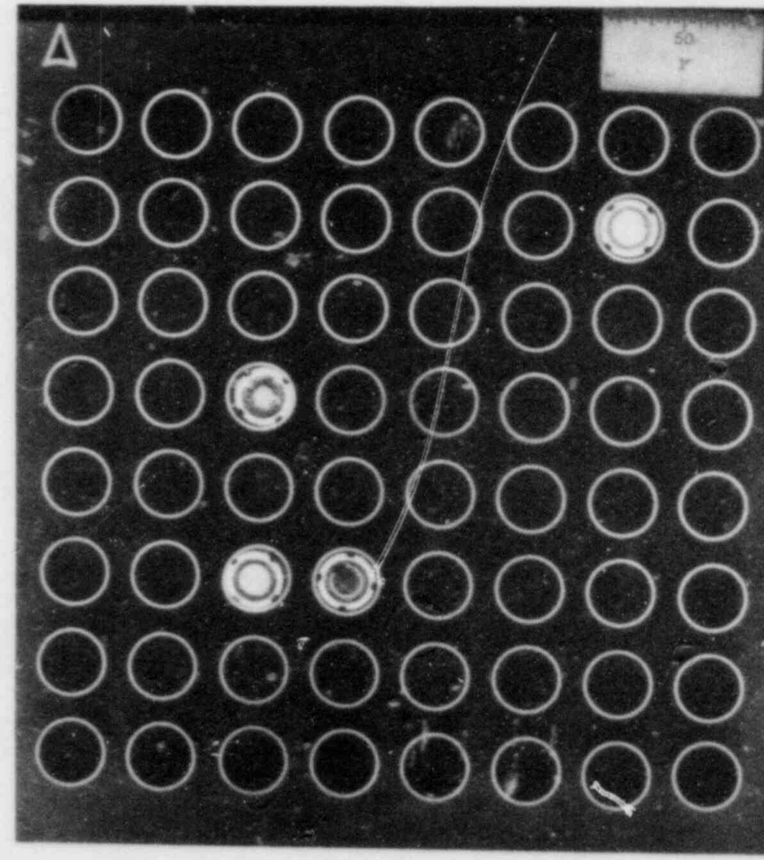

Fig. 63. Section at start of heated zone at 0.0-cm elevation.

M&C PHOTO Y-179375

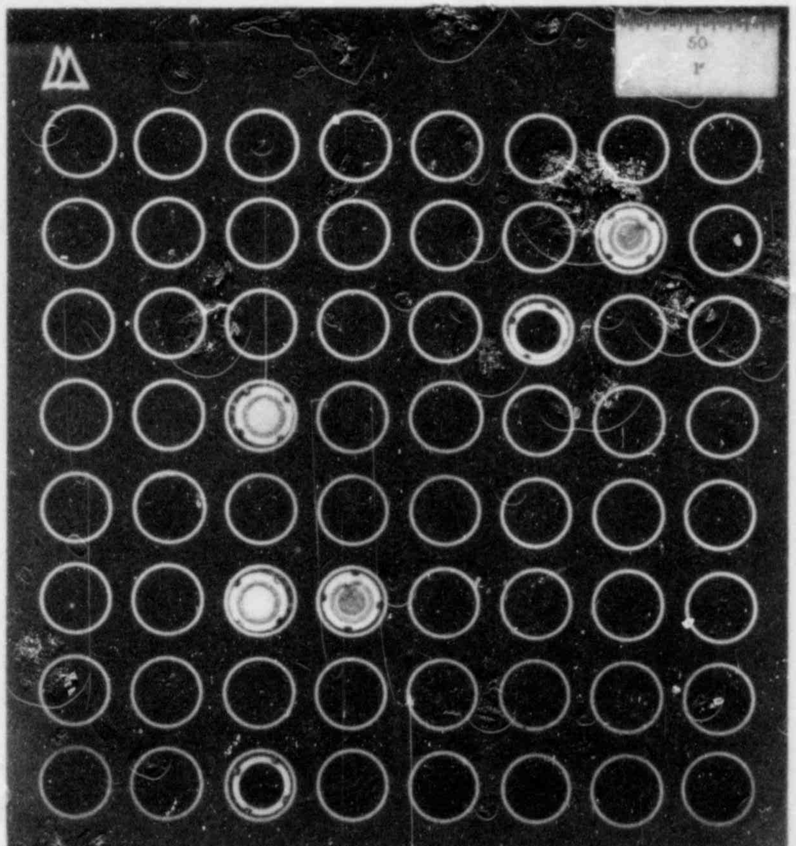

Fig. 64. Section at 1.8-cm elevation.

M&C PHOTO Y-179374

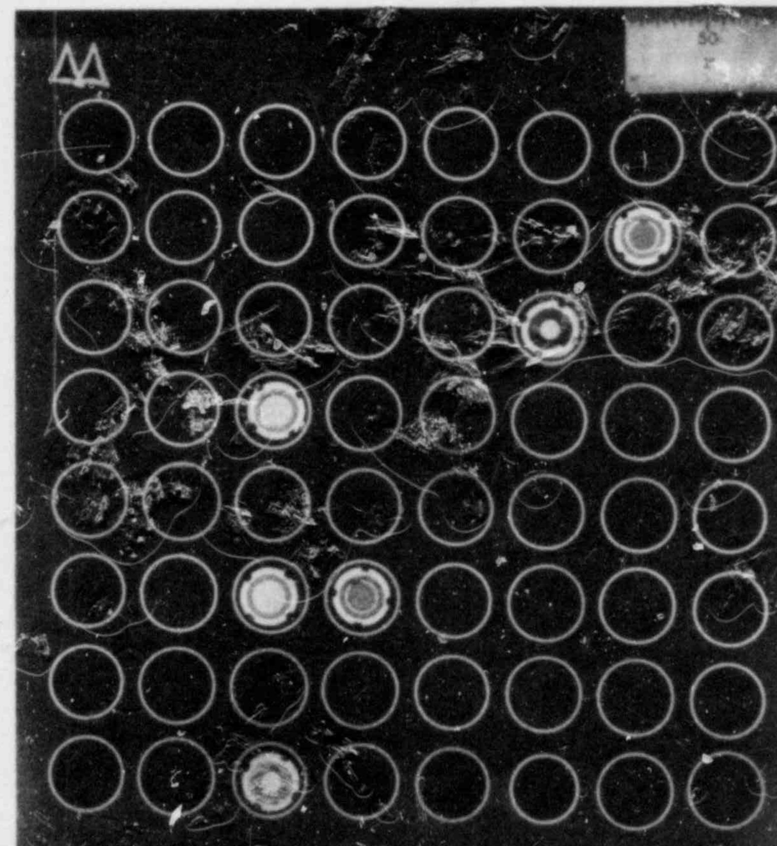

Fig. 65. Section at 3.5-cm elevation.

M&C PHOTO Y–179376

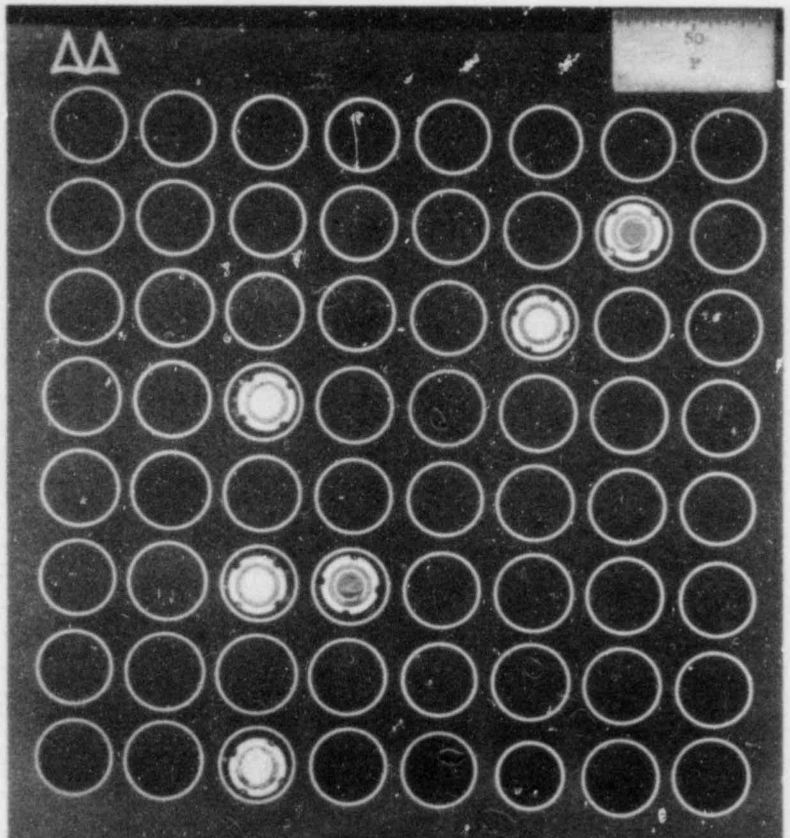

Fig. 66. Section at 5.0-cm elevation.

M&C PHOTO Y–179373

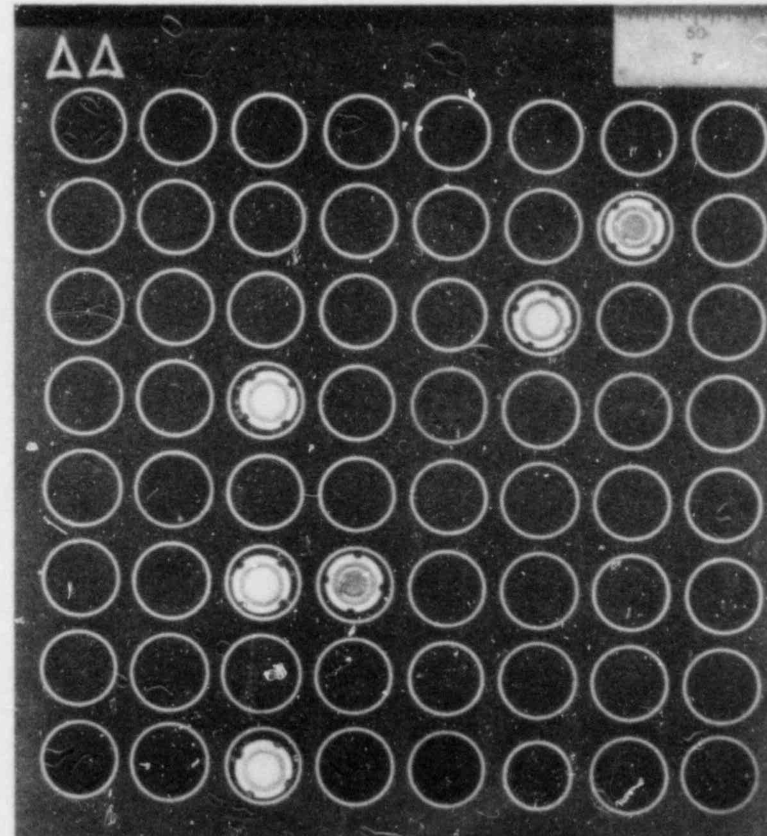

Fig. 67. Section at 6.5-cm elevation.

M&C PHOTO Y–179379

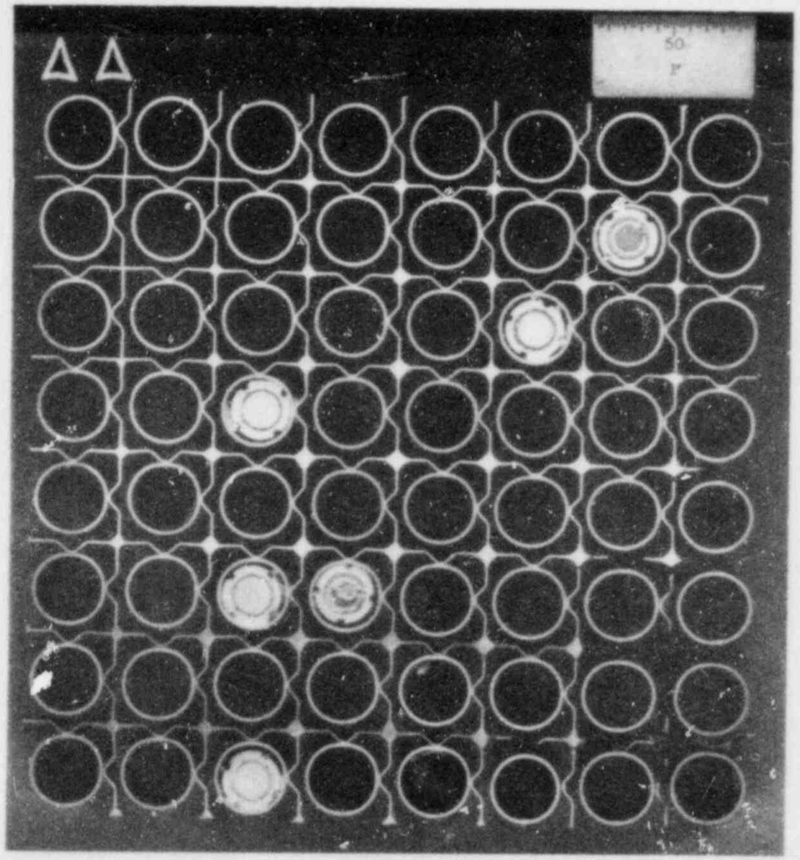

Fig. 68. Section through lower grid at 8.4-cm elevation.

M&C PHOTO Y–179384

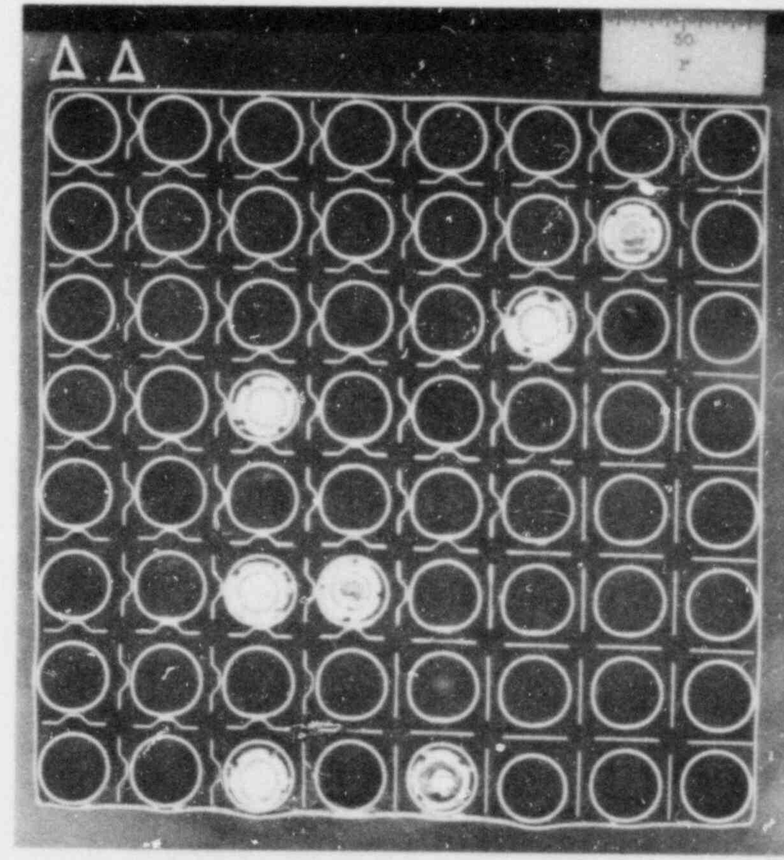

Fig. 69. Section through lower grid at 10.0-cm elevation.

M&C PHOTO Y-179738

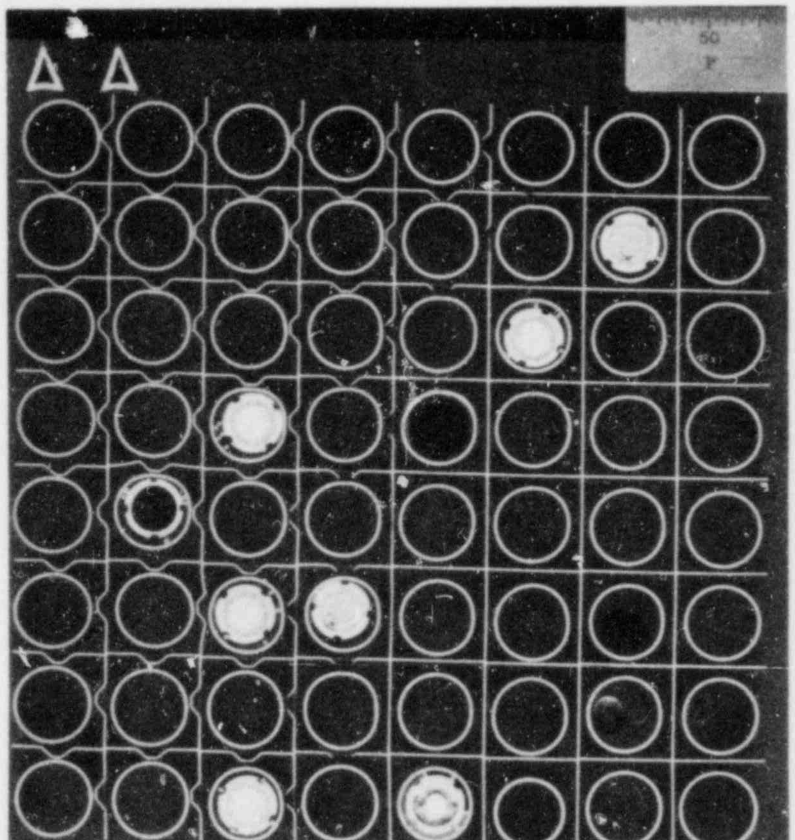

Fig. 70. Section through lower grid at 11.6-cm elevation.

M&C PHOTO Y-179381

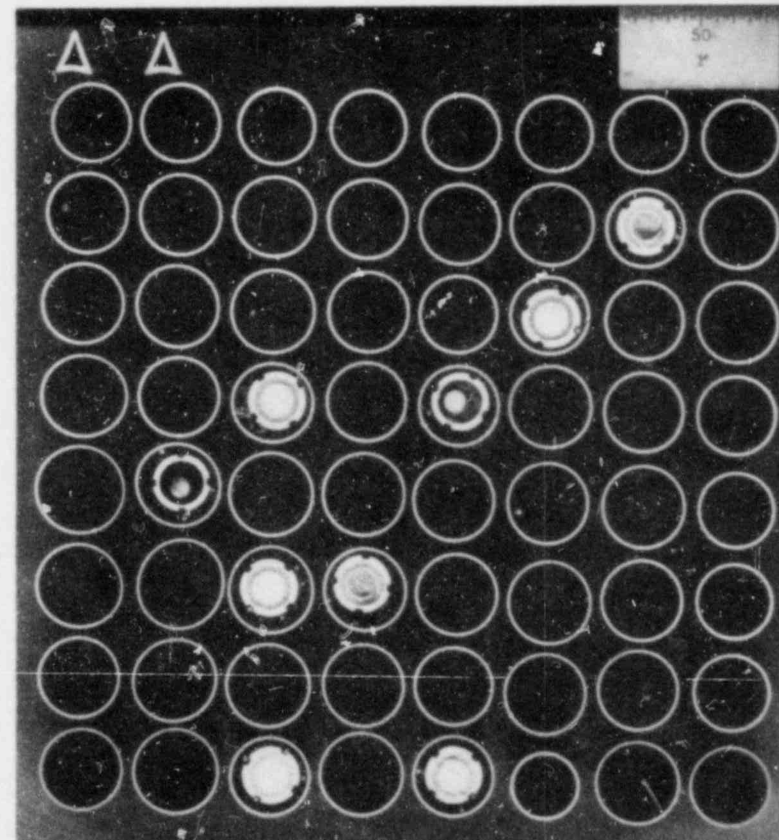

Fig. 71. Section at 13.5-cm elevation.

M&C PHOTO Y-179369

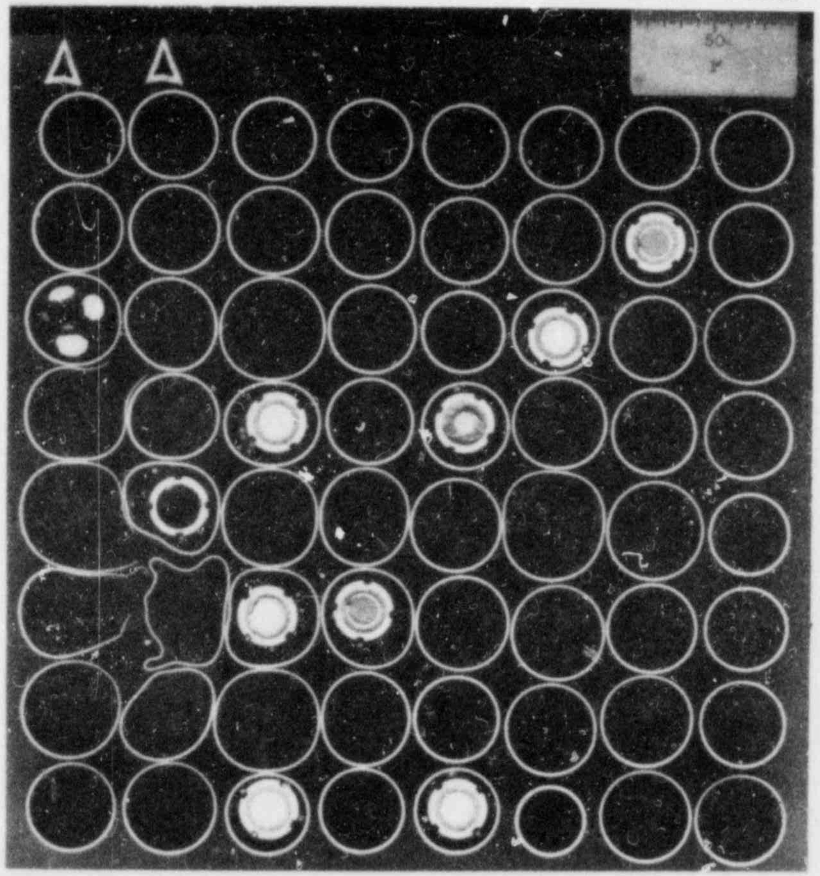

Fig. 72. Section at 15.5-cm elevation.

M&C PHOTO Y-179385

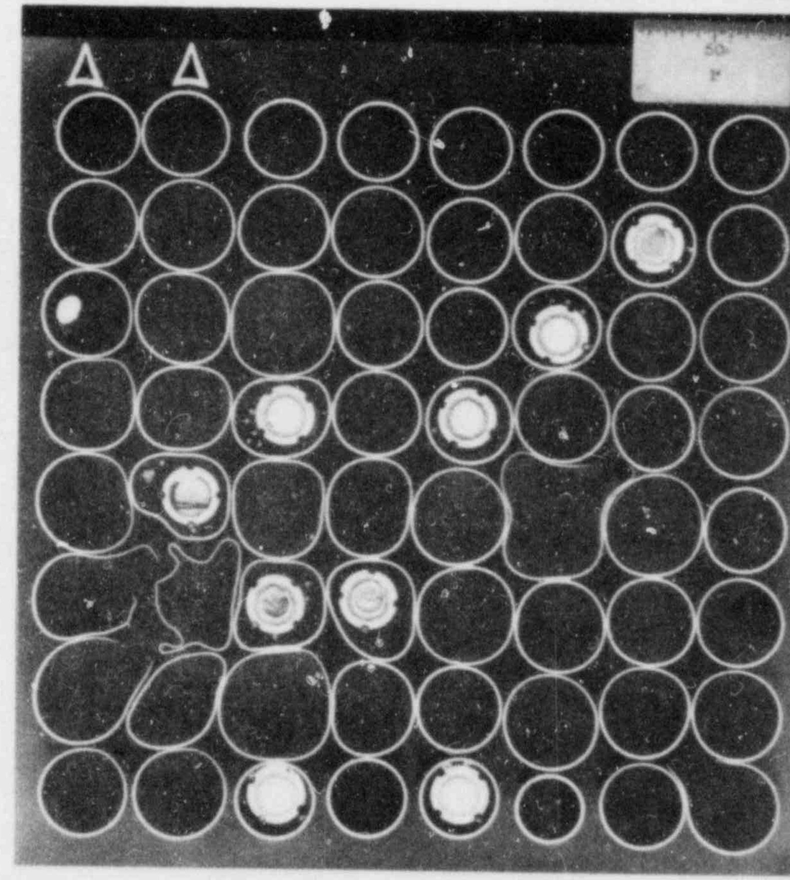

Fig. 73. Section at 17.0-cm elevation.

M&C PHOTO Y-179380

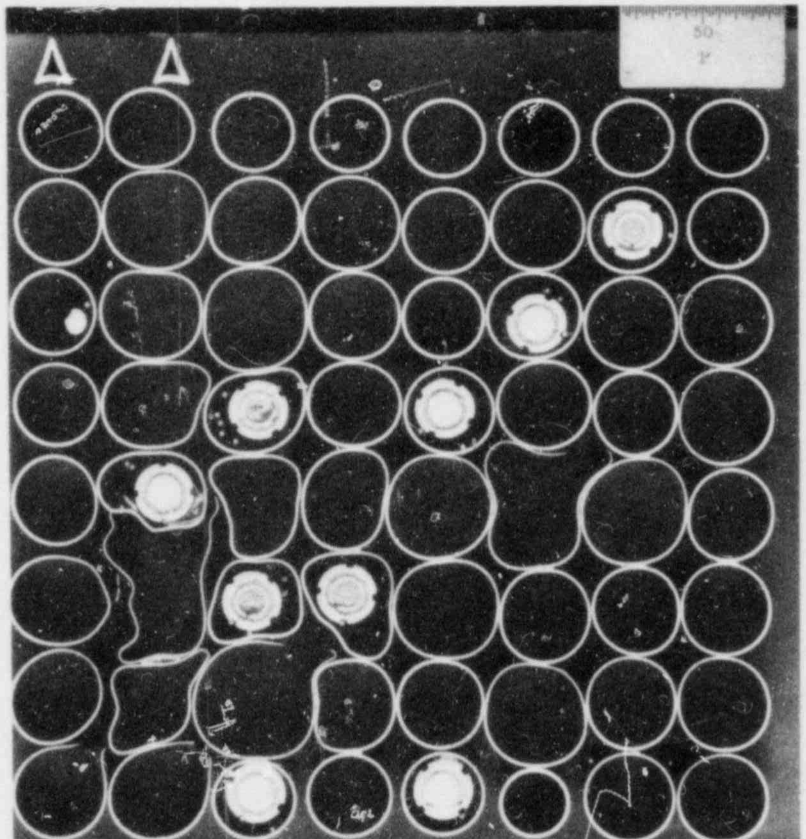

Fig. 74. Section at 18.5-cm elevation.

M&C PHOTO Y-179386

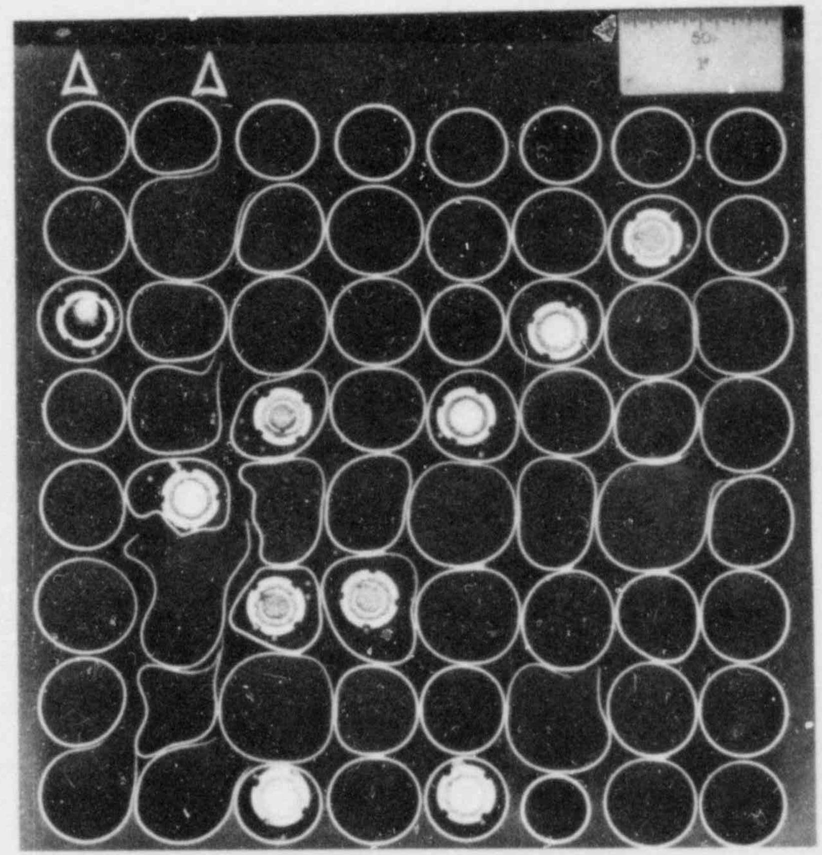

Fig. 75. Section at 20.0-cm elevation.

M&C PHOTO Y-179387

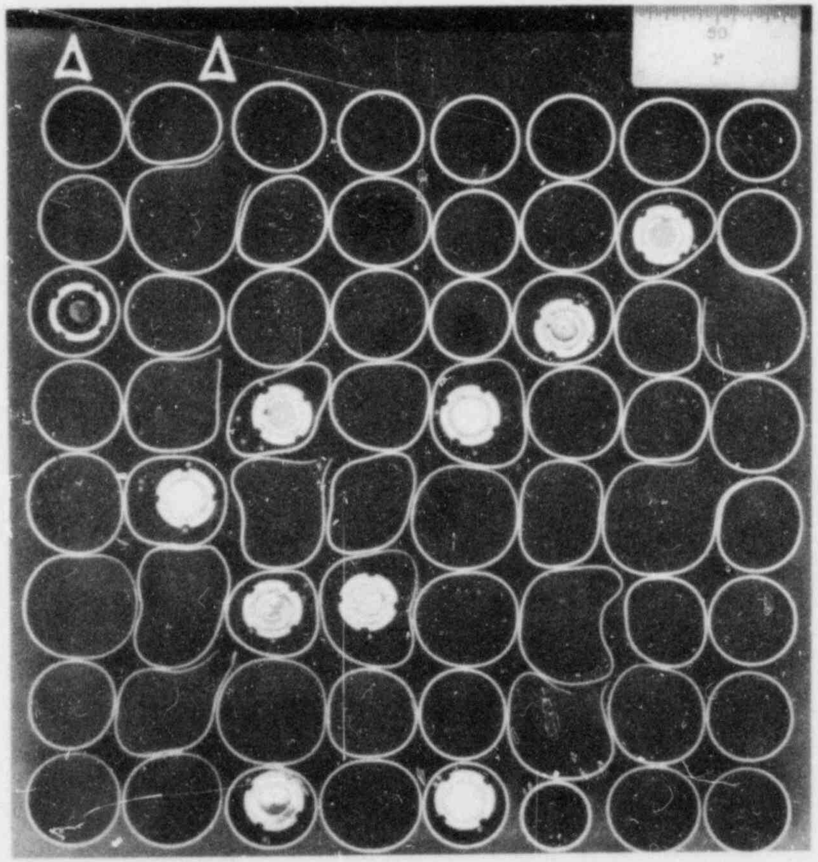

Fig. 76. Section at 21.5-cm elevation.

M&C PHOTO Y-179388

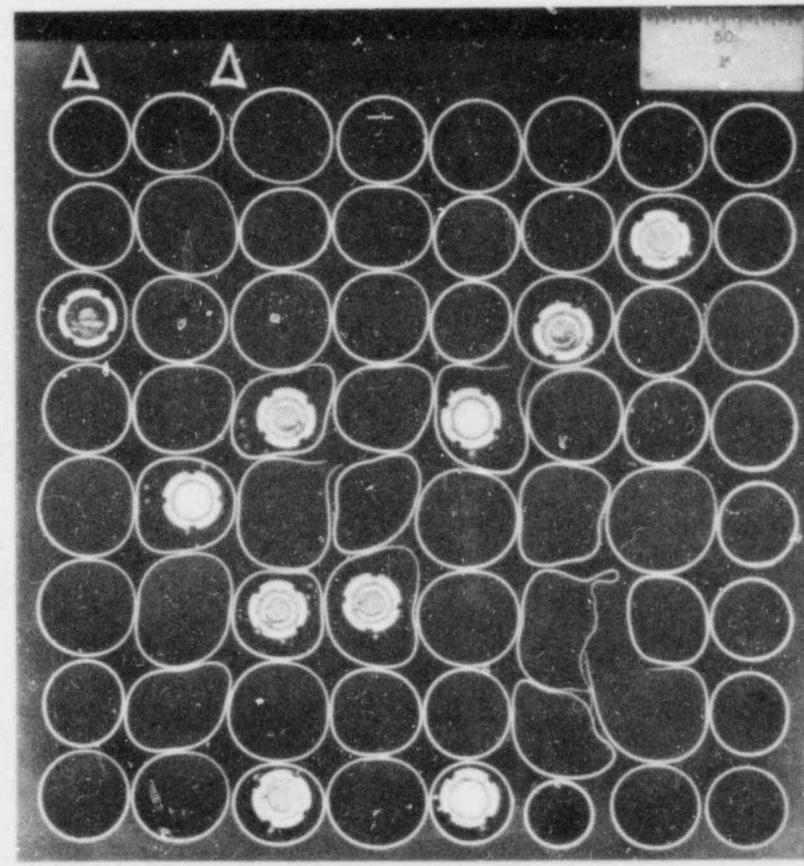

Fig. 77. Section at 23.0-cm elevation.

M&C PHOTO Y-179382

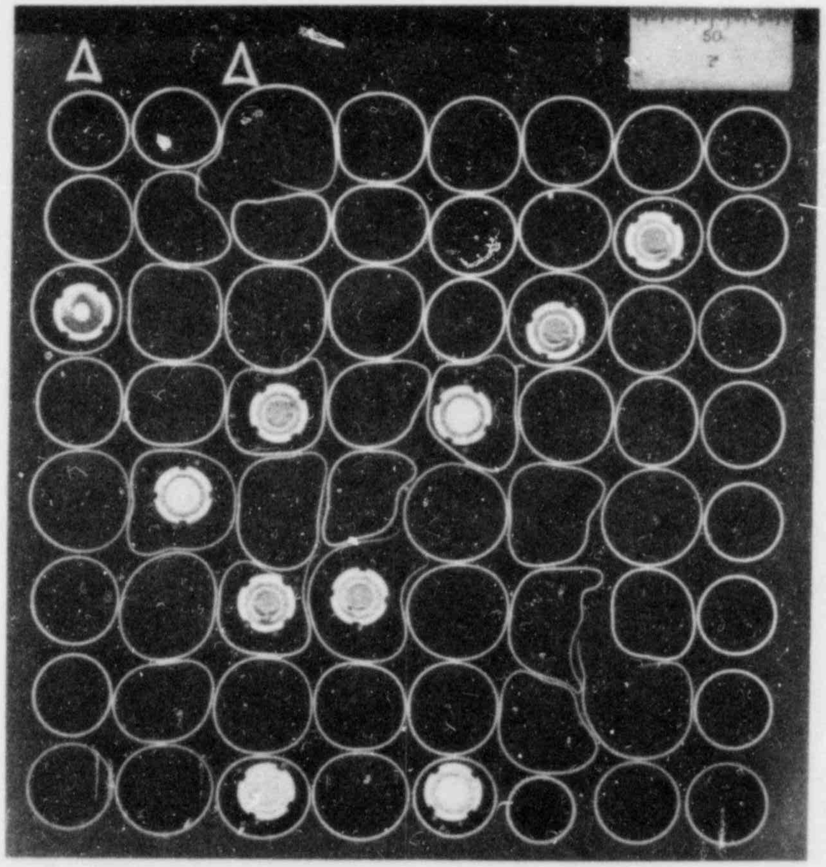

Fig. 78. Section at 24.7-cm elevation.

M&C PHOTO Y-179531

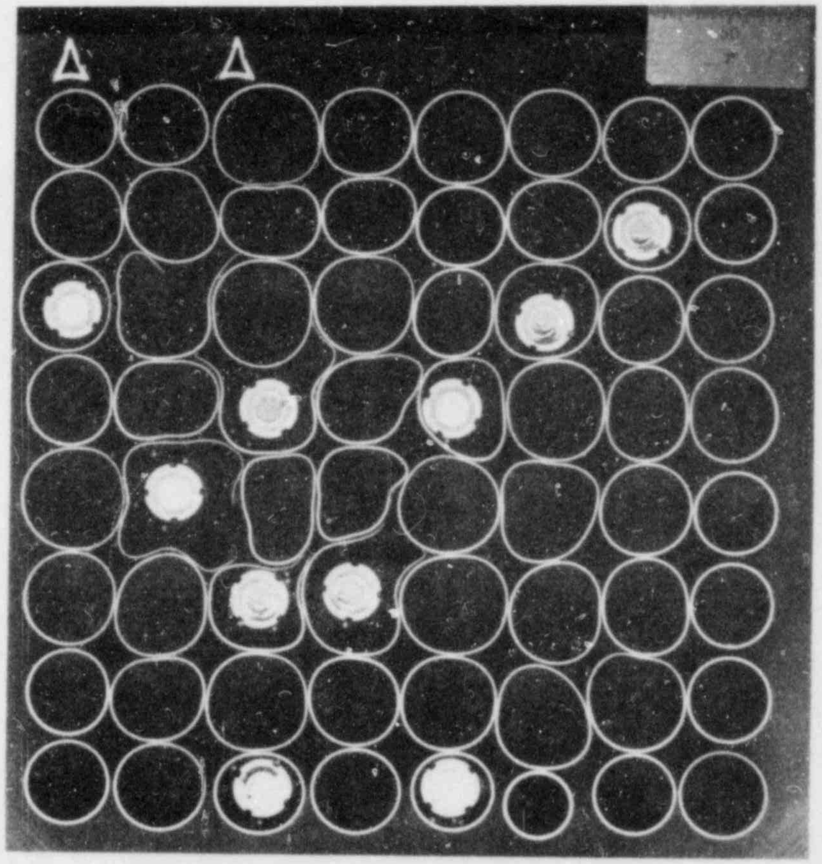

Fig. 79. Section at 26.4-cm elevation.

M&C PHOTO Y−179533

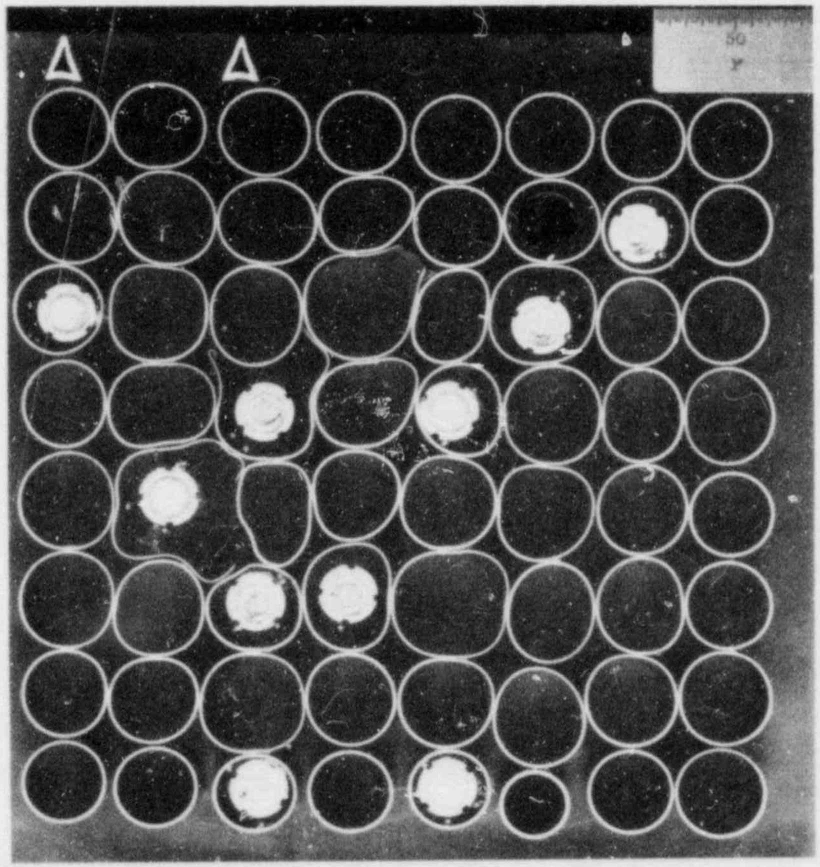

Fig. 80. Section at 28.0-cm elevation.

M&C PHOTO Y−179713

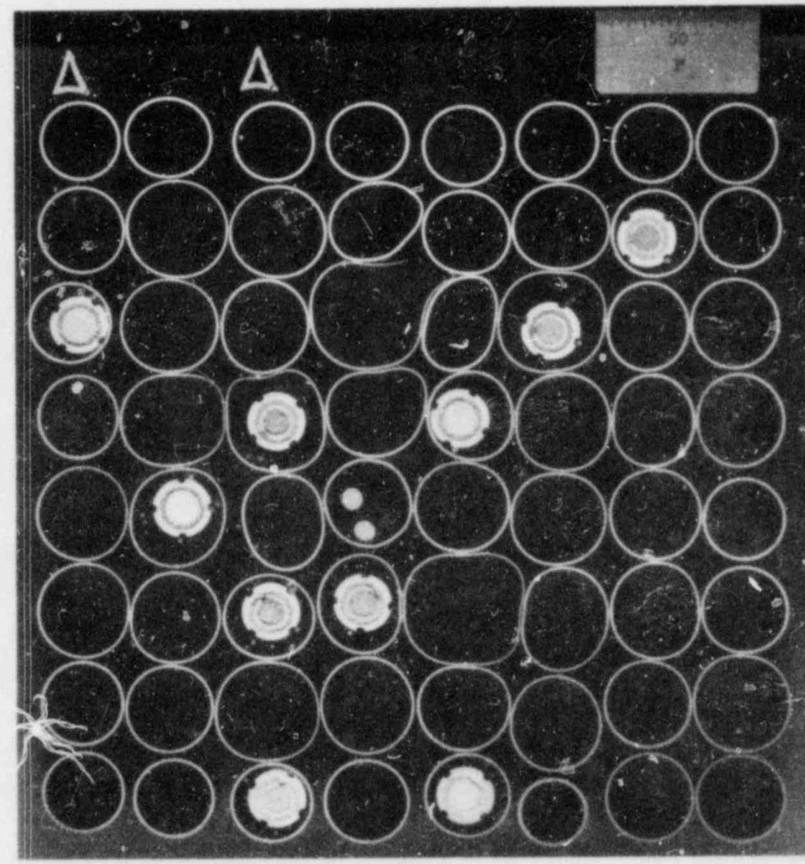

Fig. 81. Section at 29.5-cm elevation.

M&C PHOTO Y-179535

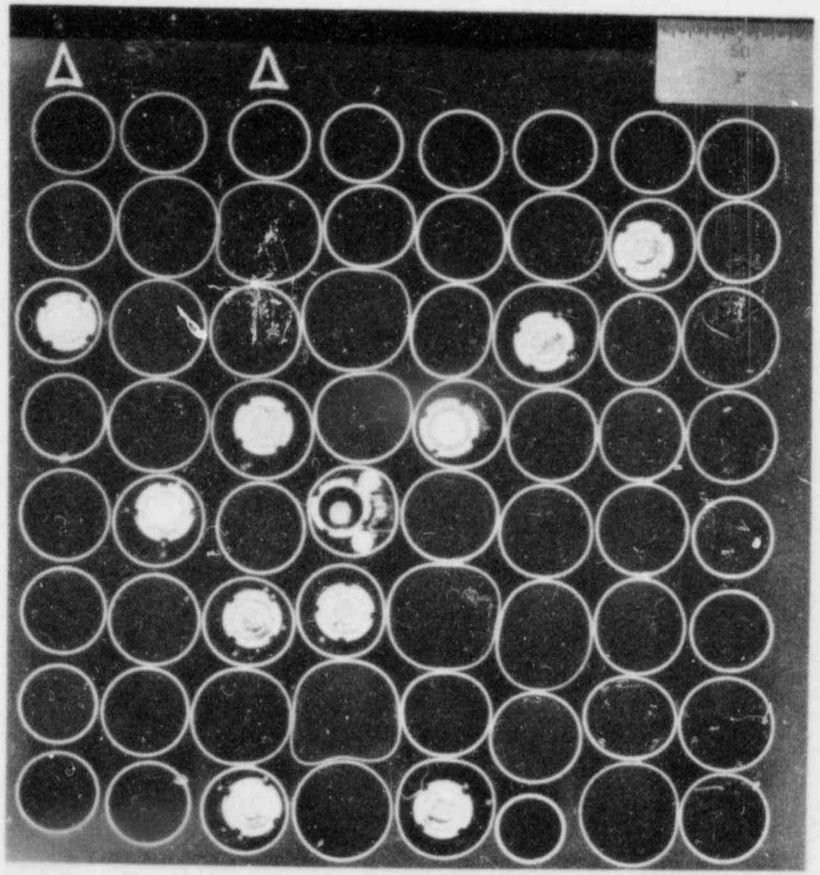

Fig. 82. Section at 31.5-cm elevation.

M&C PHOTO Y-179714

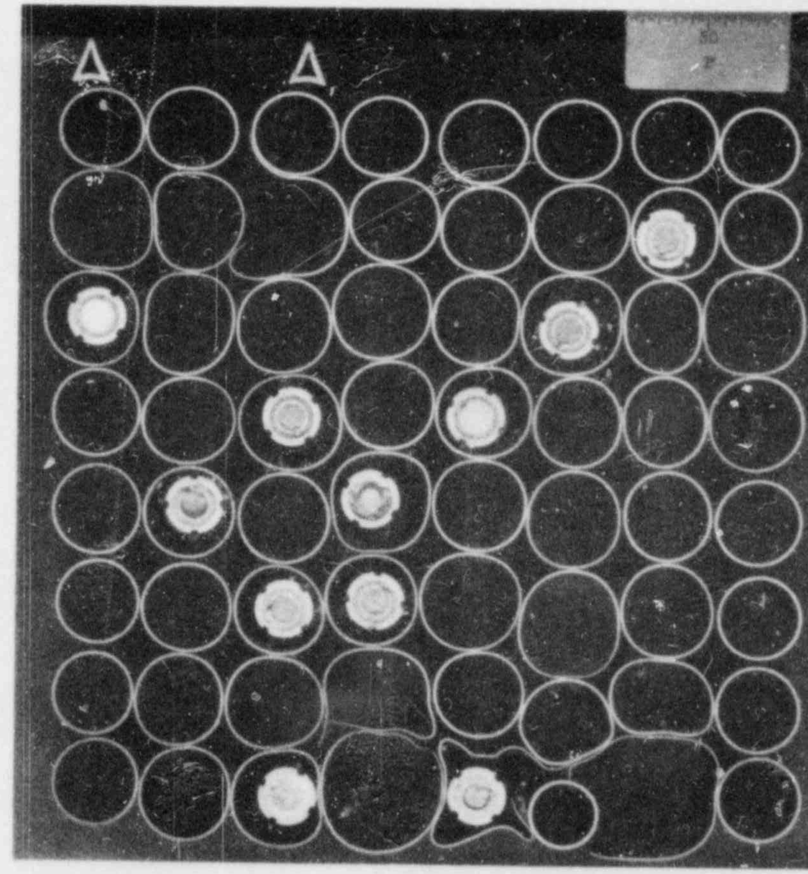

Fig. 83. Section at 33.5-cm elevation.

M&C PHOTO Y–179532

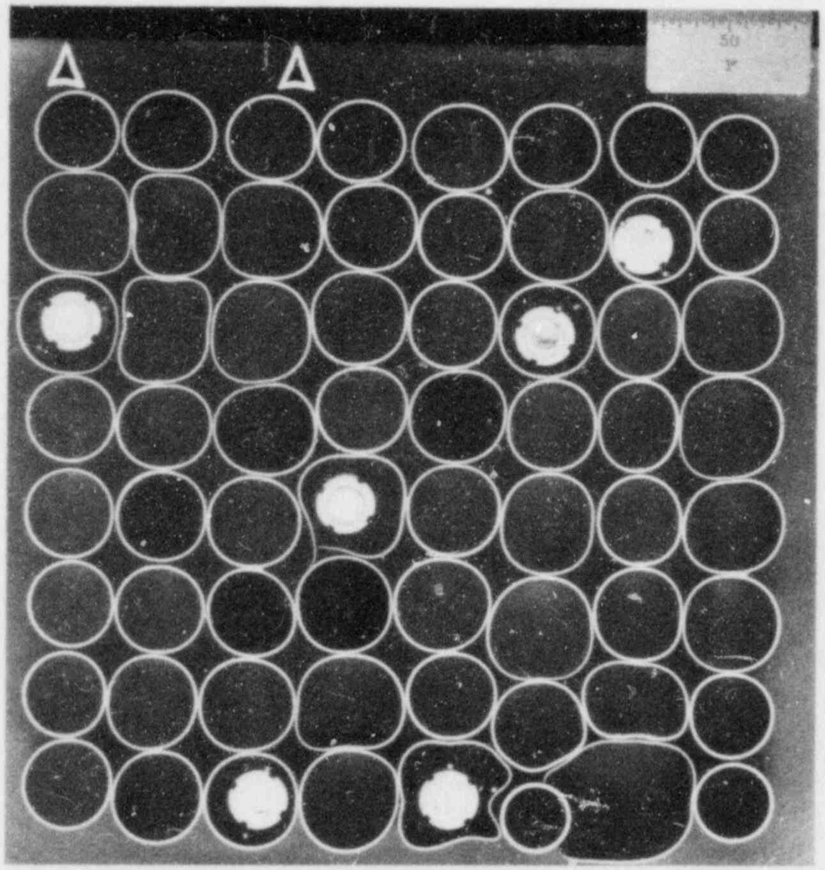

Fig. 84. Section at 35.5-cm elevation.

M&C PHOTO Y–179534

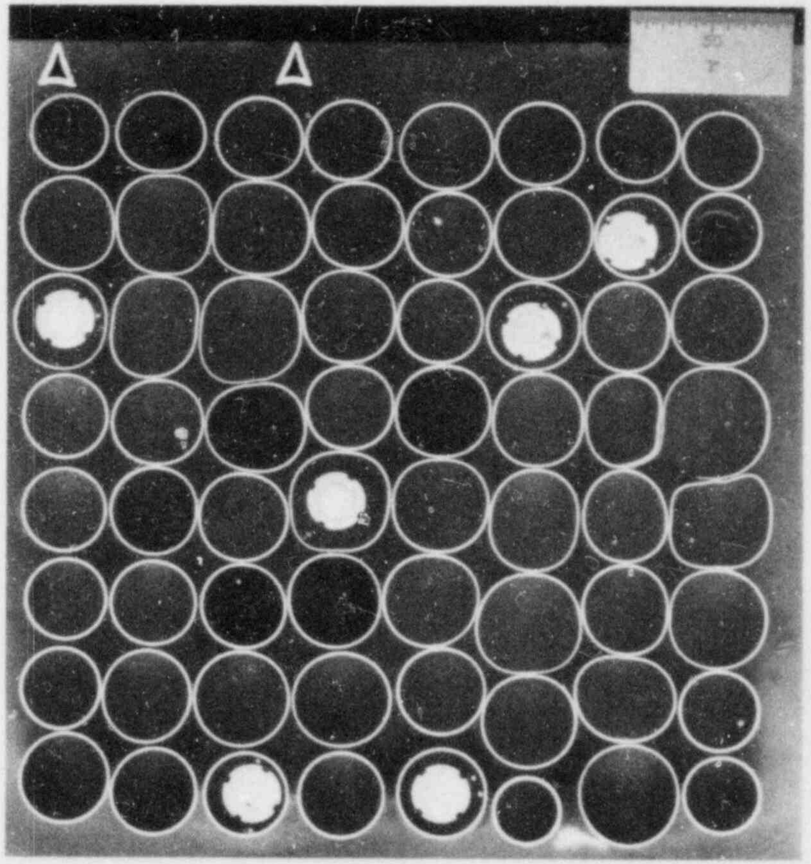

Fig. 85. Section at 37.1-cm elevation.

M&C PHOTO Y-179538

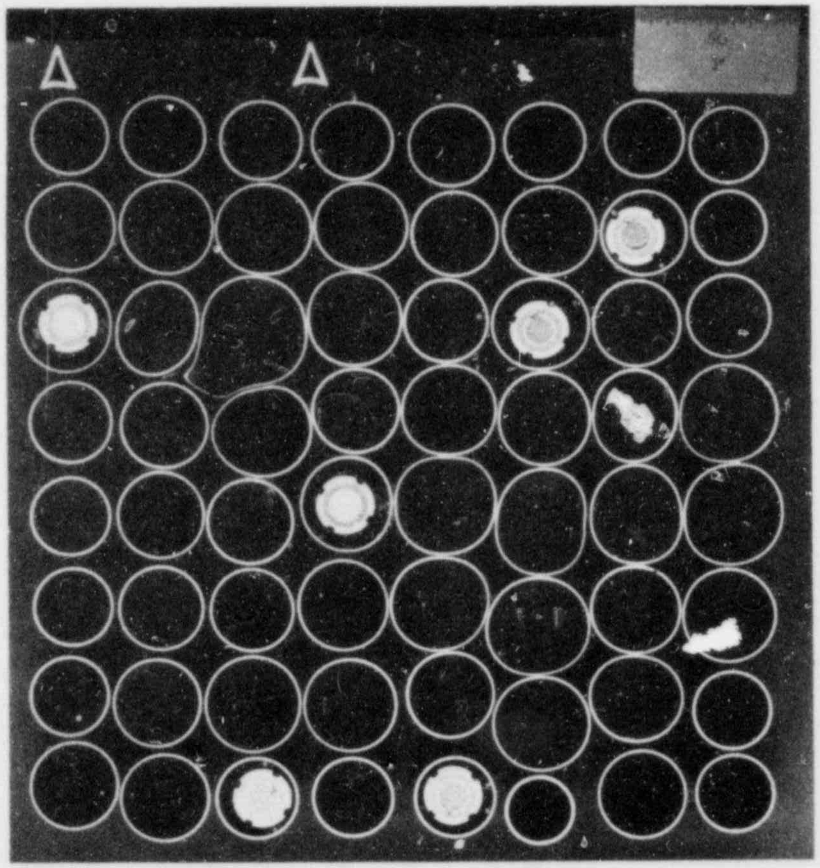

Fig. 86. Section at 39.0-cm elevation.

M&C PHOTO Y-179537

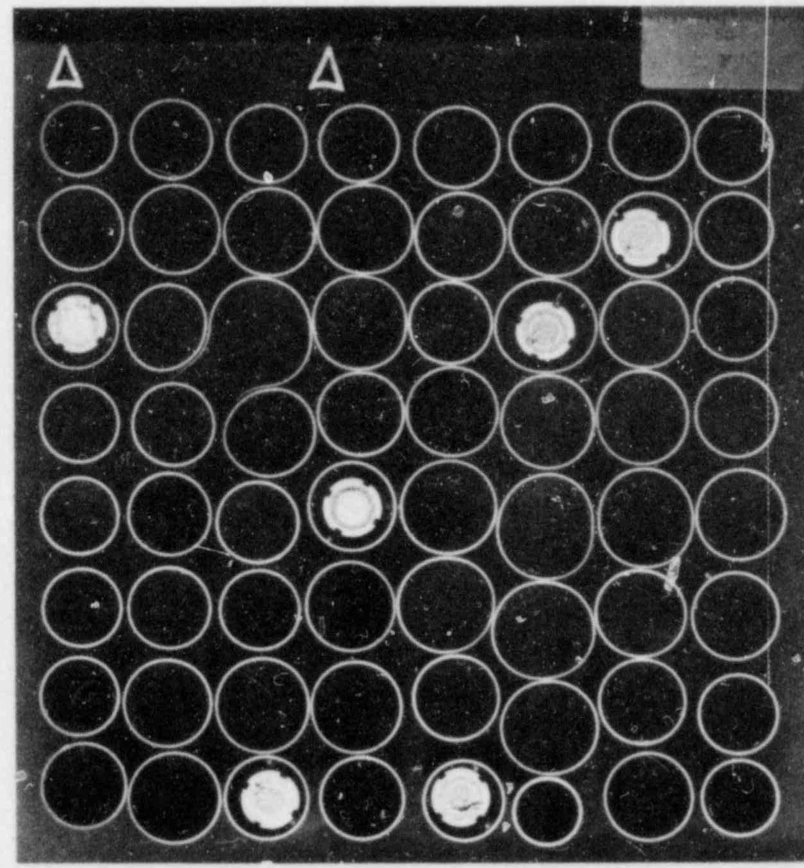

Fig. 87. Section at 40.8-cm elevation.

M&C PHOTO Y-179539

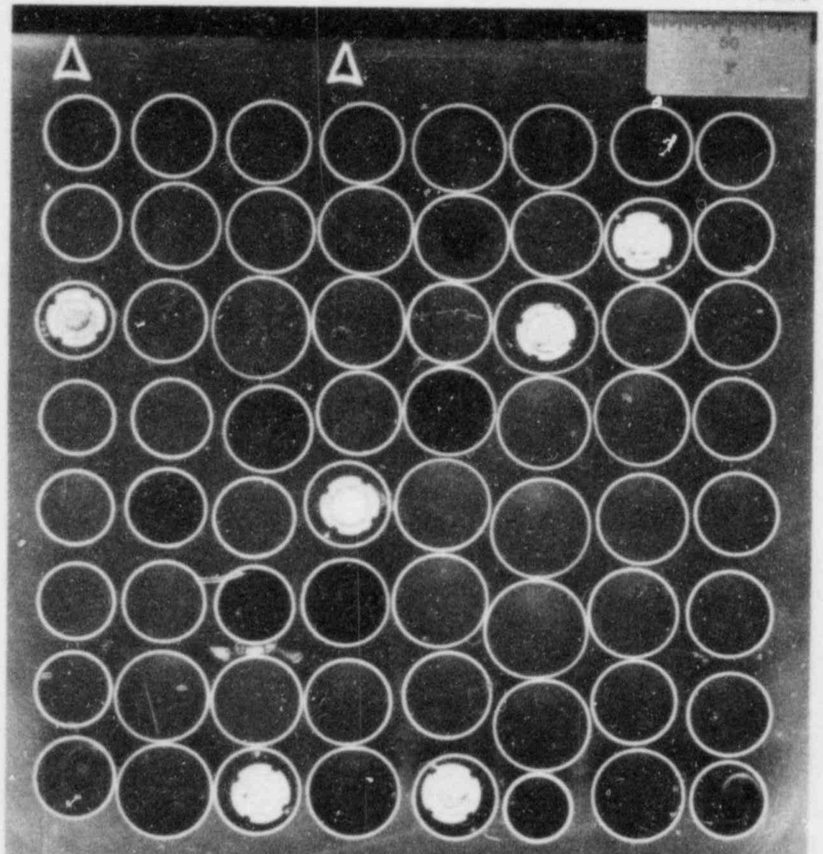

Fig. 88. Section at 42.6-cm elevation.

M&C PHOTO Y-179707

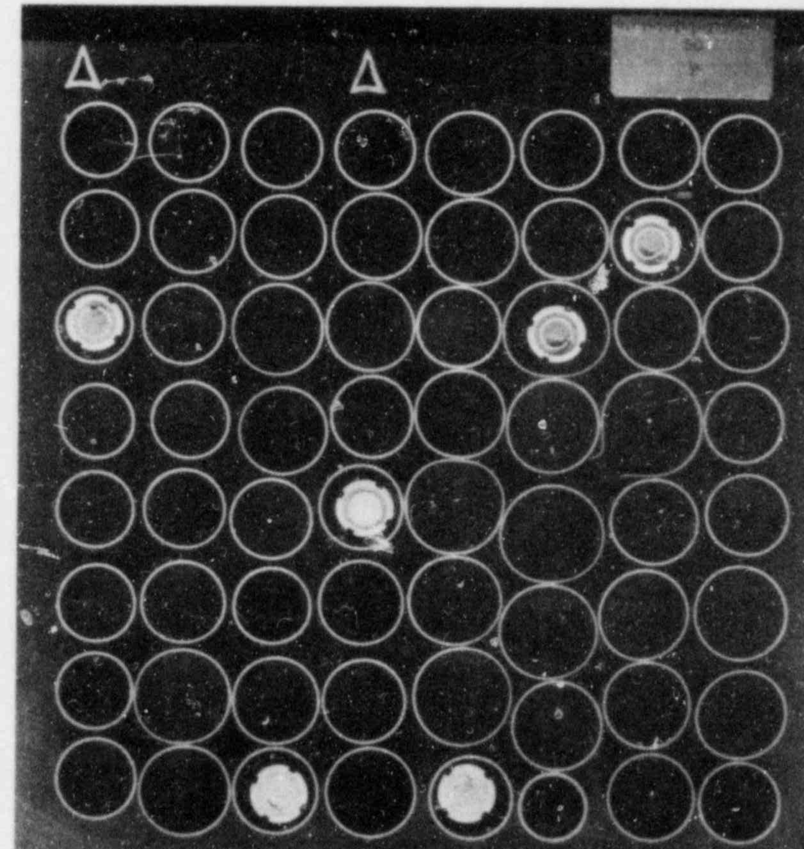

Fig. 89. Section at 44.4-cm elevation.

M&C PHOTO Y-179718

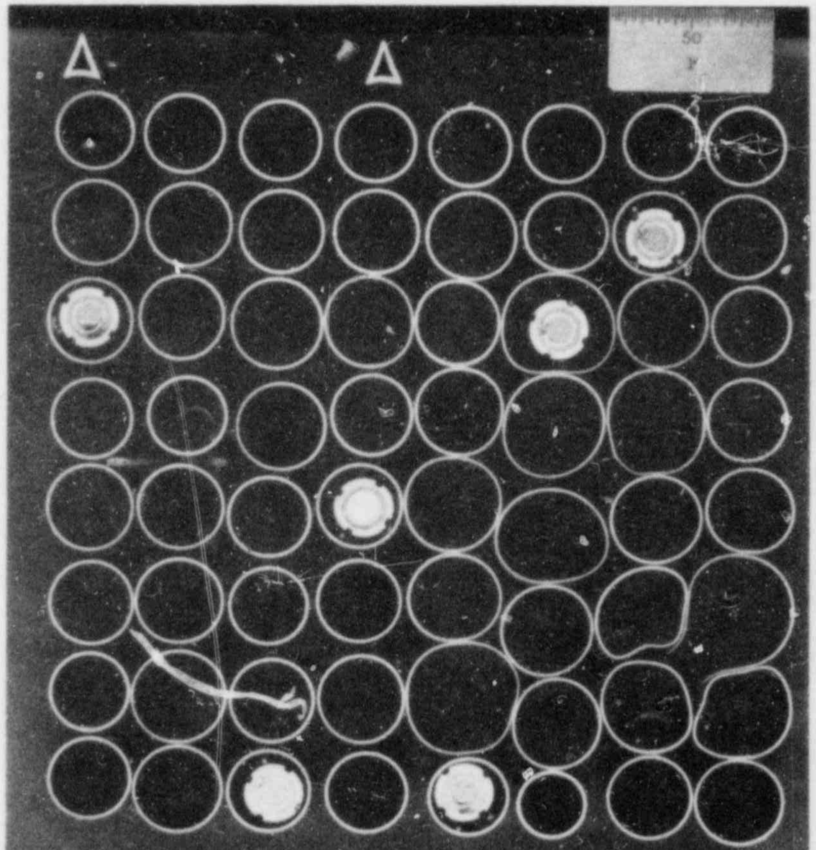

Fig. 90. Section at 46.4-cm elevation.

M&C PHOTO Y-180240

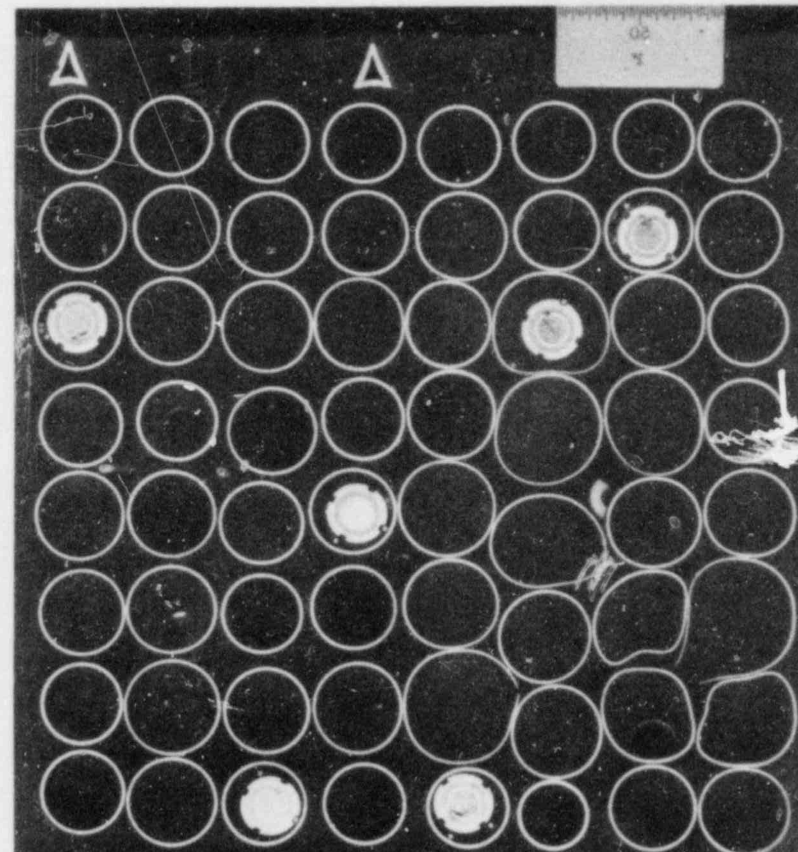

Fig. 91. Section at 46.9-cm elevation (reversed image to show tubes in correct positions).

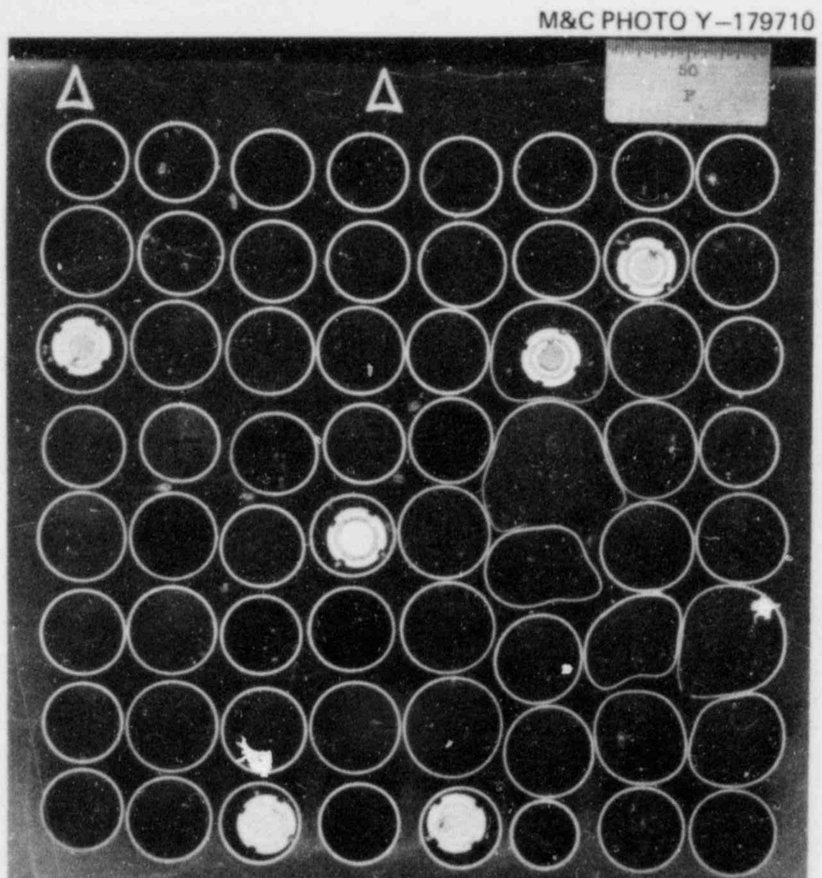

Fig. 92. Section at 48.0-cm elevation.

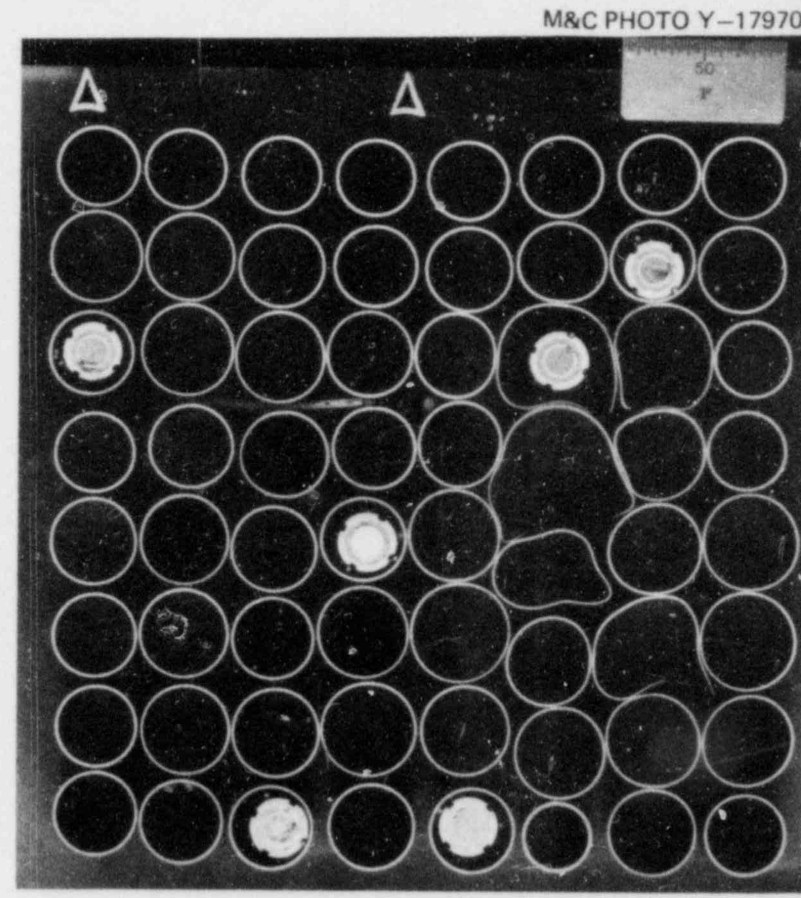

Fig. 93. Section at 49.6-cm elevation.

M&C PHOTO Y–179711

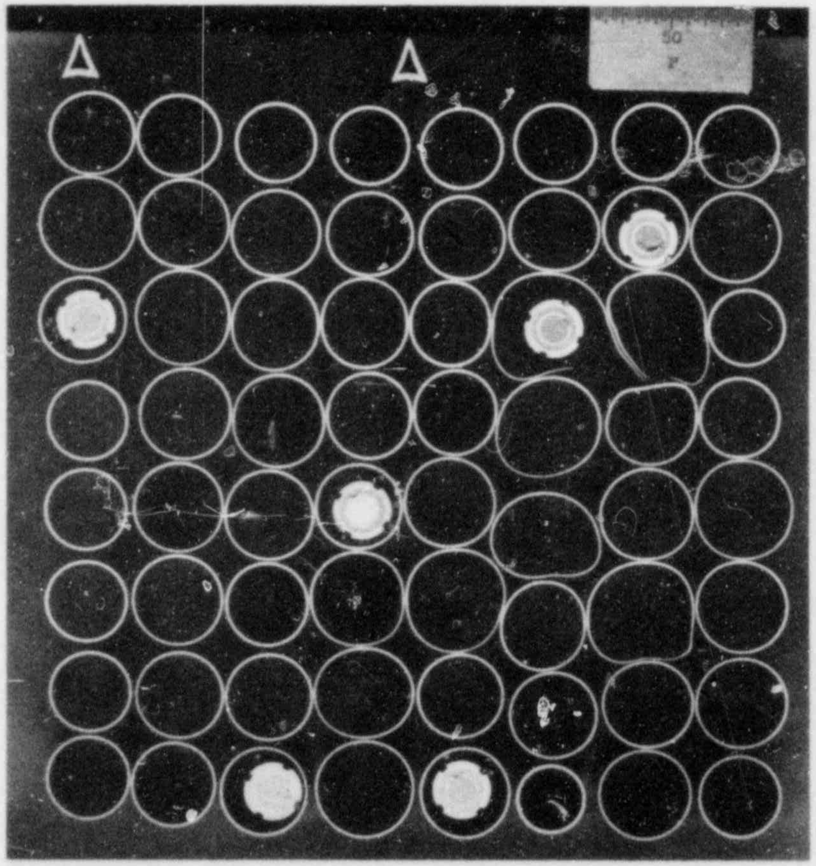

Fig. 94. Section at 51.2-cm elevation.

M&C PHOTO Y–179717

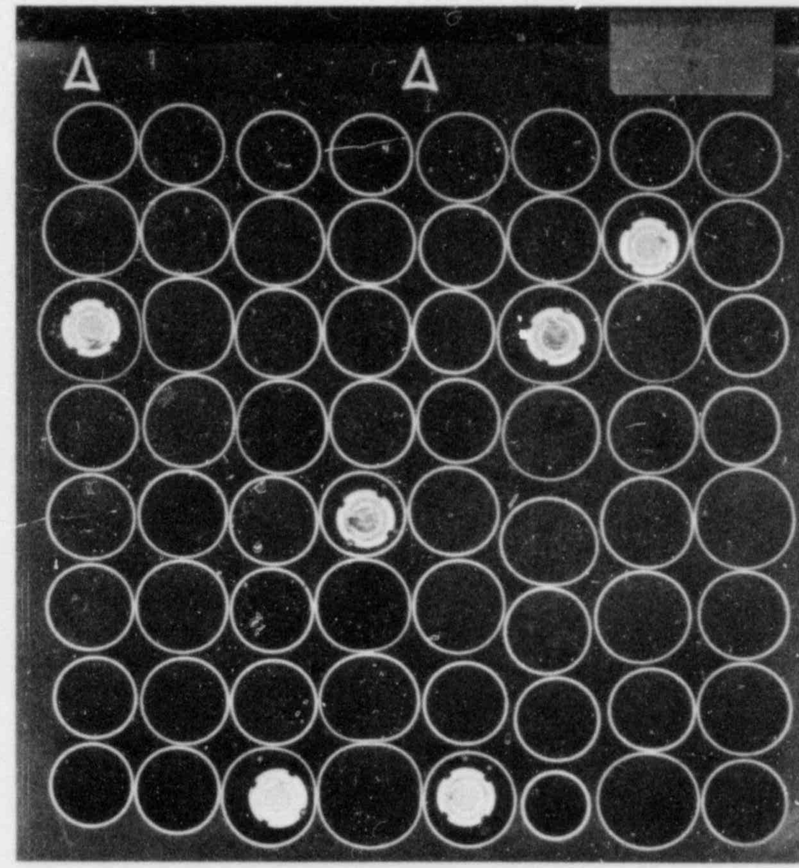

Fig. 95. Section at 53.0-cm elevation.

M&C PHOTO Y−179716

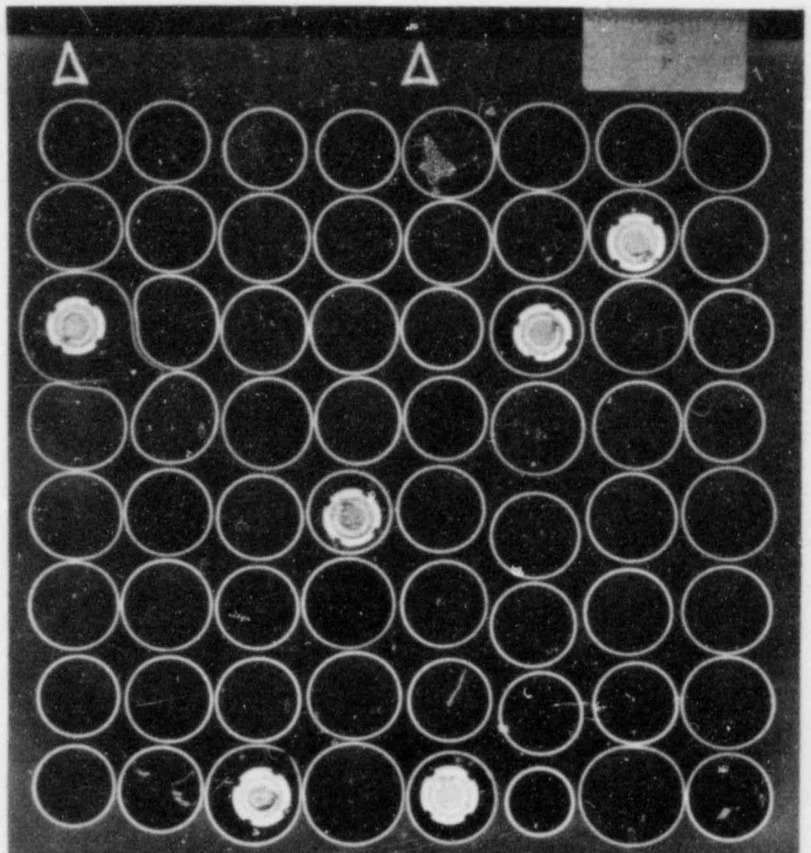

Fig. 96. Section at 54.6-cm elevation.

M&C PHOTO Y−179715

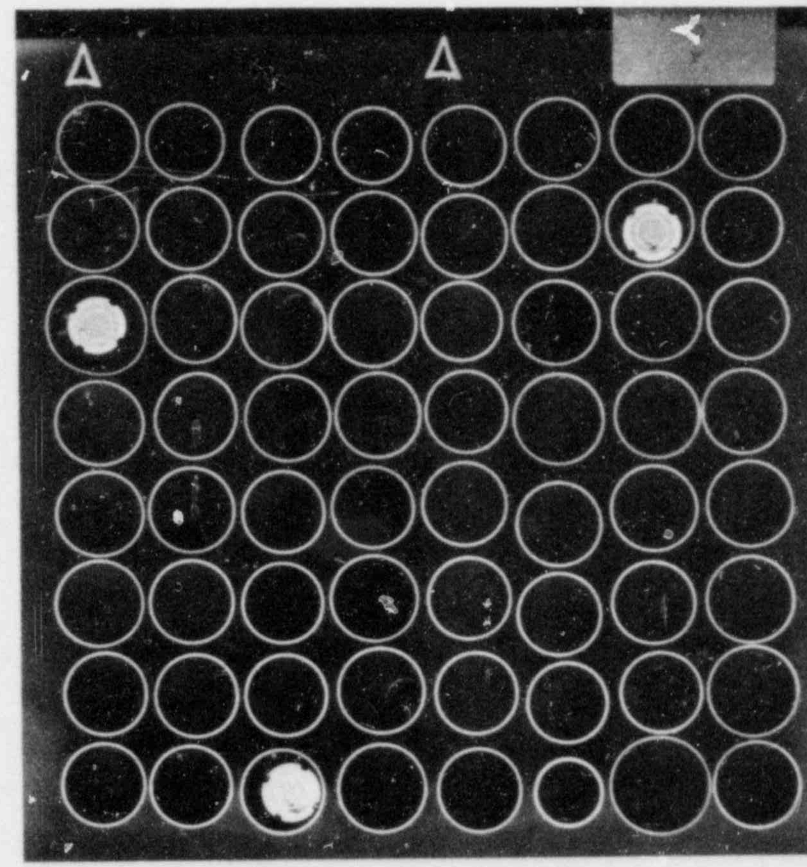

Fig. 97. Section at 56.2-cm elevation.

M&C PHOTO Y-179708

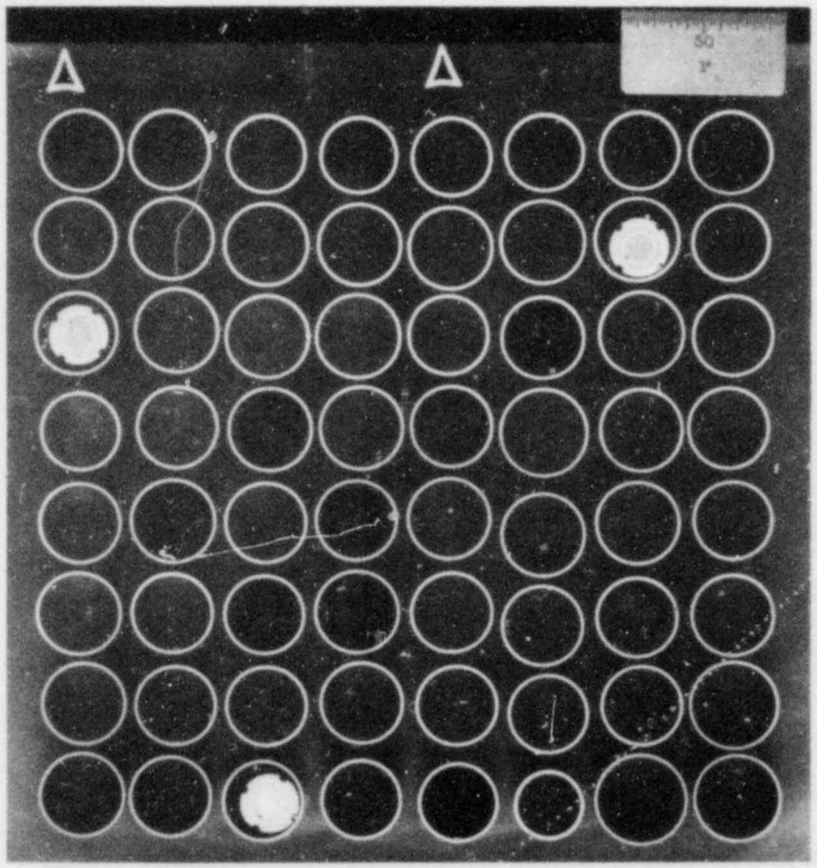

Fig. 98. Section at 57.8-cm elevation.

M&C PHOTO Y-179712

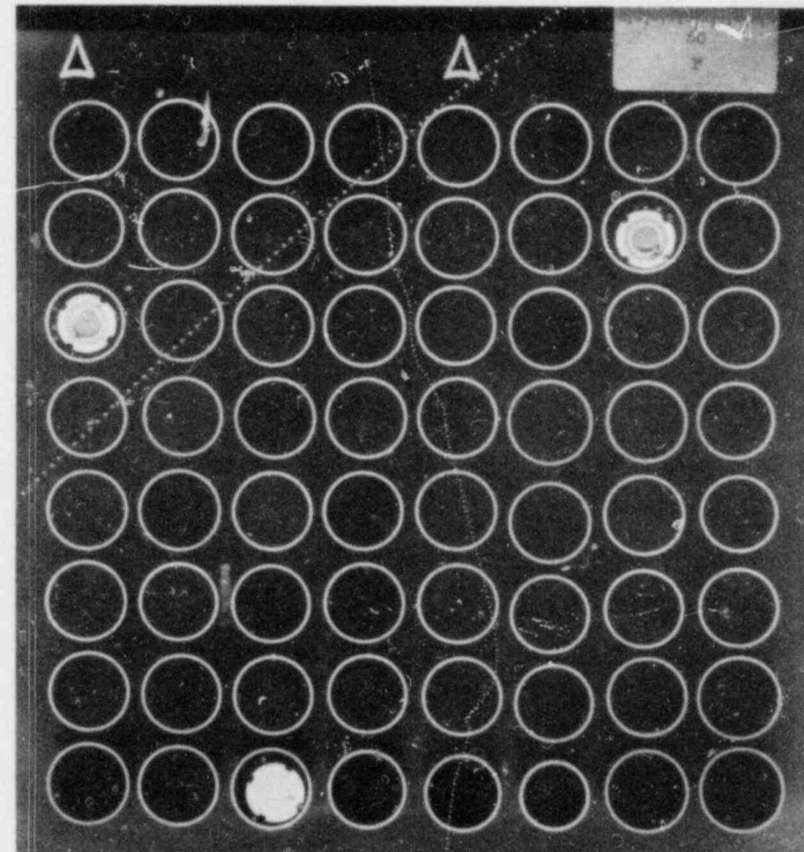

Fig. 99. Section at 59.6-cm elevation.

M&C PHOTO Y–179747

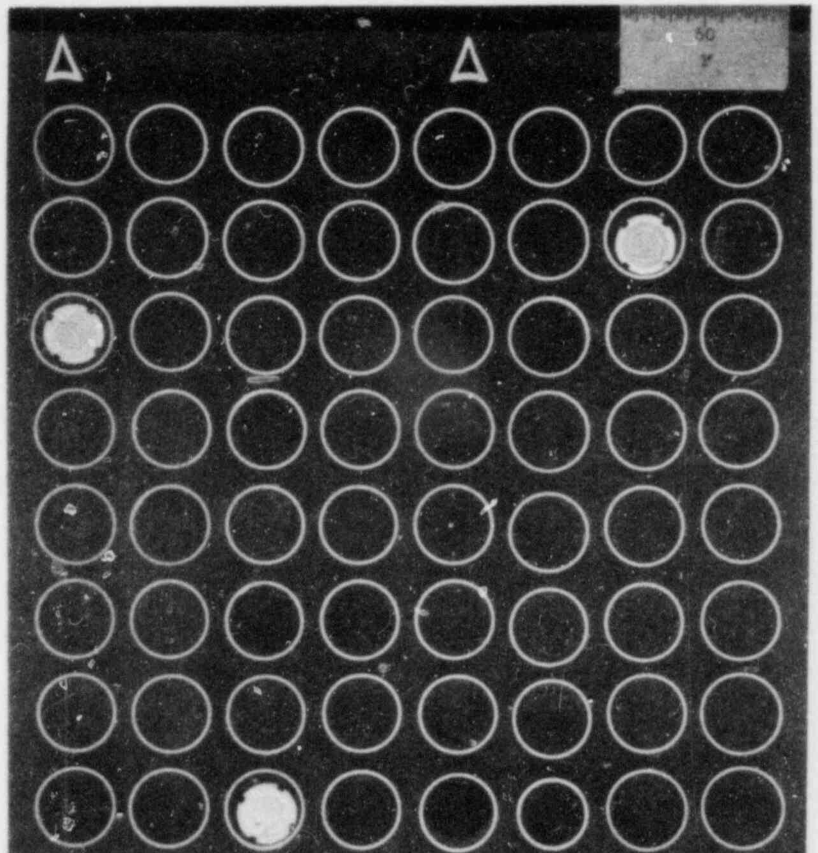

Fig. 100. Section at 61.2-cm elevation.

M&C PHOTO Y –179743

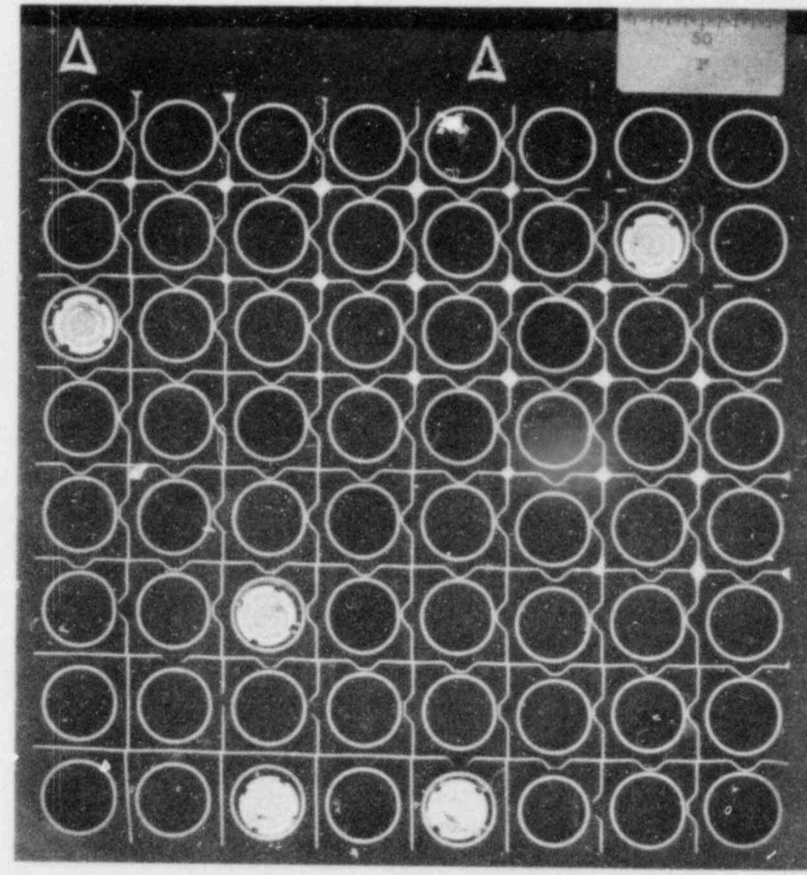

Fig. 101. Section through upper grid at 62.8-cm elevation.

M&C PHOTO Y–179742

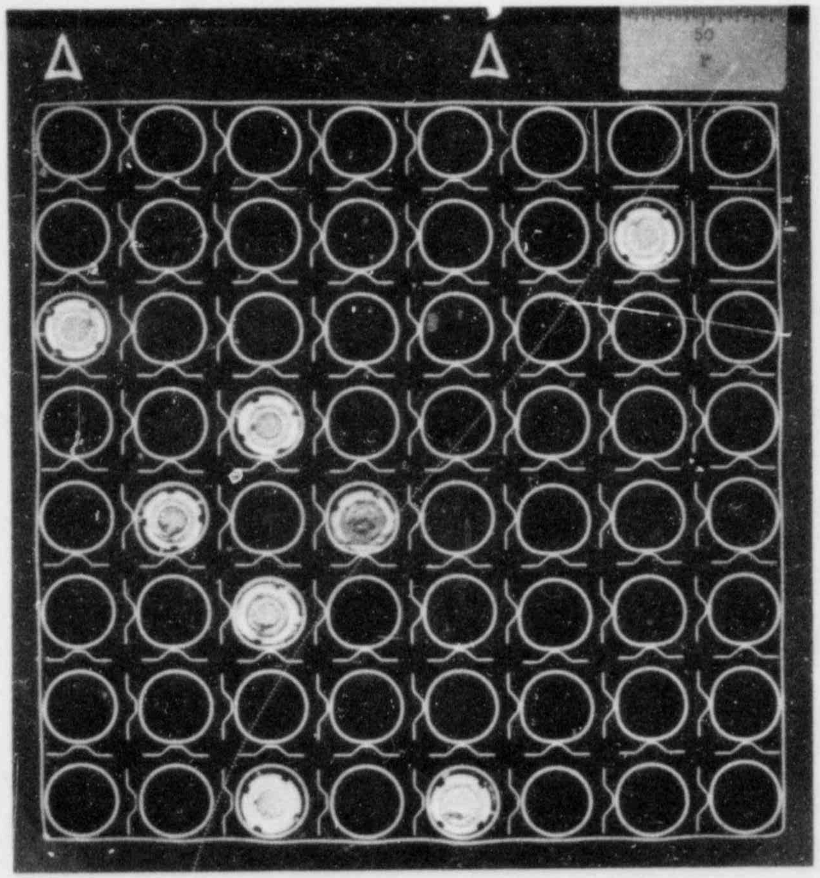

Fig. 102. Section through upper grid at 64.4-cm elevation.

M&C PHOTO Y–180238

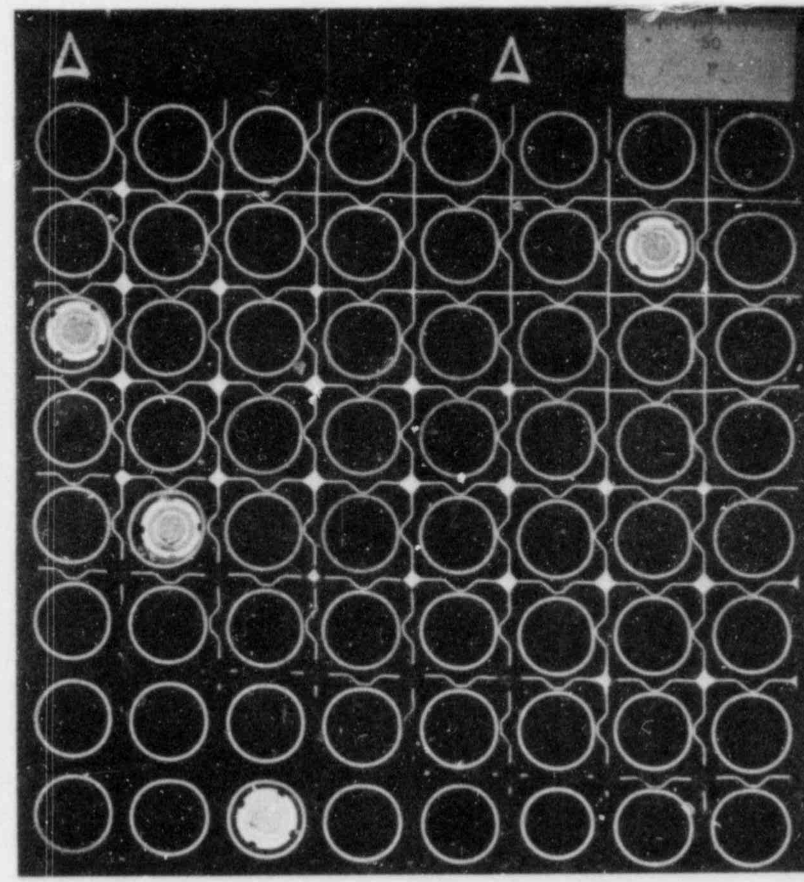

Fig. 103. Section through upper grid at 66.0-cm elevation.

M&C PHOTO Y–179744

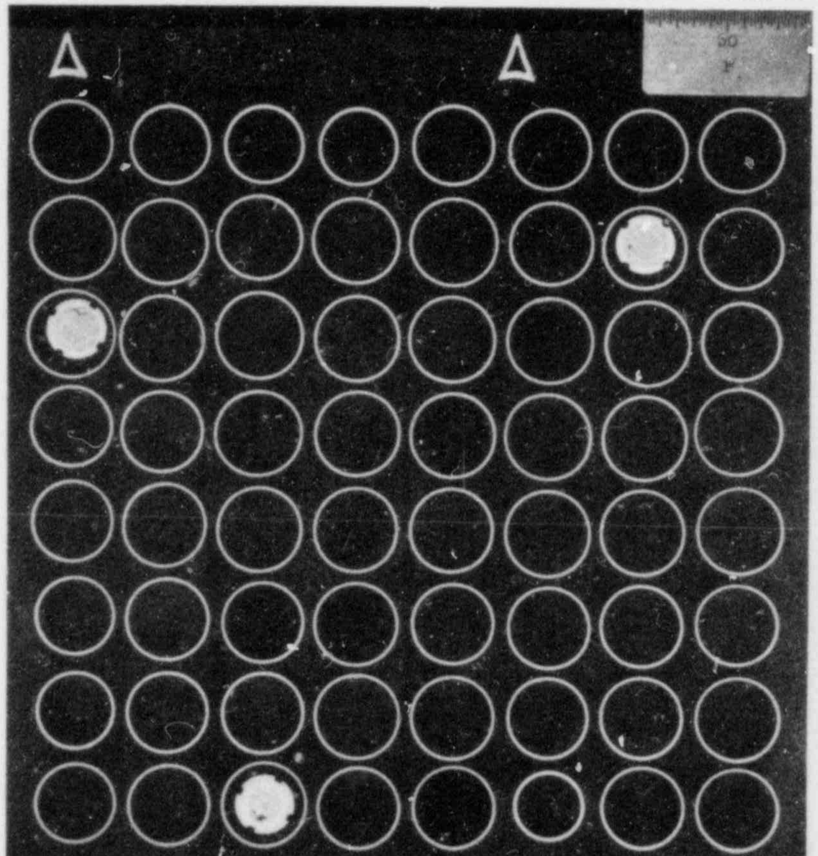

Fig. 104. Section at 67.8-cm elevation.

M&C PHOTO Y–179745

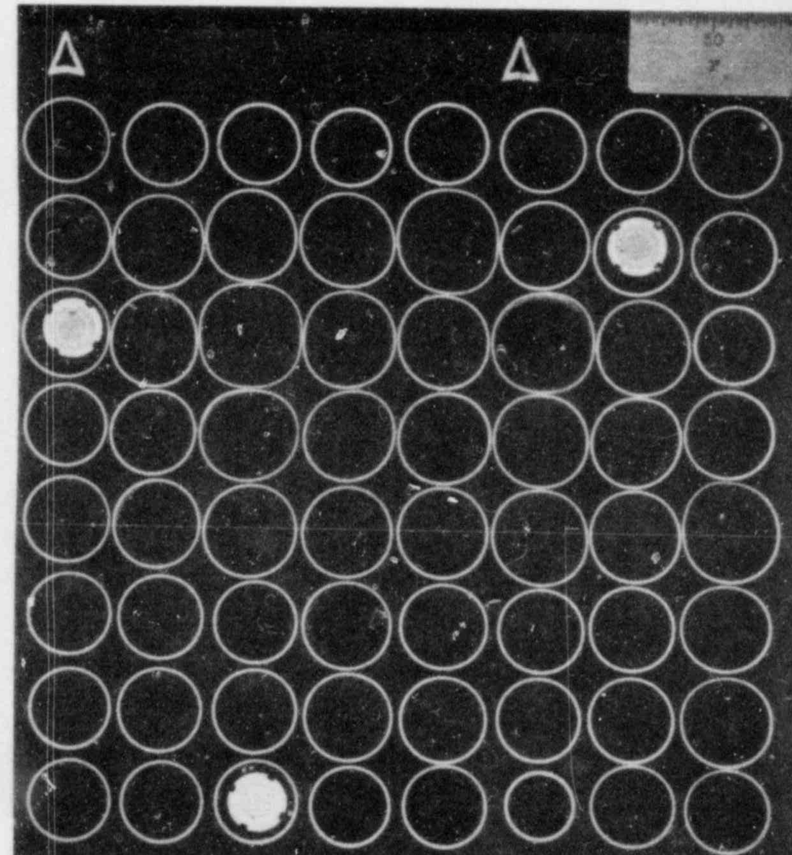

Fig. 105. Section at 69.5-cm elevation.

M&C PHOTO Y-179746

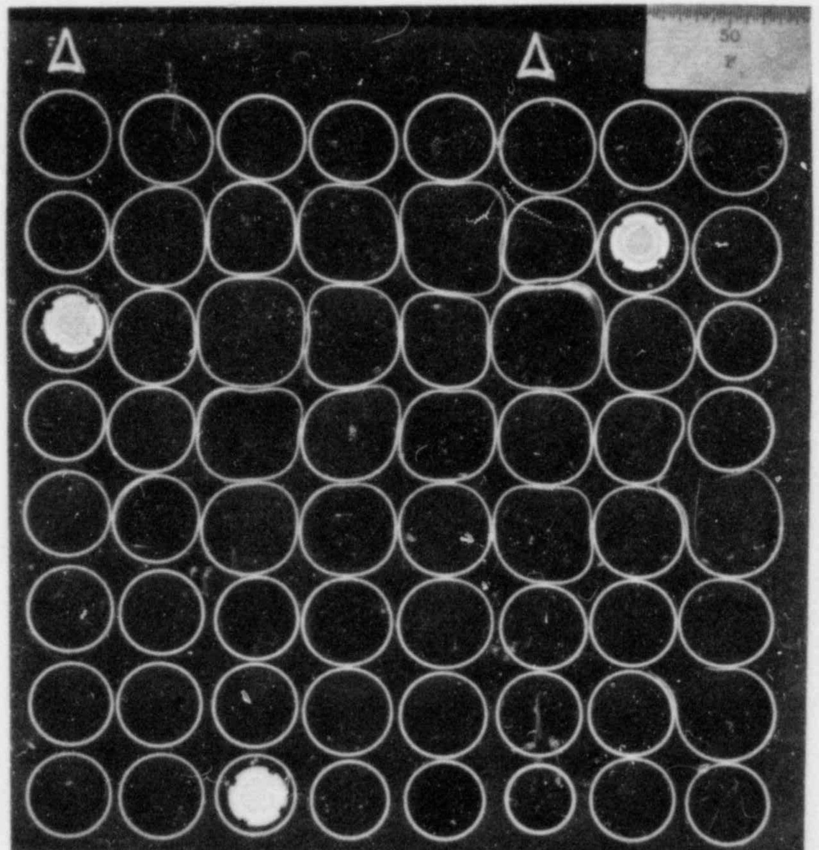

Fig. 106. Section at 71.0-cm elevation.

M&C PHOTO Y-179737

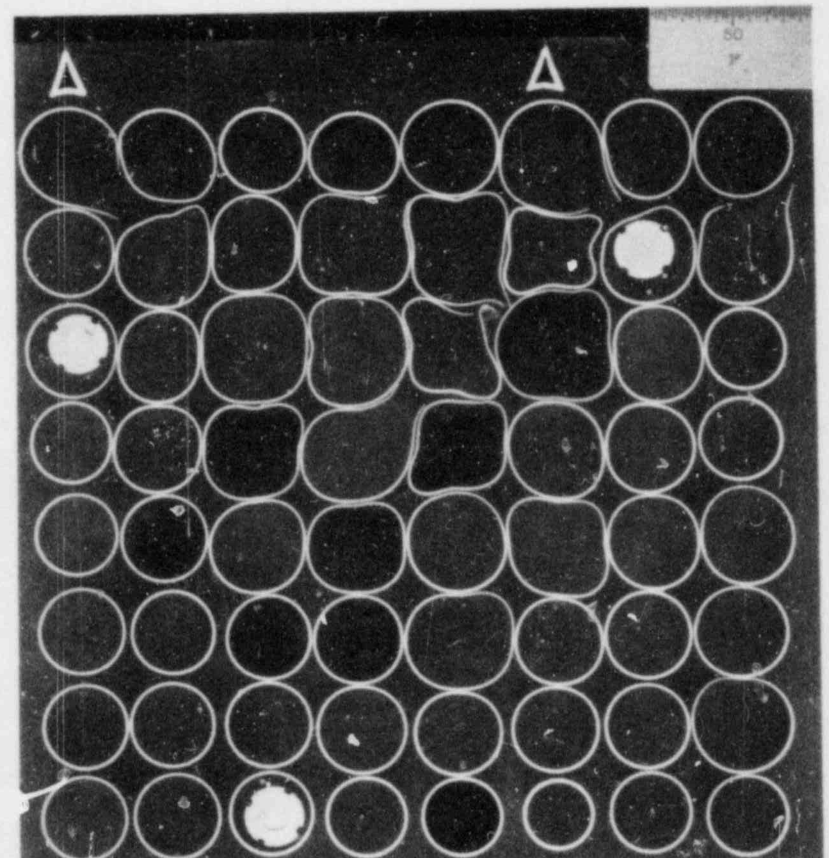

Fig. 107. Section at 72.8-cm elevation.

M&C PHOTO Y-179741

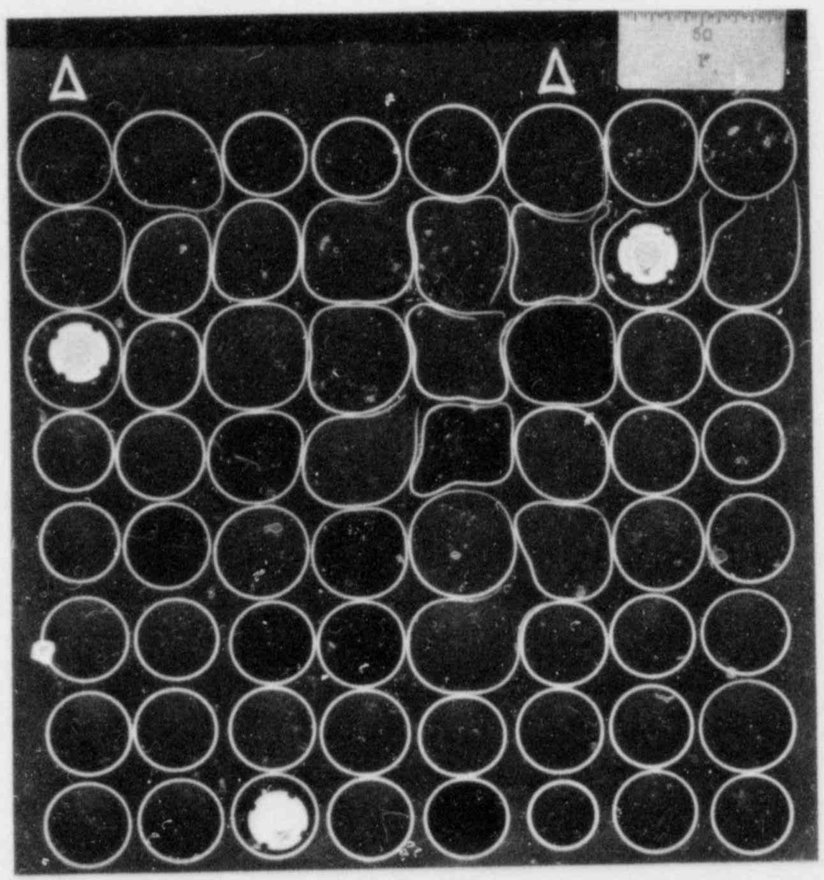

Fig. 108. Section ac 74.3-cm elevation.

M&C PHOTO Y-180242

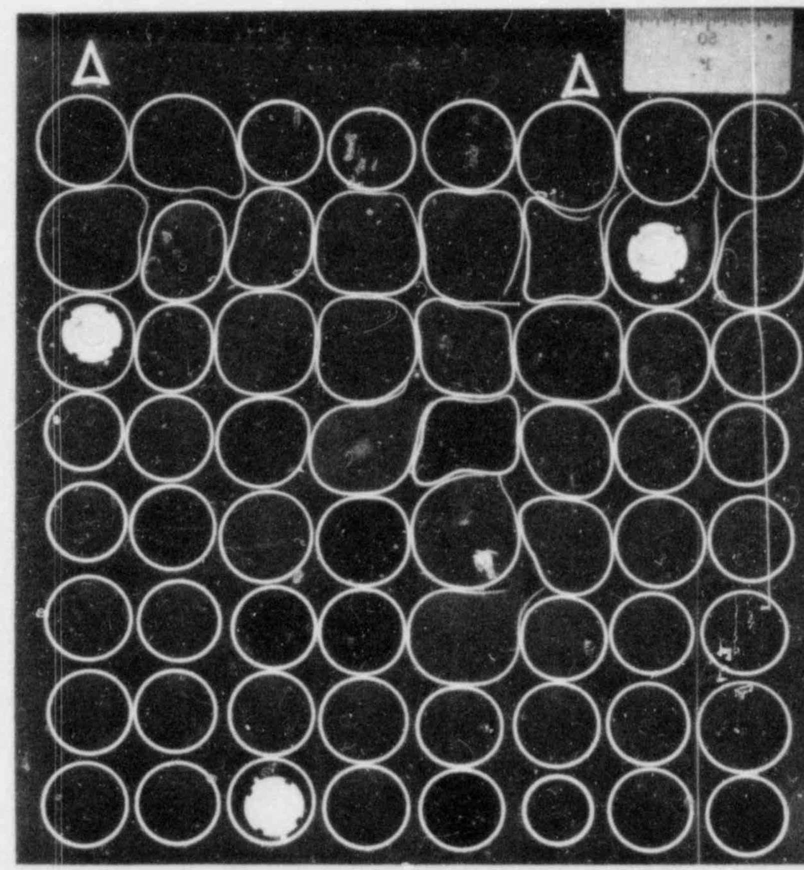

Fig. 109. Section at 74.8-cm elevation (reversed image to show tubes in correct positions).

M&C PHOTO Y–179740

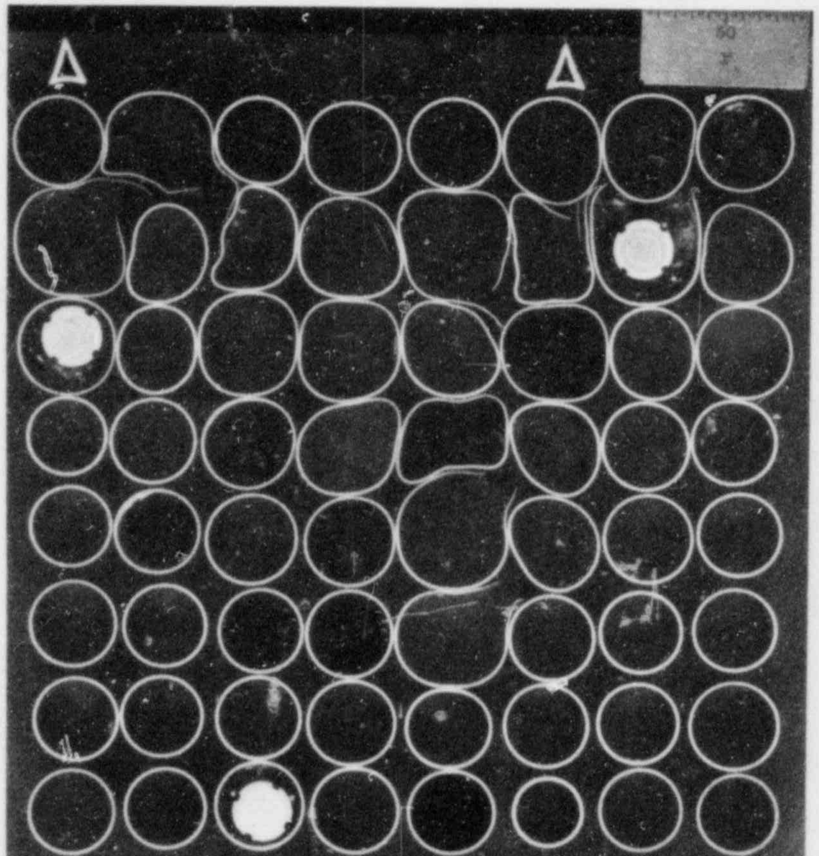

Fig. 110. Section at 75.8-cm elevation.

M&C PHOTO Y–180237

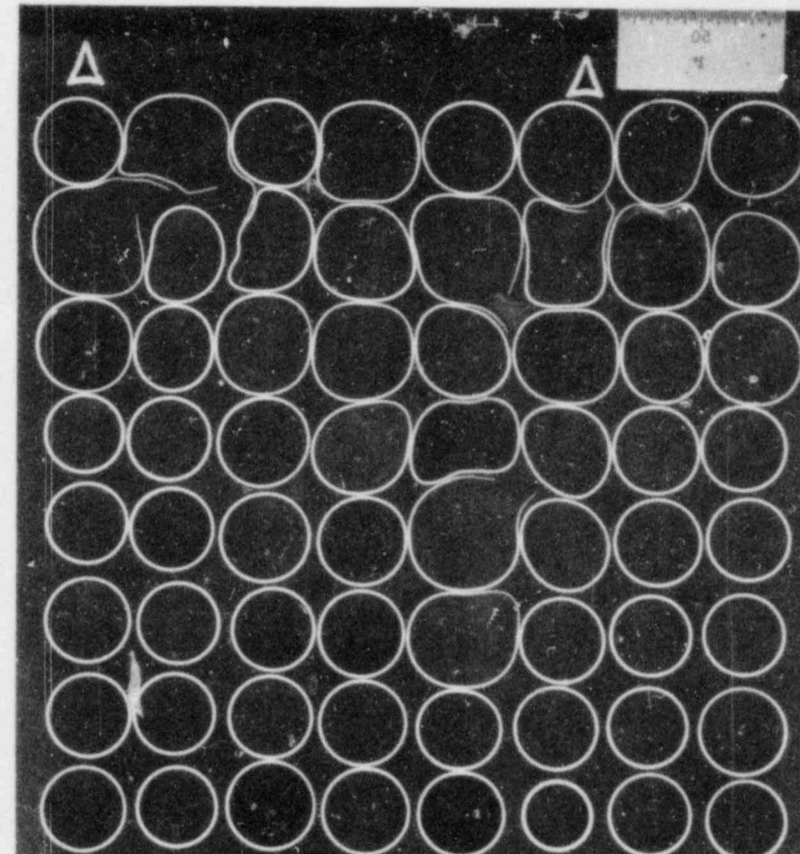

Fig. 111. Section at 76.3-cm elevation (reversed image to show tubes in correct positions).

M&C PHOTO Y–179778

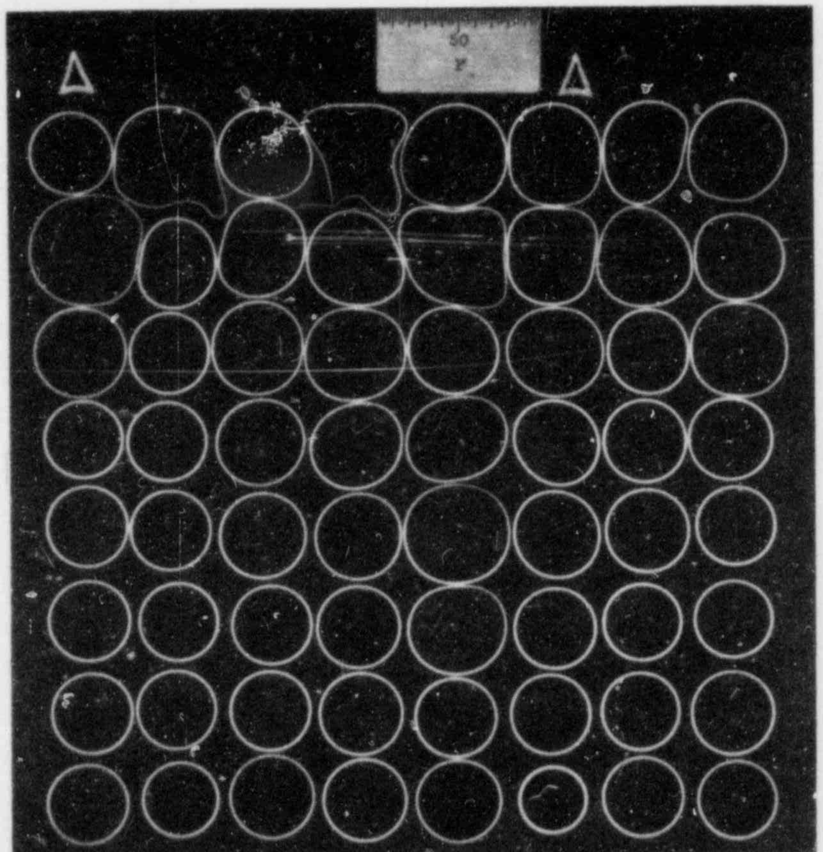

Fig. 112. Section at 77.4-cm elevation.

M&C PHOTO Y–179787

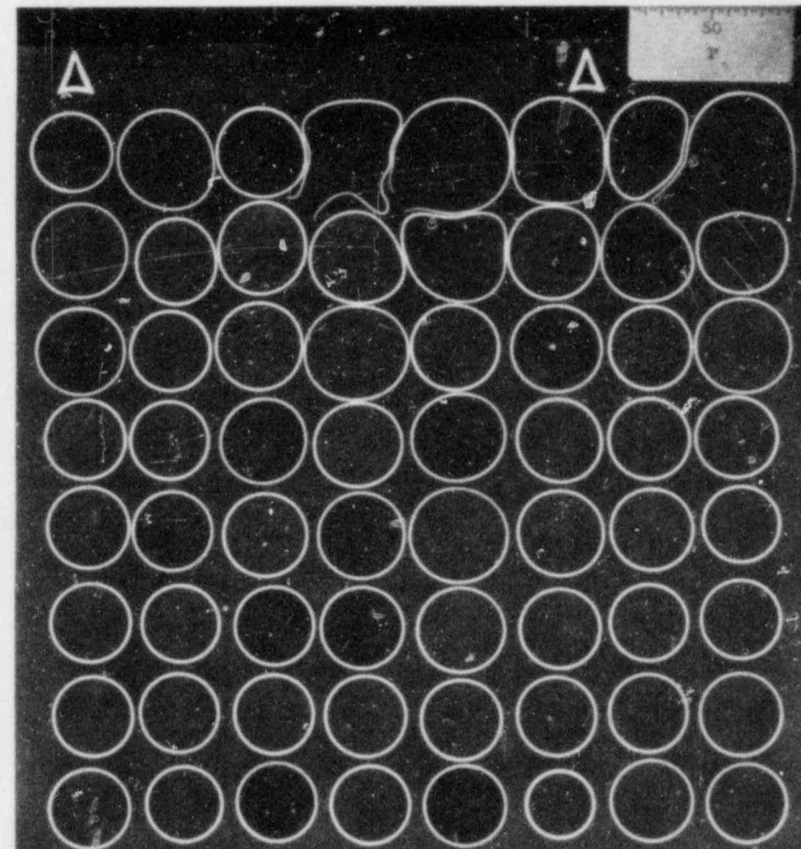

Fig. 113. Section at 78.9-cm elevation.

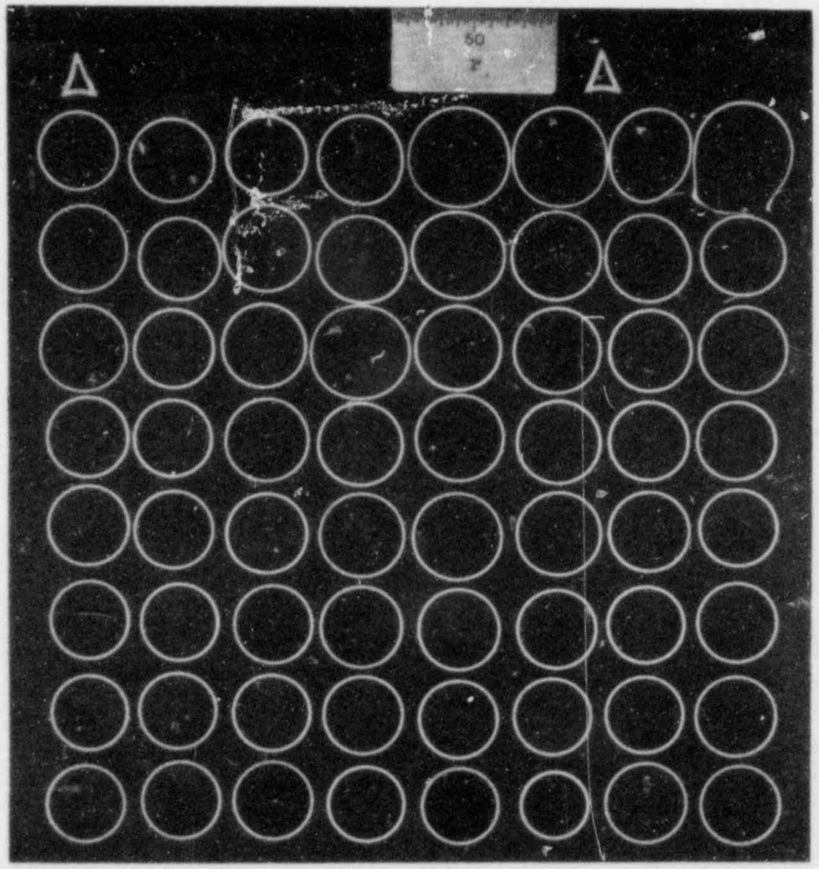

Fig. 114. Section at 80.4-cm elevation.

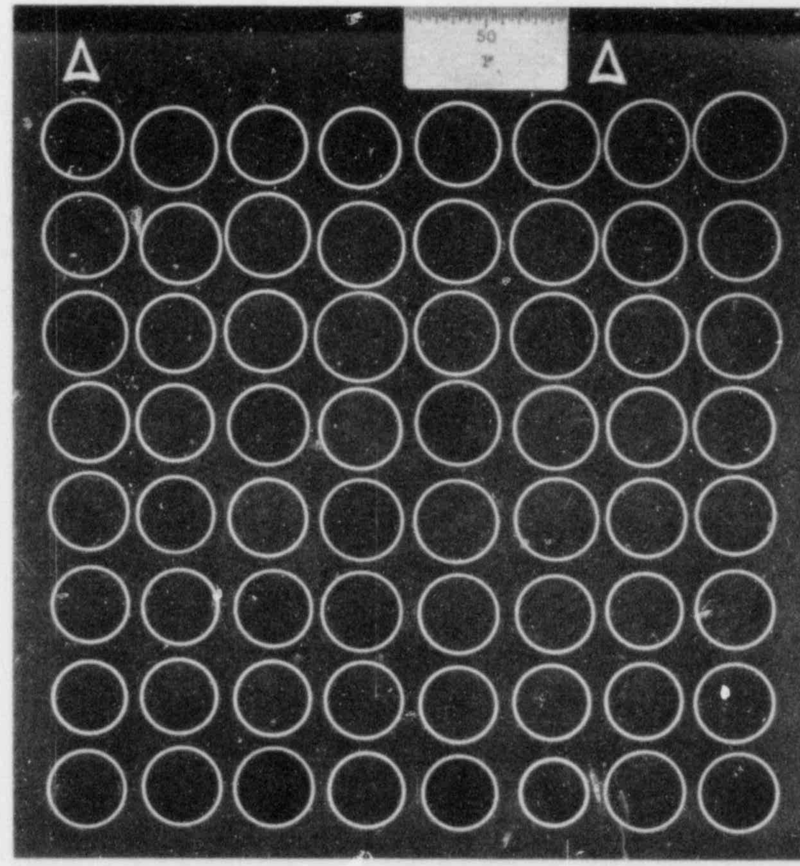

Fig. 115. Section at 81.9-cm elevation.

M&C PHOTO Y-179783

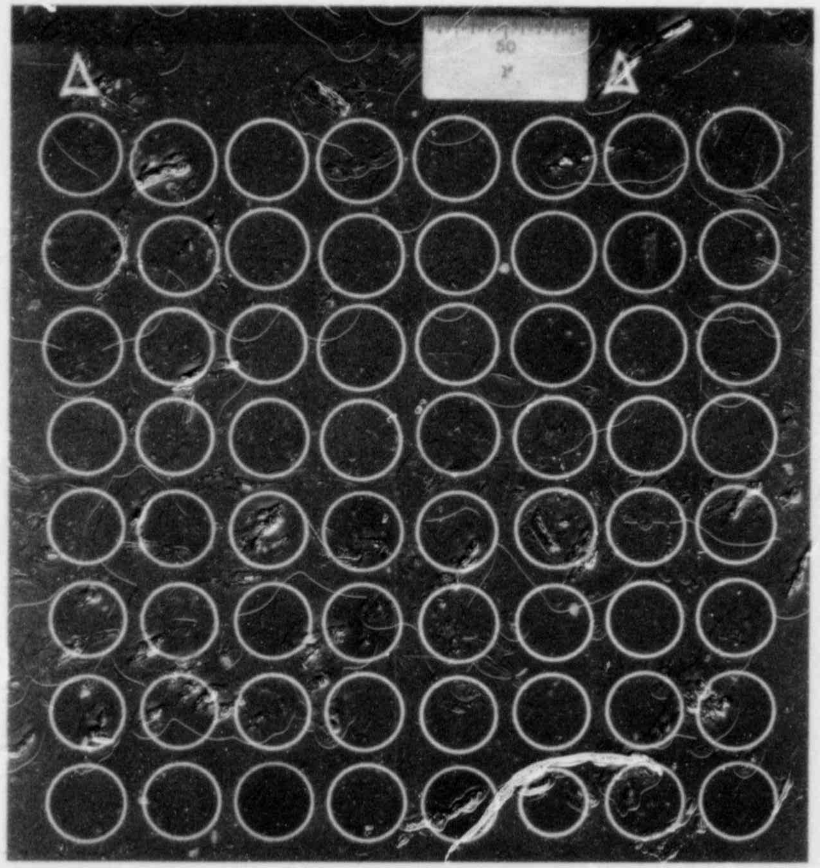

Fig. 116. Section at 83.5-cm elevation.

M&C PHOTO Y-179784

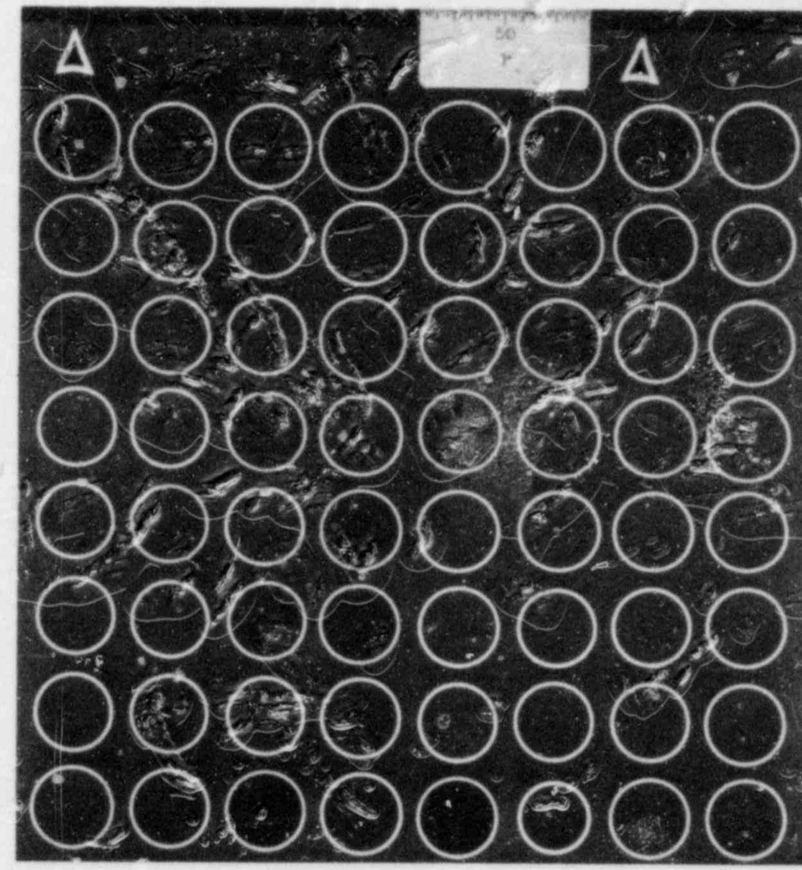

Fig. 117. Section at 85.1-cm elevation.

M&C PHOTO Y–179780

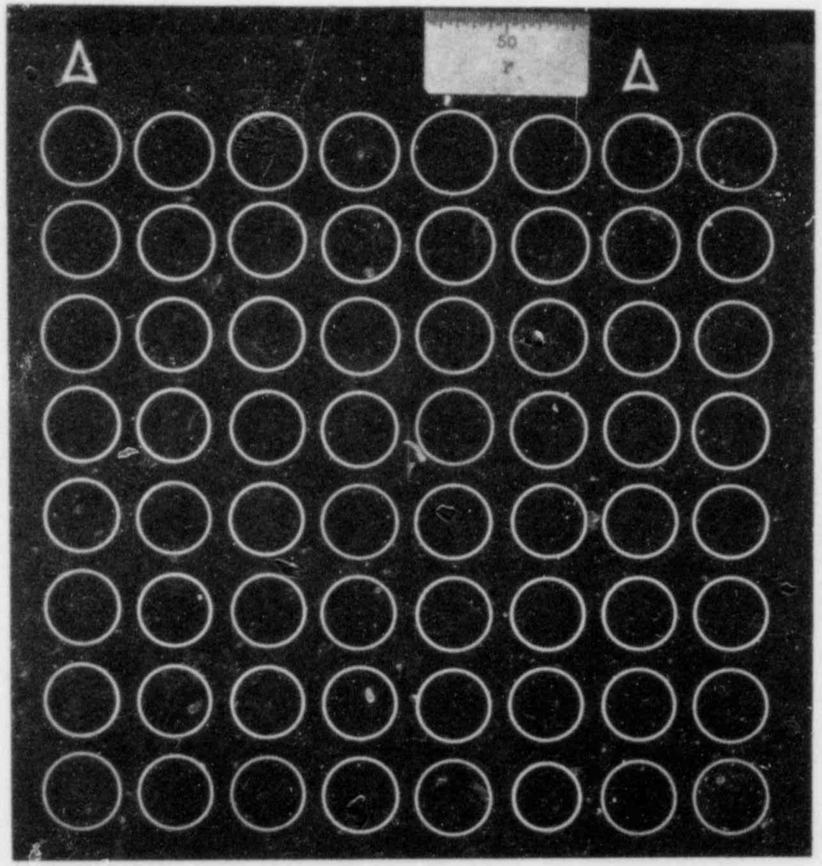

Fig. 118. Section at 86.8-cm elevation.

M&C PHOTO Y–180239

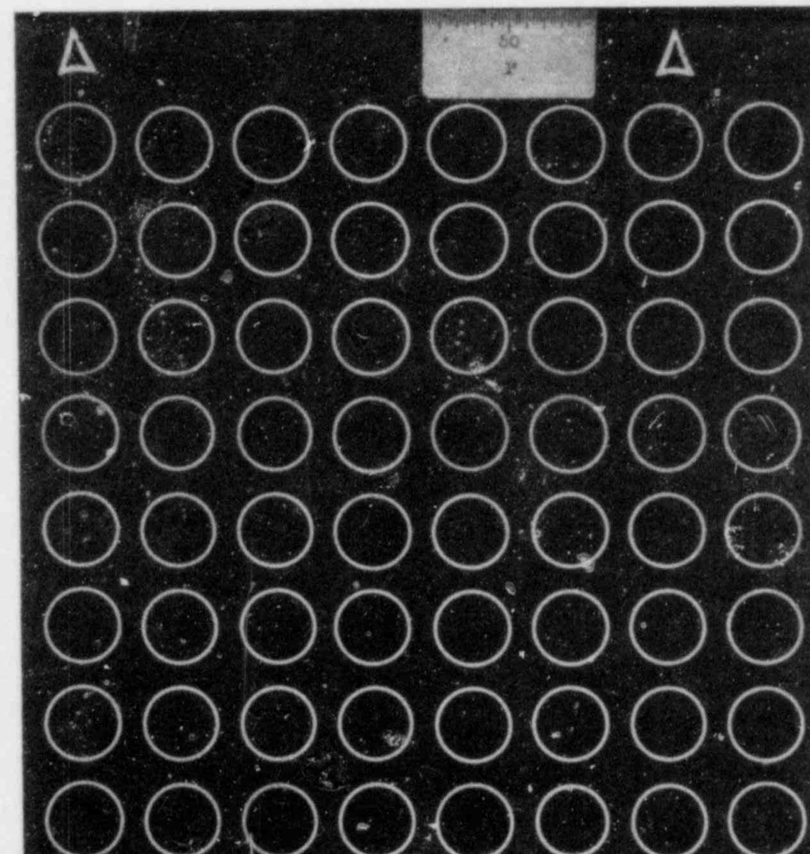

Fig. 119. Section at 88.6-cm elevation.

M&C PHOTO Y-179781

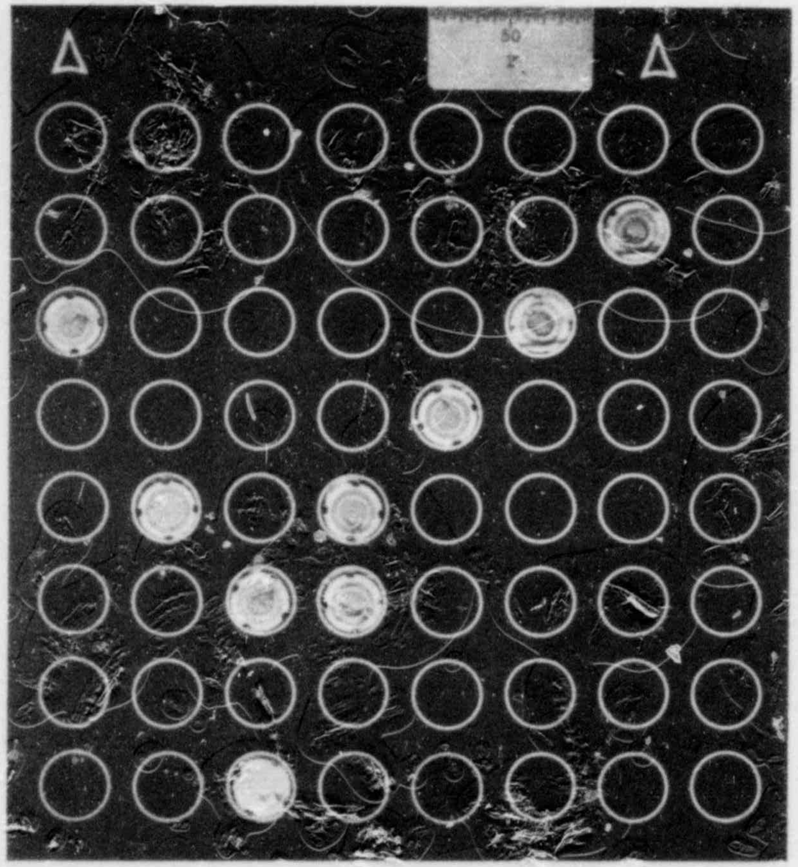

Fig. 120. Section at 90.4-cm elevation.

M&C PHOTO Y-179779

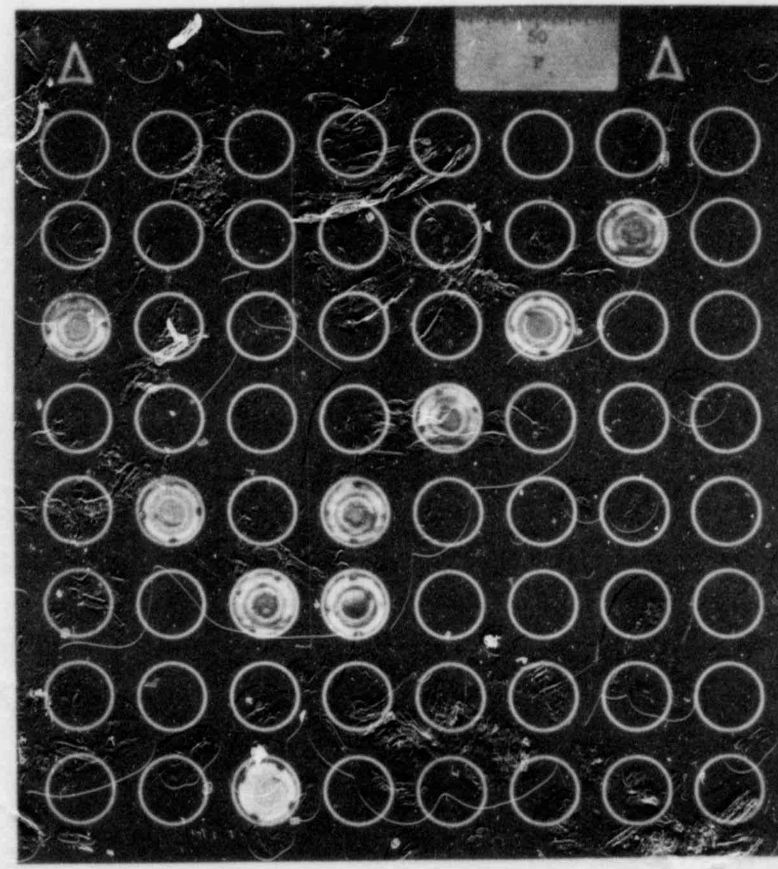

Fig. 121. Section at 92.2-cm elevation.

M&C PHOTO Y–180241

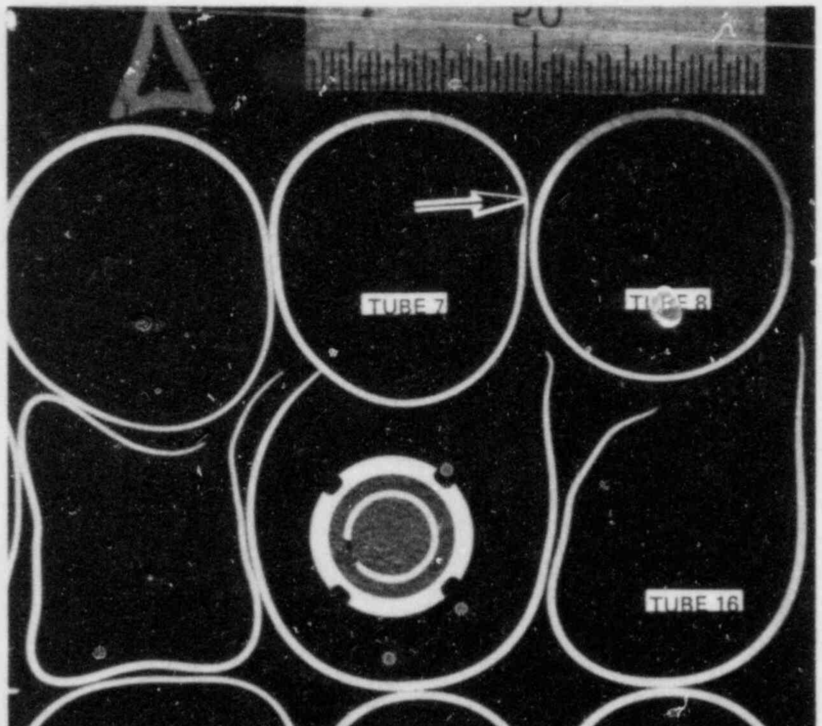

Fig. 122. Enlarged view of portion of Fig. 109 showing necked down region of tube wall at edge of pinhole failure in tube 7.

ORNL–DWG 81–16329A ETD

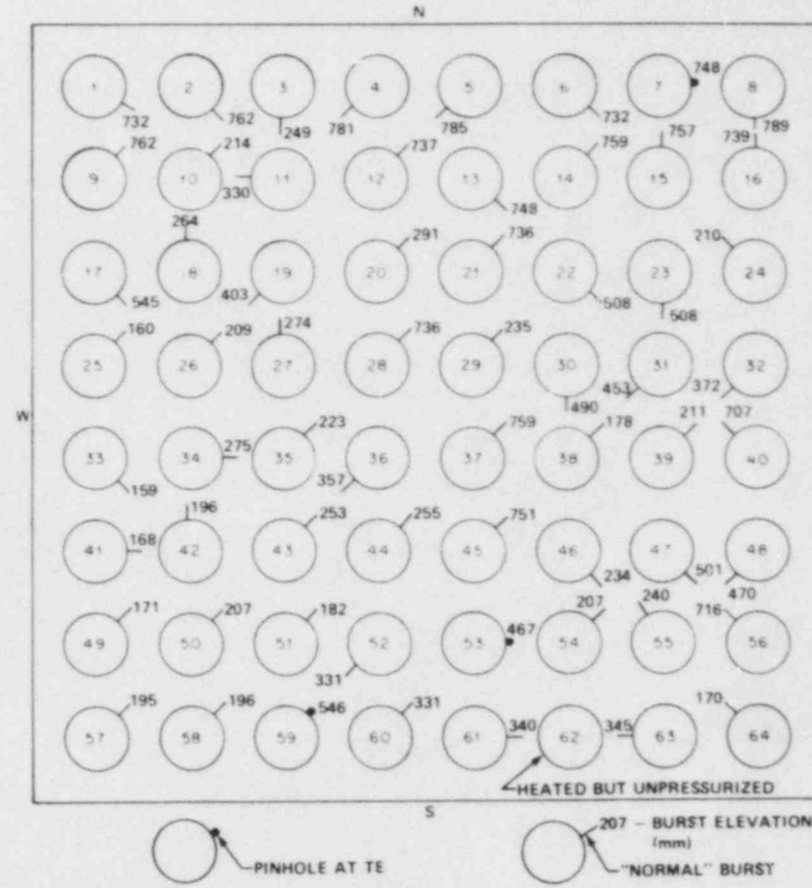

Fig. 123. Approximate burst midpoint elevations and orientations.

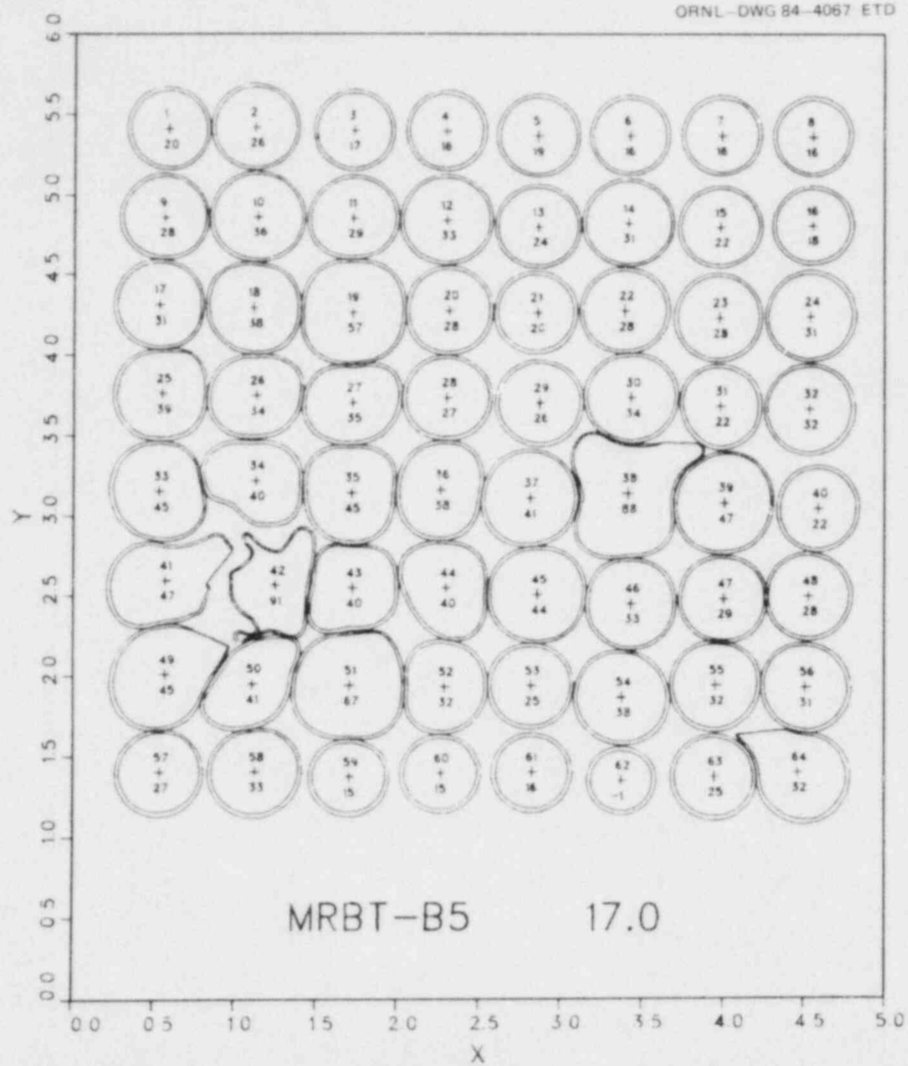

Fig. 124. Example of software reconstruction of photograph in Fig. 73.

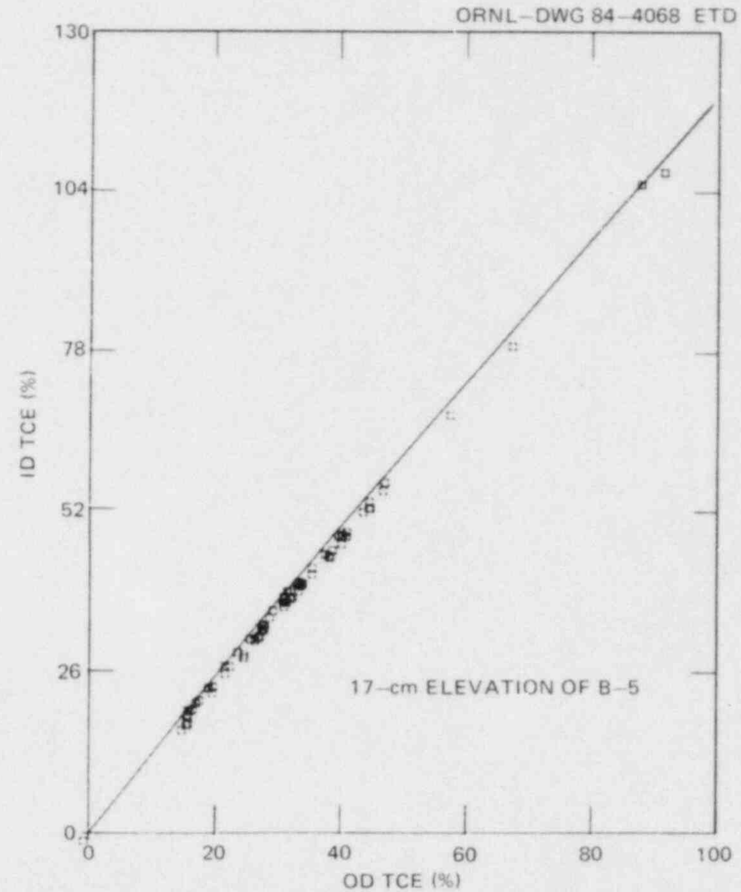

Fig. 125. Example of strain data verification procedure.

ORNL-DWG 84-4069 ETD

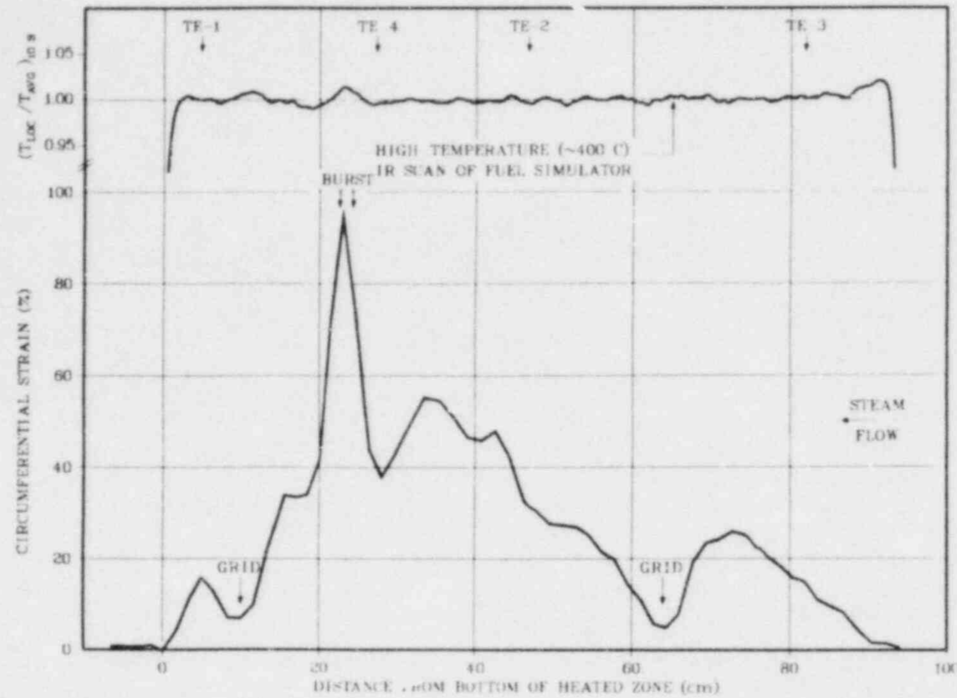

Fig. 126. Deformation profile of simulator 46 with the maximum burst strain.

ORNL-DWG 84-4070 ETD

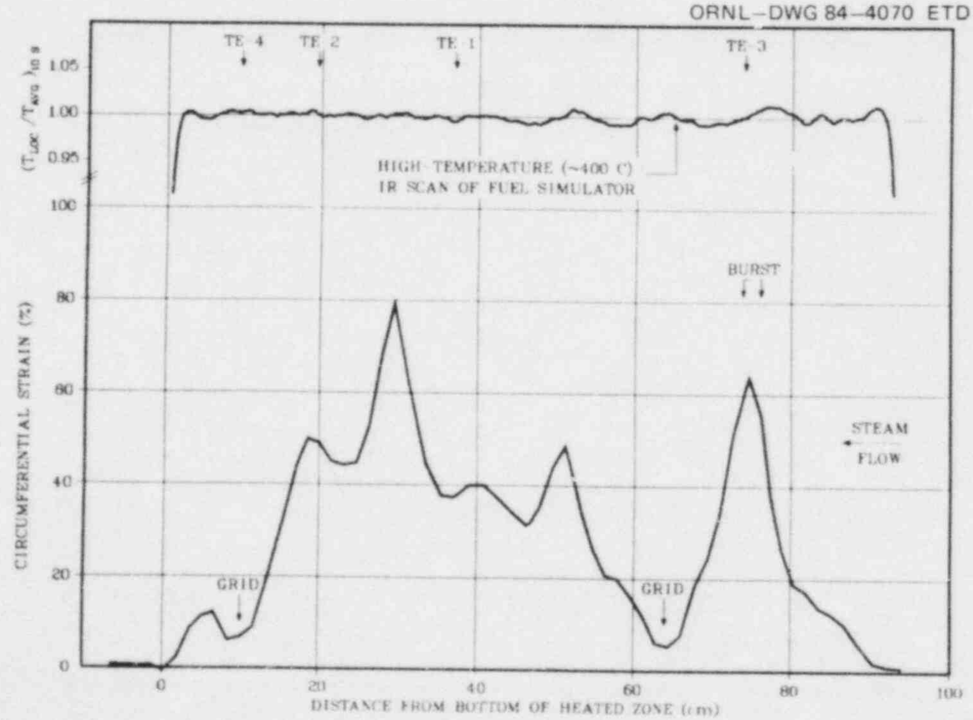

Fig. 127. Deformation profile of simulator 45 showing large ballooning in nonburst region.

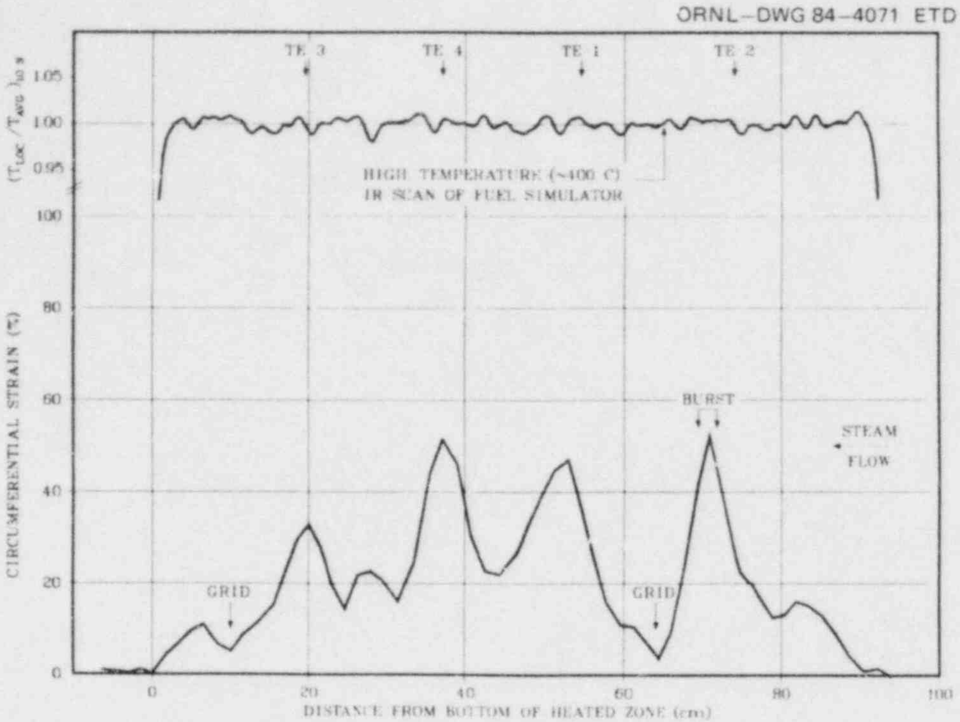

Fig. 128. Deformation profile of simulator 40 showing cyclic deformation pattern of exterior simulators.

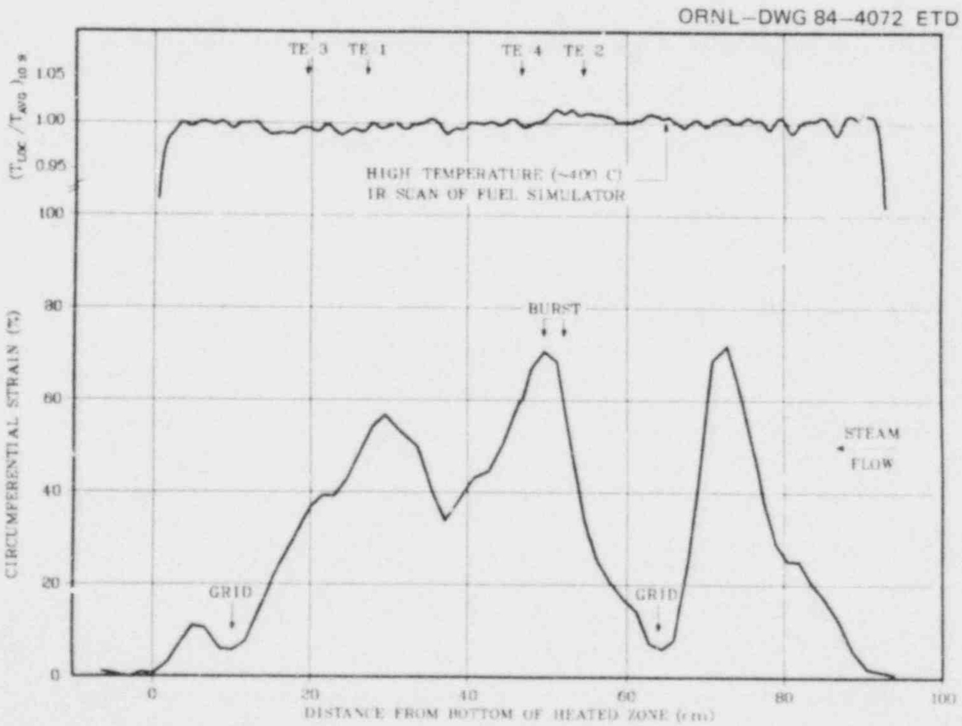

Fig. 129. Deformation profile of simulator 22 with the maximum volumetric expansion.

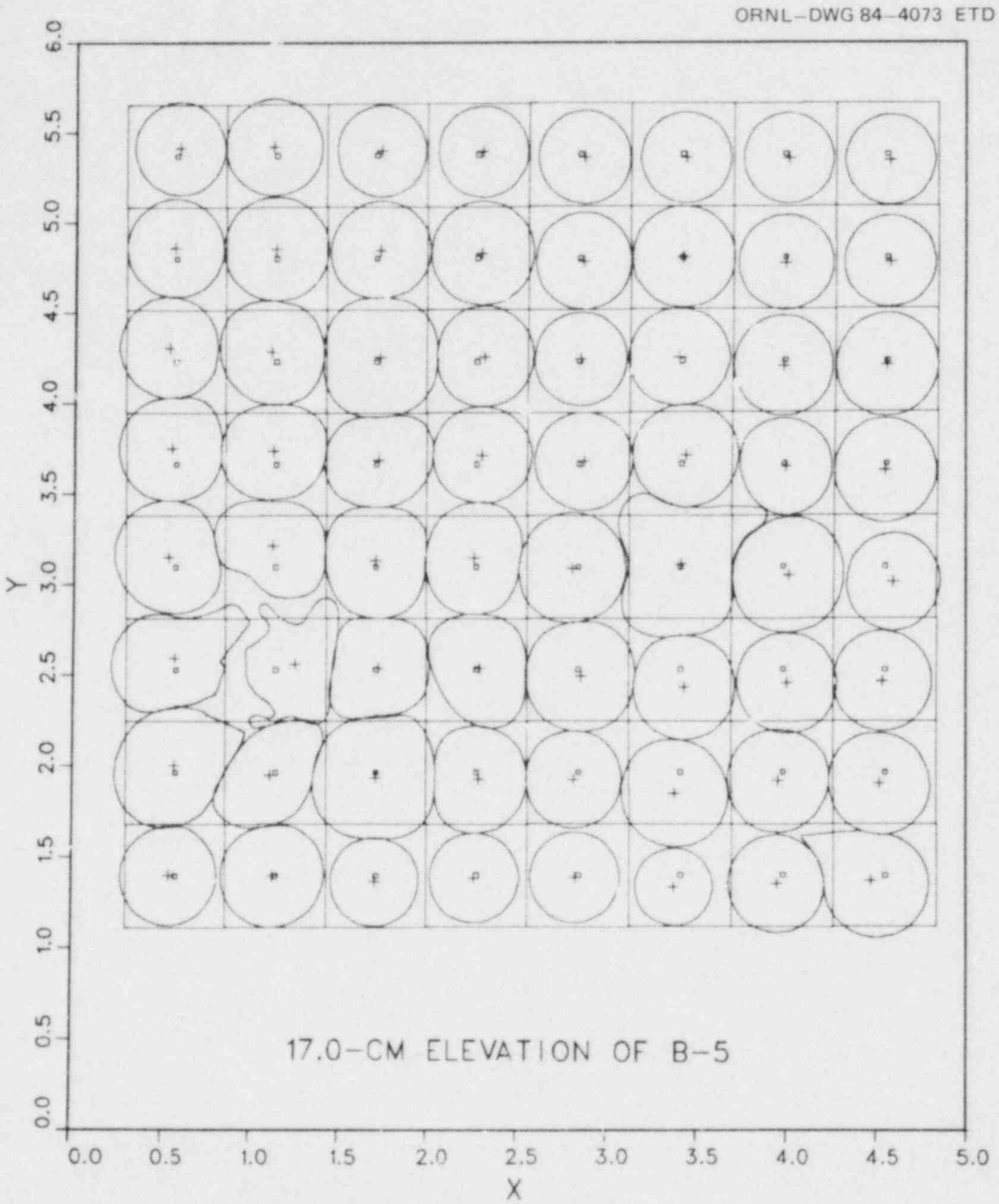

Fig. 130. Example of tube relocation at 17.0-cm elevation.

Table 6. Summary of B-5 test conditions at rod 21 burst time

TIME FROM POWER-ON 44.00 SEC. TIME FROM POWER-OFF -4.45 SEC. RECORD NUMBER 535-A

ROD NO.	DIFFERENTIAL PRESSURE (KPA)	TEMPERATURE (DEG C) TE-1	TE-2	TE-3	TE-4	AVG	TIME FROM BURST (SEC)	ROD NO.	DIFFERENTIAL PRESSURE (KPA)	TEMPERATURE (DEG C) TE-1	TE-2	TE-3	TE-4	AVG	TIME FROM BURST (SEC)
1	11425	727	725	733	711	724	-5.60	2	10456	754	736	741	740	743	-1.65
3	10938	746	738	735	748	742	-2.90	4	10295	759	742	750	739	747	-0.85
5	10745	743	721	756	759	745	-3.50	6	10955	752	749	757	743	750	-2.40
7	10614	759	749	742	766	754	-1.75	8	10978	732	737	731	720	730	-3.35
9	10960	734	744	750	754	746	-4.15	10	10366	759	742	745	735	745	-2.30
11	10042	752	744	750	753	750	-1.50	12	9942	765	773	760	757	764	-1.60
13	10209	737	745	751	749	746	-1.55	14	9731	757	768	764	759	762	-1.05
15	10501	749	752	742	753	749	-1.80	16	10097	758	764	770	760	763	-0.55
17	11050	748	736	724	746	738	-4.45	18	10083	756	762	764	761	760	-1.25
19	10246	754	752	762	723	748	-2.50	20	10130	746	743	747	748	746	-2.20
21	9110	745	752	763	766	757	0.00	22	10108	764	757	747	759	757	-2.25
23	9874	763	759	746	747	754	-1.20	24	10764	737	731	753	745	741	-2.65
25	10966	748	744	732	725	737	-2.20	26	10416	734	759	739	745	745	-1.60
27	9737	760	746	747	749	751	-1.10	28	10139	769	740	764	741	753	-1.70
29	10004	759	758	740	761	755	-1.30	30	10287	752	746	736	745	745	-2.40
31	10025	742	762	760	761	756	-0.90	32	10848	731	755	725	748	740	-2.80
33	10985	742	746	732	740	740	-3.30	34	10490	741	740	723	763	742	-1.90
35	10393	760	760	739	764	756	-1.85	36	10013	747	765	748	747	751	-1.10
37	10490	758	739	746	751	748	-3.20	38	9741	756	754	755	763	757	-1.70
39	10543	745	744	732	755	744	-2.70	40	10703	759	752	759	756	756	-2.45
41	11017	744	721	732	754	738	-2.50	42	10586	758	746	758	752	753	-2.25
43	10264	759	766	738	746	752	-0.90	44	10361	738	744	746	735	741	-2.10
45	10444	746	742	760	736	746	-2.75	46	10335	256[a]	756	741	745	625	-2.25
47	10329	762	762	751	758	758	-1.50	48	10975	725	737	746	737	736	-3.80
49	11159	727	725	719	736	727	-2.90	50	10429	731	750	731	743	739	-1.70
51	10653	751	744	750	733	745	-3.05	52	9894	746	735	749	752	746	-1.20
53	10654	726	749	727	740	736	-2.30	54	10486	753	736	750	758	749	-1.90
55	10653	732	735	731	734	733	-2.35	56	10861	754	751	740	742	747	-3.05
57	11185	709	740	713	731	723	-3.90	58	10749	735	735	714	740	731	-2.45
59	10873	734	721	737	751	736	-2.30	60	10800	718	742	738	729	731	-3.20
61	10819	741	747	748	733	742	-2.20	62	-4	740	715	731	733	730	[b]
63	10942	740	732	718	746	734	-3.75	64	11165	722	733	691	741	722	-4.65

MISCELLANEOUS INSTRUMENTS

9	TE-5-6	731 DEG C	10	TE-5-7	728 DEG C	11	TE-5-8	726 DEG C
12	TE-28-5	742 DEG C	13	TE-28-6	751 DEG C	14	TE-28-7	741 DEG C
15	TE-28-8	738 DEG C	17	TE-39-6	745 DEG C	19	PE-301	191 KPA
23	TE-44-8	741 DEG C	24	TE-320	369 DEG C	25	TE-321	358 DEG C
26	TE-322	349 DEG C	27	TE-323	676 DEG C	28	TE-324	652 DEG C
29	TE-325	666 DEG C	30	TE-326	613 DEG C	31	TE-327	602 DEG C
41	TE-91-2	525 DEG C	44	TE-92-1	586 DEG C	45	TE-92-2	514 DEG C
46	TE-92-3	652 DEG C	47	TE-92-4	475 DEG C	49	TE-93-2	496 DEG C
50	TE-93-3	662 DEG C	52	TE-94-1	630 DEG C	53	TE-94-2	486 DEG C
54	TE-94-3	532 DEG C	472	EIE-10	2385 A	473	EEE-10	81 V
488	TAV-10	755 DEG C						

[a] Thermocouple inoperative.

[b] Simulator heated but unpressurized.

Table 7. Average axial shrinkage determined from relocation of grids and bottom of bundle heated zone

Position	Change in elevation (cm)	Heated length above this position (cm)	Axial shrinkage (%)
Lower heated zone	2.24 ± 0.25[a]	91.4	2.4
Grid No. 1	2.0	81.2	2.5
Grid No. 2	0.6	25.3	2.4

[a]This represents the average of 63 simulators (No. 62 was unpressurized) from Table 8.

Table 8. Approximate axial shrinkage of tubes

Simulator No.	Heated length change		Simulator No.	Heated length change	
	cm	%		cm	%
1	1.5	1.6	33	2.3	2.5
2	2.3	2.5	34	2.3	2.5
3	2.3	2.5	35	2.3	2.5
4	1.9	2.1	36	2.6	2.8
5	2.3	2.5	37	2.4	2.6
6	2.3	2.5	38	2.5	2.7
7	2.2	2.4	39	2.5	2.7
8	2.1	2.3	40	2.2	2.4
9	2.3	2.5	41	2.3	2.5
10	2.4	2.6	42	2.6	2.8
11	2.3	2.5	43	2.0	2.2
12	2.3	2.5	44	2.5	2.7
13	2.3	2.5	45	2.5	2.7
14	2.3	2.5	46	2.5	2.7
15	2.3	2.5	47	2.3	2.5
16	1.6	1.8	48	2.3	2.5
17	2.2	2.4	49	2.0	2.2
18	1.9	2.1	50	1.6	1.8
19	2.7	2.9	51	2.4	2.6
20	2.3	2.5	52	2.3	2.5
21	1.6	1.8	53	2.5	2.7
22	2.7	2.9	54	2.3	2.5
23	2.3	2.5	55	2.3	2.5
24	2.2	2.4	56	2.3	2.5
25	2.3	2.5	57	2.3	2.5
26	2.2	2.4	58	2.1	2.3
27	2.2	2.4	59	2.1	2.3
28	2.4	2.6	60	2.1	2.3
29	2.2	2.4	61	2.2	2.4
30	2.3	2.5	62	0[a]	0[a]
31	2.0	2.2	63	2.3	2.5
32	2.2	2.4	64	1.8	2.0

[a]Simulator No. 62 was unpressurized.

Table 9. Burst locations in B-5 test array

Simulator No.	Burst location Axial[a] (cm)	Burst location Angle[b] (deg)	Burst length (cm)	Simulator No.	Burst location Axial[a] (cm)	Burst location Angle[b] (deg)	Burst length (cm)
1	73.2	120	1.5	33	15.9	135	1.4
2	76.2	135	2.2	34	27.5	90	2.9
3	24.9	180	2.6	35	22.3	45	2.7
4	78.1	225	2.4	36	35.7	225	2.2
5	78.5	225	2.1	37	75.9	45	2.1
6	73.2	135	1.6	38	17.8	45	2.3
7	74.8	90	0.1[c]	39	21.1	45	2.5
8	78.9	180	3.0	40	70.7	315	2.4
9	76.2	45	2.1	41	16.8	90	3.3
10	21.4	45	3.1	42	19.6	0	3.2
11	33.0	270	2.9	43	25.3	45	2.0
12	73.7	45	2.2	44	25.5	45	2.6
13	74.8	135	4.6	45	75.1	45	2.3
14	75.9	45	1.9	46	23.4	135	1.7
15	75.7	0	3.2	47	50.1	135	2.1
16	73.9	0	2.9	48	47.0	225	2.0
17	54.5	135	2.9	49	17.1	45	2.1
18	26.4	0	2.0	50	20.7	45	2.6
19	40.3	225	2.5	51	18.2	45	2.4
20	29.1	45	2.4	52	33.1	225	1.8
21	73.6	45	2.4	53	46.7	90	0.1[c]
22	50.8	135	2.5	54	20.7	45	2.7
23	50.8	180	2.5	55	24.0	330	3.5
24	21.0	315	2.0	56	71.6	315	1.7
25	16.0	45	1.5	57	19.5	45	2.2
26	20.9	45	2.3	58	19.6	45	2.4
27	27.4	0	3.4	59	54.6	45	0.1[c]
28	73.6	45	2.4	60	33.1	45	1.9
29	23.5	45	2.2	61	34.0	90	2.3
30	49.0	180	3.3	62	*d*	*d*	*d*
31	45.3	225	2.0	63	34.5	270	3.4
32	37.2	225	1.7	64	17.0	315	2.2

[a]Posttest elevation above bottom of heated zone. The bottom of heated zone of the bundle (zero elevation) represents an average of all rods (except rod 62, which was unpressurized).

[b]Clockwise rotation looking down on top of bundle. Estimated angle of rupture initiation.

[c]Pin hole opening probably at thermocouple attachment.

[d]Tube heated but unpressurized.

Table 10. Geometric parameters for B-5 section at 17.0-cm elevation

PHOTO IDENTIFICATION MRBT-B5 17.0 CM ELEVATION

TUBE	OD AREA (MM**2)	ID AREA (MM**2)	WALL AREA (MM**2)	OD PERIMETER (MM)	ID PERIMETER (MM)	OD CX (MM)	OD CY (MM)	ID CX (MM)	ID CY (MM)	OD STR (%)	ID STR (%)
1	134.03014	111.33742	22.69272	41.05592	37.42410	14.70337	137.45111	14.77097	137.39319	19.7	23.4
2	147.75471	125.49899	22.25572	43.10762	39.73065	28.27505	137.66435	28.32985	137.62325	25.6	31.0
3	128.06522	106.63301	21.43221	40.13997	36.61398	43.75713	137.07315	43.75482	137.04878	17.0	20.7
4	126.89470	104.63211	22.26259	39.94684	36.28079	58.21390	136.94836	58.17490	136.93269	16.4	19.6
5	132.59912	110.90289	21.69623	40.82869	37.35027	72.56067	136.13934	72.57188	136.10342	19.0	23.2
6	125.73514	104.35661	21.37852	39.76720	36.22638	86.86450	136.13315	86.86029	136.08182	15.9	19.5
7	125.45938	104.35486	21.10452	39.72469	36.22926	101.27388	136.05283	101.30309	136.02283	15.8	19.5
8	124.95486	103.13560	21.81926	39.65953	36.01450	115.62987	135.84399	115.62111	135.76682	15.6	18.8
9	152.23035	129.43390	22.79645	43.77122	40.37192	14.15999	123.44409	14.24994	123.47780	27.6	33.1
10	171.87578	148.62505	23.25069	46.51109	43.24484	28.69458	123.38681	28.76485	123.43694	35.6	42.6
11	154.85472	131.86519	22.98953	44.19212	40.77988	43.70567	123.18295	43.71735	123.21579	28.8	34.5
12	165.98427	142.57047	23.41380	45.69649	42.35[illegible]30	58.25459	122.79610	58.27625	122.83829	33.2	39.7
13	143.11555	121.48776	21.62779	42.43361	39.08[illegible]20	72.55516	121.68999	72.56496	121.68781	23.7	28.9
14	160.52527	138.91966	21.60561	44.95592	41.80983	86.60667	122.25336	86.65451	122.23651	31.0	37.9
15	138.65944	117.35182	21.30762	41.75087	38.42891	101.02176	121.47421	101.06630	121.49838	21.7	26.7
16	129.25377	107.33261	21.92116	40.32698	36.74370	115.67677	121.62994	115.62852	121.66664	17.5	21.2
17	160.27054	137.05539	23.21515	44.93102	41.54315	13.39406	109.50005	13.48280	109.49619	30.9	37.0
18	176.29027	152.66946	23.62080	47.20894	43.92911	28.19391	108.93486	28.18141	108.97688	37.6	44.9
19	230.16530	203.94681	26.21849	54.00923	50.82895	43.66960	108.21191	43.66171	108.19382	57.4	67.6
20	153.00841	128.35405	24.65436	43.88820	40.20767	58.69342	108.36545	58.72052	108.39647	27.9	32.6
21	133.90070	109.48660	24.41409	41.03897	37.11676	72.24826	108.01009	72.24620	108.03972	15.6	22.4
22	152.25058	128.10645	24.14413	43.77718	40.14722	86.12390	108.25806	86.08954	108.26851	27.6	32.4
23	153.39861	129.71996	23.67865	43.92477	40.39807	100.76172	107.04932	100.81206	107.07437	28.9	33.2
24	161.77838	137.23386	24.54453	45.11685	41.54124	115.35704	107.20895	115.25885	107.17206	31.5	37.0
25	178.45607	152.78056	25.67551	47.61646	44.11823	13.79630	95.31976	13.88180	95.41585	38.8	45.5
26	165.69958	140.91808	24.78151	45.90218	42.38126	28.48068	95.00374	28.52664	95.02852	33.8	39.8
27	166.91260	142.24286	24.66970	46.48888	42.94499	43.63052	93.81171	43.62186	93.86379	35.5	41.6
28	150.74866	125.85631	24.89235	43.57249	39.80865	58.41383	94.55507	58.44554	94.60815	27.0	31.3
29	149.63763	125.20171	24.43593	43.37796	39.67888	72.83290	93.68929	72.83960	93.73328	26.4	30.9
30	167.95445	143.31464	24.63982	45.98193	42.48445	87.17929	94.49928	87.17822	94.48489	34.0	40.1
31	138.25336	114.71588	23.53748	41.74942	38.05655	101.24716	92.99661	101.24037	93.02559	21.7	25.5
32	163.22647	138.44978	24.77669	45.32430	41.73576	115.25879	92.43820	115.15916	92.49759	32.1	37.6
33	193.55228	167.53613	26.01614	49.61617	46.21417	13.39360	80.04797	13.53510	80.05544	44.6	52.4
34	171.94199	145.39067	26.55132	48.11652	44.44618	28.47426	81.69664	28.50774	81.68147	40.2	46.6
35	192.49916	166.13655	26.36261	49.66969	46.19032	43.33116	79.66771	43.35381	79.71095	44.8	52.3
36	176.12177	149.58757	26.53419	47.46332	43.77907	57.40565	80.05861	57.42694	80.08987	38.3	44.4
37	185.60684	159.36790	26.23894	48.36459	44.79102	71.27690	78.68541	71.31934	78.74193	41.0	47.7
38	295.44922	268.65430	26.79492	64.42938	62.33578	86.62122	79.29886	86.64165	79.40585	87.8	105.6
39	201.86957	178.87430	22.99527	50.48270	47.48042	101.75800	77.74950	101.79828	77.82233	47.1	56.6
40	140.18678	117.16020	23.02658	42.01103	38.39774	116.55341	76.84090	116.55855	76.84238	22.4	26.6
41	206.26938	181.08282	25.18655	50.37234	47.07817	14.31960	65.88596	14.54050	65.94479	46.8	55.3
42	170.64084	145.42024	25.22060	65.68880	62.95493	31.69070	65.04002	31.74359	65.10349	91.4	107.6
43	173.38461	149.83022	23.55440	47.98579	44.82169	43.69392	64.55176	43.69579	64.65628	39.8	47.8
44	177.28062	153.11215	24.16847	48.16888	44.86905	58.27106	64.56458	58.33588	64.59616	40.4	48.0
45	192.68102	167.87057	24.81044	49.29065	46.00195	72.53722	63.50114	72.56477	63.47333	43.7	51.7
46	166.56793	143.74918	22.81876	45.80481	42.55405	87.15015	61.97594	87.18198	61.96870	33.5	40.3
47	156.42686	134.44087	21.98599	44.37292	41.12793	101.64333	62.61609	101.67062	62.64981	29.3	35.6
48	152.73387	129.89731	22.83656	43.84508	40.42[illegible]72	115.07092	62.94672	115.04285	62.98717	27.8	33.3
49	226.61867	200.00980	26.60887	49.63629	46.51[illegible]37	14.31865	50.86168	14.49878	51.02356	44.7	53.4
50	166.93013	141.06993	25.86020	48.41548	45.02715	28.15787	49.52211	28.13647	49.55188	41.1	48.5
51	256.78320	229.68169	27.10152	57.39864	54.31145	43.34460	49.16882	43.39334	49.22191	67.3	79.1
52	161.55016	136.53532	25.01483	45.44670	41.81160	58.14183	48.97217	58.12180	48.97061	32.5	37.9
53	145.55388	120.76625	24.78763	42.79660	38.97649	71.55910	49.03880	71.61380	49.06203	24.7	28.5
54	178.68103	152.60106	26.07997	47.44098	43.82916	85.82469	47.11360	85.79742	47.19545	38.3	44.5
55	163.67230	138.58138	25.09093	45.39516	41.77275	100.43192	48.91100	100.41563	48.99818	32.3	37.8
56	160.56921	135.56270	25.00652	44.97263	41.32887	114.68365	48.55124	114.62199	48.60286	31.1	36.3
57	151.45053	126.07997	25.37056	43.64539	39.84401	13.66026	35.45074	13.69700	35.58035	27.2	31.4
58	166.31229	140.57387	25.73842	45.77878	42.10719	28.60381	35.48334	28.62520	35.61084	33.4	38.9
59	123.11938	98.75941	24.35997	39.38077	35.28485	43.27939	34.64355	43.29539	34.71071	14.8	16.4
60	124.68553	100.20734	24.47820	39.61998	35.52214	57.53186	35.21092	57.54758	35.25224	15.5	17.1
61	125.38422	100.76323	24.62099	39.71992	35.61183	71.78920	35.30209	71.82614	35.35660	15.8	17.4
62	92.16727	71.12157	21.04570	34.04185	29.91499	85.78897	33.99754	85.79886	33.98064	-0.8	-1.3
63	145.23936	119.70985	25.52951	42.75888	38.81816	100.23407	34.44911	100.25264	34.53801	24.6	28.0
64	188.86578	162.95032	25.91547	45.15050	42.07584	113.61101	34.93686	113.44682	35.19200	31.6	38.8

Table 11. Circumferential strain in B-5 tubes

(Burst strains are underlined)

ELEVATION (CM)	CIRCUMFERENTIAL STRAIN OF TUBE NO. (%) 1	2	3	4	5	6	7	8	9	10	11	12	13	14	15	16
0.0	0.2	-0.3	0.6	0.5	0.7	0.8	0.7	0.6	0.2	0.2	0.4	0.2	0.7	0.5	0.8	0.9
1.8	4.9	3.5	4.0	2.8	2.9	2.3	1.9	2.7	2.4	2.9	2.9	3.1	4.0	3.5	3.3	4.7
3.5	8.3	8.1	8.2	5.7	6.8	4.9	4.7	7.2	6.5	8.7	7.5	8.8	8.9	9.6	9.3	7.8
5.0	10.3	9.1	8.0	7.7	9.2	6.7	7.8	9.3	11.7	11.0	10.0	11.6	10.7	12.2	10.3	7.8
6.5	8.5	9.7	8.3	7.7	9.1	7.4	8.3	9.2	11.4	10.3	9.8	10.4	9.8	11.5	9.3	7.4
8.4	4.5	5.7	5.4	4.5	6.2	5.3	5.3	6.4	4.9	4.9	4.8	4.7	5.1	4.8	4.8	4.2
10.0	3.8	3.6	3.8	3.9	4.8	3.9	3.7	4.3	4.7	5.5	5.5	4.8	5.5	5.7	5.3	4.1
11.6	11.8	9.8	8.7	9.1	8.3	7.4	7.5	8.5	10.2	9.6	8.4	8.2	8.7	9.3	7.6	9.5
13.5	16.1	15.8	13.1	12.4	13.2	13.2	12.9	13.7	18.0	19.1	18.9	16.9	18.2	21.5	15.6	15.5
15.5	19.0	25.2	17.2	18.6	20.6	18.2	18.3	15.5	25.7	26.2	27.4	25.2	23.9	27.7	19.5	17.7
17.0	19.7	25.6	17.0	16.4	19.0	15.9	15.8	15.6	27.6	35.6	28.8	33.2	23.7	31.0	21.7	17.5
18.5	18.6	22.9	16.8	13.8	16.9	14.7	15.4	16.1	23.5	50.2	30.6	38.3	24.5	33.8	26.2	16.2
20.0	18.1	22.9	19.9	14.9	17.4	16.7	19.0	14.7	25.0	60.8	31.6	37.2	24.1	33.7	28.9	17.3
21.5	16.0	25.5	28.8	20.4	24.4	22.9	24.2	17.3	25.7	59.1	29.4	36.7	22.8	32.3	32.6	17.9
23.0	16.0	24.5	42.3	29.3	35.0	30.3	27.8	21.0	24.7	49.4	26.7	36.3	23.4	31.3	35.1	17.1
24.7	15.0	22.3	61.5	36.0	40.6	34.4	29.1	22.9	26.8	38.9	27.0	29.7	23.2	27.0	25.7	16.3
26.4	16.8	26.1	56.9	33.9	38.3	33.4	26.8	24.3	33.6	38.9	33.1	27.9	24.9	29.6	24.8	18.0
28.0	16.5	30.0	28.5	24.2	27.1	23.8	19.7	21.3	32.0	39.4	34.5	26.0	24.6	31.6	25.0	17.1
29.5	15.7	22.7	17.4	17.3	19.6	18.2	16.9	19.0	25.6	46.0	37.8	26.9	26.7	35.2	27.1	18.9
31.5	16.7	19.4	14.4	14.4	18.3	16.5	18.8	15.7	25.7	45.6	53.4	26.6	28.1	36.4	29.1	18.1
33.5	20.1	26.3	22.9	21.6	27.8	24.0	23.6	15.9	50.6	41.6	54.0	28.4	28.8	36.8	29.9	17.3
35.5	17.1	26.6	26.1	23.4	32.8	27.0	22.2	15.5	56.1	45.9	47.2	30.8	26.5	40.6	25.7	16.7
37.1	12.3	24.5	24.7	21.9	32.2	26.0	20.3	15.6	35.5	45.6	43.0	31.1	24.6	39.0	23.2	14.2
39.0	12.4	20.5	18.5	17.3	22.8	17.7	16.0	14.1	27.2	35.5	36.4	31.8	24.3	33.1	24.4	9.2
40.8	9.8	17.4	15.7	15.2	21.5	17.0	14.3	12.8	23.4	30.8	31.3	35.6	29.4	31.2	26.0	12.6
42.6	8.4	19.7	20.9	18.9	31.6	23.3	16.7	12.3	13.3	27.0	26.5	34.7	33.5	30.4	24.2	14.8
44.4	12.3	18.4	19.9	18.1	27.2	20.3	18.1	14.9	16.1	25.3	25.5	30.2	32.5	23.4	28.5	18.3
46.4	13.4	16.4	18.4	17.1	18.5	16.8	13.0	16.7	23.3	23.4	22.0	23.1	29.1	18.9	24.6	22.3
46.9	13.2	16.3	17.6	16.4	17.6	16.5	13.2	16.3	25.0	22.6	21.1	21.3	27.9	18.3	23.0	22.5
48.0	17.1	17.7	18.5	16.2	17.1	17.5	16.4	18.2	32.5	23.3	20.9	19.5	25.7	19.6	21.8	23.4
49.6	20.4	20.2	16.9	15.4	18.6	20.8	18.8	21.7	35.0	30.5	25.0	22.4	26.0	25.2	22.0	27.2
51.2	23.8	22.1	17.9	15.9	20.0	18.6	14.5	20.9	41.3	32.8	29.9	26.4	25.2	27.5	25.1	32.7
53.0	21.1	24.9	24.1	22.8	32.1	26.1	19.2	22.8	38.7	32.3	34.8	27.0	25.1	32.6	28.3	31.6
54.6	20.0	22.2	21.4	21.2	35.7	32.1	21.8	25.0	34.7	29.1	32.7	27.8	26.3	32.9	30.5	24.7
56.2	20.8	15.0	15.7	14.2	20.2	22.3	19.4	24.3	31.0	23.7	26.2	24.7	24.7	26.6	27.5	16.6
57.8	19.9	17.4	15.2	12.6	16.0	14.5	15.7	21.7	18.5	21.8	22.5	21.5	22.6	23.6	23.8	13.2
59.6	14.6	17.7	16.3	16.0	17.6	15.1	15.6	18.0	14.9	19.2	19.7	19.0	19.7	19.1	20.0	15.1
61.2	13.4	13.9	13.6	13.9	14.5	13.7	13.5	16.2	14.5	14.5	14.5	14.5	14.9	14.0	14.4	11.8
62.8	9.0	8.5	8.8	9.1	9.5	9.1	8.5	11.1	8.3	7.2	7.3	7.1	7.6	6.8	7.4	7.2
64.4	5.9	5.8	5.8	5.3	5.5	5.6	5.3	5.4	5.6	6.3	6.4	6.1	5.9	5.4	5.5	3.9
66.0	8.1	7.3	7.0	6.8	8.1	7.1	7.3	8.9	7.5	8.5	8.3	8.3	8.6	7.6	7.9	9.6
67.8	19.0	14.9	13.8	13.1	16.6	17.5	18.4	22.0	23.2	23.2	22.7	24.7	26.5	20.4	20.2	19.6
69.5	24.5	21.9	19.3	15.0	19.1	22.6	22.3	31.4	22.5	34.8	33.3	37.6	50.6	28.1	26.8	21.2
71.0	29.3	32.3	26.1	24.2	28.8	38.3	27.3	39.9	19.7	44.9	37.0	51.6	69.9	33.6	32.0	27.4
72.8	38.1	38.8	24.3	26.7	40.4	57.9	36.0	42.0	29.7	46.7	37.5	62.5	75.9	48.1	38.9	33.2
74.3	36.4	53.4	21.7	22.4	35.8	58.2	43.6	40.1	51.0	39.3	39.4	62.9	73.6	72.3	41.4	41.6
74.8	32.9	64.5	22.1	22.7	32.2	52.2	45.4	38.5	61.9	35.7	39.7	60.3	72.7	64.7	43.1	38.6
75.8	28.9	76.9	26.0	35.0	30.9	45.7	44.0	37.0	77.7	30.5	39.9	49.0	75.5	63.3	41.4	37.5
76.3	28.0	79.0	28.9	54.0	35.4	46.1	44.6	39.0	77.0	28.6	39.3	45.7	72.5	58.8	57.7	35.9
77.4	23.6	74.5	37.2	88.9	55.9	47.9	40.4	48.4	66.3	25.2	36.1	41.3	64.9	42.7	43.3	31.4
78.9	19.1	45.3	32.3	83.0	69.6	51.9	35.0	50.5	38.0	23.5	32.3	36.5	49.6	35.1	36.1	26.3
80.4	17.0	24.1	18.8	28.4	47.0	42.6	29.1	53.7	27.8	20.8	27.5	30.2	32.1	30.0	26.3	20.6
81.9	19.7	24.9	15.9	18.9	23.7	26.8	25.1	32.2	25.2	20.1	24.3	26.5	24.3	25.8	21.7	17.6
83.5	19.7	24.9	18.4	22.0	23.3	19.2	21.4	23.0	16.0	16.9	19.5	22.1	19.4	20.5	17.3	15.2
85.1	19.8	22.0	19.1	22.9	29.6	18.9	20.5	20.0	15.4	14.7	16.7	18.8	17.5	16.2	14.9	14.5
86.8	15.9	15.1	13.7	14.1	22.4	14.5	14.1	13.4	13.1	10.9	11.3	13.4	13.0	11.2	11.2	9.0
88.6	8.2	4.6	5.3	5.4	8.1	6.5	5.9	6.6	6.1	5.0	4.9	5.8	6.5	6.0	5.9	3.3
90.4	2.6	1.7	1.8	1.8	2.3	2.2	1.1	1.4	2.1	1.5	1.5	1.8	1.9	1.4	1.9	0.1
92.2	1.2	1.4	1.1	1.1	1.3	0.9	0.8	0.8	1.3	1.0	1.2	1.5	1.1	0.8	1.1	1.4

Table II (continued)

ELEVATION (CM)	17	18	19	20	21	22	23	24	25	26	27	28	29	30	31	32
0.0	-0.0	0.2	0.2	0.5	0.6	0.5	0.9	0.7	-0.1	0.1	0.4	0.3	0.6	0.4	0.9	-0.0
1.8	3.4	4.3	3.4	4.4	5.4	3.1	4.4	3.7	3.5	3.6	4.6	3.3	5.2	2.7	4.0	2.8
3.5	8.1	10.2	9.8	9.0	9.6	7.4	7.7	9.5	9.8	8.4	10.6	9.9	9.8	9.1	10.6	8.6
5.0	12.4	13.9	13.6	10.9	10.6	11.1	9.4	12.4	13.8	12.5	13.6	12.1	11.8	13.3	12.9	12.3
6.5	11.6	12.3	11.6	10.5	8.4	10.6	8.5	11.3	12.1	11.3	11.9	11.0	10.0	11.8	11.2	11.8
8.4	7.0	5.2	6.1	4.6	4.8	6.0	4.4	6.5	4.6	5.2	6.0	4.4	5.5	6.8	6.4	7.2
10.0	4.6	5.3	5.9	5.5	6.2	5.9	4.5	4.9	4.0	4.8	4.7	4.4	4.3	5.2	5.6	4.2
11.6	10.4	9.4	9.2	8.6	10.4	7.8	6.7	10.1	9.8	8.8	9.3	8.2	7.9	8.6	8.0	8.8
13.5	19.8	22.1	23.4	18.4	15.5	15.0	15.4	20.1	23.8	18.8	19.6	17.5	18.5	20.9	17.3	16.6
15.5	32.8	31.4	49.0	25.2	17.6	22.8	22.5	27.8	42.6	25.9	28.9	22.9	24.4	32.0	21.3	24.8
17.0	30.9	37.6	57.4	27.9	19.6	27.6	28.0	31.5	38.8	33.8	35.5	27.0	26.4	34.0	21.7	32.1
18.5	22.2	40.9	53.2	30.4	18.1	32.1	36.1	34.1	21.0	45.8	38.9	31.0	28.8	32.9	23.0	38.8
20.0	23.6	35.0	46.4	34.0	17.8	37.0	39.8	46.8	20.6	54.0	38.6	33.9	36.3	33.7	24.4	39.1
21.5	28.1	29.5	42.2	35.6	17.7	39.2	34.8	49.2	26.4	48.4	40.5	37.4	50.4	35.2	23.8	34.6
23.0	30.1	31.5	44.7	37.4	18.5	39.3	29.5	33.4	27.6	39.5	47.6	38.4	58.4	37.6	23.8	26.3
24.7	32.3	45.7	53.6	40.3	21.2	42.9	27.5	25.4	28.0	37.2	51.6	39.6	56.5	39.2	25.5	22.5
26.4	32.8	55.9	54.0	47.8	26.1	48.8	27.3	27.1	27.9	39.0	52.2	43.3	41.6	46.1	31.5	33.6
28.0	28.4	44.9	40.8	58.5	27.6	54.2	26.1	26.3	23.2	42.7	55.6	41.7	30.9	44.1	28.4	35.3
29.5	20.8	41.2	34.6	70.5	28.0	56.7	26.3	30.8	19.9	48.3	53.2	42.1	29.3	41.8	28.9	32.5
31.5	21.6	39.0	32.6	54.6	29.0	53.0	23.9	41.6	21.0	38.9	44.5	36.5	30.3	32.5	28.1	30.8
33.5	39.0	43.5	38.8	42.3	31.8	49.8	27.5	52.6	25.6	30.6	44.7	31.8	36.9	29.1	26.8	36.7
35.5	45.4	55.0	48.5	39.1	28.5	39.5	30.5	48.1	26.3	30.9	41.4	29.9	38.8	31.6	26.1	52.9
37.1	37.6	42.7	56.3	37.2	24.8	34.0	28.9	37.3	22.6	29.3	39.7	26.6	37.4	34.6	26.3	61.1
39.0	33.7	28.9	75.9	38.3	23.2	38.7	27.6	22.7	19.5	25.8	37.9	26.0	35.6	35.8	30.1	43.4
40.8	25.2	23.5	58.3	38.6	22.0	43.2	27.8	19.9	15.2	21.4	30.8	24.8	31.8	35.3	35.1	21.1
42.6	13.9	21.0	44.5	35.0	21.7	44.5	25.9	28.8	9.7	16.6	27.7	23.0	32.2	36.0	38.9	20.0
44.4	15.2	21.9	35.5	32.2	23.9	50.4	26.6	25.6	11.5	16.1	31.0	22.0	31.6	37.1	47.1	17.7
46.4	23.6	24.0	32.4	31.8	24.0	59.2	31.6	15.8	18.1	15.4	28.3	18.9	28.4	49.1	50.4	19.1
46.9	25.2	25.0	29.7	29.9	22.8	60.4	32.5	13.9	18.4	14.7	25.6	17.2	26.1	54.1	43.3	17.9
48.0	29.0	29.2	27.5	27.8	22.8	66.8	40.3	13.8	20.9	16.4	24.3	18.4	23.6	64.3	38.6	16.5
49.6	24.4	35.7	33.5	25.9	22.8	70.5	53.1	12.5	18.0	23.3	28.4	21.6	23.6	65.1	32.9	15.9
51.2	28.0	40.0	32.7	30.8	22.6	68.4	52.0	12.8	16.4	33.4	35.1	25.3	23.0	48.7	28.5	17.0
53.0	52.4	38.8	30.5	32.0	21.8	49.1	46.1	18.4	28.9	36.0	36.2	27.2	22.5	38.1	28.8	15.0
54.6	71.0	32.7	28.8	31.5	20.4	34.1	38.3	21.8	38.8	29.9	33.4	27.5	22.3	35.6	29.5	17.8
56.2	47.2	26.7	25.9	27.7	18.3	25.6	29.5	18.5	27.1	22.7	25.0	24.4	19.3	30.4	24.2	21.6
57.8	20.9	23.1	22.3	23.7	17.2	20.8	24.2	18.2	15.4	19.3	21.6	21.8	16.6	27.4	20.6	18.0
59.6	14.0	17.2	16.2	16.8	14.1	16.8	18.1	13.8	14.6	14.6	16.5	16.6	15.4	20.4	16.0	11.0
61.2	15.2	12.7	12.5	13.0	11.7	14.2	14.1	13.6	13.8	11.6	12.7	12.5	12.5	14.4	12.1	11.0
62.8	8.6	6.9	6.5	7.3	6.2	7.3	7.1	9.2	7.2	6.3	6.5	6.6	6.5	8.0	6.4	8.0
64.4	7.5	6.5	6.2	6.7	6.8	6.1	6.3	5.0	5.4	6.2	6.4	6.4	6.5	6.4	5.7	4.9
66.0	9.9	8.0	7.6	8.1	8.2	8.1	8.1	8.4	6.5	7.0	8.7	7.9	8.5	9.2	8.8	10.4
67.8	26.2	22.7	25.5	22.9	24.4	24.4	23.0	13.9	17.1	18.2	24.1	22.6	22.3	24.2	22.1	24.6
69.5	27.2	32.0	53.2	37.4	33.5	47.1	35.0	13.0	19.3	23.5	39.0	32.0	33.2	35.5	29.7	26.6
71.0	23.2	33.1	63.9	49.6	40.1	68.6	37.3	13.0	16.9	27.2	53.4	44.6	42.0	39.0	31.2	21.9
72.8	33.1	28.1	61.3	57.7	58.7	71.7	35.0	16.0	17.6	29.1	49.2	60.3	49.2	39.7	29.0	18.6
74.3	42.0	24.7	57.2	58.6	53.3	62.7	32.5	23.1	14.7	26.7	36.9	60.1	54.4	36.9	26.1	16.2
74.8	41.8	23.4	54.4	55.3	51.5	58.8	30.7	26.5	13.7	25.4	34.7	56.7	55.2	35.8	26.0	17.4
75.8	39.4	21.3	47.8	49.4	39.3	50.9	27.4	34.8	13.1	21.8	31.3	45.7	52.0	31.5	25.1	21.0
76.3	37.8	20.2	44.3	47.2	36.7	47.4	26.3	38.9	14.6	21.4	31.5	41.4	48.6	30.0	24.8	22.5
77.4	34.0	19.2	35.8	43.9	31.1	37.5	23.1	42.4	15.9	17.8	28.5	31.5	38.4	25.5	22.4	22.0
78.9	29.3	18.5	28.5	45.9	27.3	29.2	21.5	38.3	18.4	16.1	25.6	26.9	32.2	22.9	18.8	18.7
80.4	26.2	16.4	22.2	40.0	23.6	25.2	19.9	27.1	18.7	13.4	21.0	22.3	26.5	21.3	15.7	14.6
81.9	23.9	16.0	20.2	32.7	23.3	25.1	19.3	22.2	17.0	13.8	18.1	19.8	22.9	21.0	15.3	17.4
83.5	14.9	12.5	15.3	25.3	18.4	20.3	16.0	18.5	10.9	12.0	14.2	16.5	18.3	18.1	13.4	20.6
85.1	15.6	11.8	13.7	21.1	16.4	16.9	14.6	18.8	11.3	11.1	12.6	15.8	16.2	16.2	13.4	19.2
86.8	14.2	9.1	9.7	14.3	12.3	12.5	10.0	12.2	11.3	7.8	8.7	11.6	12.5	11.8	9.7	11.7
88.6	6.0	3.1	3.0	5.2	5.9	5.7	4.9	3.7	4.8	1.5	2.2	5.0	5.3	5.8	4.9	4.7
90.4	2.0	1.6	1.0	1.2	1.4	1.9	0.8	0.4	2.0	0.5	0.4	1.3	1.1	1.5	1.0	1.3
92.2	1.3	1.2	0.9	1.4	1.1	1.3	1.5	1.5	1.9	1.3	0.9	1.3	1.1	1.0	1.3	1.5

Table 11 (continued)

ELEVATION (CM)	33	34	35	36	37	38	39	40	41	42	43	44	45	46	47	48
0.0	-0.8	-0.4	-0.6	-0.6	-0.4	-0.3	0.0	0.2	-0.9	-0.8	-0.4	-0.5	-0.6	-0.2	-0.3	-0.2
1.8	2.6	5.0	3.1	3.1	2.7	2.5	5.1	4.4	2.6	3.6	3.4	3.5	2.5	4.3	4.1	3.9
3.5	9.5	13.0	9.9	9.4	8.2	9.3	9.2	7.0	6.7	11.4	10.1	9.3	8.7	11.3	10.1	8.5
5.0	14.6	16.2	13.3	12.6	11.8	14.1	12.2	9.7	12.0	15.5	11.2	12.1	11.3	15.8	12.1	11.6
6.5	14.1	13.3	11.5	11.2	11.1	13.3	12.2	11.0	11.8	12.7	9.9	11.2	12.2	13.0	12.2	11.7
8.4	5.7	5.4	4.8	4.6	5.4	6.9	6.4	6.8	6.0	5.8	4.8	6.0	6.3	7.1	6.2	7.4
10.0	3.5	5.1	5.1	5.4	5.1	6.8	6.2	5.2	3.7	5.8	5.1	5.4	6.9	7.1	6.1	5.7
11.6	10.4	10.1	9.3	8.6	8.8	8.8	8.6	8.8	10.1	10.1	10.1	8.8	8.9	9.9	8.6	9.0
13.5	30.1	23.1	23.8	21.1	20.0	19.3	21.2	11.6	24.2	29.2	26.7	21.7	20.1	23.2	20.3	12.0
15.5	54.7	35.6	39.7	33.8	30.8	53.0	38.1	15.3	45.0	72.7	41.3	37.3	33.3	33.9	27.4	18.7
17.0	44.6	40.2	44.8	38.3	41.0	87.8	47.1	22.4	46.8	91.4	39.8	40.4	43.7	33.5	29.3	27.8
18.5	25.6	40.0	46.2	38.6	52.9	80.2	54.7	29.6	36.6	87.1	35.4	46.4	49.9	34.0	28.0	32.5
20.0	27.6	40.0	51.5	39.3	58.3	47.1	66.8	32.9	43.4	66.2	33.1	58.3	49.0	41.5	27.7	33.3
21.5	39.5	40.6	59.0	38.8	50.6	40.5	65.9	27.9	58.4	64.0	31.8	61.8	45.0	71.9	26.9	27.5
23.0	44.3	46.2	63.1	39.6	46.2	48.1	59.4	19.8	41.7	56.9	36.2	62.5	44.2	94.5	27.6	19.3
24.7	47.6	64.7	57.9	41.5	46.9	51.1	43.6	14.4	26.5	49.6	51.4	71.0	44.8	73.3	31.6	15.4
26.4	52.3	87.0	43.7	39.5	45.6	49.9	35.4	21.8	35.4	44.4	57.1	67.1	53.0	43.8	37.4	22.8
28.0	40.0	75.8	34.0	30.4	38.7	42.7	32.3	22.6	40.4	36.8	32.9	46.4	68.5	38.0	35.8	27.6
29.5	35.7	44.0	32.5	28.7	36.6	38.9	34.5	20.8	37.2	34.2	30.2	36.4	79.3	42.3	38.8	28.2
31.5	29.7	31.1	29.1	31.6	36.0	34.4	32.5	16.2	23.1	31.3	29.6	31.1	61.0	48.9	34.1	17.2
33.5	28.2	31.7	31.4	50.0	36.1	38.7	29.0	24.6	21.2	30.8	31.0	34.3	44.8	55.2	36.4	21.2
35.5	28.0	30.8	33.7	66.4	35.2	44.1	27.5	44.1	23.7	27.6	27.1	39.6	37.8	54.5	33.6	41.9
37.1	22.6	28.1	30.0	50.6	40.0	42.3	30.1	51.5	18.7	24.5	24.1	36.5	37.4	51.3	29.8	44.9
39.0	14.6	25.6	24.7	34.9	46.5	45.9	39.9	46.2	13.5	22.1	20.7	30.7	40.0	46.5	29.2	35.8
40.8	13.4	19.9	19.4	27.2	36.6	47.2	40.7	30.4	15.6	20.8	17.8	30.5	40.0	45.9	30.3	27.8
42.6	11.2	17.2	18.9	25.6	37.2	44.6	32.9	22.7	13.4	20.2	15.5	27.5	37.3	47.9	31.2	26.4
44.4	16.2	20.5	20.8	25.3	44.5	48.8	28.9	22.0	16.1	23.4	14.4	24.8	34.4	42.3	32.3	37.2
46.4	26.0	24.7	19.6	23.9	40.2	51.3	30.8	26.3	22.2	25.7	14.1	21.3	31.4	32.5	35.7	61.5
46.9	26.6	24.8	19.2	22.6	37.6	49.8	31.3	27.9	22.7	26.9	14.2	20.5	32.2	31.7	38.0	63.8
48.0	29.7	27.0	22.1	22.1	34.4	47.6	33.7	33.0	24.6	29.6	17.5	24.8	35.4	30.4	44.5	60.6
49.6	26.7	29.7	25.1	22.9	32.9	47.9	33.9	39.4	22.4	29.9	19.7	32.5	43.9	27.6	53.7	40.8
51.2	19.8	31.3	30.8	25.7	32.3	46.2	35.8	44.7	19.1	31.8	21.3	39.0	48.6	27.4	58.2	33.6
53.0	28.9	30.6	30.7	25.1	31.5	36.6	35.0	46.9	28.3	36.1	23.0	39.2	35.6	26.9	37.1	30.8
54.6	33.7	28.3	25.9	23.4	28.0	28.8	31.2	36.9	31.2	33.5	22.2	34.1	26.6	25.1	27.5	30.0
56.2	27.2	25.5	21.7	20.8	23.6	24.4	26.2	26.0	27.6	23.4	18.5	26.5	20.7	21.4	22.1	27.5
57.8	18.8	23.3	19.1	18.9	20.3	21.4	21.7	15.8	22.7	19.8	17.8	23.0	20.0	19.8	19.6	21.3
59.6	16.1	18.0	14.7	14.3	16.2	16.7	15.9	10.9	17.2	14.2	13.5	15.9	16.1	14.2	14.4	14.7
61.2	13.0	13.4	11.2	11.2	12.8	12.6	12.8	10.5	11.8	10.9	10.4	11.8	11.8	10.9	11.0	11.5
62.8	6.9	6.8	6.0	5.7	6.8	6.2	7.1	7.2	6.8	6.7	5.9	6.2	6.2	5.8	6.0	6.7
64.4	5.8	6.8	6.0	5.9	5.3	4.6	4.9	3.7	4.7	5.9	5.1	5.5	5.5	4.9	4.8	2.8
66.0	6.5	7.6	7.6	7.6	7.8	8.1	8.0	9.4	6.6	8.3	7.5	8.7	7.8	7.9	8.6	7.8
67.8	16.4	19.5	21.8	20.7	20.6	23.6	21.9	23.9	14.1	20.1	18.0	21.4	13.5	19.2	19.1	17.9
69.5	23.7	25.7	33.7	30.2	30.2	37.5	31.2	41.8	20.1	22.6	20.0	27.5	24.6	23.4	22.2	26.9
71.0	24.0	26.2	39.2	40.0	35.9	50.8	34.0	52.1	23.2	21.6	20.4	28.4	33.7	24.1	23.8	31.6
72.8	18.3	24.8	37.8	40.2	42.3	51.4	34.2	37.3	23.8	20.0	21.0	27.6	51.6	25.9	24.2	31.4
74.3	14.6	23.5	34.0	35.2	53.4	43.7	33.[illegible]	25.6	24.6	19.9	22.0	26.5	60.8	25.2	21.4	25.4
74.8	15.3	23.4	33.3	33.5	56.7	39.6	31.1	22.6	24.7	19.5	21.5	25.8	63.7	24.6	20.0	23.1
75.8	16.9	21.3	30.3	28.8	59.7	31.7	26.9	20.4	23.8	18.8	20.9	25.4	58.2	'2.4	16.9	18.0
76.3	18.1	20.5	29.4	28.1	58.4	30.2	25.3	19.8	22.3	18.2	19.4	24.2	55.4	22.2	16.7	17.3
77.4	20.0	18.3	26.5	26.9	51.2	27.3	22.6	16.6	20.0	16.2	17.3	22.3	38.7	20.2	14.8	14.7
78.9	20.7	16.8	23.1	25.9	39.7	25.0	20.4	12.6	17.7	15.1	16.3	20.8	26.3	18.2	14.2	17.0
80.4	17.3	14.3	17.6	22.2	27.8	21.7	16.9	13.1	15.0	13.1	14.4	19.0	18.9	15.8	12.7	16.7
81.9	15.8	13.8	15.6	19.8	22.1	20.8	16.2	16.0	14.4	13.0	14.1	17.8	17.3	14.9	12.6	16.0
83.5	11.2	11.5	12.1	15.4	16.9	17.1	13.0	15.1	10.6	10.2	10.5	13.8	13.9	11.0	10.4	12.7
85.1	9.2	10.1	10.8	13.5	15.0	14.0	11.6	12.9	10.0	9.3	9.6	11.6	12.4	9.7	10.0	11.6
86.8	9.7	7.9	8.8	11.2	11.7	9.6	9.1	9.2	10.5	7.8	8.0	9.0	10.2	8.3	7.8	8.5
88.6	4.6	2.8	3.7	5.3	4.8	4.3	4.3	4.1	4.5	3.0	3.8	4.4	5.7	4.6	3.9	3.7
90.4	1.2	0.5	0.7	1.9	0.7	0.8	0.9	0.9	1.5	0.9	0.8	1.3	1.8	1.6	0.6	0.9
92.2	1.1	1.0	0.9	1.2	1.5	1.0	1.3	1.4	1.3	1.0	1.1	1.4	1.0	1.5	1.4	0.9

Table II (continued)

ELEVATION (CM)	49	50	51	52	53	54	55	56	57	58	59	60	61	62	63	64
0.0	-0.7	-1.0	-0.3	-0.6	-0.5	-0.6	-0.1	0.1	-0.8	-0.8	-0.6	-0.5	-0.5	-0.8	-0.5	0.2
1.8	2.8	3.0	3.3	3.8	3.3	2.9	5.0	3.5	3.3	3.3	2.3	2.7	1.4	-0.2	4.0	5.0
3.5	6.8	10.1	12.8	10.8	7.9	9.6	11.4	8.5	8.0	11.4	7.7	7.8	6.0	-0.1	10.4	11.0
5.0	11.0	15.8	18.5	13.8	9.8	15.6	15.0	12.8	11.3	14.0	10.9	11.3	10.1	0.4	12.7	13.2
6.5	10.6	13.6	15.7	11.8	9.5	12.8	11.7	11.9	10.4	12.3	9.7	11.5	9.0	-0.7	11.1	10.6
8.4	4.6	4.7	7.1	4.8	4.1	6.8	6.4	7.0	5.0	4.9	5.5	5.9	5.3	-0.1	7.4	5.8
10.0	2.9	5.6	5.3	5.2	5.3	6.1	5.1	5.0	3.9	3.8	3.9	4.3	4.5	0.2	5.9	4.6
11.6	10.3	10.2	9.6	9.0	7.4	8.8	7.9	8.4	10.7	10.2	7.5	9.3	7.6	0.9	9.2	11.1
13.5	17.9	22.7	23.3	21.0	15.2	20.9	18.4	12.8	18.7	24.5	17.0	22.3	18.7	0.1	22.6	17.5
15.5	38.9	31.0	48.9	29.4	21.3	28.3	29.4	21.4	24.1	29.9	17.0	20.0	19.9	-0.3	28.6	27.4
17.0	44.7	41.1	67.3	32.4	24.7	38.3	32.3	31.1	27.2	33.4	14.8	15.5	15.8	-0.8	24.6	31.6
18.5	33.0	55.2	75.5	30.6	27.2	49.4	31.6	34.1	29.6	35.9	17.7	21.3	18.9	0.9	30.1	29.7
20.0	27.6	62.1	67.6	29.5	27.0	56.0	34.3	31.5	32.5	38.5	22.0	31.5	22.3	0.9	32.9	26.2
21.5	25.5	59.2	54.7	29.3	26.6	51.4	39.7	24.3	32.5	37.0	23.4	38.1	20.7	-0.2	29.0	22.9
23.0	21.4	45.1	46.5	31.0	28.5	47.1	47.4	18.2	30.7	36.1	26.1	39.0	20.2	0.3	26.1	18.6
24.7	17.7	36.1	43.8	32.7	34.2	48.1	50.2	14.8	24.3	36.4	29.6	34.5	19.4	0.3	22.3	19.5
26.4	23.8	33.4	48.1	32.9	40.4	46.7	46.0	24.2	21.9	30.4	24.8	26.3	17.6	-0.4	19.2	26.5
28.0	24.4	27.4	49.7	31.0	34.8	37.9	33.4	34.1	18.8	17.8	16.8	19.6	16.3	-0.5	23.0	29.2
29.5	21.1	26.8	49.5	38.2	31.2	35.9	27.5	42.1	18.1	16.0	18.2	23.7	24.2	0.9	29.8	29.5
31.5	12.2	25.5	42.3	63.2	26.9	30.8	26.8	35.3	17.0	20.5	25.5	41.7	43.9	-0.3	46.8	27.8
33.5	18.1	30.6	38.6	67.4	27.5	28.8	37.3	23.0	24.7	35.0	41.9	78.2	86.6	0.2	76.3	22.2
35.5	21.7	33.4	37.0	53.1	28.2	31.7	39.9	21.5	28.0	32.2	37.4	46.9	76.0	0.4	73.4	14.1
37.1	17.9	30.6	37.8	38.4	26.3	35.2	37.2	16.4	29.0	25.5	22.4	24.8	29.7	-0.6	46.8	13.2
39.0	14.4	25.9	37.6	33.0	25.0	37.3	30.0	13.0	26.1	26.8	17.0	14.5	16.0	-1.4	27.1	12.7
40.8	13.4	25.6	35.3	30.6	23.1	37.1	24.1	14.8	22.8	32.6	21.5	21.3	17.7	0.2	28.6	12.1
42.6	12.6	35.5	32.[illegible]	26.7	27.4	36.6	23.2	21.8	17.1	38.0	25.7	33.6	23.4	1.4	34.2	12.9
44.4	14.4	41.2	28.1	22.9	43.8	31.6	26.8	30.9	18.6	33.2	25.9	31.7	22.0	0.4	27.5	19.0
46.4	17.0	36.3	23.1	27.5	65.3	30.1	34.7	41.0	20.0	28.4	20.7	18.3	15.4	0.0	22.6	26.9
46.9	15.9	34.5	22.0	28.0	62.6	30.3	35.4	41.3	19.3	26.4	19.0	16.5	15.7	0.6	22.9	28.1
48.0	17.2	32.8	24.0	32.2	44.3	32.2	37.1	39.4	20.1	23.8	18.1	17.8	18.1	0.8	24.0	25.8
49.6	18.0	28.8	27.5	36.1	28.8	31.2	35.4	31.0	21.6	21.1	20.7	24.5	22.3	-0.1	26.2	17.0
51.2	20.1	28.9	28.4	40.4	25.6	28.4	31.0	33.4	21.7	23.2	27.7	41.0	30.7	0.2	31.9	19.5
53.0	20.9	28.4	26.2	39.3	23.4	24.6	24.8	36.8	23.3	26.7	42.8	55.4	37.5	1.5	45.7	25.3
54.6	19.0	26.6	23.3	32.0	21.1	21.3	21.4	35.0	19.4	24.9	41.9	47.6	31.7	0.6	49.9	25.9
56.2	21.9	22.0	20.7	26.2	20.8	18.7	19.7	32.1	21.9	19.9	23.0	28.3	21.5	0.1	43.3	25.9
57.8	23.1	19.6	19.5	21.5	19.5	17.1	18.9	29.3	24.4	19.5	17.6	15.7	14.2	0.6	31.9	25.8
59.6	15.5	14.0	14.1	13.8	14.2	12.7	14.5	18.9	17.2	15.5	15.6	11.4	9.5	-0.0	18.7	20.4
61.2	12.5	12.0	12.3	11.7	12.1	11.8	12.4	15.9	12.9	11.9	12.6	11.0	9.3	0.6	14.0	16.4
62.8	6.8	6.4	6.5	6.0	5.7	5.7	5.7	7.4	7.2	6.2	5.7	5.7	4.7	0.0	6.7	7.8
64.4	5.9	6.4	6.4	6.2	5.7	5.5	5.4	4.4	6.0	5.6	5.6	4.7	5.0	1.1	5.0	4.0
66.0	6.4	7.9	8.3	9.3	7.7	7.5	7.9	8.9	7.5	7.9	8.4	7.2	7.8	0.7	8.4	8.3
67.8	12.4	17.4	18.5	22.3	20.1	16.9	18.0	20.6	15.7	17.2	21.9	18.6	18.5	0.9	18.4	18.1
69.5	16.6	20.5	21.5	26.6	25.0	20.9	22.5	30.2	19.2	18.9	20.3	16.3	19.8	0.4	19.7	21.0
71.0	19.8	21.7	21.8	26.6	24.1	21.5	22.1	39.3	22.2	22.2	17.0	13.2	15.1	1.3	21.0	19.1
72.8	21.0	20.3	22.2	25.9	21.9	22.5	20.1	41.2	22.5	23.4	19.5	15.0	13.2	0.4	15.9	15.8
74.3	21.2	19.3	22.4	25.5	20.7	22.7	18.9	33.9	22.8	20.9	22.7	20.1	17.9	0.3	19.5	15.1
74.8	21.2	18.6	22.3	25.3	20.2	22.5	18.3	32.1	23.1	19.6	24.0	22.1	19.7	1.3	20.5	16.5
75.8	21.2	17.9	21.4	25.3	19.6	20.9	16.9	27.2	22.7	17.4	26.6	24.4	22.4	1.5	18.6	15.4
76.3	20.6	16.8	19.9	24.2	18.7	19.7	15.7	25.7	21.5	15.0	26.2	24.1	22.4	1.1	17.6	15.4
77.4	19.3	16.5	17.9	21.4	17.9	17.2	14.2	21.5	18.4	11.8	22.9	21.7	22.4	0.3	16.4	15.6
78.9	17.0	16.0	16.4	18.4	17.6	15.3	14.2	19.3	18.0	11.7	15.9	15.2	18.8	0.6	19.3	16.3
80.4	11.2	12.3	12.8	15.1	14.2	12.5	12.7	16.8	14.4	14.9	15.1	10.8	12.0	0.6	18.4	15.9
81.9	9.7	12.3	12.5	14.7	13.7	12.1	13.3	16.7	15.1	16.1	16.9	11.8	10.3	1.5	17.7	16.2
83.5	9.2	10.9	10.9	14.0	11.8	11.3	11.2	14.3	16.0	13.4	14.3	14.1	10.9	1.0	13.8	13.2
85.1	10.6	10.1	9.6	11.8	10.1	10.2	9.8	12.3	16.7	12.1	11.9	14.0	12.5	0.4	12.0	11.8
86.8	8.9	7.2	7.7	8.3	8.0	8.1	6.8	9.1	13.8	9.3	8.6	10.6	11.0	0.9	9.2	9.9
88.6	4.0	3.0	2.9	2.4	4.1	4.0	2.6	3.7	6.3	3.4	2.5	4.6	6.0	0.3	3.9	5.6
90.4	1.8	1.2	0.8	0.4	1.2	1.2	0.6	0.9	1.9	0.5	0.0	0.9	1.4	-0.2	0.2	1.3
92.2	1.4	0.9	1.1	1.3	0.9	0.9	1.0	0.9	1.1	0.8	0.9	0.7	1.1	1.2	0.9	0.9

Table 12. Area of deformed tubes in B-5 test array

ELEVATION (CM)	OUTSIDE AREA OF TUBE NO. (MM**2) 1	2	3	4	5	6	7	8	9	10	11	12	13	14	15	16
0.0	93	93	94	94	94	95	94	94	93	94	94	93	94	94	95	95
1.8	102	100	101	98	98	97	97	98	97	98	99	99	100	100	99	102
3.5	109	109	109	104	106	102	102	107	106	110	107	110	110	112	111	108
5.0	113	111	109	108	111	106	108	111	116	115	113	116	114	117	113	108
6.5	110	112	109	108	111	107	109	111	116	113	112	113	112	116	111	107
8.4	101	104	103	102	105	103	103	105	102	102	102	102	103	102	102	101
10.0	100	100	100	100	102	100	100	101	102	103	103	102	103	104	103	101
11.6	116	112	110	111	109	107	108	110	113	112	109	109	110	111	108	112
13.5	126	125	119	118	119	119	119	120	130	132	132	127	130	138	125	124
15.5	132	146	128	131	136	130	130	124	147	149	151	146	143	152	133	129
17.0	134	147	128	126	132	125	125	124	152	171	154	165	143	160	138	129
18.5	131	140	127	120	127	122	124	125	142	209	158	178	144	166	148	126
20.0	130	139	134	123	129	127	132	123	145	242	158	175	144	167	153	128
21.5	125	145	155	135	144	141	144	128	147	237	153	173	141	163	159	130
23.0	125	144	189	156	170	158	152	136	145	207	149	171	142	160	169	128
24.7	123	139	244	170	183	168	155	141	150	163	137	154	141	150	147	126
26.4	127	148	228	166	178	166	150	144	166	177	157	150	145	156	145	130
28.0	126	157	154	144	151	143	134	137	162	181	168	144	144	161	146	128
29.5	125	140	129	128	133	130	127	132	147	199	177	146	149	170	151	132
31.5	127	133	122	122	131	127	132	125	147	198	216	149	153	173	155	130
33.5	134	148	141	138	152	143	143	125	210	183	222	153	155	174	157	128
35.5	128	148	148	142	164	150	139	124	223	191	200	159	149	184	147	127
37.1	117	144	145	138	163	148	135	125	171	196	189	160	145	180	142	122
39.0	116	135	131	128	140	129	125	121	151	171	173	162	144	165	144	111
40.8	112	128	125	124	138	127	122	119	142	160	161	171	156	160	148	118
42.6	110	134	136	132	161	142	127	118	120	150	149	169	166	159	144	123
44.4	117	131	134	130	151	135	130	123	126	146	147	158	164	142	154	131
46.4	120	126	131	128	131	127	119	127	142	142	139	141	155	132	145	140
46.9	119	126	129	126	129	127	119	126	146	140	137	137	153	130	141	140
48.0	128	129	131	126	128	129	126	130	164	142	136	133	147	133	138	142
49.6	135	135	127	124	131	136	132	138	170	159	146	140	148	146	139	151
51.2	143	139	129	125	134	131	122	136	186	165	157	149	146	151	146	164
53.0	137	145	143	141	163	148	133	141	179	163	169	150	146	164	153	161
54.6	134	139	137	137	172	163	138	146	169	155	164	152	149	165	159	145
56.2	136	123	125	122	135	140	133	144	160	143	148	145	145	149	152	127
57.8	134	128	124	118	125	122	125	138	131	138	140	138	140	143	143	119
59.6	122	129	126	125	129	124	125	130	123	132	134	132	134	132	134	123
61.2	120	121	120	121	122	120	120	125	122	122	122	122	123	121	122	116
62.8	111	110	110	111	112	111	110	115	109	107	107	107	108	106	107	107
64.4	104	104	104	103	104	104	103	103	104	105	105	105	104	103	103	101
66.0	109	107	107	106	109	107	107	110	107	110	109	109	109	107	108	112
67.8	132	123	121	119	127	129	131	139	141	142	140	145	149	135	135	133
69.5	145	139	133	123	132	140	140	161	140	169	166	177	211	153	150	137
71.0	156	163	148	144	155	179	151	183	133	194	173	211	253	162	162	151
72.8	178	177	144	149	184	233	170	188	157	189	173	246	238	163	177	166
74.3	173	211	138	139	172	229	189	183	211	176	177	248	240	173	187	187
74.8	165	224	139	140	163	214	194	179	233	165	174	233	246	170	191	179
75.8	155	236	148	170	160	196	189	175	270	152	161	205	260	174	187	172
76.3	153	237	154	215	171	198	190	180	275	148	161	196	263	196	220	171
77.4	143	238	175	203	226	201	177	204	255	144	170	185	232	185	190	161
78.9	132	196	163	225	269	210	160	212	178	142	163	172	193	170	170	146
80.4	128	144	132	153	202	189	153	221	152	136	152	158	163	158	149	136
81.9	133	145	125	132	143	150	146	163	146	134	144	149	144	148	138	129
83.5	134	145	131	139	142	133	137	141	125	127	133	139	133	135	128	124
85.1	134	139	132	141	157	132	135	134	124	123	127	131	129	126	123	122
86.8	125	124	121	121	140	122	121	120	119	115	115	120	119	115	115	111
88.6	109	102	103	103	109	106	104	106	105	103	102	104	106	105	105	99
90.4	98	96	96	96	97	97	95	96	97	96	96	96	96	96	96	93
92.2	95	96	95	95	96	95	94	95	95	95	95	96	95	95	95	96

Table 12 (continued)

ELEVATION (CM)	17	18	19	20	21	22	23	24	25	26	27	28	29	30	31	32
0.0	93	94	93	94	94	94	95	94	93	93	94	94	94	94	95	93
1.8	99	101	100	102	103	99	102	100	100	100	102	99	103	98	101	98
3.5	109	113	112	111	112	107	108	112	112	110	114	113	112	111	114	110
5.0	118	121	120	115	114	115	112	118	121	118	120	117	117	120	119	117
6.5	116	118	116	114	109	114	110	115	117	115	117	115	113	116	115	116
8.4	106	103	105	102	102	105	101	106	102	103	104	101	104	106	105	107
10.0	102	103	104	104	105	104	101	102	101	102	102	101	101	103	103	101
11.6	113	111	111	110	113	108	106	113	112	110	111	109	108	110	108	110
13.5	134	139	142	131	124	123	124	134	143	132	133	129	131	136	128	127
15.5	164	160	207	146	129	141	140	152	190	147	154	141	145	163	137	145
17.0	160	176	230	153	133	152	153	161	178	165	166	150	149	167	138	163
18.5	139	183	217	158	130	162	172	167	136	187	171	159	154	164	140	179
20.0	142	166	200	167	129	175	180	196	136	183	167	166	172	167	143	180
21.5	153	154	188	171	129	180	165	208	149	185	163	172	204	169	141	169
23.0	158	161	195	176	131	180	156	166	152	178	181	173	211	176	142	149
24.7	163	193	219	183	136	190	151	146	152	171	189	172	205	180	146	140
26.4	164	217	[illegible]	203	147	205	151	151	152	172	217	178	180	199	160	166
28.0	154	194	184	235	146	220	148	149	141	183	226	180	158	193	152	170
29.5	136	186	168	272	145	227	148	159	134	202	211	182	155	187	154	163
31.5	138	180	164	221	153	217	142	187	136	179	194	173	158	163	153	159
33.5	180	189	179	189	161	208	149	216	147	159	195	162	174	155	149	174
35.5	197	207	204	180	154	181	157	203	149	159	185	157	179	161	147	216
37.1	176	186	225	175	145	167	155	175	140	156	181	149	176	169	145	243
39.0	167	153	264	178	141	179	152	140	133	148	176	148	171	172	157	191
40.8	146	141	234	179	139	191	152	134	124	137	159	145	162	171	170	137
42.6	121	137	195	170	138	195	148	155	112	127	152	141	163	173	180	134
44.4	124	139	171	163	143	210	149	147	116	126	160	139	162	175	202	129
46.4	142	143	164	162	143	232	162	125	130	124	153	132	154	207	209	132
46.9	146	146	157	157	140	234	164	121	131	123	147	128	148	221	191	130
48.0	155	156	152	152	141	248	183	121	136	126	144	131	142	252	177	126
49.6	144	172	166	148	140	268	219	118	130	142	154	138	142	255	162	125
51.2	153	183	164	159	140	265	216	118	126	166	170	146	141	205	150	127
53.0	216	179	158	162	138	207	199	131	155	172	173	151	140	178	154	123
54.6	273	161	154	161	135	168	178	138	176	156	166	152	139	172	156	129
56.2	202	149	148	152	130	147	157	131	150	140	146	144	133	158	144	138
57.8	136	141	139	143	128	136	144	130	124	133	138	138	131	151	136	130
59.6	121	128	126	127	121	127	130	121	122	122	127	127	124	135	125	115
61.2	124	118	118	119	116	122	121	120	121	116	118	118	118	122	117	115
62.8	110	106	105	107	105	107	107	111	107	105	106	106	106	109	105	109
64.4	108	105	105	106	106	104	105	103	103	105	105	105	105	105	104	102
66.0	113	109	108	109	109	109	108	109	106	107	110	108	109	111	110	113
67.8	149	140	147	141	144	144	141	121	128	130	144	140	140	144	139	145
69.5	151	162	218	176	166	202	170	119	133	142	180	162	165	171	157	149
71.0	141	164	247	201	177	256	174	119	127	151	209	189	185	180	157	139
72.8	165	151	239	223	174	262	168	125	129	155	197	234	186	181	155	131
74.3	188	143	228	228	191	240	163	141	123	150	173	223	180	173	148	126
74.8	187	140	220	220	196	230	159	149	120	147	168	221	180	169	148	128
75.8	181	136	202	205	177	209	150	169	119	138	160	189	179	157	146	136
76.3	177	134	193	201	172	201	148	180	122	137	161	182	181	155	145	140
77.4	167	133	172	193	160	176	141	188	125	129	154	161	176	146	140	139
78.9	156	131	154	198	151	156	138	178	131	126	147	150	163	141	132	131
80.4	148	126	139	183	142	146	134	151	131	120	137	140	149	137	125	122
81.9	143	125	135	164	142	146	133	139	128	121	130	134	141	137	124	128
83.5	123	118	124	146	130	135	125	131	115	117	121	127	130	130	119	135
85.1	124	116	120	137	126	128	122	132	115	115	118	125	126	126	120	132
86.8	121	111	112	122	119	118	113	117	115	108	110	116	118	116	112	116
88.6	105	99	99	103	104	104	102	100	102	96	97	103	103	104	103	102
90.4	97	96	95	95	96	97	95	94	97	94	94	95	95	96	95	96
92.2	96	95	95	96	95	95	96	96	97	95	95	95	95	95	95	96

Table 12 (continued)

ELEVATION (CM)	33	34	35	36	37	38	39	40	41	42	43	44	45	46	47	48
0.0	91	92	92	92	92	93	93	94	91	91	92	92	92	93	92	93
1.8	98	103	99	99	98	98	103	101	98	100	100	100	98	101	101	101
3.5	112	119	112	112	109	111	111	107	106	116	113	111	110	116	113	110
5.0	122	126	120	118	117	121	117	112	117	124	115	117	115	125	117	116
6.5	121	120	116	115	115	120	117	115	116	118	112	115	117	119	117	116
8.4	104	103	102	102	103	106	106	106	105	104	102	104	105	107	105	108
10.0	100	103	103	103	103	106	105	103	100	104	102	103	106	106	105	104
11.6	113	113	111	110	110	110	110	110	113	113	113	110	110	112	110	111
13.5	158	141	143	137	134	133	137	116	144	155	150	138	134	141	135	117
15.5	224	164	182	166	159	217	178	124	197	179	181	174	165	167	151	131
17.0	193	171	192	176	185	295	201	140	201	170	173	177	192	165	156	152
18.5	146	163	175	173	217	266	221	156	173	260	157	177	208	16[illegible]	152	163
20.0	151	156	172	173	232	189	260	163	192	258	155	215	206	186	150	166
21.5	181	182	206	167	211	177	257	151	232	225	159	225	196	228	147	152
23.0	193	195	225	165	199	189	235	133	187	222	169	226	194	195	148	133
24.7	202	234	210	158	201	195	192	122	149	205	178	266	195	183	158	124
26.4	216	327	172	162	198	203	171	138	171	192	185	261	217	191	174	141
28.0	183	289	154	157	179	188	163	140	183	174	162	194	260	176	171	152
29.5	171	193	161	154	174	180	169	136	175	168	158	171	291	185	179	153
31.5	157	160	155	161	172	169	164	126	141	161	156	160	239	204	168	128
33.5	153	162	161	207	172	179	155	145	137	159	160	168	195	222	173	137
35.5	153	159	166	221	170	192	151	193	143	152	150	182	177	221	166	188
37.1	140	153	157	209	182	187	157	202	131	144	143	174	176	213	157	196
39.0	122	147	145	169	199	195	182	199	120	139	136	159	182	200	156	172
40.8	120	134	133	151	174	201	185	159	125	136	129	159	183	198	158	152
42.6	115	128	132	147	176	195	165	140	120	135	124	152	176	204	160	149
44.4	126	135	136	147	194	206	155	139	126	142	122	145	168	189	163	176
46.4	148	145	133	143	183	211	160	149	139	147	121	137	161	164	160	244
46.9	150	145	132	140	177	204	161	152	140	150	122	135	163	162	163	251
48.0	157	150	139	139	169	183	167	165	145	157	129	145	171	158	178	241
49.6	150	157	146	141	164	175	167	181	140	157	133	164	193	151	221	185
51.2	134	161	160	147	163	193	172	195	132	162	137	180	205	151	225	166
53.0	155	159	159	146	161	174	170	201	153	173	141	180	171	150	175	160
54.6	167	154	148	142	153	155	161	175	160	166	139	168	150	146	151	158
56.2	151	147	138	136	143	144	149	148	152	142	131	149	136	137	139	151
57.8	132	142	132	132	135	138	138	125	140	134	129	141	134	134	133	137
59.6	126	130	123	122	126	127	125	115	128	122	120	125	126	121	122	123
61.2	119	120	115	115	119	118	118	114	117	115	114	116	116	114	115	116
62.8	106	106	105	104	106	105	107	107	106	106	104	105	105	104	105	106
64.4	104	106	104	104	103	101	102	100	102	104	103	103	103	102	102	98
66.0	106	108	108	108	108	109	109	111	106	109	108	110	108	108	110	108
67.8	126	133	138	136	136	142	139	143	121	135	130	137	131	133	132	130
69.5	143	147	167	158	158	176	160	187	134	140	134	151	145	140	139	150
71.0	143	149	180	182	172	205	167	216	141	138	135	154	166	143	143	161
72.8	130	145	176	180	189	203	168	175	143	134	136	152	210	148	144	161
74.3	122	142	167	169	219	181	166	147	145	134	139	149	242	146	137	147
74.8	124	142	166	166	229	172	160	140	145	133	138	148	234	145	134	141
75.8	127	137	158	155	238	159	150	135	143	132	136	147	232	140	127	130
76.3	130	135	156	153	235	157	147	134	140	130	133	144	217	139	127	128
77.4	134	130	149	150	213	151	140	127	134	126	128	140	179	135	123	123
78.9	136	127	141	148	182	146	135	118	129	123	126	136	149	130	122	128
80.4	128	122	129	139	152	138	127	119	123	119	122	132	132	125	118	127
81.9	125	121	124	134	139	136	126	125	122	119	121	130	128	123	118	125
83.5	115	116	117	124	127	128	119	123	114	113	114	121	121	115	113	118
85.1	111	113	114	120	123	121	116	119	113	111	112	116	118	112	113	116
86.8	112	108	110	115	116	112	111	111	114	108	109	111	113	109	108	110
88.6	102	98	100	103	102	101	101	101	102	99	100	101	104	102	100	100
90.4	95	94	95	97	94	95	95	95	96	95	95	96	96	96	94	95
92.2	95	95	95	95	96	95	96	96	95	95	95	96	95	96	96	95

Table 12 (continued)

ELEVATION (CM)	49	50	51	52	53	54	55	56	57	58	59	60	61	62	63	64	TOTAL
0.0	92	91	92	92	92	92	93	93	91	92	92	92	92	92	92	93	5985
1.8	98	99	99	100	99	98	102	100	99	99	97	98	96	93	101	103	6401
3.5	106	113	119	114	108	112	116	110	109	116	108	108	105	93	113	115	7086
5.0	115	125	131	121	112	124	123	118	115	121	115	115	113	94	118	119	7483
6.5	114	120	125	116	112	118	116	117	114	118	112	116	111	92	115	114	7348
8.4	102	102	107	102	101	106	105	107	102	102	103	104	103	93	107	104	6662
10.0	98	103	103	103	103	105	103	102	100	100	100	101	101	93	104	102	6573
11.6	113	113	112	110	107	110	108	110	114	113	108	111	108	95	111	115	7101
13.5	130	140	142	136	124	136	131	118	131	145	127	140	131	93	140	129	8452
15.5	180	154	207	156	137	153	156	137	144	157	127	134	134	92	154	151	9835
17.0	196	166	256	161	145	178	163	160	151	166	123	124	125	92	145	162	10333
18.5	163	159	288	153	150	207	161	167	157	172	129	137	131	95	158	157	10495
20.0	151	143	258	155	150	227	168	161	164	179	138	161	139	95	165	149	10676
21.5	147	193	223	155	149	209	180	144	164	174	141	177	136	93	155	141	10824
23.0	137	181	200	159	154	171	203	130	159	172	148	180	135	94	148	131	10727
24.7	129	167	192	163	168	187	211	123	144	173	156	168	133	93	139	133	10710
26.4	143	163	204	164	183	197	196	144	139	158	145	149	129	92	133	149	11052
28.0	144	151	208	160	169	177	166	168	132	129	127	133	126	92	141	156	10544
29.5	137	150	208	178	159	172	152	188	130	125	130	143	144	95	157	156	10419
31.5	117	147	189	231	150	160	149	171	128	135	147	187	193	92	200	152	10255
33.5	130	159	179	193	152	152	165	141	144	169	183	296	197	93	291	139	10789
35.5	138	166	174	211	153	160	171	138	153	163	176	200	237	94	281	121	10907
37.1	129	160	177	179	149	171	173	126	155	147	140	145	157	92	201	119	10352
39.0	122	148	177	165	146	176	157	119	148	150	128	122	125	90	151	118	9819
40.8	120	147	171	159	141	175	144	123	141	164	138	137	129	93	154	117	9515
42.6	118	171	163	150	151	174	142	138	128	178	147	166	142	96	168	119	9477
44.4	122	186	153	141	193	161	150	160	131	165	148	162	139	94	152	132	9560
46.4	128	173	141	151	253	158	168	178	134	154	136	130	124	93	140	150	9645
46.9	125	169	139	153	244	158	169	177	133	149	132	127	125	94	141	153	9573
48.0	128	165	143	163	194	163	174	179	134	143	130	129	130	95	143	147	9689
49.6	130	155	152	173	155	161	171	160	138	137	136	144	139	93	148	127	9852
51.2	135	155	154	184	147	154	160	166	138	141	152	185	159	94	162	133	10088
53.0	136	154	148	180	142	145	145	175	142	150	190	225	176	96	198	146	10285
54.6	132	149	142	162	137	137	137	170	133	145	188	203	162	94	210	148	10010
56.2	139	139	136	149	136	131	134	163	138	134	141	154	138	93	191	148	9183
57.8	141	133	133	138	133	128	132	156	144	133	129	125	122	94	162	148	8626
59.6	124	121	121	121	121	118	122	132	128	124	124	116	112	93	131	135	8009
61.2	118	117	117	116	117	116	118	125	119	117	118	115	111	94	121	126	7603
62.8	106	105	106	105	104	104	104	107	107	105	104	104	102	93	106	108	6844
64.4	104	105	105	105	104	103	103	101	105	104	104	102	103	95	103	101	6656
66.0	105	108	109	111	108	108	108	110	108	108	110	107	108	94	109	109	6966
67.8	118	128	131	140	135	127	130	135	125	128	139	131	131	95	131	130	8604
69.5	127	135	138	150	146	136	140	158	133	132	135	126	134	94	134	136	9652
71.0	134	138	138	149	144	138	139	181	139	139	128	119	124	95	137	132	10331
72.8	136	135	139	148	138	140	134	185	140	142	133	123	119	94	125	125	10588
74.3	137	133	140	147	136	140	132	167	141	136	140	134	129	94	133	123	10599
74.8	137	131	139	146	135	140	131	163	141	133	143	139	133	95	135	127	10510
75.8	137	130	137	146	133	136	127	151	141	129	150	144	140	96	131	124	10295
76.3	136	127	134	144	131	134	125	147	138	123	149	144	140	95	129	124	10313
77.4	133	127	130	137	130	128	122	138	131	116	141	138	140	94	131	125	9959
78.9	128	126	126	131	129	124	121	133	130	116	125	124	132	94	133	126	9487
80.4	115	117	118	123	122	118	118	127	122	123	124	114	117	94	131	125	8748
81.9	112	118	118	123	121	117	120	127	124	126	127	116	113	96	129	126	8395
83.5	111	115	115	121	116	115	115	122	125	120	122	121	115	95	121	120	7973
85.1	114	113	112	116	113	113	112	118	127	117	117	121	118	94	117	116	7809
86.8	110	107	108	109	109	109	106	111	121	111	110	114	115	95	111	113	7333
88.6	101	99	99	98	101	101	98	100	105	99	98	102	105	94	100	104	6546
90.4	97	95	95	94	95	95	94	95	96	94	93	95	96	93	93	96	6132
92.2	96	95	95	95	95	95	95	95	95	94	95	94	95	95	95	95	6124

Table 13. Flow area restriction in B-5 test array

Elevation (cm)	Entire 8 × 8 array		Inner 6 × 6 array		Central 4 × 4 array	
	Maximum (%)	Minimum (%)	Maximum (%)	Minimum (%)	Maximum (%)	Minimum (%)
0.0	0.1	0.1	0.1	0.1	0.1	0.1
1.8	5.5	5.5	6.0	6.0	5.8	5.8
3.5	14.9	14.9	16.5	16.5	16.1	16.1
5.0	20.3	20.3	22.1	22.1	21.6	21.6
6.5	18.5	18.5	19.6	19.6	19.2	19.2
8.4	9.1	9.1	9.1	9.1	9.3	9.3
10.0	7.9	7.9	8.8	8.8	9.0	9.0
11.6	15.1	15.1	14.9	14.9	15.1	15.1
13.5	33.5	33.5	36.1	36.1	36.5	36.5
15.5	52.9	52.4	57.7	57.7	62.5	62.5
17.0	60.0	59.2	68.8	68.8	74.5	74.5
18.5	62.0	61.4	75.4	75.2	74.5	74.5
20.0	65.5	63.9	78.0	76.5	75.3	75.3
21.5	66.8	65.9	78.3	77.2	79.3	79.3
23.0	65.1	64.6	76.9	76.1	81.5	81.5
24.7	65.1	64.4	76.8	76.1	85.6	85.6
26.4	69.2	69.0	82.5	82.1	90.7	89.9
28.0	63.2	62.1	77.3	75.3	84.8	83.0
29.5	60.5	60.4	74.9	74.7	84.1	83.6
31.5	58.1	58.1	69.9	69.9	74.7	74.7
33.5	66.6	65.4	70.2	69.6	76.2	76.2
35.5	68.0	67.0	70.1	70.1	75.9	75.9
37.1	59.7	59.5	66.6	66.6	73.0	73.0
39.0	52.2	52.2	63.7	63.7	72.4	72.4
40.8	48.5	48.0	60.5	59.8	68.3	66.5
42.6	47.5	47.5	56.9	56.9	62.3	62.3
44.4	48.9	48.7	58.3	57.8	62.3	62.3
46.4	50.2	49.8	58.1	58.1	60.6	60.6
46.9	49.0	48.8	56.4	56.4	58.8	58.8
48.0	51.5	50.4	59.2	57.4	64.2	60.3
49.6	53.8	52.7	64.3	62.2	69.4	64.9
51.2	56.0	55.9	65.2	64.9	68.1	67.5
53.0	58.6	58.6	60.2	60.2	60.1	60.1
54.6	55.0	54.8	53.0	53.0	52.2	52.2
56.2	43.5	43.5	43.5	43.5	42.7	42.7
57.8	35.9	35.9	38.0	38.0	37.7	37.7
59.6	27.5	27.5	28.6	28.6	28.0	28.0
61.2	21.9	21.9	21.8	21.8	21.2	21.2
62.8	11.6	11.6	10.9	10.9	10.8	10.8
64.4	9.0	9.0	9.6	9.6	9.5	9.5
66.0	13.2	13.2	13.5	13.5	13.5	13.5
67.8	35.6	35.6	38.8	38.8	40.1	40.1
69.5	49.9	49.9	58.3	58.3	64.4	64.4
71.0	59.5	59.2	69.6	69.6	81.3	81.3
72.8	63.9	62.7	72.2	72.2	87.3	87.3
74.3	63.6	62.8	71.4	70.5	85.2	85.1
74.8	63.0	61.6	69.9	68.2	83.0	82.5
75.8	59.9	58.7	64.2	62.0	75.3	73.9
76.3	59.3	58.9	61.5	60.9	71.8	70.4
77.4	54.1	54.1	52.6	52.6	59.6	59.6
78.9	48.9	47.7	45.2	45.2	50.6	50.6
80.4	37.7	37.6	36.7	36.7	41.0	41.0
81.9	32.8	32.8	33.2	33.2	36.7	36.7
83.5	27.0	27.0	26.5	26.5	28.4	28.4
85.1	24.8	24.8	23.1	23.1	24.7	24.7
86.8	18.3	18.3	16.9	16.9	18.2	18.2
88.6	7.5	7.5	7.1	7.1	7.7	7.7
90.4	1.9	1.9	1.8	1.8	1.9	1.9
92.2	1.7	1.7	1.8	1.8	1.8	1.8

Table 14. Tube displacements at 17.0-cm elevation

B-5 BUNDLE SECTION AT 17.0-CM ELEVATION
TUBE CENTROID LOCATIONS BASED ON AREA ENCLOSED BY O.D. PERIMETER
WITH ORIGIN ARBITRARILY LOCATED AT PRETEST CENTROID OF TUBE NO. 1
(NOTE: POSITIVE X IS LEFT TO RIGHT. POSITIVE Y IS TOP TO BOTTOM.)

-------PRETEST	CENTROID---	POSTTEST	CENTROID---	CTR	DISPLACEMENT--	
TUBE NO.	X-DIM. (MM)	Y-DIM. (MM)	X-DIM. (MM)	Y-DIM. (MM)	X-DIRECT (MM)	Y-DIRECT (MM)
1	0.000	0.000	0.427	-1.054	0.427	-1.054
2	14.427	-0.045	13.999	-1.267	-0.428	-1.222
3	28.854	-0.089	29.481	-0.676	0.626	-0.586
4	43.282	-0.134	43.938	-0.551	0.656	-0.417
5	57.709	-0.179	58.284	0.258	0.576	0.437
6	72.136	-0.224	72.588	0.264	0.452	0.488
7	86.563	-0.268	86.998	0.345	0.434	0.613
8	100.990	-0.313	101.354	0.553	0.363	0.866
9	0.045	14.427	-0.116	12.953	-0.161	-1.474
10	14.472	14.382	14.418	13.011	-0.054	-1.372
11	28.899	14.338	29.430	13.215	0.530	-1.123
12	43.326	14.293	43.978	13.601	0.652	-0.692
13	57.754	14.248	58.279	14.707	0.525	0.459
14	72.181	14.204	72.330	14.144	0.150	-0.060
15	86.608	14.159	86.746	14.923	0.138	0.764
16	101.035	14.114	101.400	14.768	0.365	0.653
17	0.089	28.854	-0.882	26.897	-0.972	-1.957
18	14.517	28.810	13.918	27.462	-0.599	-1.347
19	28.944	28.765	29.393	28.186	0.450	-0.579
20	43.371	28.720	44.417	28.032	1.046	-0.688
21	57.798	28.676	57.972	28.387	0.174	-0.288
22	72.225	28.631	71.848	28.139	-0.378	-0.491
23	86.653	28.586	86.486	29.348	-0.167	0.762
24	101.080	28.541	101.081	29.188	0.001	0.647
25	0.134	43.282	-0.480	41.078	-0.614	-2.204
26	14.561	43.237	14.205	41.394	-0.357	-1.843
27	28.989	43.192	29.354	42.586	0.366	-0.607
28	43.416	43.147	44.138	41.842	0.722	-1.305
29	57.843	43.103	58.557	42.708	0.714	-0.395
30	72.270	43.058	72.903	41.898	0.633	-1.160
31	86.697	43.013	86.971	43.401	0.274	0.387
32	101.125	42.969	100.983	43.959	-0.142	0.991
33	0.179	57.709	-0.883	56.349	-1.061	-1.359
34	14.606	57.664	14.198	54.701	-0.408	-2.963
35	29.033	57.619	29.055	56.730	0.022	-0.890
36	43.460	57.575	43.130	56.339	-0.331	-1.236
37	57.888	57.530	57.001	57.712	-0.887	0.182
38	72.315	57.485	72.345	57.099	0.030	-0.387
39	86.742	57.441	87.482	58.648	0.740	1.208
40	101.169	57.396	102.277	59.557	1.108	2.161
41	0.224	72.136	0.043	70.511	-0.180	-1.625
42	14.651	72.091	17.415	71.357	2.764	-0.734
43	29.078	72.047	29.418	71.846	0.340	-0.201
44	43.505	72.002	43.995	71.833	0.490	-0.169
45	57.932	71.957	58.261	72.896	0.329	0.939
46	72.360	71.912	72.874	74.421	0.514	2.509
47	86.787	71.868	87.367	73.781	0.580	1.914
48	101.214	71.823	100.795	73.451	-0.419	1.628
49	0.268	86.563	0.042	85.536	-0.226	-1.027
50	14.695	86.518	13.882	86.875	-0.814	0.357
51	29.123	86.474	29.068	87.229	-0.054	0.755
52	43.550	86.429	43.866	87.425	0.316	0.996
53	57.977	86.384	57.283	87.359	-0.694	0.974
54	72.404	86.340	71.549	89.284	-0.856	2.944
55	86.831	86.295	86.156	87.486	-0.676	1.192
56	101.259	86.250	100.408	87.846	-0.851	1.596
57	0.313	100.990	-0.616	100.947	-0.929	-0.044
58	14.740	100.946	14.327	100.914	-0.413	-0.032
59	29.167	100.901	29.003	101.754	-0.164	0.853
60	43.595	100.856	43.256	101.186	-0.339	0.330
61	58.022	100.812	57.513	101.095	-0.509	0.284
62	72.449	100.767	71.513	102.400	-0.936	1.633
63	86.876	100.722	85.958	101.948	-0.918	1.226
64	101.303	100.677	99.335	101.461	-1.969	0.783

5. SOME OBSERVATIONS AND LIMITED INTERPRETATIONS OF RESULTS

The conditions used in this test were conducive to large deformation, and thus, rod-to-rod mechanical interactions were a significant factor in the deformation. In addition, vestiges of small variations in the initial temperature distribution remained during the transient and influenced the deformation behavior in an important manner. On casual examination, the test results appear anomalous and, perhaps, confusing. However, detailed examination leads to clarification and proper interpretation. A number of observations are noted and discussed in this section to provide additional insight and understanding and to facilitate interpretation of the data.

Direct measurement of the true burst temperature was not possible because of the limited number (4) of thermocouples available in each simulator. In previous tests, we defined the burst temperature to be the maximum temperature measured on that simulator at the time of burst without consideration of deformation patterns and failure locations. Experience with single-rod tests, in which more thermocouples (12) were used for this purpose, had shown that this expediency gave acceptable estimates. However, it presented some difficulties in our analysis and evaluation of the B-5 data, and we used different criteria to define the burst temperature. Figure 131 shows the data from simulator 22 plotted on expanded scales and will be used to illustrate the discussion.

The first reported[2] burst temperature data were obtained from tabular outputs, essentially the same as given in Table 4, and were based on the above definition; these corresponded to data recorded at the time of burst by, for example, TE-2 in the figure. Later, when the transient temperature plots, like Fig. 131, became available, it was noted that the traces of many thermocouples that had indicated the highest temperature during most of the transient exhibited what was assumed at the time to be erratic behavior (i.e., an unexplained reduction in temperature) during the final 2 or 3 s before burst. This type behavior is illustrated by TE-1 and TE-4 in Fig. 131. The traces of those thermocouples exhibiting this behavior were extrapolated to provide estimates of the temperature that would have been measured if the earlier trend had continued until burst, and these extrapolated values, if higher than the recorded values, were reported[3] as "corrected" burst temperature data. Justification of this approach assumed that (1) the true burst temperature was at least as high as the maximum value recorded on that simulator regardless of location and (2) the erratic behavior observed near the end of the transient was caused by malfunctioning of the thermocouple and should be corrected.

Further analysis[5] of the data indicated that both of these assumptions may be incorrect in a bundle test with a very uniform temperature distribution and extensive rod-to-rod interactions. Firstly, it was observed that interaction of the exterior simulators with the thin shroud (Fig. 61) could be correlated with simulator thermocouple response. This is illustrated best by the temperature data plotted in Fig. 132 for simulator 62, which was heated but unpressurized. The slight temperature reduction (10° to 15°C) recorded by TE-3 (facing the shroud at the 28-cm pretest elevation; see Fig. 3) at about 46 s after power-on is attributed to contact between the hot simulator and the relatively cool shroud.

Figures 79 and 130 show this tube was displaced against the shroud; this most likely occurred when simulator 38 burst at 45.70 s.

Secondly, it was observed that the maximum temperatures, whether recorded or extrapolated, at the time of burst did not correspond in a consistent manner with posttest strain measurements at the thermocouple. For example, larger-than-average deformation was noted in ~75% of the simulators at axial locations of those thermocouples that had indicated maximum temperatures at the onset of significant deformation (i.e., at the time of maximum pressure about 32 to 38 s after power-on). However, at the time of burst, the temperature at these locations was not necessarily the highest recorded in a given simulator. Compare the traces of TE-1, TE-2, and TE-4 in Fig. 131 to the deformation profile in Fig. 129. This suggests that the temperature distribution prior to the onset (and during the early phase) of deformation may be more important in determining the burst location than the distribution at the time of burst. Because stress is a function of instantaneous tube wall thickness (i.e., local strain), the failure stress can be reached at a site where the strain is higher (due to its prior temperature history) but the temperature is lower (due to greater cooling and/or interaction with adjacent tubes) before it is reached at another site where the temperature is higher but the strain is lower. Also, local stress patterns can be altered by rod-to-rod contact forces.

For this reason, we reevaluated the temperature measurements and correlated the data with the deformation profiles and the burst locations. Based on this evaluation, the extrapolated temperatures were not, in general, representative of the temperature at the burst site at the time of failure. Instead, we believe the thermocouples measured the correct temperature (at the sites where they were attached), and we revised[5] ~60% of the previously "corrected" data.[3] The revised data and the thermocouples on which they are based are given in Table 15 (the data are also given in Table 5); the maximum observed temperatures at the time of burst (from Table 4) are included for comparison. In the absence of more definitive data and analysis, we believe the "selected" temperature is the best estimate of the burst temperature.

In addition to this general behavior, there were local temperature perturbations, caused by contact between the shroud and the exterior simulators, that influenced the axial distribution of the deformation. The thin reflector strips used in the shroud panels were preloaded axially with high-temperature springs (Fig. 44) to compensate for differential expansion and to keep the strips taut during the test. As evidenced by the discoloration and distortion patterns in Fig. 61, the strips wrinkled (localized inward bowing) and contacted the exterior simulators at more or less regular intervals along the length. The simulators were cooled, enhancing the azimuthal temperature gradients and limiting the deformation, in the contact areas. In contrast, the temperature was slightly higher, with less pronounced gradients, and the deformation was greater in the noncontact areas. This behavior resulted in a periodic variation in the amplitude of the deformation, as typified by Fig. 128. Further, the cyclic pattern of all the simulators on a given face were aligned, as illustrated for the north face in Fig. 133 (see Fig. 3 for relative positions). The effect was less pronounced at the corner positions than at the intermediate positions (compare the profiles of rods 1 and 8 with those of rods 3–6) because shroud box corner restraints prevented the transverse buckling patterns from bowing inward and contacting the corner simulators as frequently.

Figure 134 is a similar plot that compares the profiles of the first layer of simulators with those of the second layer. Although some cyclic behavior is evident in the latter, it is less pronounced, except for simulators 9 and 16, which were located on the west and east faces of the array and thus were in contact with the shroud. The cyclic effect was practically dissipated with two layers of simulators as shown by the comparison in Fig. 135 of the deformation profiles of the second and third layers of simulators.

As shown in Fig. 123, there was, in general, a preferred direction for the orientation of the bursts in the outer ring of simulators and the next inner ring to a lesser extent, indicating an influence of azimuthal temperature gradients in each ring. Burst strain data for these simulators, depicted in Fig. 12, also showed the influence of the temperature gradients, although some burst strains were unexpectedly large. This is explained by the mechanism discussed above. That is, areas in contact with the shroud had higher azimuthal temperature gradients and reduced burst strains, while areas not in contact had smaller gradients and larger burst strains. The gradients and the burst strains in the next inner ring were also affected (but to a lesser extent) by contact with the exterior simulators, as inferred from Fig. 134. Because of the cyclic behavior in the deformation profile, the volumetric expansion (and the average strain) over the heated length of the exterior simulators was also less than that of the interior simulators, as illustrated in Fig. 11. These data comparisons clearly show that the azimuthal temperature gradient effect was sufficient to influence both the burst locations and the volumetric expansion and, as a result, the magnitude of the local flow restriction in the two outer rings of simulators. Altogether, the data show that the equivalent of two rows of deforming guard simulators is necessary in small bundles to duplicate temperature and mechanical boundary conditions of large bundles.

The burst frequency histogram depicted in Fig. 8 was based on the number of bursts per 0.5-s time interval and showed that the distribution was fairly normal. However, a more detailed analysis, based on the number of bursts per 0.1-s interval, showed that the bursts were clustered in three or four groups (ignoring the outlying ones) and that the clustering could be correlated with test vessel pressure, as illustrated in Fig. 136. The hot, high-pressure gas escaping from the simulators caused the vessel pressure to increase about 225 kPa for a few seconds. With each burst, the vessel pressure increased incrementally, and the differential pressure and the deformation rate in the simulators decreased. After several bursts, the pressure increase was sufficient to delay the bursts momentarily; following a very short recovery period, the bursts resumed to repeat the cycle.

Analysis of the differential pressure vs time plots for the simulators indicated slightly different deformation behavior that we believe marked the onset of rod-to-rod interactions in neighboring simulators and may have been associated with the clustering. For example, the pressure data of three such simulators (Nos. 37, 38, and 46) that had large volumetric expansions (65% to 75%) are plotted in Fig. 137 from about the time of maximum pressure to failure; the steam pressure is also included for reference. Although displaced in time, the rate of pressure decrease was approximately the same for each simulator until the last few seconds of deformation. Comparing simulators 38 and 46, the rates were nearly identical until the time of the first tube burst at 44.00 s; after this time, the pressure in simulator 46 decreased at a faster rate until the simulator failed at 46.25 s. Comparing simulators 38 and 37, the rates were nearly identical until simulator 38 burst at 45.70 s; after this time, the pressure in simulator 37 decreased at a much slower rate until the simulator failed at 47.20 s.

As depicted in Fig. 9, the simulators burst in a very narrow temperature range for a wide range of pressure; the interior simulators, in general, burst at lower pressures, indicating higher volumetric expansions for these simulators (Fig. 11). Evidently, the larger volumetric expansion was caused by smaller azimuthal temperature gradients and more intense rod-to-rod interactions. In comparing the results of the B-5 test with the B-3 test, which was tested under the same nominal conditions but without rod-to-rod interactions, it was concluded[7] that mechanical interactions were the primary factor contributing to the greater volumetric expansion in the B-5 test. This is explained as follows.

During the B-5 test, tube expansion throughout the array caused the tubes to touch and generate contact forces. Because the simulators were constrained, these forces could not be relieved by tube bowing and creation of additional void space. With further expansion, the tubes tended toward square cross sections to fill the available space. (See for example tube 19 in Fig. 108.) The external contact forces caused redistribution of the straining pattern in both the azimuthal and longitudinal directions. As a result, the rate of expansion decreased at those axial locations in contact and continued unimpeded at other ballooning locations. Redistribution and growth of the ballooned regions occurred with great rapidity as evidenced by the pressure histories (Fig. 137). These dynamic processes, enhanced by the very uniform temperature distribution in the interior of the array, continued until local conditions at some point in each tube caused failure; this was usually in the direction of the open coolant channel areas (Fig. 123). The sequence of bursting also influenced the interactions because a burst tube offered less resistance to encroachment of neighboring tubes still undergoing deformation. For example, tube 37 burst after all its neighbors, and it was able to maintain a nearly circular shape (Fig. 108) until it burst because its highly ballooned (and burst) neighbors offered little resistance to encroachment. In contrast, however, note in Fig. 109 that tube 4, although already burst, had sufficient strength at this elevation to resist encroachment by its neighbor (tube 12), which burst at a later time. The temperature increased very little (it may have decreased in the highly ballooned regions) during the time these rapid and complex interactions were taking place; and as a result, a large variation in volumetric expansion (and burst pressure) was observed for a small variation in burst temperature.

The above discussion suggests that temperature uniformity and rod-to-rod interactions are at least as important as heating rate in determining first the amount of deformation and secondly the burst pressure.

The wide scatter observed when deformation data are plotted as a function of burst temperature and heating rate is probably the result of not taking these factors into consideration.

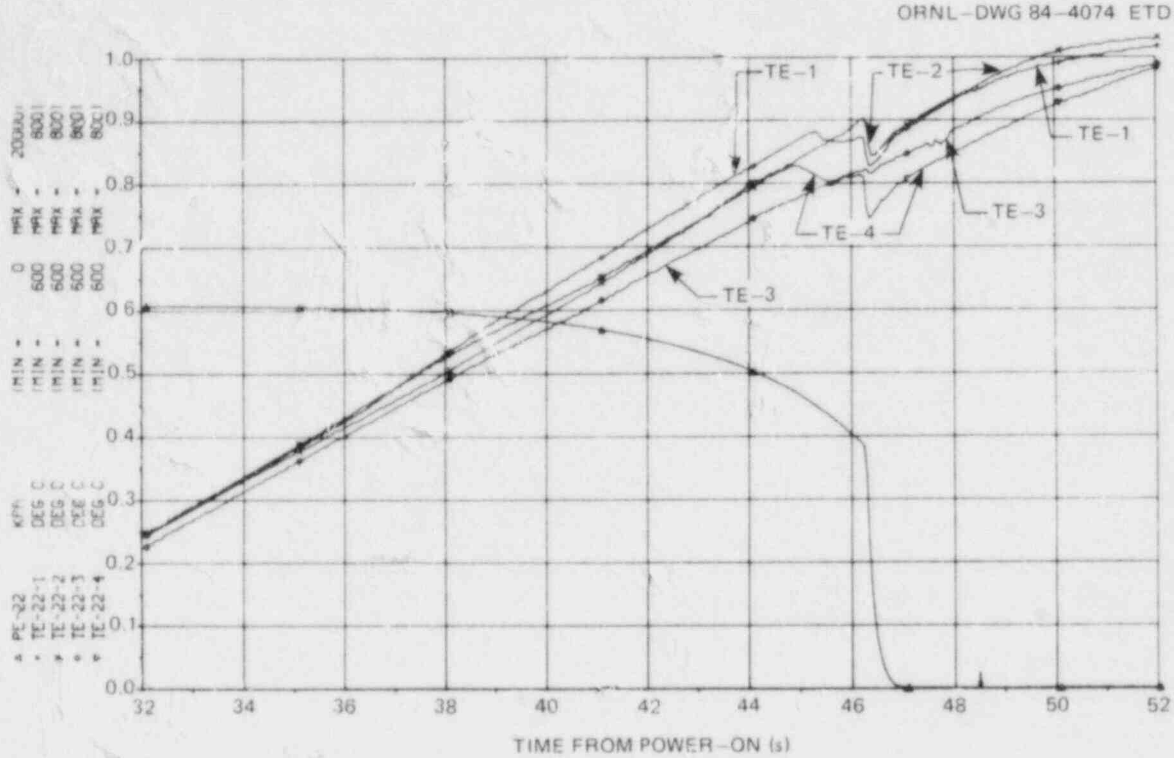

Fig. 131. Pressure and temperatures measured in simulator 22.

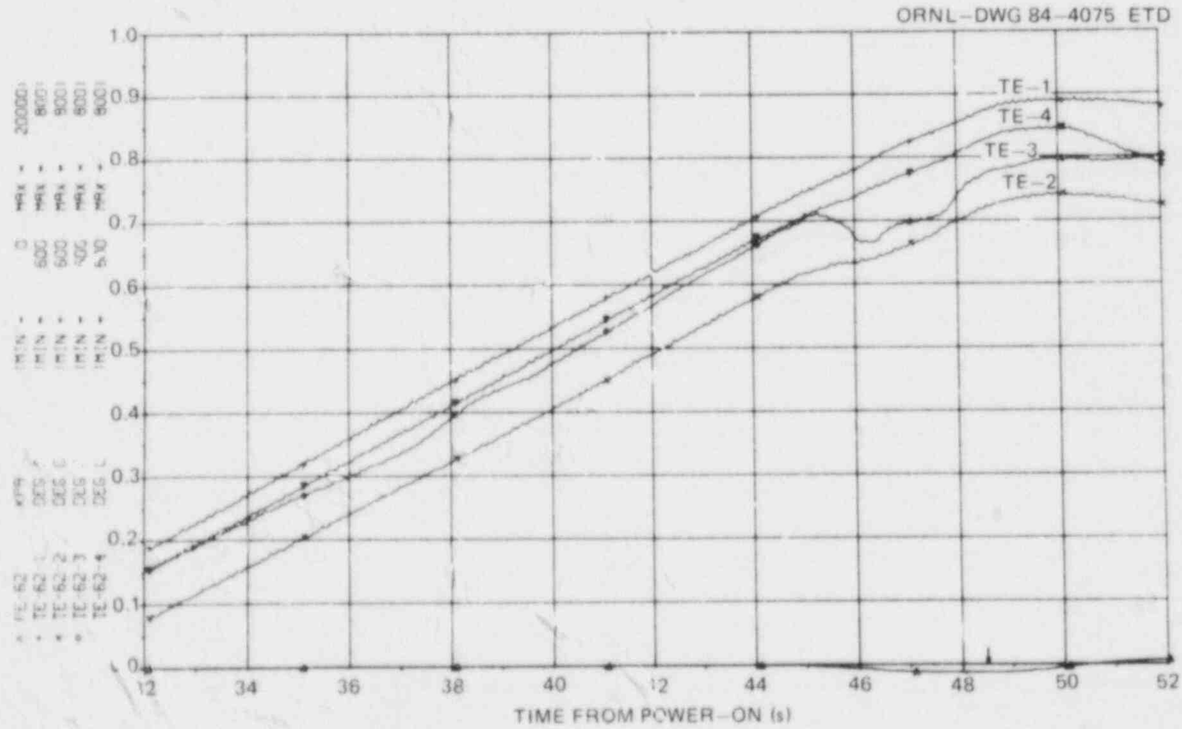

Fig. 132. Temperatures measured in simulator 62.

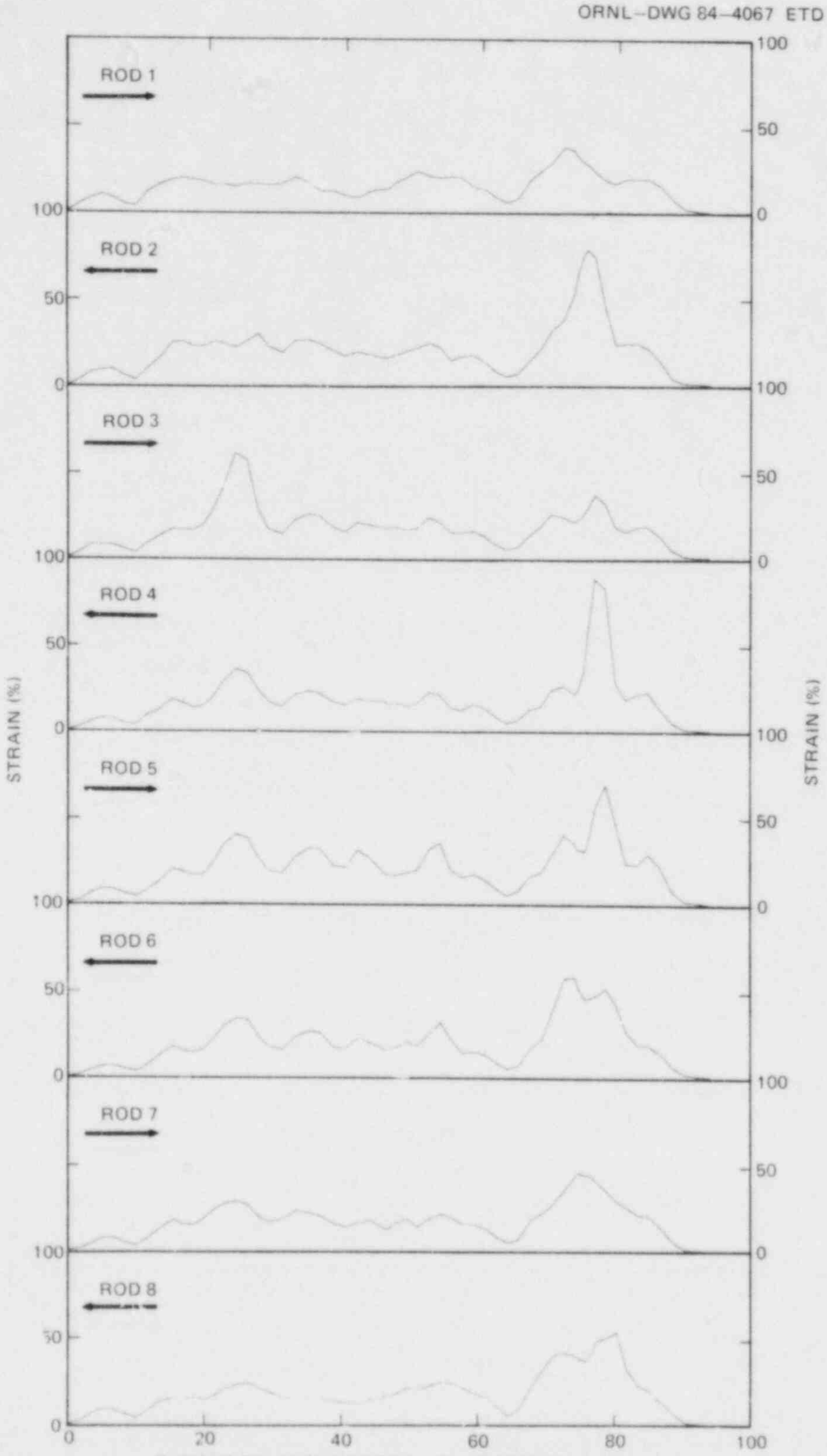

Fig. 133. Comparison of deformation profiles of first layer of tubes on north side of bundle.

ORNL-DWG 84-4077 ETD

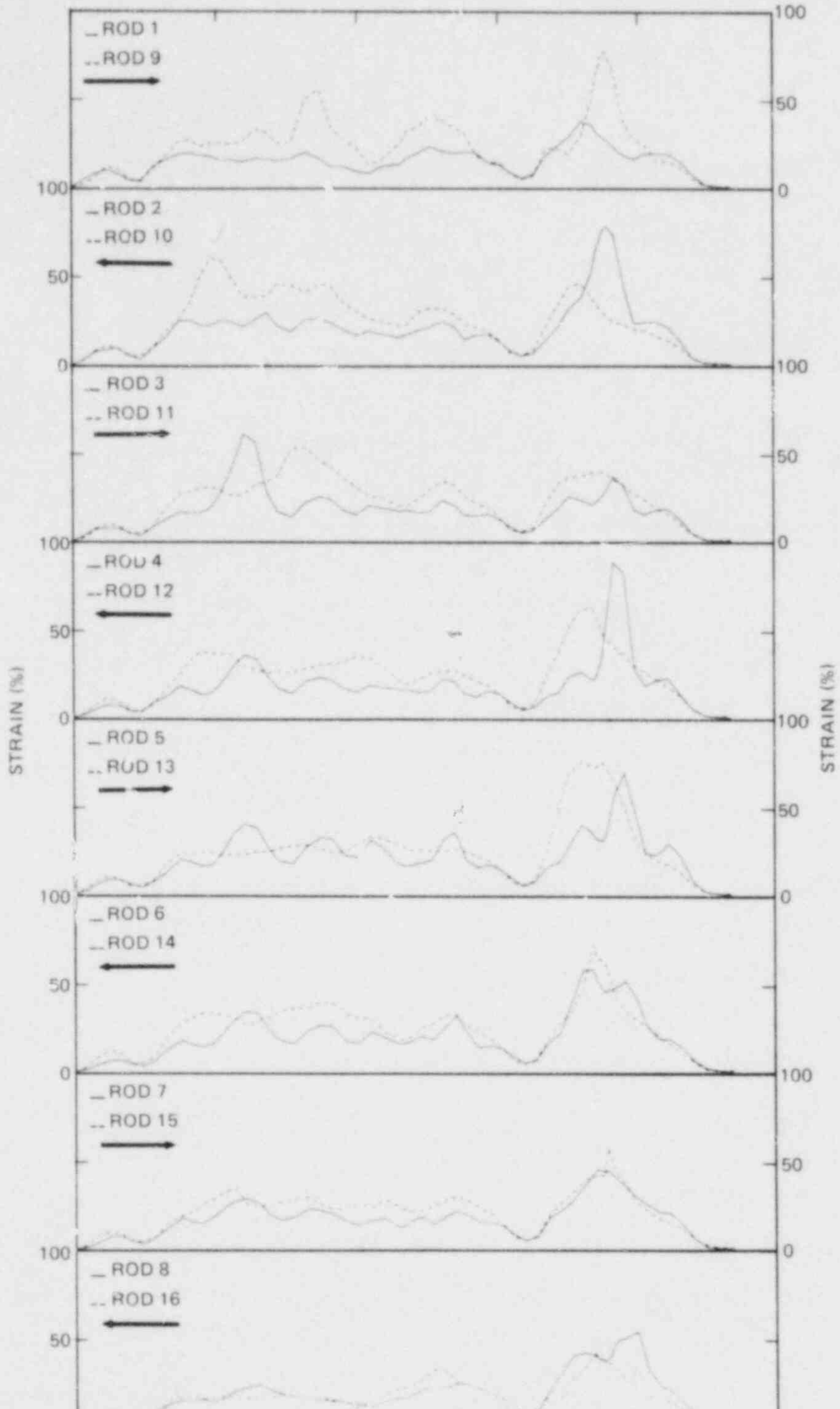

Fig. 134. Comparison of deformation profiles of first and second layers of tubes on north side of bundle.

ORNL-DWG 84-4078 ETD

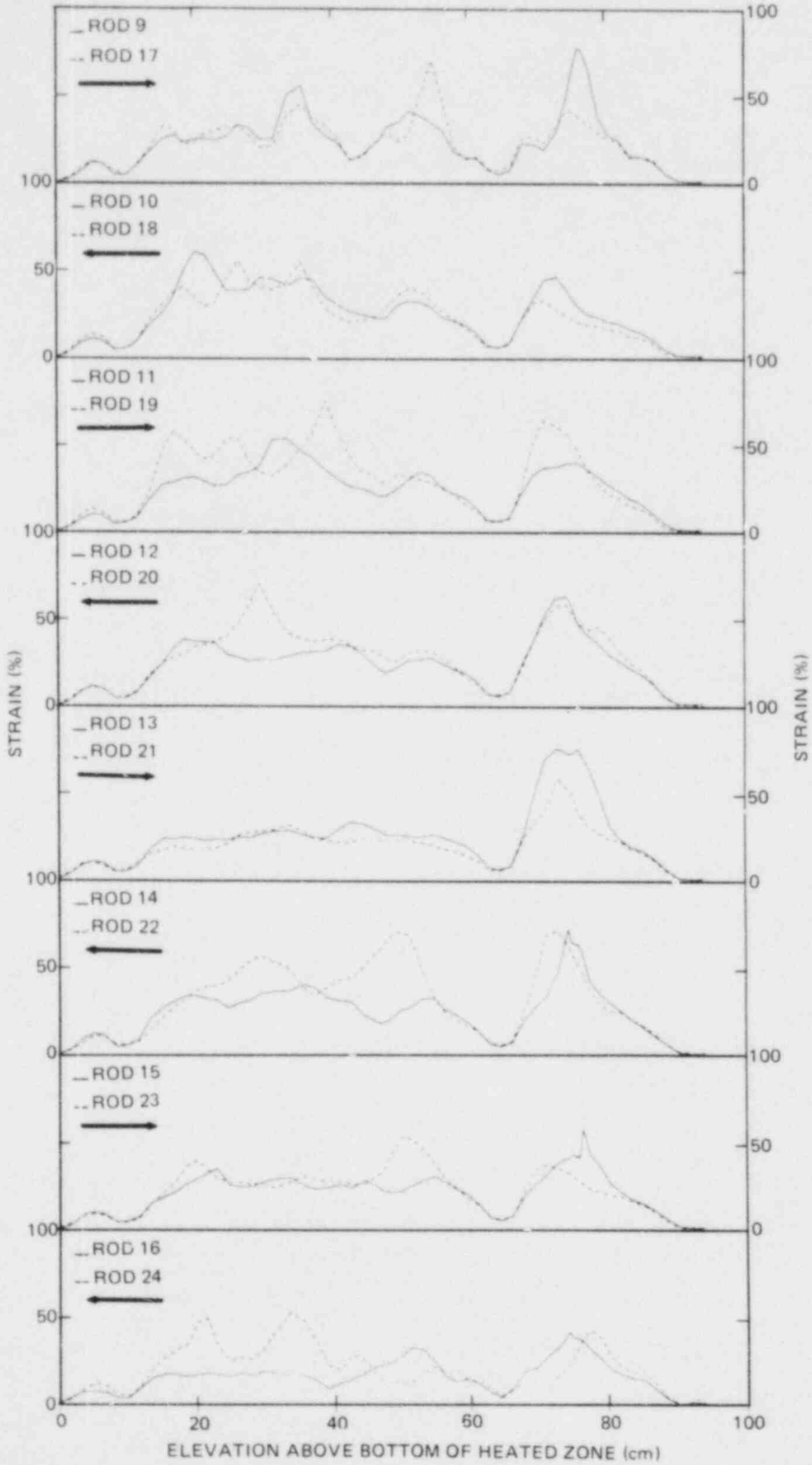

Fig. 135. Comparison of deformation profiles of second and third layers of tubes on north side of bundle.

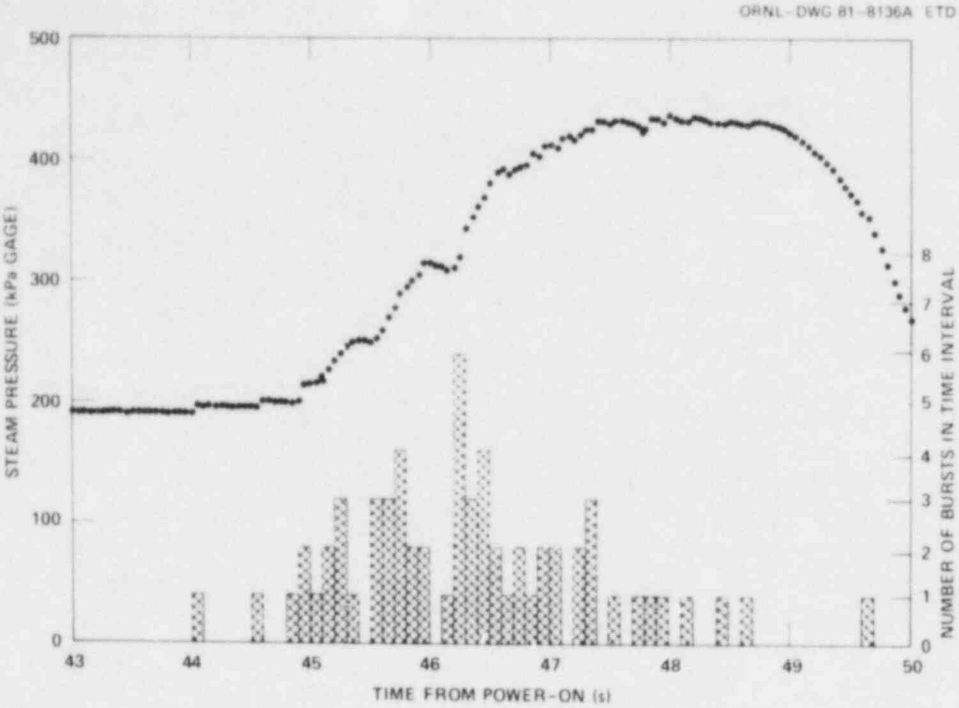

Fig. 136. Correlation of burst frequency with vessel pressure.

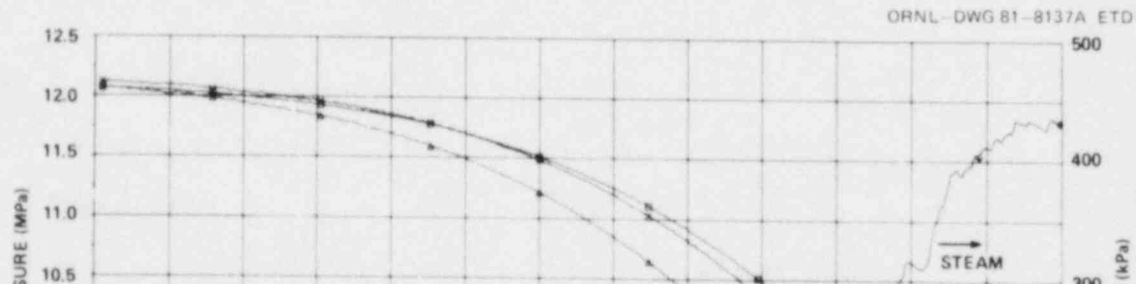

Fig. 137. Comparison of pressure behavior in simulators 37, 38, and 46.

Table 15. Estimated burst temperatures in B-5 test

Rod No.	Observed[a]		Selected[b]		Number of TE nearest to failure[c]	Rod No.	Observed[a]		Selected[b]		Number of TE nearest to failure[c]
	Temperature (°C)	TE No.	Temperature (°C)	TE No.			Temperature (°C)	TE No.	Temperature (°C)	TE No.	
1	776	3	776	3	2	33	772	1	762	4	2
2	770	3	765	1	2	34	773	4	773	4	4
3	755	3	762	4	1	35	779	4	774	2	2
4	769	1	769	1	2	36	768	2	756	1	1
5	778	4	778	4	4	37	783	1	771	4	2
6	778	3	778	3	1	38	777	4	770	2	1
7	766	4	773	4	4	39	773	4	773	4	4
8	768	2	768	2	1	40	782	1	773	4	2
9	787	3	766	4	3	41	769	4	769	4	2
10	772	3	772	3	3	42	773	1	773	1	1
11	768	4	768	4	3	43	775	2	775	2	2
12	780	2	774	3	3	44	763	3	763	3	3
13	767	3	767	3	3	45	769	1,3	769	1,3	3
14	777	2	763	1	1	46	762	2,4	763	4	4
15	766	1	766	1	1	47	777	1	774	2	1
16	775	3	775	3	4	48	763	3	763	3	4
17	786	4	776	1	2	49	761	4	761	4	2
18	774	2	770	4	1	50	768	2	768	2	4
19	774	3	774	3	1	51	771	1	759	3	3
20	764	2	764	2	2	52	765	4	757	3	3
21	766	4	763	3	3	53	769	2	760	4	4
22	780	2	776	1	2	54	771	1	766	4	2
23	772	1	772	2	2	55	763	2	763	2	2
24	771	1	769	3	3	56	781	1	781	1	2
25	763	1	763	1	3	57	752	3	753	2	2
26	770	2	770	2	2	58	757	1	757	1	3
27	768	1	760	4	3	59	770	4	770	4	4
28	783	1	783	1	1	60	755	2	755	2	2
29	770	1	770	4	4	61	768	1	768	1,3	1
30	784	1	784	1	4	62	*d*	*d*	*d*	*d*	*d*
31	773	2	773	2	2	63	775	1	775	1	1
32	768	2	768	2	4	64	743	1	756	4	4

[a] Maximum temperature indicated by listed TE at time of rupture.

[b] Best-estimate value based on evaluation of preburst temperature data of listed TE and of posttest deformation profiles.

[c] Excluding TEs located at grid elevations.

[d] Simulator unpressurized (but heated) and did not burst.

ACKNOWLEDGMENTS

Data presented in this report reflect the combined efforts of a number of people over an extended period of time, spanning fabrication, testing, pretest and posttest examination of the test array, and reducing and processing the test data.

We wish to acknowledge the contribution of W. A. Bird for his careful attention to all the instrumentation and control aspects of the test; E. L. Biddle, J. N. Money, and C. Cross for assembly of the test array and for the many other necessary support tasks; F. R. Gibson for programming and operating the CCDAS and for processing much of the data; C. M. Boles for excellent pretest and posttest photography; F. G. Childress for developing procedures and casting the array in a high-quality epoxy matrix; B. C. Leslie for the sectioning, polishing, and excellent photography of the bundle cross sections; L. Jung and coworkers for developing software and digitizing the photographic data; N. J. Price for developing software and processing much of the digitized data; the Fuel Pin Simulator Development Group, under the leadership of R. W. McCulloch, for development and fabrication of the fuel simulators; and the many other groups and individuals who had a part in the test and in the preparation and publication of this report.

We would like also to express our appreciation for the support and guidance provided by the NRC Program Managers: Dr. M. L. Picklesimer for several years prior to his retirement and, afterward, Dr. R. Van Houten.

REFERENCES

1. R. H. Chapman et al., *Quick-look Report on MRBT B-5 (8 × 8) Bundle Test*, Internal Report ORNL/MRBT-5, Union Carbide Corp. Nuclear Div., Oak Ridge Natl. Lab., July 1980.

2. R. H. Chapman, *Multirod Burst Test Program Prog. Rep. January–June 1980*, NUREG/CR-1883 (ORNL/NUREG/TM-426), Union Carbide Corp. Nuclear Div., Oak Ridge Natl. Lab.

3. A. W. Longest, *Multirod Burst Test Program Prog. Rep. January–June 1981*, NUREG/CR-2366, Vol. 1 (ORNL/TM-8058), Union Carbide Corp. Nuclear Div., Oak Ridge Natl. Lab.

4. J. L. Crowley, *Multirod Burst Test Program Prog. Rep. July–December 1981*, NUREG/CR-2366, Vol. 2 (ORNL/TM-8190), Union Carbide Corp. Nuclear Div., Oak Ridge Natl. Lab.

5. R. H. Chapman, *Multirod Burst Test Program Prog. Rep. January–June 1982*, NUREG/CR-2911 (ORNL/TM-8485), Union Carbide Corp. Nuclear Div., Oak Ridge Natl. Lab.

6. A. W. Longest, R. H. Chapman, and J. L. Crowley, "Boundary Effects on Zircaloy-4 Cladding Deformation in LOCA Simulation Tests," *Trans. Am. Nucl. Soc.* 41, 383 (1982).

7. R. H. Chapman, J. L. Crowley, and A. W. Longest, "Effect of Bundle Size on Cladding Deformation in LOCA Simulation Tests," in *Zirconium in the Nuclear Industry: Sixth International Symposium, ASTM STP 824*, eds. D. G. Franklin, R. B. Adamson, and B. Cox, American Society for Testing and Materials (in publication).

8. A. W. Longest, J. L. Crowley, and R. H. Chapman, *Variations in Zircaloy-4 Cladding Deformation in Replicate LOCA Simulation Tests*, NUREG/CR-2810 (ORNL/TM-8413), Union Carbide Corp. Nuclear Div., Oak Ridge Natl. Lab., September 1982.

9. R. H. Chapman et al., *Bundle B-3 Test Data*, ORNL/NUREG/TM-360, Union Carbide Corp. Nuclear Div., Oak Ridge Natl. Lab., January 1980.

10. R. H. Chapman, A. W. Longest, and J. L. Crowley, *Experiment Data Report for Multirod Burst Test (MRBT) Bundle B-6*, NUREG/CR-3460 (ORNL/TM-8890) (in publication).

11. R. H. Chapman et al., *Bundle B-1 Test Data*, ORNL/NUREG/TM-322, Union Carbide Corp. Nuclear Div., Oak Ridge Natl. Lab., June 1979.

12. R. H. Chapman et al., *Bundle B-2 Test Data*, ORNL/NUREG/TM-337, Union Carbide Corp. Nuclear Div., Oak Ridge Natl. Lab., August 1979.

13. A. W. Longest, R. H. Chapman, and J. L. Crowley, *Experiment Data Report for Multirod Burst Test (MRBT) Bundle B-4*, NUREG/CR-2968 (ORNL/TM-8509), Union Carbide Corp. Nuclear Div., Oak Ridge Natl. Lab., December 1982.

14. R. W. McCulloch, P. T. Jacobs, and D. L. Clark, *Development of a Fabrication Procedure for the MRBT Fuel Simulator Based on the Use of Cold-Pressed Boron Nitride Preforms*, NUREG/CR-1111 (ORNL/NUREG/TM-362), Union Carbide Corp. Nuclear Div., Oak Ridge Natl. Lab., March 1980.

15. W. A. Simpson, Jr., et al., *Infrared Inspection and Characterization of Fuel-Pin Simulators*, ORNL/NUREG/TM-55, Union Carbide Corp. Nuclear Div., Oak Ridge Natl. Lab., November 1976.

16. R. H. Chapman (comp.), *Characterization of Zircaloy-4 Tubing Procured for Fuel Cladding Research Programs*, ORNL/NUREG/TM-29, Union Carbide Corp. Nuclear Div., Oak Ridge Natl. Lab., July 1976.

17. R. H. Chapman, *Multirod Burst Test Program Prog. Rep. July—September 1976*, ORNL/NUREG/TM-77, Union Carbide Corp. Nuclear Div., Oak Ridge Natl. Lab.

18. J. E. Lewis et al., "Texture Measurement Techniques for Zircaloy Cladding: A Round-Robin Study," pp. 39—62 in *Zirconium in the Nuclear Industry: Fifth Conference*, ASTM STP 754, ed. D. G. Franklin, American Society for Testing and Materials, 1982.

19. W. E. Baucum and R. E. Dial, *An Apparatus for Spot Welding Sheathed Thermocouples to the Inside of Small-Diameter Tubes at Precise Locations*, ORNL/NUREG/TM-33, Union Carbide Corp. Nuclear Div., Oak Ridge Natl. Lab., August 1976.

20. R. L. Anderson, K. R. Carr, and T. G. Kollie, *Thermometry in the Multirod Burst Test Program*, NUREG/CR-2470 (ORNL/TM-8024), Union Carbide Corp. Nuclear Div., Oak Ridge Natl. Lab., March 1982.

21. R. H. Chapman, *Multirod Burst Test Program Prog. Rep. April—June 1979*, NUREG/CR-1023 (ORNL/NUREG/TM-351), Union Carbide Corp. Nuclear Div., Oak Ridge Natl. Lab.

22. D. A. Powers and R. O. Meyer, *Cladding Swelling and Rupture Models for LOCA Analysis*, NUREG-0630, U.S. Nuclear Regulatory Commission, April 1980.

23. R. T. Bailey, *Steady-State Pressure Losses for Multirod Burst Test (MRBT) Bundle B-5*, NUREG/CR-2597 (ORNL/Sub/80-40441/1), Union Carbide Corp. Nuclear Div., Oak Ridge Natl. Lab., April 1982.

24. J. F. Mincey, Steady-State Axial Pressure Losses Along the Exterior of Deformed Fuel Cladding: Multirod Burst Test (MRBT) Bundles B-1 and B-2, NUREG/CR-1011 (ORNL/NUREG/TM-350), Union Carbide Corp. Nuclear Div., Oak Ridge Natl. Lab., January 1980.

Appendix A

TRANSIENT PRESSURE AND TEMPERATURE PLOTS

Individual pressure (differential) and temperature plots are presented for the simulators as a function of time after power-on in Figs. A.1—A.64 on sheet 1 of the microfiche enclosures in the pocket attached to the inside back cover of this report. A typical example of the plots was given in Fig. 40 to illustrate the type of data available from the microfiche records.

Temperatures measured on the four faces of the shroud are plotted in Figs. A.65—A.72. These plots are grouped to provide information on the axial and circumferential temperature distributions in the shroud. The characteristic bundle average temperature (TAV-10) is also included in the plots for comparison. Typical examples of these plots were shown in Figs. 38 and 39 to illustrate the type and format of the data presented in the microfiche records.

Temperatures obtained at up to four azimuthal locations on the outside surface of the simulators (Fig. 3) are presented in Figs. A.73—A.76. The plots include the temperature measured by an internal thermocouple at the same elevation for comparison. Typical examples of the plots were shown in Figs. 41 and 42 to illustrate the type of data available in the microfiche records.

Appendix B

MEASURED CONDITIONS AT SELECTED TIMES OF INTEREST

Summary tables of the bundle conditions measured at the times of the individual tube bursts are presented in Tables B.1—B.64 on sheet 2 of the microfiche enclosures in the pocket attached to the inside back cover of this report. An example was given in Table 6 to illustrate the type, format, and identification of the data available from the microfiche records.

Similar tables, giving summary test conditions over a 70-s time span, are presented in Tables B.65—B.107. These tables, with 2-s time intervals for the first 34 s, 1-s intervals for the next 16 s, and 2-s intervals for the remaining 20 s, can be used to approximate either the transient of an individual simulator or that of the bundle as a whole from power-on until ~20 s after the last tube burst.

Appendix C

GEOMETRIC PARAMETERS OF SECTION PHOTOGRAPHIC DATA

The section photographs were digitized and reduced to tables of geometric parameters that were used for verification of the digitized data and as source files for further processing. For documentary purposes, Tables C.1—C.64 are reproduced on sheet 3 of the microfiche enclosures in the pocket attached to the inside back cover of this report. An example was given as Table 10 to illustrate the type, format, and identification of the data available from the microfiche records.

Appendix D

DEFORMATION PROFILES

The strain matrix (Table 11) was used to generate axial profiles of the circumferential strain in each of the tubes. These are presented in Figs. D.1—D.64 on sheet 4 of the microfiche enclosures in the pocket attached to the inside back cover of this report. Example plots were presented in Figs. 126—129 to elucidate certain features and to illustrate the type and format of the information available from the microfiche records.

Appendix E

TUBE CENTROID DISPLACEMENTS AT EACH AXIAL NODE

A least-squares fitting routine was used to minimize the average displacement between the pretest and posttest centroids of the 64 tubes as described in Sect. 4.3.4. The results are presented in Tables E.1—E.64 on sheet 5 of the microfiche enclosures in the pocket attached to the inside back cover of this report. An example was given in Table 14 to illustrate the type and format of the data available from the microfiche records.

Appendix F

PLOTS OF TUBE DISPLACEMENTS AT EACH AXIAL NODE

The least-squares fitting routine that was used to minimize the average displacement between the pretest and posttest centroids of the 64 tubes was combined with the routine that reconstructed the images of the section photographs to produce a plot of the posttest tube locations relative to an imaginary grid at the respective axial node. The plots show, in effect, the permanent displacement of the tubes within their individual unit cells and aid visualization of subchannel flow area restriction. The plots are presented in Figs. F.1—F.64 on sheet 6 of the microfiche enclosures in the pocket attached to the inside back cover of this report. An example was depicted in Fig. 130 to illustrate the type and format of the data available from the microfiche records.

NUREG/CR-3459
ORNL/TM-8889
Dist. Category R2, R3

Internal Distribution

1-5. R. H. Chapman
6-10. J. L. Crowley
11. D. S. Griffith
12. D. O. Hobson
13-17. A. W. Longest
18. A. P. Malinauskas
19. H. E. Trammell
20. Patent Office
21. Nuclear Safety Information Center
22. Central Research Library
23. Document Reference Section
24-25. Laboratory Records Department
26. Laboratory Records (RC)

External Distribution

27. Office of Assistant Manager for Energy Research and Development, DOE, ORO, Oak Ridge, TN 37830
28. Chief, Fuel Behavior Branch, Office of Nuclear Regulatory Research, Nuclear Regulatory Commission, Washington, DC 20555
29. Chief, Core Performance Branch, Office of Nuclear Reactor Regulation, Nuclear Regulatory Commission, Washington, DC 20555
30. R. Van Houten, Fuel Behavior Branch, Office of Nuclear Regulatory Research, Nuclear Regulatory Commission, Washington, DC 20555
31. G. P. Marino, Fuel Behavior Branch, Office of Nuclear Regulatory Research, Nuclear Regulatory Commission, Washington, DC 20555
32. R. A. Adamson, Mail Code V-03, General Electric Company, Vallecitos Atomic Laboratory, P.O. Box 846, Pleasanton, CA 94566
33. D. L. Burman, Westinghouse Nuclear Fuel Division, P.O. Box 355, Pittsburgh, PA 15230
34. C. E. Crouthamel, Exxon Nuclear, Inc., 2955 George Washington Way, Richland, WA 99352
35. F. J. Erbacher, Project Nukleare Sicherheit, Kernforschungszentrum Karlsruhe, Postfach 3640, 75 Karlsruhe, Federal Republic of Germany
36. M. D. Freshley, Pacific Northwest Laboratories, P.O. Box 999, Richland, WA 99352
37. R. Potter, UKAEA Atomic Energy Research Establishment, Harwell, Didcot, Oxfordshire, OX11 ORA, England
38. D. L. Hagrman, EG&G Idaho, Inc., INEL, Idaho Falls, ID 83401
39. T. Healey, CEGB Berkeley Nuclear Laboratories, Berkeley, Gloucestershire, GL13 9PB, England
40. E. D. Hindle, UKAEA Springfields Nuclear Laboratories, Salwick, Preston, PR4 ORR, England
41. S. Saito, Japan Atomic Energy Research Institute, Tokai-Mura, Naga-Gum, Ibaraki-Ken, Japan
42. T. Howe, EG&G Idaho, Inc., INEL, Idaho Falls, ID 83401
43. S. Kawasaki, Japan Atomic Energy Research Institute, Tokai-Mura, Naga-Gum, Ibaraki-Ken, Japan
44. E. T. Laats, EG&G Idaho, Inc., INEL, Idaho Falls, ID 83401

45-46. W. Lowenstein, Electric Power Research Institute, 3412 Hillview Avenue, P.O. Box 10412, Palo Alto, CA 94304
47. A. L. Lowe, Babcock and Wilcox Company, P.O. Box 1260, Lynchburg, VA 24505
48. R. Duffey, Electric Power Research Institute, 3412 Hillview Avenue, P.O. Box 10412, Palo Alto, CA 94304
49. H. Rininsland, Projekt Nukleare Sicherheit, Kernforschungszentrum Karlsruhe, Postfach 3640, 75 Karlsruhe, Federal Republic of Germany
50. P. A. Smerd, Combustion Engineering, Inc., 1000 Prospect Hill Road, Windsor, CT 06093
51. W. Spencer, EG&G Idaho, Inc., INEL, Idaho Falls, ID 83401
52-53. Technical Information Center, DOE, Oak Ridge, TN 37830
54-438. Distribution as shown for NRC categories R2 and R3 (NTIS-10)

☆U.S. GOVERNMENT PRINTING OFFICE: 1984-746-067/4095

NRC FORM 335 (11-81)

U.S. NUCLEAR REGULATORY COMMISSION

BIBLIOGRAPHIC DATA SHEET

1. REPORT NUMBER (Assigned by DDC)
NUREG/CR-3459
ORNL/TM-8889

4. TITLE AND SUBTITLE (Add Volume No., if appropriate)
Experiment Data Report for Multirod Burst Test (MRBT) Bundle B-5

2. (Leave blank)

3. RECIPIENT'S ACCESSION NO.

7. AUTHOR(S)
R. H. Chapman, J. L. Crowley, and A. W. Longest

5. DATE REPORT COMPLETED

MONTH	YEAR
July	1984

9. PERFORMING ORGANIZATION NAME AND MAILING ADDRESS (Include Zip Code)
Oak Ridge National Laboratory
Post Office Box X
Oak Ridge, TN 37830

DATE REPORT ISSUED

MONTH	YEAR
August	1984

6. (Leave blank)

8. (Leave blank)

12. SPONSORING ORGANIZATION NAME AND MAILING ADDRESS (Include Zip Code)
Division of Accident Evaluation
Office of Nuclear Regulatory Research
U.S. Nuclear Regulatory Commission
Washington, DC 20555

10. PROJECT/TASK/WORK UNIT NO.

11. FIN NO.
B0120

13. TYPE OF REPORT
Topical

PERIOD COVERED (Inclusive dates)

15. SUPPLEMENTARY NOTES

14. (Leave blank)

16. ABSTRACT (200 words or less)

B-5 test data are presented and interpreted to the extent necessary for understanding pertinent features of the 8 x 8 test. Objectives of the test were to investigate the effects of array size and rod-to-rod interactions on cladding deformation in the high-alpha-Zircaloy temperature range under conditions that simulated the adiabatic heatup (reheat) phase of a light-water-reactor loss-of-coolant accident. Test conditions, nominally the same as used in an earlier 4 x 4 (B-3) test, were conducive to large deformation. The fuel pin simulators were electrically heated (3.0 kW/m) and were slightly cooled with a very low flow (Re $\sim$ 140) of low-pressure superheated steam. Cladding temperature increased at a rate of 9.8°C/s. The simulators burst in a very narrow temperature range, with an average of 768°C. Cladding burst strain ranged from 32 to 95%, with an average of 61%. Heated length volumetric expansion ranged from 35 to 79%, with an average of 52%. Average burst strain was slightly greater for the interior than for the exterior simulators; average volumetric expansion was significantly greater. Maximum coolant channel flow area reduction was 69% for the entire 8 x 8 array, 83% for the interior 6 x 6 array, and 91% for the central 4 x 4 array. The results show deformation was greater in the bundle interior and suggest rod-to-rod mechanical interactions caused axial propagation of the deformation.

17. KEY WORDS AND DOCUMENT ANALYSIS

Zircaloy
Nuclear fuel cladding
Loss-of-coolant accident simulation
Bundle burst tests
Flow blockage
Fuel pin simulators

17a. DESCRIPTORS

Tubes
Deformation
Rod-to-rod interactions
Boundary conditions
Light-water-reactor

17b. IDENTIFIERS/OPEN-ENDED TERMS

18. AVAILABILITY STATEMENT
Unlimited

19. SECURITY CLASS (This report)
Unclassified

20. SECURITY CLASS (This page)
Unclassified

21. NO. OF PAGES

22. PRICE
$

NRC FORM 335 (11-81)